Efficient Thermohydrodynamic Radial and Thrust Bearing Modeling for Transient Rotor Simulations

Vom Fachbereich Maschinenbau
der Technischen Universität Darmstadt
zur Erlangung des Grades eines
Doktor-Ingenieurs (Dr.-Ing.)
eingereichte

Dissertation

von

Ioannis Chatzisavvas

aus Ptolemaida, Griechenland

Referent: Prof. Dr.-Ing. Bernhard Schweizer
Korreferent: Prof. Dr.-Ing. Wolfgang Seemann

Tag der Einreichung: 24.10.2017
Tag der mündlichen Prüfung: 28.02.2018

Darmstadt, 2018
D17

Foreword

The following research was conducted between October 2013 and April 2017 during my doctoral studies at the Institute of Applied Dynamics in Technische Universität Darmstadt.

I would like to thank the head of the institute, Prof. Dr.-Ing. B. Schweizer, for his motivating supervision. His ideas, comments and suggestions are highly appreciated as well as the really many hours he devoted to my research.

I would also like to thank Prof. Dr.-Ing. W. Seemann from Karlsruhe Institute of Technology (KIT) for his valuable feedback as a second reviewer. His comments and suggestions improved significantly the present work.

Many thanks go to Dr.-Ing. Aydin Boyaci for his guidance and advices during the largest part of my research. His ideas and his thorough supervision ensured the quality of this work. Special thanks to Dr. techn. Fadi Dohnal for his supervision at the beginning of my doctoral studies and for all his useful scientific and administrative help. I gratefully appreciate the help of Dr. Athanasios Chasalevris for his valuable help and the many discussions. The help of Dr.-Ing. Panagiotis Koutsovasilis is greatly acknowledged. His ideas as well as his constant help shaped the thesis in its current format.

A huge thanks goes also to my colleagues Dr.-Ing. Pu Li, Dr.-Ing. Daixing Lu, Gerrit Nowald, Marcel Mahner and Dr.-Ing. Andreas Lehn for their help and the useful discussions. Of course, a big thank you goes also to the secretaries of the institute, Helga Lorenz and Maria Rauck for making my life easier throughout these years.

Many thanks deserve the students of Technische Universität Darmstadt, who during their B.Sc. or M.Sc. theses assisted our research. Namely, Oliver Jörg and Marcel Bauer for developing thermal models for radial bearings, Aleksej Stange and Hambo Kan for developing efficient ball bearing models, Tim Ahlswede and Waldemar Kan for the simulations and the experimental results in the area of turbocharger rotor balancing, Mark Fellner for assisting in the area of rotor modeling and Liliang Wang for developing a thrust bearing optimization toolbox.

I gratefully acknowledge the 3-year scholarship for doctoral students from the German Academic Exchange Service (DAAD).

Finally, a huge thank you for Angeliki, for her love and patience.

To my parents, Konstantino and Dafni

Contents

Abstract

Hydrodynamic bearings are usually employed to support rotating machines, both in the axial as well as in the radial direction. Both bearing types influence the vibration behavior of rotors. Moreover, the oil-temperature influences the hydrodynamic bearing forces. In this work, efficient thermohydrodynamic bearing models for thrust and radial bearings are developed. Run-up simulations are performed for the identification of the influence of the bearings on the nonlinear rotor vibrations.

The Reynolds equation, which describes the hydrodynamic pressure distribution in the bearings, is solved using a highly efficient approach. The Global Galerkin approach, using appropriate trial and test functions, is used for the approximation of the solution of the Reynolds equation, leading to heavily reduced simulation times when compared with Finite Difference or Finite Element approaches. For radial bearings, a novel semi-analytical method is developed using also the Global Galerkin approach. The oil-temperature in the thrust bearings is captured through the energy equation, which is decoupled from the Reynolds equation under appropriate assumptions. For the oil-temperature in radial bearings with full- as well as semi-floating rings a global thermal energy balance is used between the two oil-films and the bearing ring. The transient temperature terms in this energy balance are taken into consideration and their significance for the numerical stability of the solver is demonstrated.

A turbocharger rotor is modeled in a multibody simulation software. The complete system consists of a flexible shaft, a turbine and a compressor wheel, as well as a thrust bearing and two full-floating ring bearings. The equations of motion of the turbocharger rotor are coupled with the equations of the thermohydrodynamic bearing models and they are solved simultaneously at each time-integration step during a run-up simulation. The simulation results show that the oil-temperature and the gas forces in the axial direction exert a large influence on the rotor vibrations.

The geometry of the pads in thrust bearings will be optimized using a novel approach. In this work, statistical and neural network methods are used, avoiding the drawbacks of optimization algorithms. Usually, thrust bearings are optimized for higher load capacity and lower friction losses. Using the proposed optimization approach, thrust bearings can be optimized not only for load capacity and friction losses but also towards a better vibration behavior of the complete rotordynamic system.

The validation of the thrust and the radial bearing modeling is performed through

comparisons with experimental results. For radial bearings, a standard shaft motion test is used and for the thrust bearing a new testing approach is implemented. The simulation results are in a good agreement with the experimental data.

Abstract in German

Bei rotierenden Maschinen werden häufig hydrodynamischen Lager eingesetzt, sowohl in axialer als auch in radialer Richtung. Die beiden Lagerarten beeinflussen das Schwingungsverhalten des Rotors. Außerdem beeinflusst die Öltemperatur die hydrodynamischen Lagerkräfte. Im Rahmen dieser Arbeit werden effiziente thermohydrodynamische Modelle für Axial- und Radiallager entwickelt. Die Identifizierung des Einflusses der Lagergestaltung auf die nichtlinearen Schwingungen der Rotoren wird mithilfe transienter Hochlaufsimulationen durchgeführt.

Die Reynoldsgleichung, die den hydrodynamischen Schmierdruck beschreibt, wird anhand eines rechenzeit-effizienten Verfahrens gelöst. Die Globale Galerkin Methode liefert mit geeigneten Ansatz- und Testfunktionen eine approximierte Lösung, deren Rechenzeit gegenüber anderen Verfahren, wie der Finiten Elemente oder der Finiten Differenzen Methode, mindestens eine Größenordnung kleiner ist. Für die Approximation der Lösung der Reynoldsgleichung in kreiszylindrischen Radiallagern mit und ohne Umfangsnut wird eine semi-analytische Methode entwickelt. Innerhalb des Axiallagermodells wird die Energiegleichung verwendet um die Öltemperatur zu bestimmen. Diese wird durch eine geeignete Annahme von der Reynoldsgleichung entkoppelt. Für die Radiallagerung, sowohl mit rotierenden als auch mit stehenden Lagerbuchsen, wird eine globale thermische Bilanz zwischen den beiden Ölfilmen und der Buchse erstellt. Die transienten Temperaturterme werden in dieser Bilanz berücksichtigt und es zeigt sich, dass sie maßgeblich die numerische Stabilität des Solvers beeinflussen.

Ein Turbolader-Rotor wird in einer Mehrkörpersimulation-Software erstellt. Das Gesamtsystem besteht aus einer flexiblen Welle, einem Turbinen- und einem Verdichterrad, sowie einem Axiallager und zwei radialen Schwimmbuchsenlagern. Die Bewegungsgleichungen des Turbolader-Rotors werden mit den thermohydrodynamischen Gleichungen der Lager in jedem Zeitschritt während einer transienten Hochlaufsimulation simultan gelöst. Die Simulationsergebnisse zeigen, dass die Öltemperatur und die in axialer Richtung wirkenden Gaskräfte einen großen Einfluss auf das Schwingungsverhalten des Rotors ausüben.

Zur Optimierung des Axiallagers wird ein neues Optimierungsverfahren eingeführt. Die Geometrie der Pads eines Axiallagers ist üblicherweise auf eine möglichst große Tragfähigkeit und eine möglichst kleine Reibleistung optimiert. Im Rahmen dieser Arbeit findet die Optimierung nicht mit einem Optimierungsalgorithmus statt, sondern

wird mit statistischen Methoden und neuronalen Netzwerken durchgeführt. Dadurch wird das Axiallager neben der Tragfähigkeit und der Reibleistung auch für ein verbessertes Schwingungsverhalten optimiert.

Die Validierung der Axial- und die Radiallagermodelle erfolgt experimentell. Für die Radiallagerung wurde eine Wellenbahn-Messung durchgeführt. Für die Axiallagerung wurde ein spezifisches Experiment konzipiert. Die Simulationsergebnisse zeigen eine gute Übereinstimmung mit der Experimenten.

Chapter 1

Introduction

1.1 Motivation

Turbocharging internal combustion engines in the automotive industry improves their efficiency and may lead to lower fuel consumption. In this way, turbochargers support the trend for the engine downsizing and assist car manufacturers in reducing the fuel emissions.

The turbocharger rotor consist of a shaft and two wheels, the turbine and the compressor. They are usually supported by hydrodynamic bearings, both in the radial and the axial direction, however, the use of rolling element bearings is not rare. In Figure 1.1 the basic components of a turbocharger rotor/bearing system are illustrated. The exhaust gases from the engine drive the rotor of the turbocharger and the com-

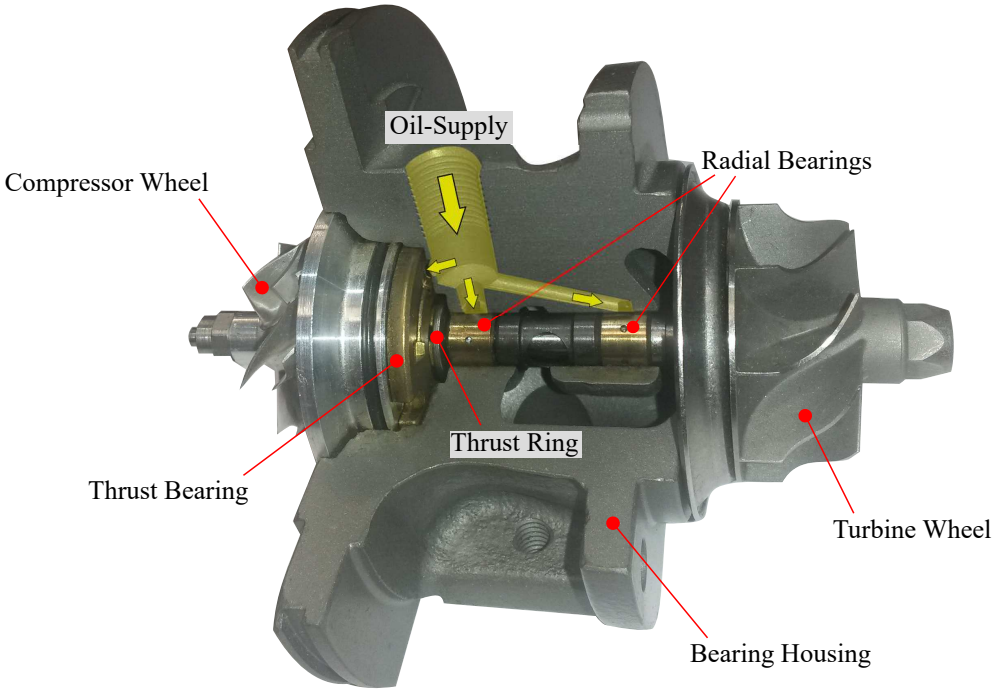

Figure 1.1: Turbocharger rotor/bearing system

pressor wheel supplies the engine with high-pressure air. Due to this procedure, they are also called exhaust-gas turbochargers. Despite their small size, a collaboration of several scientific branches like rotordynamics, acoustics, fluid dynamics, flow dynamics, thermodynamics and others is needed for the description and the modeling

of a turbocharger system. Their harsh operating conditions make them susceptible to acoustic and vibration problems and may lead to their premature replacement or even to failure. This thesis is therefore motivated by the need for a better understanding of the vibrational behavior of turbocharger rotors, where complex nonlinear phenomena usually occur.

The main sources of the rotor vibrations are the floating-ring hydrodynamic bearings. Their modeling is a rather challenging task. Detailed bearing models, although well-established, prohibit thorough parameter studies in transient simulations, as they entail an enormous computational cost. The nonlinear hydrodynamic bearing forces − significantly influenced by the oil-temperature and the temperature of the surrounding solids (shaft, floating ring and housing) − in combination with a rotor, which operates under highly transient conditions, constitute a rather complex system regarding the rotor vibrations. Self-excited vibrations, mode interactions, internal resonances, combination frequencies are some of the nonlinear phenomena that can be observed during the operation of such rotors. A better understanding of these phenomena is rather imperative for robuster systems with maximum life-span and reduced losses, free from unwanted vibration and acoustic problems. However, this not a trivial issue. Together with the complex nonlinear phenomena, several unknown parameters have to be accounted for, e.g. the mass unbalance of the rotor, the thermal boundary conditions of the system, the exact radial/thrust bearing geometry (which due to low production costs may have large construction tolerances) and the aerodynamic bearing forces during the operation, to name a few. As a consequence, time-efficient but accurate models for the thrust and the radial bearings are needed, validated through suitable experimental procedures.

1.2 State of the Art

Hydrodynamic lubrication in fluid-film bearings − considering both the oil-pressure (Reynolds equation) and the oil-temperature (energy equation) − has been extensively investigated in [51, 59, 64, 90, 113]. The influence of the oil-film as well as the phenomena related to its properties on rotordynamic applications have been discussed in detail in [27, 49, 81, 124], among others. Hydrodynamic bearings can be divided in two major categories regarding the direction of the supported load, namely the radial and the thrust bearings. These two types share several common characteristics like the governing equations and the lubrication regime. Despite these common characteristics they will be considered separately due to their differences in geometry, kinematics, boundary conditions as well as the thermohydrodynamic modeling approaches that will be applied to them.

1.2.1 Radial bearings

In Figure 1.2 various types of radial bearings used in automotive turbochargers are illustrated. Radial (journal) bearings are commonly modeled using simplified closed-

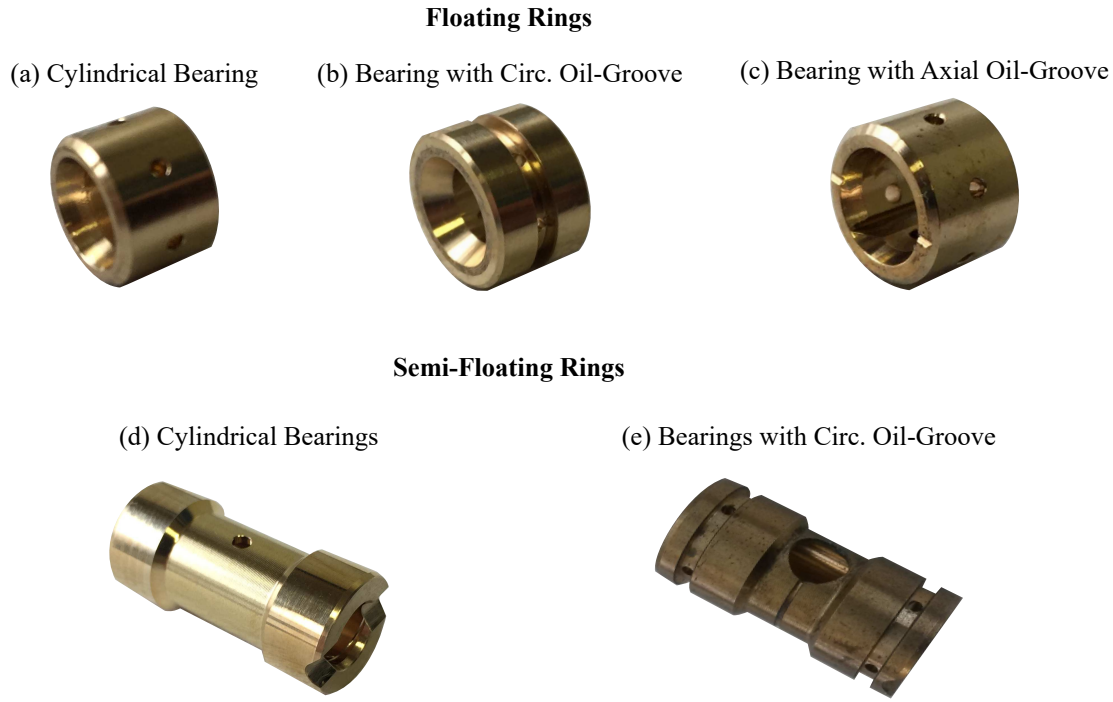

Figure 1.2: Types of radial bearings: floating rings (a) cylindrical bearing, (b) bearing with circumferential oil-groove, (c) bearing with axial oil-groove; semi-floating rings (d) cylindrical bearings, (e) bearings with circumferential oil-groove

form analytical solutions of the Reynolds equation, i.e. the short or the long bearing approximation [113, 124]. The short bearing solution has become a standard tool in bearing simulations since its comprehensive analysis from Ocvirk [86]. Its application range is, however, limited only for low length to diameter ratios. Several extensions of the short bearing theory tried to improve this range, see e.g. [6, 98]. Exact solutions of the Reynolds equation for finite bearings utilizing the method of separation of variables and series expansion have been presented [90, 105]. These analytical solutions were evaluated in stationary and transient simulations in [18–20, 105]. However, these analytical approaches are rather cumbersome to handle in numerical simulations, since they usually require the solution of an eigenvalue problem. Simplifications to these exact analytical solutions have also been proposed, see for example [17], where a 1D Finite Difference approximation is used for avoiding a solution using power series. Approximate solutions of the Reynolds equation can be obtained using Finite Difference, Finite Volume or Finite Element methods. Contrary to these local approaches, time-efficient approximate solutions can be found with global approaches. A Global Galerkin approach, which uses global trial and test functions, can be used to this

end. The application of this method for cylindrical single oil-film bearings has been presented in [14, 108]. Global Galerkin approach has also been used for full-floating ring bearing with a circumferential oil-groove [25]. Moreover, spectral methods for the solution of the Reynolds equation were also presented in [83].

It is well-established for almost half a century, that the thermal effects in the oil are important for the determination of the oil-pressure distribution and therefore for the bearing load capacity [89]. The need for the consideration of the temperature variations in the oil was emphasized, when parallel surface thrust bearings were shown in [47] to be able to support a load, contrary to the predictions of the Reynolds equation. Dowson in [36] presented a generalized Reynolds equation that may consider variations of the oil-temperature across the oil-film. Thermohydrodynamic (THD) models for journal bearings have been presented in [9, 37, 43, 114]. In [46] a reduced (global) thermal model was proposed. Simplification approaches for elastohydrodynamic modeling for tilting pad journal bearing were discussed in [118]. In the more complicated case of full-floating ring bearings, detailed quasi-static thermal models using the energy equation of the oil [28, 93, 100] as well as reduced (global) approaches [39, 99] have been presented. The predictions of the temperature distribution in the oil-film, either with a global approach [46] or by using the energy equation of the oil [111], include a time-dependent temperature term. This time-dependent term is not treated always in the same way. In [46], this term was ignored from the calculations, however, in [111] it was included in the transient analysis.

Rotating machines may exhibit self-excited subsynchronous vibrations − oil-whirl/oil-whip oscillations − due to the hydrodynamic bearings. These nonlinear phenomena are well understood for single oil-film bearings [16, 80–82, 97]. Turbocharger rotors are usually equipped with full- or semi-floating ring bearings, mainly due to their advantage of mutual damping between the oil-films [101]. Numerical simulations as well as experimental results have shown that the nonlinear response of turbochargers with floating ring bearings is enriched in comparison to the rotors supported by single oil-film bearings [32, 66, 85, 102–104, 122, 123]. The stability analysis of turbochargers using the classical linear analysis [49] is not adequate. The dynamics and stability of rotors supported by floating ring bearings were investigated analytically in [10] and through numerical simulations in [12, 13, 103]. The nonlinear oscillations of a turbocharger rotor with engine excitation were investigated in [115]. The influence of the outer bearing clearance as well as the influence of the rotor unbalance were studied in [116] and [117], respectively. In [72], a methodology was applied for the case of a turbocharger rotor with full-floating ring bearings that allows the quantification of the subsynchronous vibrations during run-up simulations. The influence of circumferential grooves in full-floating ring bearings using a short bearing solution and a co-simulation approach was presented in [84].

1.2.2 Thrust bearings

The application area of hydrodynamic thrust bearings in turbomachinery ranges from small turbocharger rotors to large steam turbogenerators. The type of the thrust bearing used in a rotor system depends on the specific application. Fluid-film thrust bearings can be subdivided into hydrodynamic and hydrostatic bearings. Additionally, one can distinguish between tilting- and fixed-pad thrust bearings. In Figure 1.3 a few types of turbocharger thrust bearings are illustrated. An overview on different

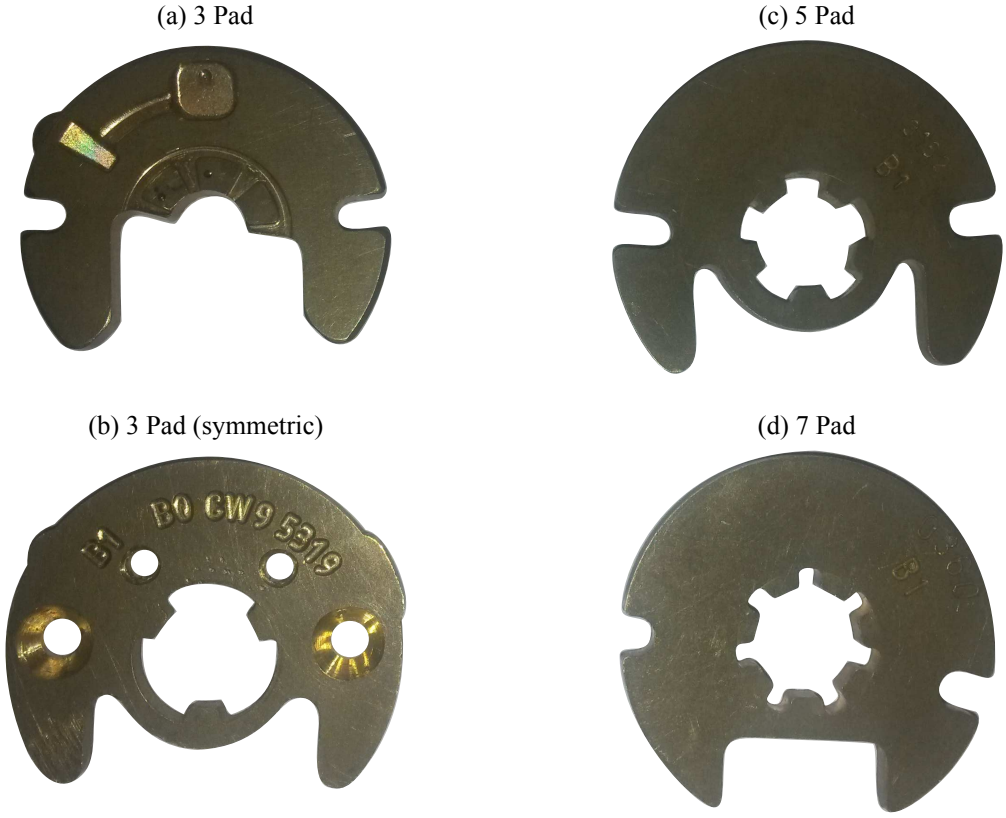

Figure 1.3: Types of thrust bearings: (a) 3 pad, (b) 3 pad (symmetric), (c) 5 pad, (d) 7 pad

bearing geometries and a discussion of their advantages and disadvantages can be found in Refs. [59, 64, 90, 113]. In Ref. [48], for instance, the characteristics of fixed- and titling-pad thrust bearings are discussed.

To investigate qualitatively the main effects of thrust bearings on nonlinear rotor vibrations, isothermal thrust bearing models without centrifugal forces may be sufficient. The assumptions in the classical isothermal Reynolds equation render it in certain applications, however, inadequate to describe accurately the physics of the oil-film lubrication [36]. Especially, higher loads necessitate more detailed models. The thermohydrodynamic analysis for finite sliders was developed from Ezzat and Rodhe [42] and for sector thrust bearings from Huebner [62]. The models described in [62] couple the pressure distribution predicted from the Reynolds equation with a

variable temperature distribution of the oil-film as well as with the exchange of heat between the oil and the solids, i.e. housing and shaft. Additionally, Huebner in [61] investigated the oil-pressure and the oil-temperature in thrust bearings under turbulent regime. The thermal effects in thrust bearings with special geometries are often analyzed using CFD methods as in [87, 88]. The generalized Reynolds equation and the 3D energy equation for thrust bearings in small and medium sized automotive turbochargers were presented in [75, 120]. In [53, 54], a thermohydrodynamic model for large thrust bearings considering the deformation of the pad surfaces was investigated. Sector-shaped, titling-pad thrust bearings were investigated in [65] using three-dimensional analysis. Furthermore, centrifugal effects [92] should be also taken into consideration for a thorough analysis.

Considering run-up simulations of high-speed rotor systems, the thrust bearings are normally not incorporated into the analysis. The exclusion of thrust bearings from transient rotor calculations is mainly attributed to the fact that the Reynolds equation needs to be solved at each time-integration step for every bearing pad separately. The relatively large number of bearing pads results therefore in very large computation times. Precise but computationally demanding models although they may exhibit good physical accuracy, they are not suitable for transient simulations over a wide range of rotational speeds. Therefore, reduction approaches or analytical solutions are needed. For hydrodynamic thrust bearings, an efficient model was presented in [21], however, no thermal effects were included. In [41, 75] several reduction approaches, which minimize the computational cost, were demonstrated. When the variations of the temperature distribution across the oil-film can be neglected, a 2D energy equation may be used. The Reynolds and the energy equation are coupled and they have to be solved simultaneously. For journal bearings it was shown in [76, 91] that a decoupling approach is possible, if the pressure gradients in the energy equation are ignored. Heshmat and Pinkus in [57] applied this procedure also to thrust bearings. It is noted here, that this decoupling can be also found in the earlier work of Raimondi [95]. Physically, the neglect of the pressure gradients means that the circumferential velocity of the oil is linear and that the energy that is produced due to viscous shear is convected away by the oil. Computationally, the neglect of the pressure gradients means that these two equations (the Reynolds and the energy equation) may be solved sequentially and no simultaneous solution is needed. It is then obvious, that this decoupling approach may offer time-efficient simulations [22, 24]. Efficient run-up simulations could be achieved with analytical thrust bearing models. However, only for special thrust bearing geometries, the solution of the Reynolds equation can be derived analytically. In [51], an analytical solution for a step thrust bearing is proposed. A set of analytical solutions for rectangular fixed-incline pads is presented in [74]. These solutions are available only in simplified cases and only for an aligned shaft, however, the importance of the shaft misalignment for thrust bearings was

shown in [57]. Since for a thrust bearing with misaligned thrust ring, no such analytical expression of the solution of the Reynolds equation exists, approximate solutions in terms of Finite Difference, Finite Element, Finite Volume or Spectral methods are used for the calculation of the thrust bearing forces and moments.

The computational burden of solving the Reynolds equation in each time-integration step can also be avoided by calculating the linearized stiffness and damping coefficients [119]. The influence of a hydrodynamic thrust bearing in rotordynamic simulations based on linearized bearing coefficients has, for instance, been investigated in [63]. In Refs. [78,110], the dynamic characteristics of thrust bearings including thermal effects were studied in terms of their linearized stiffness and damping coefficients. The usage of linearized stiffness and damping coefficients is on the one hand very time-efficient. On the other hand, the field of application is, however, restricted to the linearization point. Here, we are interested in nonlinear run-up simulations with highly transient axial forces. Therefore, a linearization with respect to a stationary operating point is not easily possible.

Hydrodynamic thrust bearings were experimentally investigated in [55]. An experimental device was presented for tapered land thrust bearings with fixed geometry, where the oil-pressure and the oil-temperature distributions as well as the frictional moments and the minimum film thicknesses were identified. The influence of the geometric uncertainties of the pad surfaces were studied in detail therein. Thermal effects in hydrodynamic thrust bearings were presented experimentally in [30]. Detailed comparisons between experimental and numerical simulations were shown in [31]. The operating conditions were proved to have a great effect on the oil-pressure and the oil-temperature distributions as well as on the minimum film thickness. In Ref. [121], the performance of a large hydrodynamic thrust bearing was compared with experimental results. In Ref. [2], similar comparisons were performed for tilting pad thrust bearings. Numerical and experimental results of cavitation effects for hydrodynamic tapered land thrust bearings were presented in [109]. The friction losses from a thrust bearing of an automotive turbocharger were evaluated in [58].

1.3 Thesis Objectives

1.3.1 Efficient bearing modeling in multibody systems

The present work aims in a better understanding of the nonlinear self-excited subsynchronous rotor vibrations of turbocharger systems through numerical simulations. Thorough investigation and parameter studies require accurate and time-efficient bearing models. Therefore, for the governing equations − the Reynolds equation and the energy equation or the thermal energy balance equations − approximate solutions are needed, suitable for transient simulations. Semi-analytical solution and approaches that can decouple complex nonlinear systems are extensively discussed, showing both their advantages as well as their limitations.

1.3.2 Thermohydrodynamic modeling

As the modeling accuracy in hydrodynamic lubrication is increased by including the thermal effects in the oil, special attention should be paid on the implementation of a thermohydrodynamic model. Different modeling accuracy levels and modeling approaches should be introduced for the thrust and the radial bearings. Reduced solutions should be compared either with detailed models or with experimental results.

1.3.3 Thrust bearing optimization

A further goal of this work is the geometry optimization of the thrust bearing pads. For this purpose an optimizer is usually employed. However, in this work, the optimization will be performed using a stochastic approach, avoiding the drawbacks of an optimizer, e.g. encountering a local minimum. The well-established stationary optimization, considering the load capacity and the friction losses of thrust bearings, should be extended in transient simulations. A dynamic optimization needs to be introduced, where besides the load capacity and the friction losses, the thrust bearing moments are also appraised. Therefore, the overall vibration behavior of turbocharger rotors can be improved.

1.3.4 Experimental validation

Finally, the modeling of the thrust and the radial bearings needs to be verified with experimental results. Shaft motion tests can validate the radial bearings models. A different approach is needed to verify the influence of the thrust bearing, since the axial displacement of the rotor should be controlled.

1.4 Thesis Outline

In the following chapter (Chapter 2), the theoretical framework for hydrodynamic lubrication is presented. The chapter is divided in two parts. The first part is dedicated to the radial and the second to the thrust bearings. The governing equations for hydrodynamic lubrication and thermohydrodynamic modeling are shown. The Global Galerkin approach is implemented both for the radial and the thrust bearings. Detailed comparisons for various modeling approaches are discussed and the most suitable models are chosen for the transient simulations presented in the following chapters.

In Chapter 3, the multibody modeling of a turbocharger rotor/bearing system is considered. The vibration modes − conical and cylindrical − related with the self-excited subsynchronous vibrations of turbocharger rotors are illustrated. Additionally, linear analysis is performed and the influence of the thrust bearing on the conical, the cylindrical and the first bending mode of a turbocharger rotor is shown.

In Chapter 4, numerical simulations of a turbocharger rotor/bearing model are presented. An important highlight of the thesis is the identification of the influence of the thrust bearing on the subsynchronous rotor vibrations. The influence of the oil-viscosity, the number of the thrust bearing pads and the magnitude of the external axial force are investigated in detail.

In Chapter 5, stationary and transient optimization results for thrust bearings are presented. Instead of employing an optimizer, a stochastic approach is used. Initially, in the stationary optimization, optimum thrust bearing geometries are identified, regarding the bearing load capacity and the friction losses. The approach is extended in transient simulations including also the thrust bearing moments. In this case, the thrust bearing geometry is optimized not only for maximum load capacity and minimum friction losses but also for minimizing the amplitudes of the subsynchronous vibrations.

In Chapter 6, the experimental part is presented. The experimental validation of the radial bearing models is performed using standard shaft motion tests in transient run-up simulations. A special experimental device was implemented for the validation of the influence of the thrust bearing on the subsynchronous rotor vibrations.

Finally, in Chapter 7 the conclusions of the current work are drawn and the important aspects for extending the modeling and the results of the current thesis are discussed.

In Figure 1.4 the thesis outline is presented schematically.

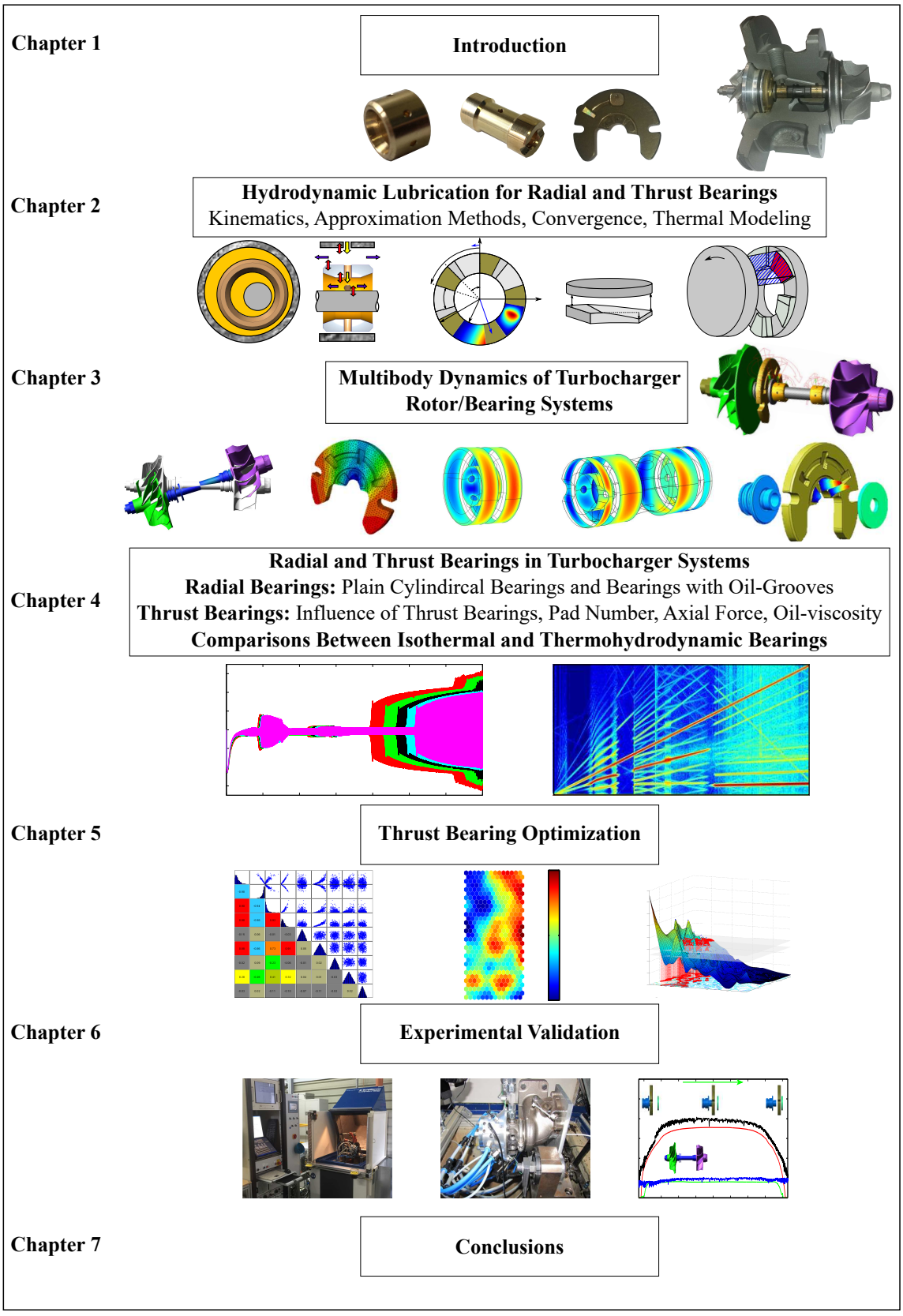

Figure 1.4: Turbocharger rotor/bearing system

Chapter 2

Hydrodynamic Lubrication for Radial and Thrust Bearings

In this chapter, the theoretical framework for hydrodynamic radial and thrust bearings is presented. The chapter is divided in two sections, where the first is devoted to the radial and the second to the thrust bearings. The Reynolds equation, which describes the hydrodynamic pressure distribution generated in the oil-film will be written in a suitable form for both cases and for all three solution approaches, i.e. the Finite Element (FE), the Finite Difference (FD) and the Global Galerkin (GG) approach. Comparisons with the analytical solution using the short bearing approximation theory will also be shown for the radial bearings. For both the radial and the thrust bearings the same cavitation model will be used and its details will be briefly presented in the following.

The main types of radial bearings used in turbochargers will be analyzed, namely plain cylindrical bearings, bearings with circumferential oil-groove and bearings with axial oil-grooves. The radial bearing modeling will be extended to take into account the thermal effects using a thermal energy balance approach between the oil-films and the surrounding solids. The thermal expansion of the shaft, the floating rings and the outer bearings has a significant influence on the thermohydrodynamic modeling and it is therefore also considered.

The thrust bearing kinematics will be detailed and the three dimensional rotations of the thrust ring will be described using the first and the second Bryant angle. The influence of centrifugal effects and cavitation in the oil as well as the misalignment of the thrust ring will also be quantified here. Moreover, various thermohydrodynamic modeling approaches for thrust bearings will be utilized using the energy equation of the oil and will be compared in terms of their numerical accuracy and their time-efficiency.

2.1 Radial Bearings

2.1.1 Reynolds equation for radial bearings

The type of the radial/journal bearings used in turbocharger applications may depend on many factors. Among them, the production/installation costs and the stability of the rotor/bearing system are of utmost importance. Figure 2.1 illustrates the main radial bearing constellations that will be used in this work.

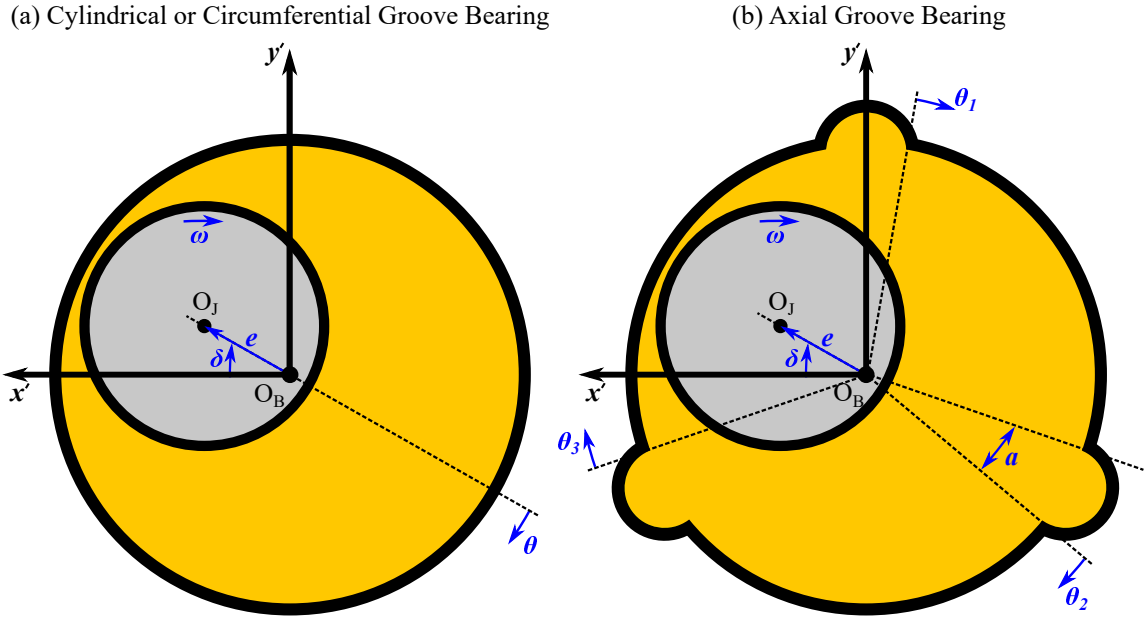

Figure 2.1: Types of radial bearings: (a) (plain) cylindrical or with circumferential groove, (b) axial groove

The Reynolds equation for radial bearings in Cartesian coordinates is

$$\frac{\partial}{\partial z}(h^3\frac{\partial p}{\partial z}) + \frac{\partial}{\partial x}(h^3\frac{\partial p}{\partial x}) = 6\mu U\frac{\partial h}{\partial x} + 12\mu\frac{\partial h}{\partial t}, \tag{2.1.1}$$

where p is the pressure distribution, h the oil-film thickness, μ the oil-viscosity and U the velocity of the journal. The variables x and z denote the spatial coordinates. Due to the geometry of the radial bearings, the Reynolds equation is usually transformed into cylindrical coordinates

$$\frac{\partial}{\partial z}(h^3\frac{\partial p}{\partial z}) + \frac{1}{R^2}\frac{\partial}{\partial \theta}(h^3\frac{\partial p}{\partial \theta}) = 6\mu\omega\frac{\partial h}{\partial \theta} + 12\mu\frac{\partial h}{\partial t}, \tag{2.1.2}$$

where R is the radius of the journal. The oil-film thickness for radial bearings is $h = C(1 + \varepsilon\cos\theta)$ [113], where $\varepsilon = e/C$ is the relative bearing eccentricity. For cylindrical bearings and bearings with the circumferential oil-groove $0 \leq \theta \leq 2\pi$. For radial bearings with axial oil-grooves $\theta_i \leq \theta \leq \theta_{i+1} - a$, where i is the number of the considered area between the axial oil-grooves.

An important aspect for the solution of the Reynolds equation is the selection of the boundary conditions. In Figure 2.2 the boundary conditions for a cylindrical, a bearing with a circumferential oil-groove and a bearing with three axial oil-grooves are illustrated. In the groove area of bearings with circumferential oil-groove, usually

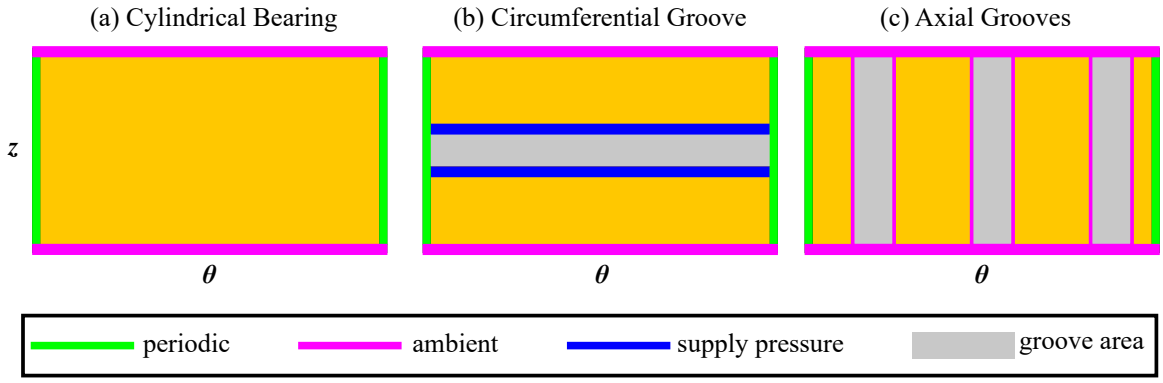

Figure 2.2: Boundary conditions for the Reynolds equation: (a) cylindrical, (b) circumferential groove, (c) axial groove bearing

supply holes exist and the pressure in this area is assumed equal to the supply pressure. For bearings with axial oil-grooves, the pressure in the groove areas is assumed to be zero.

2.1.2 Analytical and approximate solutions of the Reynolds equation

Short bearing approximation

The Reynolds equation using the short bearing approximation [86] is given by

$$\frac{\partial}{\partial z}(h^3\frac{\partial p}{\partial z}) = 6\mu\omega\frac{\partial h}{\partial \theta} + 12\mu\frac{\partial h}{\partial t}. \tag{2.1.3}$$

Assuming L the length of the bearing and $0 < z < L$, the pressure distribution for cylindrical bearings can be calculated analytically

$$p_{SB} = \frac{3\mu(2\dot{e}\cos\theta - e(\omega - 2\dot{\delta})\sin\theta)(z-L)z}{h^3}, \tag{2.1.4}$$

where $\dot{\varepsilon}$ is the relative normal velocity of the journal and $\dot{\delta}$ is the time derivative of the line of the minimum film thickness δ (see Fig. 2.1). The hydrodynamic bearing forces are found after an integration of the pressure distribution using the Gümbel cavitation approach [11, 15]. The integration can be performed either analytically or numerically. In the case of radial bearings with a circumferential oil-groove with pressure p_S at the oil-groove, the pressure distribution is

$$p_{SB_{CG}} = p_{SB} + p_S\frac{z}{L}, \tag{2.1.5}$$

assuming an effective length L for each side of the oil-groove. Therefore, the total effective length for bearings with circumferential oil-groove is taken as $2L$. Bearings with axial oil-grooves are not solved using the short bearing approximation.

Finite Element approximate solution for finite bearings

The first studies implementing Finite Element approaches in lubrication problems were presented in 1969 by Argyris and Scharpf [5] as well as by Reddi [96].

Many commercial software packages, e.g. COMSOL Multiphysics, allow the solution of hydrodynamic lubrication problems using the weak formulation of the Reynolds equation. The partial differential equation (Reynolds equation) is discretized, multiplied by appropriate test functions and then integrated over the whole domain. A common choice for the test functions is the use of 2D Lagrangian elements. The mesh can be triangular or rectangular.

The resulting system of algebraic equations is solved using a parallel sparse direct solver, e.g. MUMPS [3, 4]. Iterative solvers that are less memory demanding can also be used for the solution of the Reynolds equation, but as the size of the problem is relatively small, they can be rather slow in comparison with direct solvers.

In this work, the approximate solution of the Reynolds equation using the Finite Element method will be used only as a reference for comparison with the Finite Difference and the Global Galerkin method. A very fine mesh has been used and the error analysis was performed by increasing the number of elements step by step until the solution at the last step had an absolute and a relative error less than 1e-6 compared to the previous step.

Finite Difference approximate solution for finite bearings

Similarly to the Finite Element approach, several Finite Difference methods can be used to approximate the solution of the Reynolds equation. The two most common approaches utilize either the direct discretization of the terms $\frac{\partial}{\partial z}(h^3\frac{\partial p}{\partial z})$ and $\frac{\partial}{\partial \theta}(h^3\frac{\partial p}{\partial \theta})$ or they develop these terms before the discretization. During the first approach, these terms can be discretized using Central Differences for $\frac{\partial p}{\partial z}$ and $\frac{\partial p}{\partial \theta}$ at the mid-points $z_{i+1/2}$, $z_{i-1/2}$ as well as $\theta_{j+1/2}$,$\theta_{j-1/2}$ followed by Central Differences between these

points to estimate the second order derivative term, namely

$$\frac{\partial}{\partial\theta}(h^3\frac{\partial p}{\partial\theta}) = \frac{h^3_{i,j+1/2}\dfrac{p_{i,j+1}-p_{i,j}}{\Delta\theta} - h^3_{i,j-1/2}\dfrac{p_{i,j}-p_{i,j-1}}{\Delta\theta}}{\Delta\theta}, \tag{2.1.6a}$$

$$\frac{\partial}{\partial z}(h^3\frac{\partial p}{\partial z}) = \frac{h^3_{i+1/2,j}\dfrac{p_{i+1,j}-p_{i,j}}{\Delta z} - h^3_{i-1/2,j}\dfrac{p_{i,j}-p_{i-1,j}}{\Delta z}}{\Delta z}, \tag{2.1.6b}$$

$$\frac{\partial h}{\partial\theta} = \frac{h_{i,j+1/2}-h_{i,j-1/2}}{\partial\theta}. \tag{2.1.6c}$$

In the latter approach, the following approximations are performed for the first

$$\frac{\partial p}{\partial\theta} = \frac{p_{i,j+1}-p_{i,j-1}}{2\Delta\theta}, \quad \frac{\partial p}{\partial z} = \frac{p_{i+1,j}-p_{i-1,j}}{2\Delta z}, \quad \frac{\partial h}{\partial\theta} = \frac{h_{i,j+1}-h_{i,j-1}}{2\Delta\theta}, \tag{2.1.7}$$

and the second order derivatives

$$\frac{\partial^2 p}{\partial\theta^2} = \frac{p_{i,j+1}-2p_{i,j}+p_{i,j-1}}{\Delta\theta^2}, \quad \frac{\partial^2 p}{\partial z^2} = \frac{p_{i+1,j}-2p_{i,j}+p_{i-1,j}}{\Delta z^2}. \tag{2.1.8}$$

In Figure 2.3 a developed domain of a cylindrical journal bearing is discretized using a Finite Difference approach. The Finite Difference approaches lead to a system of linear

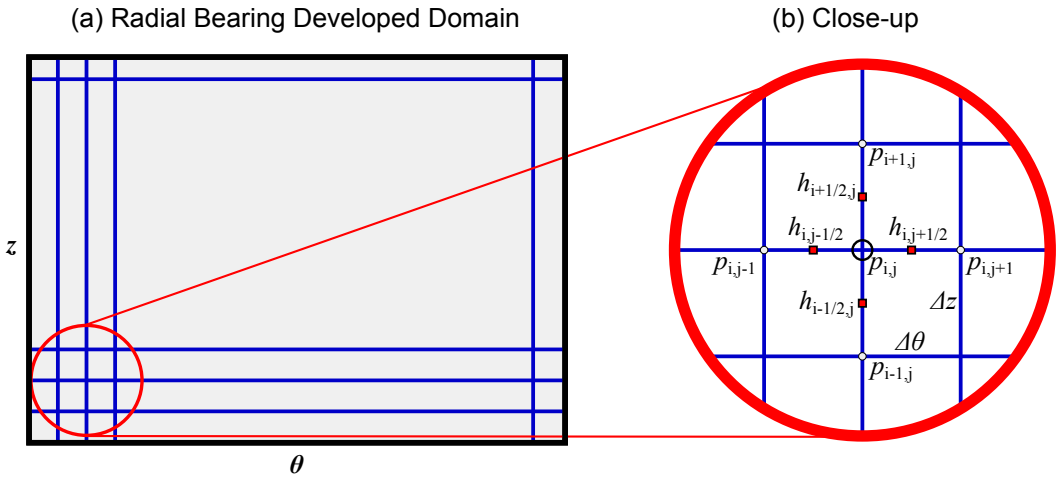

Figure 2.3: Finite Difference mesh for a cylindrical radial bearing

equations. Many solution methodologies exist (direct or iterative), but in this work only direct methods will be used. Both in the radial and thrust bearings, the solution of the remaining sparse linear systems will be performed using LU decomposition with the software UMFPACK [33, 34].

Global Galerkin approximate solution for finite bearings

The Global Galerkin approach will be used for finding an approximate solution of Eq. (2.1.2), which is written here in a nondimensional form [85]

$$\left(\frac{R}{L}\right)^2 \frac{\partial}{\partial \hat{z}}(\hat{h}^3 \frac{\partial \hat{p}}{\partial \hat{z}}) + \frac{\partial}{\partial \theta}(\hat{h}^3 \frac{\partial \hat{p}}{\partial \theta}) = \varepsilon(2\frac{\dot{\delta}}{\omega} - 1)\sin\theta + 2\frac{\dot{\varepsilon}}{\omega}\cos\theta, \tag{2.1.9}$$

with $\hat{z} = z/L$ and $\hat{h} = \frac{h}{C}$. The relative bearing eccentricity is denoted by ε and the relative velocity by $\dot{\varepsilon}$

$$\varepsilon = \frac{e}{C}, \qquad \dot{\varepsilon} = \frac{\dot{e}}{C}. \tag{2.1.10}$$

The nondimensional pressure distribution $\hat{p}$ reads

$$\hat{p} = \left(\frac{C}{R}\right)^2 \frac{p}{6\mu\omega}. \tag{2.1.11}$$

In cylindrical bearings, the pressure distribution in circumferential direction is approximated using Fourier series and in the axial direction using sine functions. For the selection of the trial functions, the nature of the solution as well as the boundary conditions are of paramount importance. In the circumferential direction, cylindrical bearings admit periodic boundary conditions and in the axial direction the pressure distribution is zero (or ambient) at the boundaries. The non-dimensional pressure distribution of cylindrical bearings is approximated by

$$\hat{p} \approx \tilde{p}(\theta, \hat{z}) = \sum_{n=0}^{N}\sum_{m=1}^{M}(a_{n,m}\sin(n\theta) + b_{n,m}\cos(n\theta))\sin(m\pi\hat{z}), \tag{2.1.12}$$

where N, M are sufficiently large for $\tilde{p}$ to converge to $\hat{p}$.

For bearings with circumferential oil-groove, the pressure distribution in the circumferential direction is also approximated using Fourier series. In the axial direction, however, the non-dimensional pressure distribution is approximated by a pressure distribution similar to that of the cylindrical bearings (sine function) superimposed with a linear term satisfying the boundary conditions. The non-dimensional pressure distribution of bearings with circumferential oil-groove is approximated for by

$$\hat{p} \approx \tilde{p}(\theta, \hat{z}) = p_s\hat{z} + \sum_{n=0}^{N}\sum_{m=1}^{M}(a_{n,m}\sin(n\theta) + b_{n,m}\cos(n\theta))\sin(m\pi\hat{z}), \tag{2.1.13}$$

where p_s is the pressure of the oil in the groove.

For bearings with axial oil-grooves, the pressure distribution in circumferential direction is also approximated using sine functions. In the axial direction, the same

procedure as in the cylindrical bearings is used. The non-dimensional pressure distribution of bearings with axial oil-grooves is approximated by

$$\hat{p} \approx \tilde{p}(\tilde{\theta}, \hat{z}) = \sum_{n=1}^{N} \sum_{m=1}^{M} a_{n,m} \sin(n\pi\tilde{\theta}) \sin(m\pi\hat{z}), \tag{2.1.14}$$

where $\tilde{\theta} = \dfrac{\theta - \theta_i}{\theta_{i+1} - \theta_i - a}$. For cylindrical bearings and bearings with circumferential oil-groove the following integrals are calculated for $n = 0, ..., N$ and $m = 1, 3, 5, ..., M$

$$\int_0^1 \int_0^{2\pi} \left\{ \left(\frac{R}{L}\right)^2 \frac{\partial}{\partial\hat{z}}(\hat{h}^3 \frac{\partial\tilde{p}}{\partial\hat{z}}) + \frac{\partial}{\partial\theta}(\hat{h}^3 \frac{\partial\tilde{p}}{\partial\theta}) - \varepsilon(2\frac{\dot{\delta}}{\omega} - 1)\sin\theta - 2\frac{\dot{\varepsilon}}{\omega}\cos\theta \right\} \tag{2.1.15}$$
$$(\sin(n\theta) + \cos(n\theta)) \sin(m\pi\hat{z}) \mathrm{d}\theta \mathrm{d}\hat{z} = 0.$$

For bearings with axial oil-grooves the following integrals are calculated for $n = 1, ..., N$ and $m = 1, 3, 5, ..., M$.

$$\int_0^1 \int_0^1 \left\{ \left(\frac{R}{L}\right)^2 \frac{\partial}{\partial\hat{z}}(\hat{h}^3 \frac{\partial\tilde{p}}{\partial\hat{z}}) + \frac{\partial}{\partial\theta}(\hat{h}^3 \frac{\partial\tilde{p}}{\partial\theta}) - \varepsilon(2\frac{\dot{\delta}}{\omega} - 1)\sin\theta - 2\frac{\dot{\varepsilon}}{\omega}\cos\theta \right\} \tag{2.1.16}$$
$$\sin(n\pi\tilde{\theta}) \sin(m\pi\hat{z}) \mathrm{d}\tilde{\theta} \mathrm{d}\hat{z} = 0.$$

It is noted here that the integral in the circumferential direction is calculated from 0 to 1 and this procedure is applied for every area separated from the axial grooves. It is then clear that the coordinate θ in the bearings with the axial oil-groove is not the same as in the other two bearing types, but the same notation is used for brevity.

The analytical evaluation of the above integrals leads to the linear system of equations

$$\begin{pmatrix} \mathbf{H} & \mathbf{0} \\ \mathbf{0} & \mathbf{G} \end{pmatrix} \begin{pmatrix} \mathbf{a} \\ \mathbf{b} \end{pmatrix} = \begin{pmatrix} \mathbf{c} \\ \mathbf{d} \end{pmatrix}, \tag{2.1.17}$$

where $\mathbf{a} = a_{1,1}, a_{1,2}, ..., a_{N,M}$ and $\mathbf{b} = b_{1,1}, b_{1,2}, ..., b_{N,M}$. The matrices $\mathbf{H}$ and $\mathbf{G}$ depend on the geometric characteristics of the bearing and the relative bearing eccentricity. Generally, the system matrices are dense, for more details see [23]. The orthogonality of sine and cosine functions combined with the form of the equation produce a sparse linear system. This is an important advantage of the Global Galerkin procedure leading to a small sparse system, contrary to Finite Difference or Finite Element approaches, where the sparse systems are rather large. The sparse linear system is solved using a multifrontal method with LU factorization [34]. Due to the structure of the linear system matrices, the coefficients $\mathbf{a}$ and $\mathbf{b}$ can also be calculated symbolically. This approach creates of course bulky expressions for each coefficient, however, a linear system solver is no longer needed. The task of calculating the pressure distribution is then trivial and can be performed by simple evaluations of the analytical expressions. The evaluation time for a pressure distribution should be no more than the evaluation

time using the short or the long bearing theory, creating a easy tool for rotordynamic engineers. In practice, however, the evaluation of the bulky analytical expression should make this approach slightly slower. This method is called here semi-analytical solution of the Reynolds equation. Using all the above, numerical run-up simulations are now highly efficient.

2.1.3 Convergence of approximate solutions

The quality of an approximate solution is usually evaluated using an analytical or a reference solution. Using the short bearing theory, an analytical solution of the pressure distribution can achieved and therefore a convergence test for the Finite Difference and the Global Galerkin method will be performed here using Eq. (2.1.3). For the Finite Difference approach, three different grids are selected, namely 10, 50 and 90 points for each coordinate (θ and z). For the Global Galerkin approach, three different number of trial functions are selected, i.e. 3, 11 and 16 for the θ and 3, 5 and 7 for the z-direction. The comparison is performed for three relative bearing eccentricities, $\varepsilon = 0.2$, $\varepsilon = 0.5$ and $\varepsilon = 0.8$.

In Figure 2.4 and Table 2.1 the difference of the Finite Difference approach and the analytical solution is illustrated.

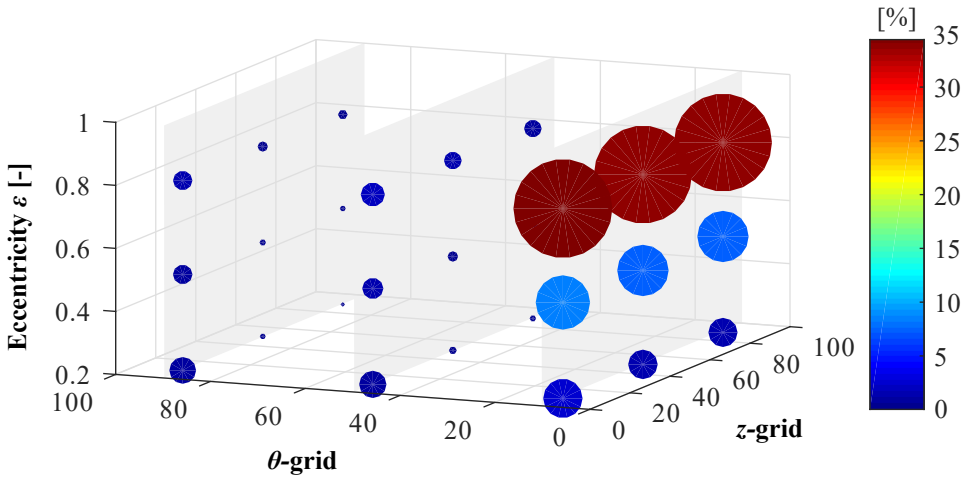

Figure 2.4: Difference in % of the Finite Difference approach and the analytical solution using the short bearing theory

It is observed that for a low eccentricity $\varepsilon = 0.2$, a coarse mesh is enough to approximate the solution of the Reynolds equation. Even with a grid 10×10 the relative percentage error is 2.18%. Increasing the relative eccentricities to $\varepsilon = 0.5$ and $\varepsilon = 0.8$, the percentage error is increased and is exceeds 30% for a coarse grid. Using a fine grid 90×90 the percentage error is very low reaching 0.34% for $\varepsilon = 0.8$. The finer the grid, the higher the computational cost for the calculation of the approximate solution. For

Table 2.1: Difference in % of the Finite Difference approach and the analytical solution using the short bearing theory

		$\varepsilon = 0.2$			$\varepsilon = 0.5$			$\varepsilon = 0.8$		
z \ θ		**10**	**50**	**90**	**10**	**50**	**90**	**10**	**50**	**90**
	10	2.18	1.05	1.01	8.32	1.27	1.08	33.41	2.06	1.33
	50	1.23	0.09	0.05	7.43	0.31	0.12	33.78	1.11	0.37
	90	1.2	0.06	0.03	7.41	0.29	0.1	33.76	1.09	0.34

the grid 10×10, a linear system with size 100×100 should be solved and for the grid 90×90, a linear system with size 8100×8100 should be solved. So large systems are rather cumbersome for transient simulations and therefore more efficient approaches are needed. It is noted here that for each coordinate θ and z is not necessary to have the same grid. From the comparison it is seen that the increase of the grid size in the θ-direction remarkably increases the accuracy of the method. On the contrary, for the z-direction a relatively coarse grid may also deliver good results.

In Figure 2.5 and Table 2.2 the difference of the Global Galerkin approach and the analytical solution is presented.

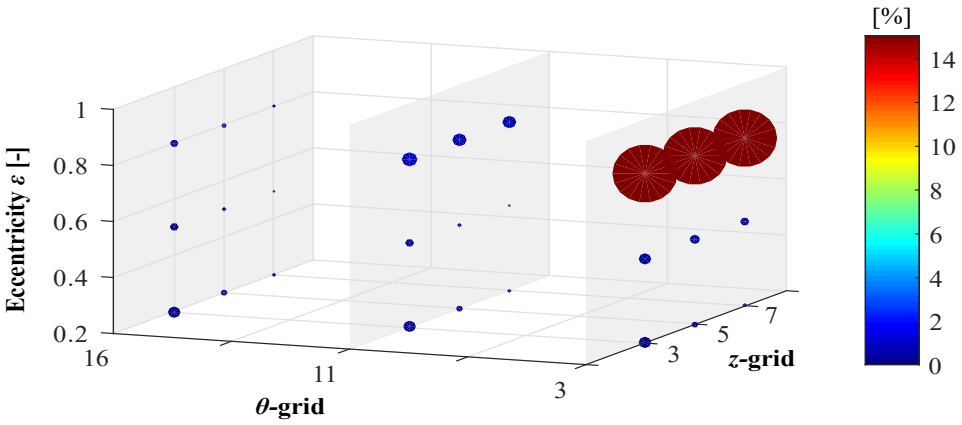

Figure 2.5: Difference in % of the Global Galerkin approach and the analytical solution using the short bearing theory

The Global Galerkin approach may deliver excellent results using only a small number of trial functions. Only three trial functions in both directions can approximate adequately the solution of the Reynolds equation even for a medium eccentricity $\varepsilon = 0.5$. It should be mentioned that the Global Galerkin approach with 3 trial functions delivers better results even if it is compared to a Finite Difference grid 90×10.

In Figure 2.6 the pressure distribution at the middle of the bearing using the short

Table 2.2: Difference in % of the Global Galerkin approach and the analytical solution using the short bearing theory

	$\varepsilon = 0.2$			$\varepsilon = 0.5$			$\varepsilon = 0.8$		
z \ θ	**3**	**11**	**16**	**3**	**11**	**16**	**3**	**11**	**16**
3	0.23	0.23	0.23	0.45	0.23	0.23	15.04	0.88	0.26
5	0.07	0.07	0.07	0.3	0.07	0.07	14.91	0.73	0.1
7	0.03	0.03	0.03	0.25	0.03	0.03	14.87	0.69	0.06

bearing theory, the Finite Difference method and the Global Galerkin approach is illustrated.

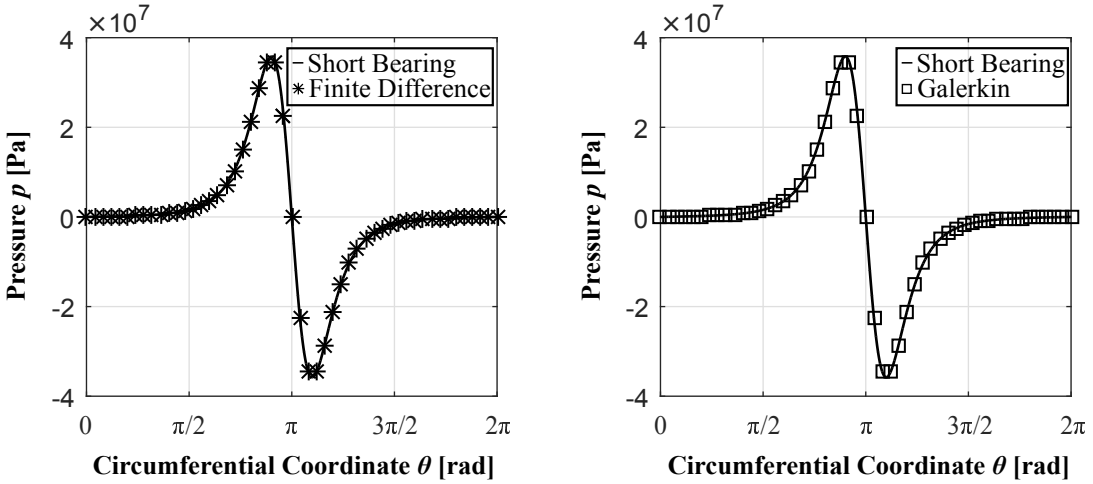

Figure 2.6: Pressure distribution at the middle of bearing using the short bearing theory, the Finite Difference method and the Global Galerkin approach

2.1.4 Cavitation in hydrodynamic radial bearings

The solution of the Reynolds equation predicts both positive and negative pressures. The oil-film in hydrodynamic bearings can sustain only a small amount of tensile stress before cavitation occurs. Cavitation is a rather complicated issue in hydrodynamic bearings, both in the radial and the thrust bearings. A vast majority of literature exists regarding prediction and experimental results [38]. The most common approach − due its simplicity − is the neglect of the negative pressure, namely the Gümbel cavitation approach [90]. However, this approach does not fulfill the fluid-film continuity and is also not mass-conserving. Another common approach that fulfills the fluid-film continuity, but it is still not mass-conserving, is the Stieber-Swift or Reynolds cavitation approach. The Jacobson, Floberg and Olsson approach and the proposed

cavitation algorithm from Elrod [40] can be used as a mass-conserving cavitation method. The physical accuracy of each method comes with a computational cost and increased implementation complexity. Although large differences in the resultant hydrodynamic bearing forces are not usually observed, mass-conserving algorithms may have an influence on the thermal modeling as well as on the calculation of the friction losses.

A comparison between the Gümbel cavitation approach and two mass-conserving algorithms using the Finite Element [1] and the Boundary Element [125] method are shown in Fig. 2.7.

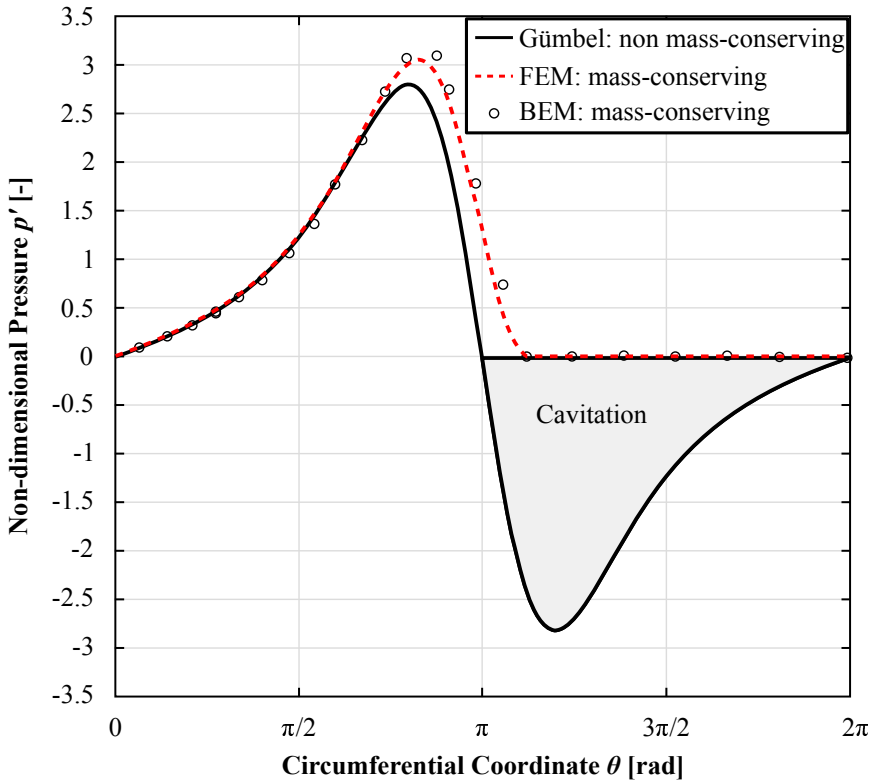

Figure 2.7: Comparison between the Gümbel cavitation approach and two mass-conserving algorithms using the Finite Element [1] and the Boundary Element [125] method

In this work the Gümbel cavitation approach will be used both for the radial and thrust bearings.

2.1.5 Radial bearings for turbocharger rotors

The turbocharger rotors are usually supported in the radial direction by full-floating or by semi-floating ring bearings. A full-floating ring bearing is depicted in Fig. 2.8.

In Figure 2.9, the developed nondimensional domains for the Reynolds equation along with the respective boundary conditions are presented.

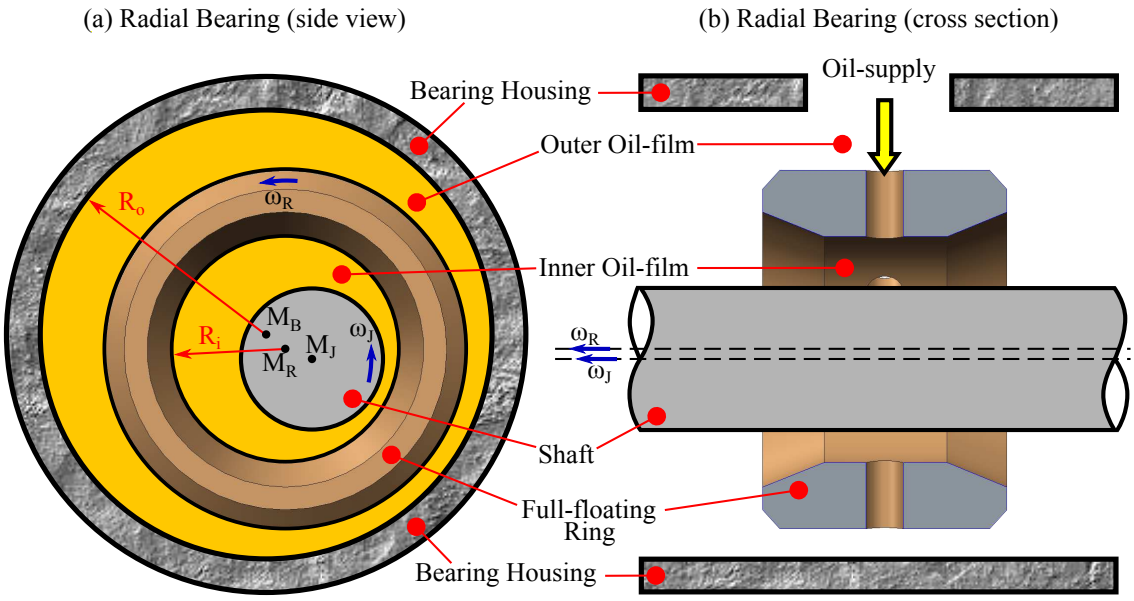

Figure 2.8: Full-floating ring bearing

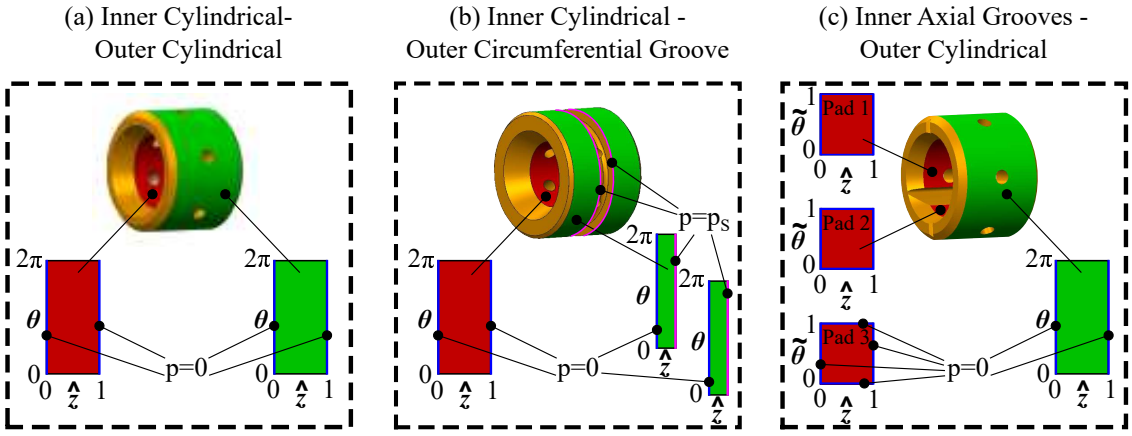

Figure 2.9: Non-dimensional developed domains for the inner and outer bearings: (a) cylindrical-cylindrical, (b) cylindrical-circumferential groove, (c) axial grooves-cylindrical

2.1.6 Thermohydrodynamic (THD) modeling for full-floating ring bearings

The variation of the temperature in the oil-film can be determined using a 3D energy equation of the oil. However, such an approach creates an immense computational load for transient simulations and therefore a reduced thermal energy model is often needed. The heat exchange between the oil-film and the surrounding solids should be also considered as it plays a significant role in the oil-temperature increase.

The pressure distribution p_i/p_o for the inner/outer bearing in a full-floating ring is

calculated by

$$\left(\frac{R_i}{L_i}\right)^2 \frac{\partial}{\partial \hat{z}}(\hat{h}_i^3 \frac{\partial \hat{p}_i}{\partial \hat{z}}) + \frac{\partial}{\partial \theta}(\hat{h}_i^3 \frac{\partial \hat{p}_i}{\partial \theta}) = \varepsilon_i (2\frac{\dot{\delta}_i}{\omega_i} - 1)\sin\theta + 2\frac{\dot{\varepsilon}_i}{\omega_i}\cos\theta, \tag{2.1.18a}$$

$$\left(\frac{R_o}{L_o}\right)^2 \frac{\partial}{\partial \hat{z}}(\hat{h}_o^3 \frac{\partial \hat{p}_o}{\partial \hat{z}}) + \frac{\partial}{\partial \theta}(\hat{h}_o^3 \frac{\partial \hat{p}_o}{\partial \theta}) = \varepsilon_o (2\frac{\dot{\delta}_o}{\omega_o} - 1)\sin\theta + 2\frac{\dot{\varepsilon}_o}{\omega_o}\cos\theta. \tag{2.1.18b}$$

The relative bearing eccentricity of the inner/outer bearing is denoted by $\varepsilon_i/\varepsilon_o$ and the inner/outer relative velocity by $\dot{\varepsilon}_i/\dot{\varepsilon}_o$

$$\varepsilon_{i,o} = \frac{e_{i,o}}{C_{i,o}}, \qquad \dot{\varepsilon}_{i,o} = \frac{\dot{e}_{i,o}}{C_{i,o}}. \tag{2.1.19}$$

The variable $\dot{\delta}_i$ denotes the time derivative of the line of minimum film thickness between the journal and the floating-ring. Respectively, $\dot{\delta}_o$ is time derivative of the line of minimum film thickness between the floating-ring and the bearing housing. The inner/outer effective hydrodynamic velocity is

$$\omega_{\text{eff}_i} = \omega_J + \omega_R - 2\dot{\delta}_i, \quad \omega_{\text{eff}_o} = \omega_R - 2\dot{\delta}_o. \tag{2.1.20}$$

The nondimensional pressure distribution $\hat{p}_i/\hat{p}_o$ reads

$$\hat{p}_i = \left(\frac{C_i}{R_i}\right)^2 \frac{p_i}{6\mu_i\omega_i}, \quad \hat{p}_o = \left(\frac{C_o}{R_o}\right)^2 \frac{p_o}{6\mu_o\omega_o}. \tag{2.1.21}$$

The inner/outer oil-viscosity μ_i/μ_o of the oil-film are assumed to be constant in the axial and the circumferential direction, but they are allowed to vary with time during a simulation. They can be calculated from the following thermal energy balance equations [99]

$$c_p\rho(V_i\dot{T}_i + Q_iT_i - Q_iT_s) + Z_J(T_i - T_R) + Z_J(T_i - T_J) = \Phi_i, \tag{2.1.22a}$$

$$c_p\rho(V_o\dot{T}_o + Q_oT_o - Q_oT_o) + Z_B(T_o - T_R) + Z_B(T_o - T_B) = \Phi_o, \tag{2.1.22b}$$

$$c_{p_R}\rho_R V_R\dot{T}_R - Z_J(T_R - T_i) + Z_B(T_R - T_o) = 0. \tag{2.1.22c}$$

The time-dependent temperature terms in Eq. (2.1.22) are important in transient simulations for avoiding large and abrupt oscillations of the oil-temperature and of the radial bearing clearances. Considering the inner oil-film, the rate of change in the thermal energy is calculated by the convected heat transfer through the radial grooves ($c_pQ_iT_s$) and the mechanical power generated in the fluid film Φ_i subtracting the convection through the axial flow Q_i and the surrounding solids, i.e. the journal and the ring. The rate of change of the thermal energy in the outer oil-film is calculated in a similar manner. In the floating ring, the rate of change of its thermal energy should be equal to the convected thermal energy from the inner oil-film to the ring and from the ring to the outer oil-film. The calculation of the inverse of the thermal resistances Z_J and Z_B is performed assuming that at the boundary between the oil-film and the

solid the relative velocity of the fluid is zero and therefore the heat transfer takes place only through conduction [7]. Applying the Fourier's law and the Newton's law of cooling the convection coefficients can be obtained [7]

$$h_c = \frac{-k\partial T/\partial r|_{\text{boundary}}}{T_b - T_{i,o}}, \tag{2.1.23}$$

where T_b is the temperature at the boundaries, i.e. the journal surface, the inner/outer surface of the ring and the outer bearing surface. The variable k denotes the thermal conductivity of the material. The term $\partial T/\partial r|_{\text{boundary}}$ describes the boundary temperature gradient (in the radial direction), which however cannot be calculated precisely without a 3D temperature model. Therefore, assuming a linear temperature distribution from the middle radius of the fluid to the respective boundary the convection coefficients can be calculated. The inverse of the thermal resistances are given by

$$Z_J = \frac{A_J k}{C_i/2}, \quad Z_B = \frac{A_B k}{C_o/2}, \tag{2.1.24}$$

where A_J and A_B are the areas of the journal and the outer bearing respectively.

A schematic sketch of the energy balance is shown in Fig. 2.10. The temperature

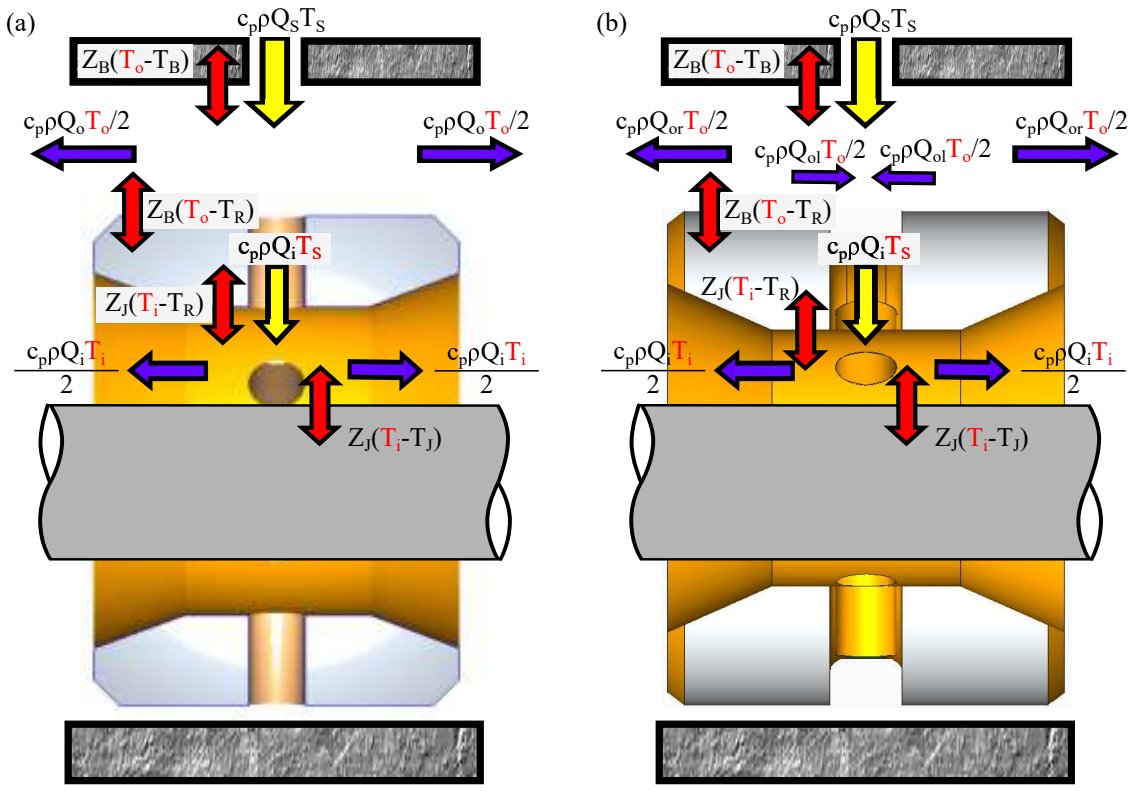

Figure 2.10: Thermal energy balance in a full-floating ring bearing: (a) cylindrical outer bearing, (b) outer bearing with circumferential oil-groove

of the journal T_J can be described using a thermal conduction model for the whole turbocharger rotor, however, in this work it will be assumed constant. The same

applies for the temperature of the outer bearing T_B. The heat transfer between the oil and the floating ring in the axial direction will also be ignored. The coupling of the two oil-films will be considered only in the thermal energy balance equations and the coupling in the pressure distributions will be neglected.

The inner/outer axial flow Q_i/Q_o is calculated at the axial boundaries of each oil-film [25, 99]

$$Q_i = 2\int_0^{2\pi}\left(\frac{-h_i^3}{12\mu_i}\frac{\partial p_i}{\partial z}\right)R_i\,\mathrm{d}\theta, \tag{2.1.25a}$$

$$Q_{o_l} = 2\int_0^{2\pi}\left(\frac{-h_o^3}{12\mu_o}\frac{\partial p_o}{\partial z}\right)R_o\,\mathrm{d}\theta, \tag{2.1.25b}$$

$$Q_{o_r} = 2\int_0^{2\pi}\left(\frac{-h_o^3}{12\mu_o}\frac{\partial p_o}{\partial z}\right)R_o\,\mathrm{d}\theta. \tag{2.1.25c}$$

The axial flows for both sides of the bearing from the inner oil-film have equal magnitudes. The outer bearing is divided into two domains, separated by the circumferential oil-groove. Each domain has one axial flow towards outside the bearing Q_{o_r} and one towards the oil-groove Q_{o_l}. These two flows are in general not equal. The total axial flow from the outer oil-film is given by $Q_o = Q_{o_l} + Q_{o_r}$. It is noted here that the integrals of Eq. (2.1.25) are calculated only for $p_{i,o} > 0$.

The mechanical power dissipation for the inner/outer oil-film is described by the variables Φ_i and Φ_o [99]

$$\Phi_i = \int_0^{L_i}\int_0^{2\pi}\{\frac{h_i^3}{12\mu_i}\left[\frac{1}{R_i^2}\left(\frac{\partial p_i}{\partial\theta}\right)^2+\left(\frac{\partial p_i}{\partial z}\right)^2\right]+ \\ +\frac{\mu_i}{h_i}(\omega_J-\omega_R)^2R_i^2\}R_i\,\mathrm{d}\theta\mathrm{d}z, \tag{2.1.26a}$$

$$\Phi_o = \int_0^{L_o}\int_0^{2\pi}\{\frac{h_o^3}{12\mu_o}\left[\frac{1}{R_o^2}\left(\frac{\partial p_o}{\partial\theta}\right)^2+\left(\frac{\partial p_o}{\partial z}\right)^2\right]+ \\ +\frac{\mu_o}{h_o}(\omega_R R_o)^2\}R_o\,\mathrm{d}\theta\mathrm{d}z. \tag{2.1.26b}$$

The power dissipation in hydrodynamic bearings is of paramount importance in full-floating ring bearings as it is closely related to the rotational speed of the floating rings and is therefore also related with the self-excited vibrations. Similarly to the equations for the axial flow, the pressure gradients are calculated only for $p_{i,o} > 0$. At the area where cavitation takes place, it is assumed that the dissipation is caused by the shear stresses only.

The temperature in the oil-film affects the radial bearing clearances due to the thermal expansion of the journal, the floating ring and the outer bearing. The inner and outer clearances can be calculated by

$$C_i = C_i' - \alpha_J R_i (T_J - T_0) + \alpha_R R_i (T_R - T_0), \tag{2.1.27a}$$

$$C_o = C_o' + \alpha_B R_o (T_B - T_0) - \alpha_R R_o (T_R - T_0). \tag{2.1.27b}$$

The variables α_J, α_R and α_B denote the thermal expansion coefficients for the journal, the ring and the outer bearing. C_i'/C_o' are the inner and outer clearances at the ambient temperature $T_0 = 20\,^{\circ}\mathrm{C}$.

The temperature-viscosity relationship for the radial bearings used in this work is

$$\mu_{i,o} = e^{A+B/(Ti,o+D)}, \tag{2.1.28}$$

where the variables A, B, D depend on the oil-type.

The radial/tangential hydrodynamic bearing force F_R/F_T acting on the rotor and on the floating ring can be calculated by integrating the pressure distribution over the corresponding bearing surface $A_{i,o}$

$$F_{R_{i,o}} = \iint\limits_{A_{i,o}} p_{i,o} R_{i,o} \cos\theta \, \mathrm{d}\theta \mathrm{d}z, \quad F_{T_{i,o}} = \iint\limits_{A_{i,o}} p_{i,o} R_{i,o} \sin\theta \, \mathrm{d}\theta \mathrm{d}z. \tag{2.1.29}$$

The radial and tangential forces are referring to the respective line of the minimum film thickness. The frictional moment M_{z_i}/M_{z_o} from the inner/outer oil-film acting on the full-floating ring is calculated by integrating the shear stress $\tau_{i,o}$ over the respective bearing surface

$$M_{z_i} = \iint\limits_{A_J} \tau_i R_i^2 \, \mathrm{d}\theta \mathrm{d}z, \tag{2.1.30a}$$

$$M_{z_o} = \iint\limits_{A_B} \tau_o R_o^2 \, \mathrm{d}\theta \mathrm{d}z \tag{2.1.30b}$$

The resultant moment acting on the ring is $M_z = M_{z_i} + M_{z_o}$ and its calculation is very critical in full-floating ring bearings, since this moment dictates the rotational speed of the ring.

The pressure distribution in a full-floating ring bearing can be calculated either by the simultaneous solution of the nonlinear system of equations i.e. the Reynolds equation presented in Eq. (2.1.18) and the thermal energy balance equations presented in Eqs. (2.1.22, 2.1.25, 2.1.26, 2.1.27, 2.1.28) or by an iterative approach. In the latter, the Reynolds equation is initially solved for the pressure distributions p_i/p_o followed by the thermal energy balance equations, which are solved for the oil-viscosity μ_i/μ_o and the radial bearing clearances C_i/C_o until convergence is obtained. Both approaches

create a heavy computational load. Using a semi-analytical solution of the Reynolds equation, the pressure gradients needed for the solution of the thermal energy balance equations can be calculated analytically. In this way, the small nonlinear system of the thermal energy balance equations can be solved first and the identified viscosity and radial bearing clearances are substituted in the Reynolds equation for the calculation of the pressure distribution. It is also mentioned here, that the differential equations describing the thermal energy balance are solved using an implicit Euler time-integration approach.

2.1.7 Influence of the boundary conditions on the oil-temperature in radial bearings

The temperature of the inner and the outer oil-film is heavily influenced by the boundary conditions. The temperature of the journal, the temperature of the bearing as well as the oil-supply temperature affect the oil-film temperature. In Figure 2.11, the influence of the boundary conditions on the inner and the outer oil-film temperatures is presented.

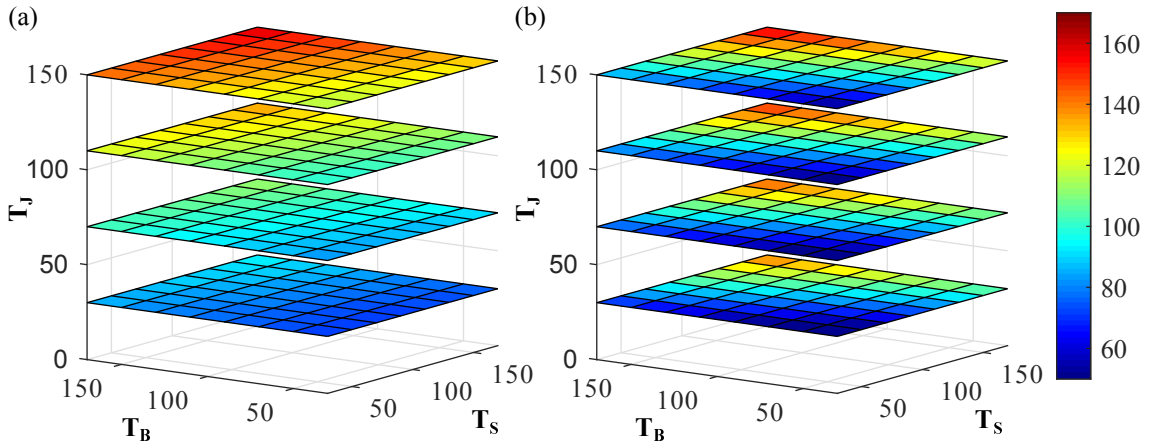

Figure 2.11: Influence of the journal, bearing and oil-supply temperature on (a) the inner and (b) the outer oil-film temperature

The parameters used for the calculations in Fig. 2.11 are shown in Table 2.3. It is observed that the inner oil-film temperature is heavily affected by the temperature of the journal. For a low journal temperature (30°C) the inner oil-film temperature remains low for almost all the values of the bearing and the oil-supply temperature. Only in the case where both bearing and oil-supply temperature are 150 °C, the inner oil-film is attaining almost 90 °C. For high journal temperature (150 °C), the T_i is always high except for the case that T_B and T_s are 30 °C. For an accurate determination of the journal temperature, a thermal model for the turbocharger rotor is also needed. However, in this work, the temperature of the rotor will be only given as a boundary

Table 2.3: Parameter for THD model

Parameter	Value	Unit
L_i/D_i	0.57	-
L_o/D_o	0.64	-
C_i	6.5e-6	m
C_o	35e-6	m
ω_J	10000	rad/s
ω_R	1000	rad/s
ε_i	0.5	-
ε_o	0.5	-

condition to the respective equations. It is mentioned here, that the journal temperature of the turbine-side bearing is usually higher than the journal temperature at the compressor-side bearing. The outer oil-film is mainly influenced by the oil-supply and the outer bearing temperature.

2.2 Thrust Bearings

In automotive turbochargers, tapered-flat thrust bearings are usually implemented. A 5-pad tapered-flat thrust bearing is shown in Fig. 2.12. Details for the calculations

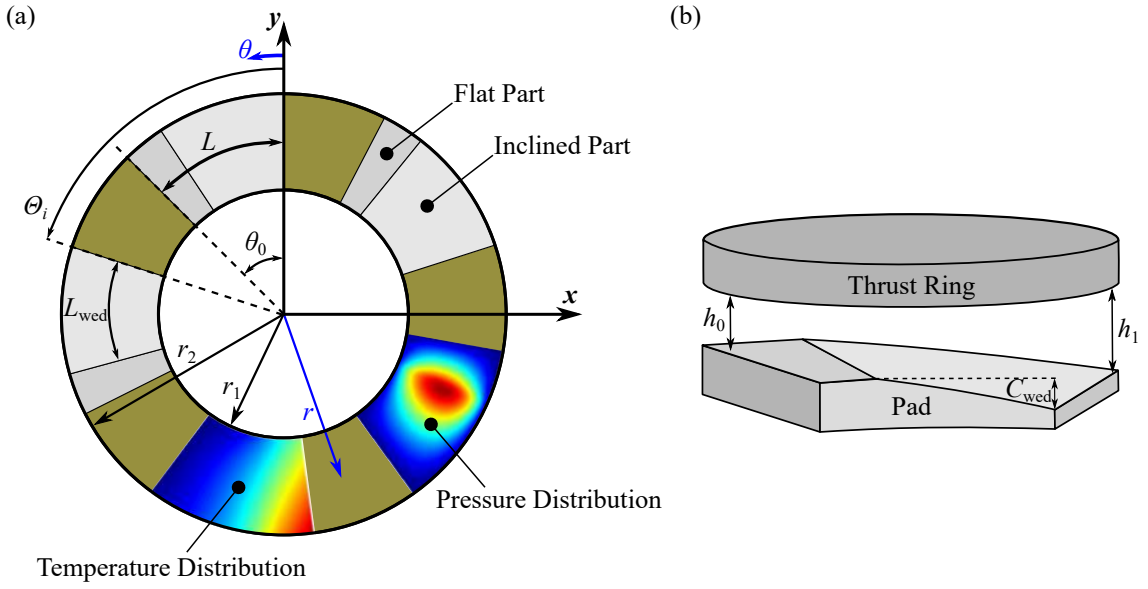

Figure 2.12: 5-pad thrust bearing: (a) bearing geometry, (b) pad geometry

of the oil-pressure and the oil-temperature distributions of two bearing pads depicted in Fig. 2.12 will be shown later in this section. The inner radius of the bearing pads

is r_1, the outer radius is r_2 and θ_0 is the angular extent of a pad. L is the length at the middle radius of a pad and L_{wed} is the length of the inclined part at the middle radius of a pad. The angle of the leading edge of the pad i is Θ_i. The taper height is denoted by C_{wed} and h_0 is the distance between the thrust ring and the flat part of a bearing pad in an aligned configuration. The axial distance between the leading edge of the pad and the thrust ring is given by $h_1 = h_0 + C_{\text{wed}}$.

2.2.1 Reynolds equation for thrust bearings and kinematics

For calculating the pressure distribution $p(r, \theta)$ of a thrust bearing pad, the Reynolds equation in cylindrical coordinates is used

$$\frac{\partial}{\partial r}(rh^3\frac{\partial p}{\partial r}) + \frac{1}{r}\frac{\partial}{\partial \theta}(h^3\frac{\partial p}{\partial \theta}) = 6\mu\omega r\frac{\partial h}{\partial \theta} + 12\mu r\frac{\partial h}{\partial t}, \tag{2.2.1}$$

where h is the oil-film thickness, μ the viscosity of the oil, ω the rotational speed of the rotor and t the time. The radial and circumferential coordinates are r and θ, respectively. The pressure at the boundaries is assumed to be equal to zero, i.e.

$$p(r_1, \theta) = p(r_2, \theta) = 0, \qquad p(r, \Theta_i) = p(r, \Theta_i + \theta_0) = 0.$$

The solution of Eq. (2.2.1) necessitates the determination of the oil-film thickness, namely the distance between a bearing pad and the misaligned thrust ring. For an aligned thrust ring, the distance $h_{\text{al}}(r, \theta, h_0)$ is

$$h_{\text{al}} = \begin{cases} h_1 - (h_1 - h_0)\dfrac{\theta}{\theta_0\dfrac{L_{\text{wed}}}{L}}, & 0 < \theta < \theta_0\dfrac{L_{\text{wed}}}{L} \\ h_0, & \theta_0\dfrac{L_{\text{wed}}}{L} < \theta < \theta_0 \end{cases}. \tag{2.2.2}$$

It was shown in [57] that the misalignment of the thrust ring is important for the hydrodynamic forces of thrust bearings. In this work, we derive the film thickness in the case of a misaligned thrust ring using the first two Bryant angles α and β. It is noted here that the translational displacements of the thrust ring in x- and y-directions are neglected for the calculation of the oil-film thickness. The change of the thrust bearing forces and moments due to these displacements are negligible [78]. For the determination of the misalignment of the thrust ring, the transformation matrix parametrized with Bryant angles is used [106]

$${}^{03}\mathbf{T} = \begin{bmatrix} \mathrm{c}(\beta)\mathrm{c}(\gamma) & -\mathrm{c}(\beta)\mathrm{s}(\gamma) & \mathrm{s}(\beta) \\ \mathrm{c}(\alpha)\mathrm{s}(\gamma) + \mathrm{s}(\alpha)\mathrm{s}(\beta)\mathrm{c}(\gamma) & \mathrm{c}(\alpha)\mathrm{c}(\gamma) - \mathrm{s}(\alpha)\mathrm{s}(\beta)\mathrm{s}(\gamma) & -\mathrm{s}(\alpha)\mathrm{c}(\beta) \\ \mathrm{s}(\alpha)\mathrm{s}(\gamma) - \mathrm{c}(\alpha)\mathrm{s}(\beta)\mathrm{c}(\gamma) & \mathrm{s}(\alpha)\mathrm{c}(\gamma) + \mathrm{c}(\alpha)\mathrm{s}(\beta)\mathrm{s}(\gamma) & \mathrm{c}(\alpha)\mathrm{c}(\beta) \end{bmatrix}. \tag{2.2.3}$$

The third Bryant angle γ is set to zero, since the third rotation is not required for calculating the film-thickness. Therefore, the transformation matrix is reduced to

$$ {}^{02}\mathbf{T} = \begin{bmatrix} \cos\beta & 0 & \sin\beta \\ \sin\alpha\sin\beta & \cos\alpha & -\sin\alpha\cos\beta \\ -\cos\alpha\sin\beta & \sin\alpha & \cos\alpha\cos\beta \end{bmatrix}. \tag{2.2.4} $$

In Figure 2.13, the sequential rotations of the thrust ring using Bryant angles are illustrated. Note that for the film thickness function, only the first two Bryant angles are required (the third rotation is connected with the rotor speed ω, i.e. $\dot{\gamma} = \omega$). The first Bryant angle α describes the rotation about the body-fixed x_1-axis, which coincides with the space-fixed x-axis. The second Bryant angle β describes the rotation about the body-fixed y_2-axis, see Ref. [106]. Changing the coordinates from Cartesian to

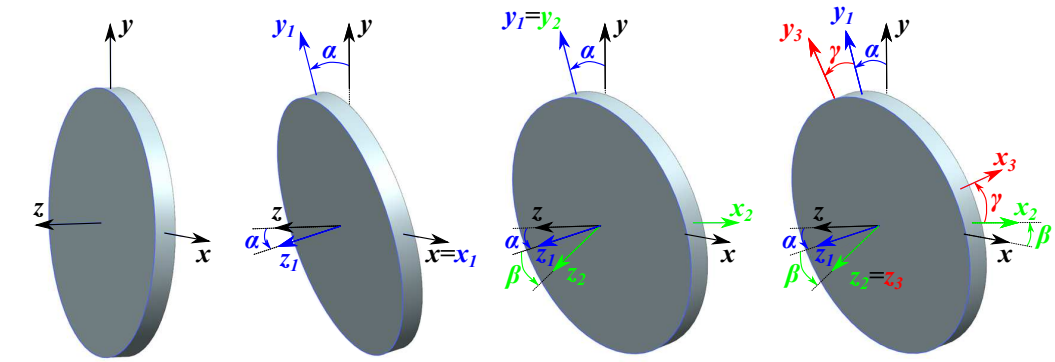

(a) Initial Position (b) First Rotation: Bryant Angle α (c) Second Rotation: Bryant Angle β (d) Third Rotation: Bryant Angle γ

Figure 2.13: Sequential rotations of the thrust ring using Bryant angles

cylindrical dictates the change of variables from x, y, z to r, θ, z, i.e. $x = -r\sin\theta$ and $y = r\cos\theta$. The additional term h_{mis} of the film-thickness due to misalignment of the thrust ring is calculated as follows

$$ \begin{aligned} {}^{0}\mathbf{r} = {}^{02}\,\mathbf{T}\,{}^{2}\mathbf{r} = \begin{bmatrix} \cos\beta & 0 & \sin\beta \\ \sin\alpha\sin\beta & \cos\alpha & -\sin\alpha\cos\beta \\ -\cos\alpha\sin\beta & \sin\alpha & \cos\alpha\cos\beta \end{bmatrix} \begin{bmatrix} -r\sin\theta \\ r\cos\theta \\ 0 \end{bmatrix} = \\ \begin{bmatrix} -r\cos\beta\sin\theta \\ -r\sin\alpha\sin\beta\sin\theta + r\cos\alpha\cos\theta \\ r\cos\alpha\sin\beta\sin\theta + r\sin\alpha\cos\theta \end{bmatrix}, \end{aligned} \tag{2.2.5} $$

where ${}^{2}\mathbf{r}$ is an arbitrary point in the thrust ring plane $z_2 = 0$. The last row of Eq. (2.2.5) gives the axial distance of every point of the misaligned thrust ring. Therefore, the additional oil-film thickness h_{mis} due to misalignment is

$$ h_{\text{mis}} = r\cos\alpha\sin\beta\sin\theta + r\sin\alpha\cos\theta. \tag{2.2.6} $$

The Bryant angles α and β are usually very small and therefore, Eq. (2.2.6) can be linearized around zero (α=0, β=0). The linearized film thickness due to misalignment reads

$$h_{\mathrm{mis}_{\mathrm{lin}}} = r(\alpha \cos\theta + \beta \sin\theta). \tag{2.2.7}$$

Combining Eq. (2.2.2) and Eq. (2.2.7), the linearized minimum film thickness due to axial displacement and misalignment of the thrust ring ($h(r, \theta, h_0, \alpha, \beta)$) is obtained

$$h = \begin{cases} h_1 - C_{\mathrm{wed}} \dfrac{\theta - \Theta_i}{\theta_0 \dfrac{L_{\mathrm{wed}}}{L}} + r(\alpha \cos\theta + \beta \sin\theta), & \Theta_i < \theta < \Theta_i + \theta_0 \dfrac{L_{\mathrm{wed}}}{L} \\ h_0 + r(\alpha \cos\theta + \beta \sin\theta), & \Theta_i + \theta_0 \dfrac{L_{\mathrm{wed}}}{L} < \theta < \Theta_i + \theta_0 \end{cases}. \tag{2.2.8}$$

The instationary term $\frac{\partial h}{\partial t}$ of Eq. (2.2.1) can be calculated by time-differentiation of the oil-film thickness function (2.2.8). Assuming again that $\alpha, \beta \ll 1$, the linearized time-derivative of the film thickness function reads

$$\frac{\partial h}{\partial t} = \dot{h}_0 + r(\dot{\alpha} \cos\theta + \dot{\beta} \sin\theta). \tag{2.2.9}$$

In all subsequent calculations, the linearized expressions for the film thickness (2.2.8) and for the axial velocity (2.2.9) are used for solving the Reynolds equation (2.2.1).

2.2.2 Approximate solutions of the Reynolds equation for thrust bearings

The approximate solutions of the Reynolds equation using Finite Difference, Finite Element or Finite Volume methods, although well established, create an extensive computational load for a run-up simulation. In this work, due to the simple geometry of the pads, a time-efficient approach is proposed for the solution of the Reynolds equation. The Global Galerkin approach, which uses global trial and test functions over a domain, is applied. The pressure distribution p described in the Reynolds equation is approximated by p_G

$$p \approx p_G(r, \theta) = \sum_{n=1}^{N} \sum_{m=1}^{M} a_{n,m} \sin(n\pi \frac{\theta - \Theta_i}{\theta_0}) \sin(m\pi \frac{r - r_1}{r_2 - r_1}), \tag{2.2.10}$$

where the coefficients $a_{n,m}$ have to be determined. The variables N and M introduce the number of trial functions that are assumed in θ- and r-direction, respectively. In the subsequent simulations, the Global Galerkin approach is applied using $N = M$. The number of trial and test functions is to be chosen for a satisfying accuracy between the approximation (Global Galerkin) and the precisely calculated reference solution.

Substituting Eq. (2.2.10) in Eq. (2.2.1) and applying the Global Galerkin method, for $n = 1, ..., N$ and $m = 1, ..., M$, the following weighted residual is produced and assumed to be zero

$$\int_{r_1}^{r_2} \int_{\Theta_i}^{\theta_0+\Theta_i} \left\{ \frac{\partial}{\partial r}(rh^3 \frac{\partial p_G}{\partial r}) + \frac{1}{r}\frac{\partial}{\partial \theta}(h^3 \frac{\partial p_G}{\partial \theta}) - 6\mu\omega r \frac{\partial h}{\partial \theta} - 12\mu r \frac{\partial h}{\partial t} \right\} \sin(n\pi \frac{\theta - \Theta_i}{\theta_0}) \sin(m\pi \frac{r - r_1}{r_2 - r_1}) = 0. \tag{2.2.11}$$

In general, the integrals may be evaluated numerically or analytically. An appropriate re-arrangement of the equations yields the linear system of equations

$$\begin{pmatrix} G^1_{1,1} & G^1_{1,2} & \cdots & G^1_{N,M} \\ G^2_{1,1} & G^2_{1,2} & \cdots & G^2_{N,M} \\ \vdots & \vdots & \ddots & \vdots \\ G^{NM}_{1,1} & G^{NM}_{1,2} & \cdots & G^{NM}_{N,M} \end{pmatrix} \begin{pmatrix} a_{1,1} \\ a_{1,2} \\ \vdots \\ a_{N,M} \end{pmatrix} = \begin{pmatrix} b_{1,1} \\ b_{1,2} \\ \vdots \\ b_{N,M} \end{pmatrix} \tag{2.2.12}$$

for calculating the unknowns $a_{n,m}$. The matrix $\mathbf{G} \in \mathbb{R}^{NM \times NM}$ and the vector $\mathbf{b} \in \mathbb{R}^{NM}$ depend on the parameters of the system. The analytical evaluation of the governing integrals creates very large algebraic expressions for all the elements of the matrix $\mathbf{G}$. Since the largest part of those expressions is constant during a simulation, $\mathbf{G}$ is decomposed according to

$$G^k_{n,m} = \hat{G}^k_{n,m}(h_0(t), \alpha(t), \beta(t)) + \tilde{G}^k_{n,m}, \qquad k = 1, ..., NM \tag{2.2.13}$$

where $\tilde{G}^k_{n,m}$ is constant, depending only at the geometric parameters of the bearing. A similar approach is also applied to the elements of the vector $\mathbf{b}$. It should be pointed out that the decomposition of $\mathbf{G}$ and $\mathbf{b}$ into a small time-varying and a large constant part will significantly accelerate the simulation time.

For generating a reference solution, the pressure distribution is calculated using a Finite Difference (FD) method with a fine grid (150×150). The considered thrust bearing exhibits the following geometric characteristics $r_1 = 3.55\,\text{mm}$, $r_2 = 6.3\,\text{mm}$, $\theta_0 = 0.775\,\text{rad}$, $L_{\text{wed}}/L = 0.7$ and $C_{\text{wed}} = 10\,\mu\text{m}$. The angular velocity of the thrust ring is $\omega = 1000\,\text{rad/s}$.

Figure 2.14 shows the pressure distribution approximated with a Finite Difference (reference) and with the Global Galerkin approach using 4 trial functions for every coordinate (r,θ). The two pressure distributions are plotted over the nondimensional coordinates $\hat{r}$ and $\hat{\theta}$, where $\hat{r} = \frac{r-r_1}{r_2-r_1}$ and $\hat{\theta} = \frac{\theta}{\theta_0}$. In Figure 2.15, the pressure distributions $p_G\left(\hat{r} = 0.5, \hat{\theta}\right)$ for different number of trial functions (Global Galerkin approach) are compared with the pressure distribution $p\left(\hat{r} = 0.5, \hat{\theta}\right)$ using the reference (FD) solution.

These comparisons are performed using a quite low minimum film thickness ($h_0 = 5\,\mu m$) under aligned conditions. It can be observed that the Global Galerkin approach

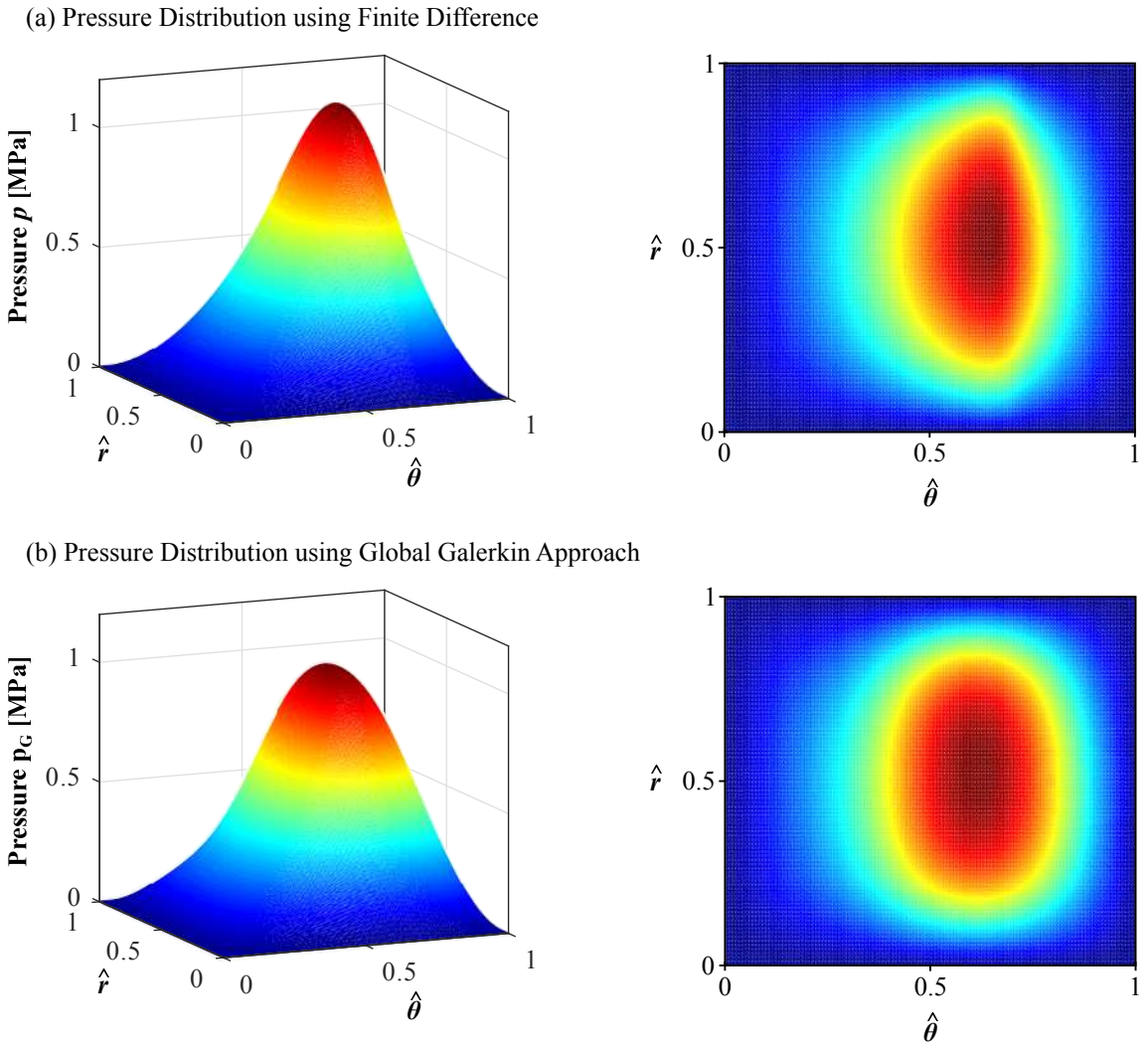

Figure 2.14: Pressure distributions for $h_0 = 5\,\mu m$ and $\omega = 1000\,\mathrm{rad/s}$ using (a) a Finite Difference and (b) the Global Galerkin approach

converges to the reference (FD) solution as the number of trial functions increases. With respect to the proper choice of the number of trial functions, there is a trade-off between numerical accuracy and computational efficiency. As the film thickness decreases, the pressure distribution becomes more steep and therefore, more trial functions are needed for its approximation.

The pressure distribution calculated from Eq. (2.2.1) is integrated over the area of the pad i ($i = 1, ..., n_{pad}$) to calculate the resultant hydrodynamic forces and moments from the bearing pad i

$$\begin{aligned} F_z^i &= \iint_A p\, r \mathrm{d}r\mathrm{d}\theta, \\ M_x^i &= \iint_A p\, r\, r\cos\theta \mathrm{d}r\mathrm{d}\theta, \\ M_y^i &= \iint_A p\, r\, r\sin\theta \mathrm{d}r\mathrm{d}\theta, \end{aligned} \tag{2.2.14}$$

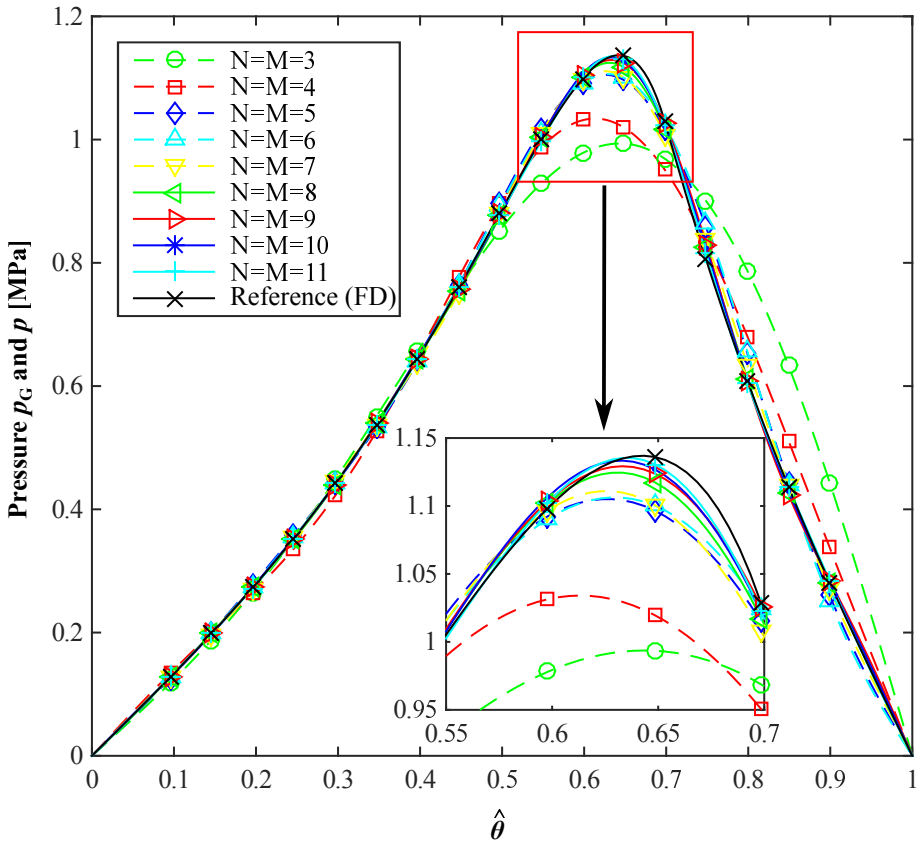

Figure 2.15: Pressure distributions $p_G\left(\hat{r}=0.5,\hat{\theta}\right)$ for different number of trial functions (Global Galerkin approach) in comparison with the pressure distribution $p\left(\hat{r}=0.5,\hat{\theta}\right)$ of the reference solution (FD)

where A is the area of a pad and n_{pad} the number of bearing pads. It should be mentioned that in this work, the Gümbel cavitation approach has been used for calculating the forces and moments.

The total thrust bearing force and the total moments are calculated by summing up the resultant forces/moments of all pads. The thrust bearing force F_z^i is depicted in Fig. 2.16a as a function of the minimum film thickness h_0 and the axial velocity $\dot{h}$. For the calculations, the rotational speed of the thrust ring is set to $\omega = 10000\,\mathrm{rad/s}$ and the thrust ring is assumed to be aligned. A nonlinear behavior between the thrust bearing force and the minimum film thickness and a linear behavior between the thrust bearing force and the axial velocity is observed. It should be mentioned that if cavitation is present, the relationship between the thrust bearing force and axial velocity is no longer linear. The moment M_x^i is shown in Fig. 2.16b as a function of the minimum film thickness h_0 and the first Bryant angle α (the second Bryant angle is assumed to be zero). The axial displacement as well as the angle α show a nonlinear behavior to the moment M_x^i. It should be mentioned that the plots in Fig. 2.16 have been generated with a Finite Difference approach for discretizing the Reynolds equation using a very fine grid. Figure 2.17 shows the relative error in the

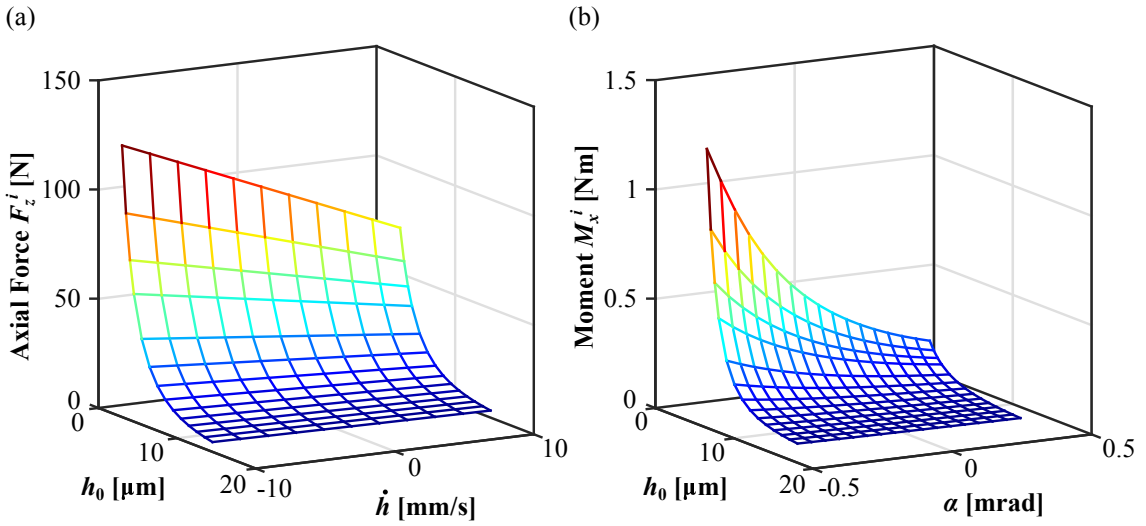

Figure 2.16: (a) Thrust bearing force F_z^i as a function of the minimum film thickness h_0 and the axial velocity $\dot{h}$, (b) thrust bearing moment M_x^i as a function of the minimum film thickness h_0 and the first Bryant angle α, for one bearing pad

pressure distribution p and in the thrust bearing force F_z^i for different numbers of trial functions. Although the relative error in the pressure distribution is quite large,

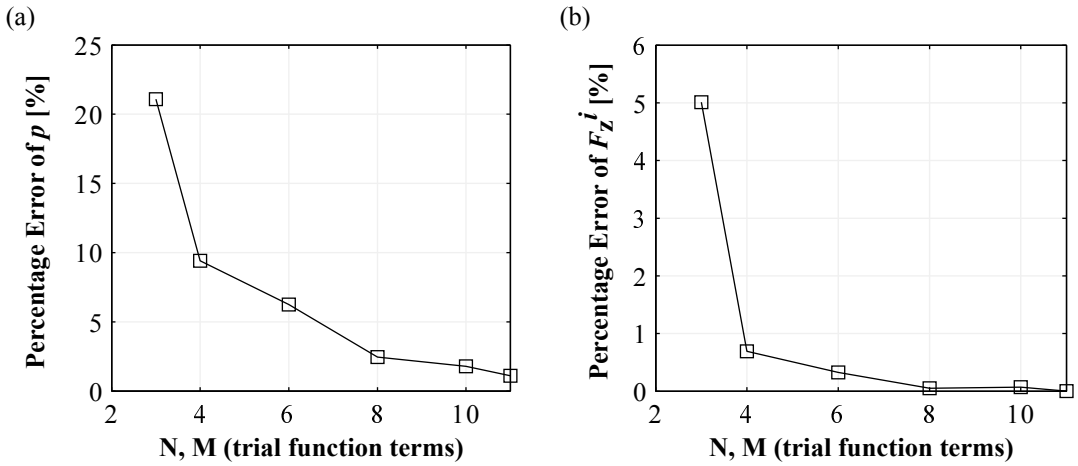

Figure 2.17: Relative errors between the reference solution (FD) and the Global Galerkin approach for different number of trial functions: (a) relative error in the pressure distribution p, (b) relative error in the thrust bearing force F_z^i

only the error in the resultant thrust bearing force and the resultant moments is of interest. As the pressure is integrated to obtain the thrust bearing force, the relative error in the force in the case of 4 trial functions is less than 1%. Therefore, with the Global Galerkin approach, a time-efficient solution can be obtained with quite high accuracy. In this work, all the simulations are performed using 4 trial functions in r- and θ-direction ($N = M = 4$).

In Table 2.4 a comparison of the of the nondimensional thrust bearing force F_B^* be-

tween the DIN 31653 [35] and the Global Galerkin approach is presented. The nondi-

Table 2.4: Comparison of the nondimensional thrust bearing force F_B^* in DIN 31653 [35] with the the Global Galerkin approach

h_0/C_{wed} \ $(r_2-r_1)/L$	2	1.5	1	0.75	0.5
10 (DIN)	0.0003	0.0003	0.0002	0.0002	0.0001
10 (Galerkin)	0.0003	0.0003	0.0002	0.0002	0.0001
2 (DIN)	0.0267	0.0230	0.0167	0.0121	0.0068
2 (Galerkin)	0.0266	0.0229	0.0167	0.0121	0.0068
1 (DIN)	0.1341	0.1169	0.0865	0.0637	0.0364
1 (Galerkin)	0.1336	0.1166	0.0866	0.0640	0.0366
0.5 (DIN)	0.5220	0.4628	0.3552	0.2700	0.1612
0.5 (Galerkin)	0.5238	0.4657	0.3593	0.2744	0.1651
0.33 (DIN)	1.0107	0.9081	0.7164	0.5598	0.3483
0.33 (Galerkin)	1.0328	0.9313	0.7404	0.5820	0.3668
0.2 (DIN)	2.0675	1.8875	1.5475	1.2525	0.8300
0.2 (Galerkin)	2.1547	1.9805	1.6421	1.3465	0.9130
0.1 (DIN)	4.5200	4.2100	3.6200	3.0800	2.2400
0.1 (Galerkin)	4.5875	4.3127	3.7594	3.2479	2.4265

mensional force F_B^* is given by

$$F_B^* = F^* \left(\frac{C_{\text{wed}}}{h_0} \right)^2, \tag{2.2.15}$$

where the nondimensional quantity F^* is

$$F^* = \frac{2F_z^i h_0^2}{\omega \mu L^2 (r_2^2 - r_1^2)}. \tag{2.2.16}$$

The thrust bearing force F^* as well as the damping and stiffness coefficients are compared in Fig. 2.18 with [78], for various relative film thicknesses h_0/C_{wed}. The stiffness and damping coefficients are calculated using a central difference approach. The effect of misalignment on the pressure distribution of a 5-pad thrust bearing is shown in Fig. 2.19. Due to the low minimum film thickness in the aligned case (h_0=5 μm), the rather small misalignment of α =0.2 mrad has a distinct impact on the oil-pressure distribution and therefore on the hydrodynamic bearing force. Thus, the misalignment of the thrust ring should be always included in the modeling of thrust bearings. The Global Galerkin approximation is compared with a Finite Element Method using a fine mesh for various misalignment angles in Table 2.5. A symmetric 5-pad thrust bearing was used and the leading edge of the first pad was $\Theta_1 = 0$.

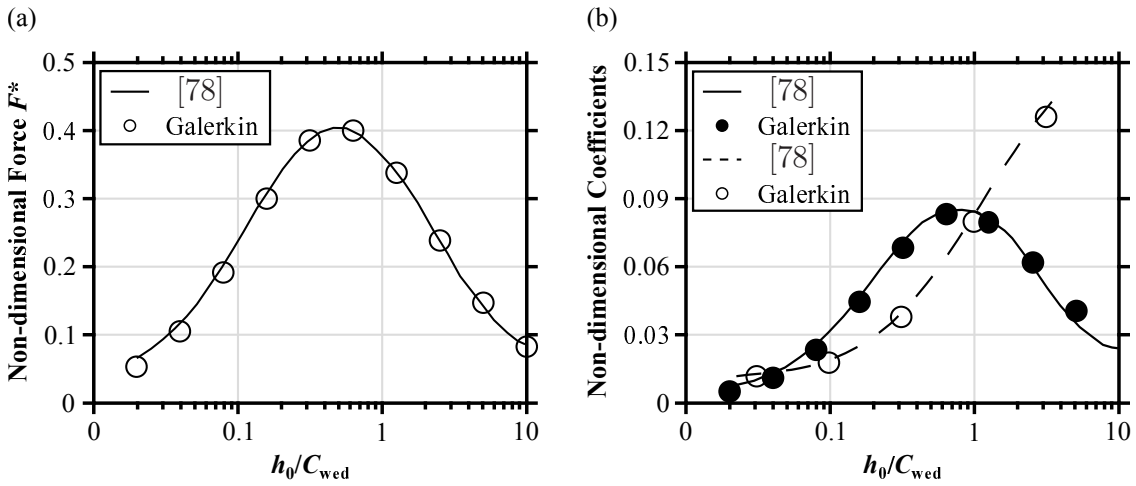

Figure 2.18: (a) Nondimensional thrust bearing force in [78] (—) and Global Galerkin approach (o). (b) Stiffness (—) and damping (- -) coefficients from [78] together with the stiffness (•) and damping (o) coefficients using the Global Galerkin approach.

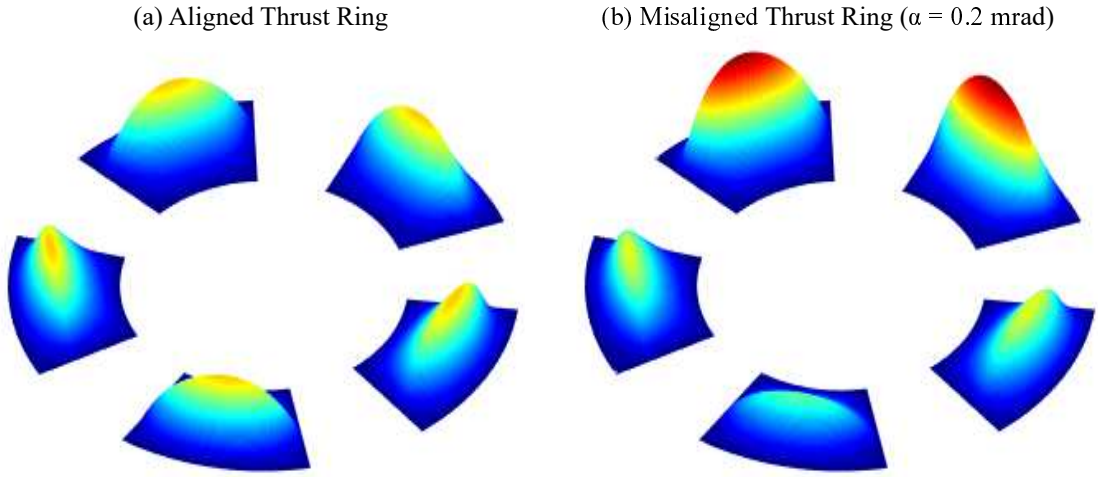

Figure 2.19: Pressure distributions for a 5-pad thrust bearing: (a) aligned case, (b) misaligned case with α =0.2 mrad

Table 2.5: Finite Element and Global Galerkin approach for several misalignment angles

Angle α	Relative Error				
	Pad 1	Pad 2	Pad 3	Pad 4	Pad 5
0 [mrad]	0.4%	0.4%	0.4%	0.4%	0.4%
0.2 [mrad]	1%	0.1%	0.0%	0.3%	1.2%
0.4 [mrad]	2.1%	-0.1%	-0.2%	0.1%	2.4%
0.6 [mrad]	4.1%	-0.3%	-0.4%	-0.1%	2.8%

Higher misalignment induces a very low film thickness for some bearing pads, creating a higher error in the approximation of pressure distribution and therefore in the force. However, an error of 4.1% in the force can be considered acceptable.

2.2.3 Cavitation effects in statically and dynamically loaded thrust bearings

Cavitation in hydrodynamic thrust bearings is manifested similarly to radial journal bearings. Considering a thrust bearing model, cavitation can occur either by the positive axial velocity of the thrust ring (the thrust ring is diverging from the bearing) or by the misalignment of the thrust ring that may create divergence over portions of a the bearing pad. Figure 2.20 shows the pressure distribution for a thrust ring that is diverging from the bearing. In this case the aligned thrust ring is diverging from the

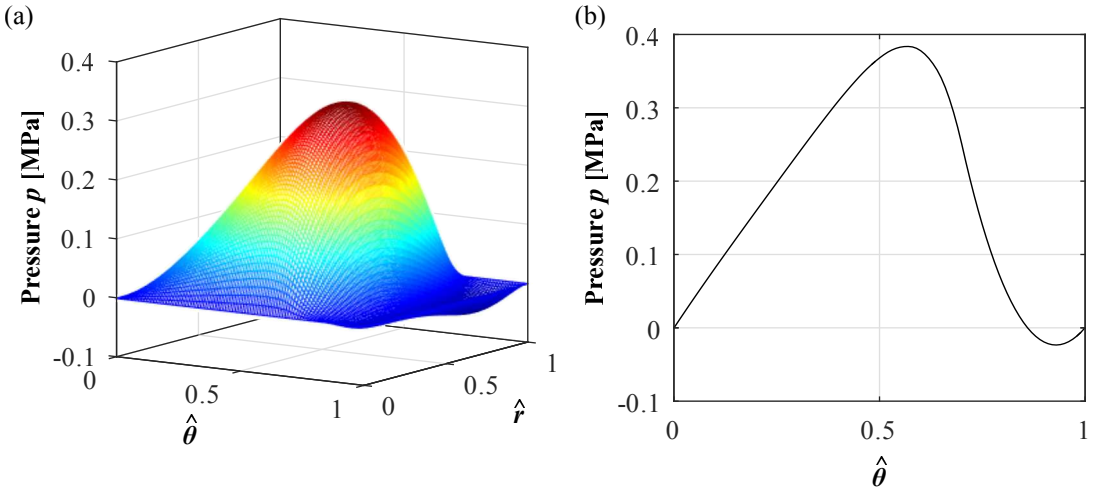

Figure 2.20: Cavitation effect due to axial movement of the thrust ring: (a) 3D pressure, (b) 2D pressure at the middle radius of the bearing

thrust bearing with axial velocity $\dot{h} = 5\,\mathrm{mm/s}$. The effect of cavitation is observed at the trailing edge of the pad. The maximum negative pressure is located in the area near the outer radius r_2. Figure 2.21 shows the pressure distribution for a misaligned thrust ring with the second Bryant angle $\beta = 2\,\mathrm{mrad}$. Towards the trailing edge of the pad, cavitation is encountered. The maximum negative pressure in this example is also found in the area of the outer radius r_2. Misalignment of the thrust ring may cause cavitation in some of the bearing pads. On the contrary, the divergence of the thrust ring can cause cavitation in all bearing pads.

2.2.4 Centrifugal effects in turbocharger thrust bearings

Inertia forces in the oil-film were considered in [26, 52, 79]. By including inertia effects, a modified but complicated Reynolds equation can be obtained, which however

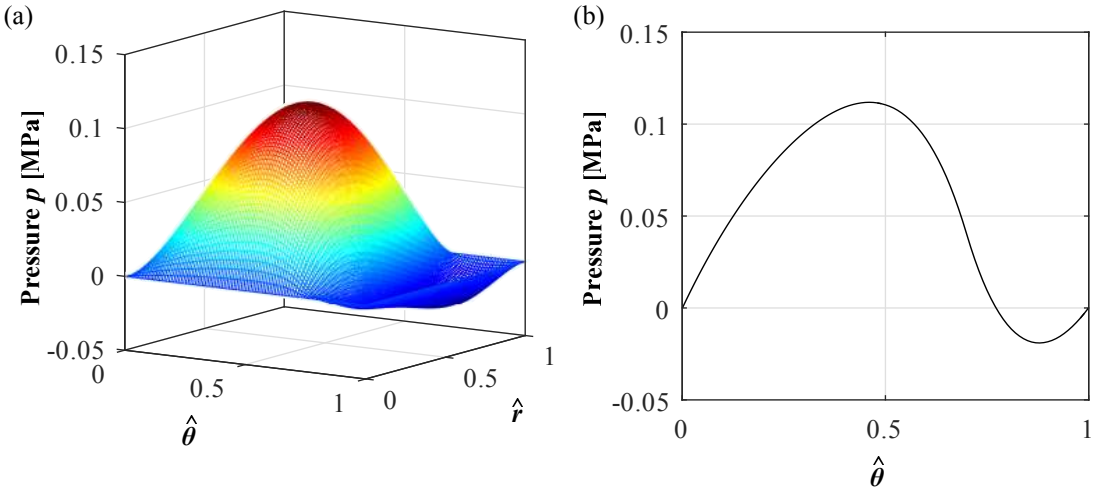

Figure 2.21: Cavitation effect due to misalignment of the thrust ring: (a) 3D pressure, (b) 2D pressure at the middle radius of the bearing

is inappropriate for time-efficient run-up simulations. The question arises, whether inertia effects have to be taken into account for calculating the pressure in thrust bearings in the framework of high-speed rotor applications. In the following analysis, the influence of inertia effects is discussed. In order to keep the analysis concise, the convective inertia terms are ignored and only the centrifugal terms are investigated. In [59, 92], the Reynolds equation is derived including these terms. The circumferential and radial flow velocities, including the shear induced flow and the flow caused by the pressure gradients, can be calculated by

$$\mu \frac{\partial^2 u_\theta}{\partial z^2} = \frac{1}{r}\frac{\partial p}{\partial \theta}, \tag{2.2.17a}$$

$$\mu \frac{\partial^2 u_r}{\partial z^2} = \frac{\partial p}{\partial r} - \frac{\rho u_\theta^2}{r}, \tag{2.2.17b}$$

with the boundary conditions

$$u_\theta(z=h)=0, \qquad u_\theta(z=0)=r\omega, \qquad u_r(z=0)=u_r(z=h)=0.$$

Assuming that the pressure gradient of the circumferential velocity (2.2.17a) can be neglected and considering stationary operating conditions, the Reynolds equation becomes [92]

$$\frac{\partial}{\partial r}(rh^3\frac{\partial p}{\partial r}) + \frac{1}{r}\frac{\partial}{\partial \theta}(h^3\frac{\partial p}{\partial \theta}) = 6\mu\omega r\frac{\partial h}{\partial \theta} + \frac{3}{10}\rho\omega^2\frac{\partial (rh^3)}{\partial r}, \tag{2.2.18}$$

where ρ is the density of the oil. The last term of Eq. (2.2.18) gives the influence of the centrifugal effects. If this term is ignored, the classical Reynolds equation is obtained.

In Figure 2.22, the resultant thrust bearing forces F_z^i for the case with and without centrifugal effects are shown as a function of the minimum film thickness. Two different rotor speeds are considered, namely $\omega = 2000\,\mathrm{rad/s}$ and $\omega = 20000\,\mathrm{rad/s}$. It can

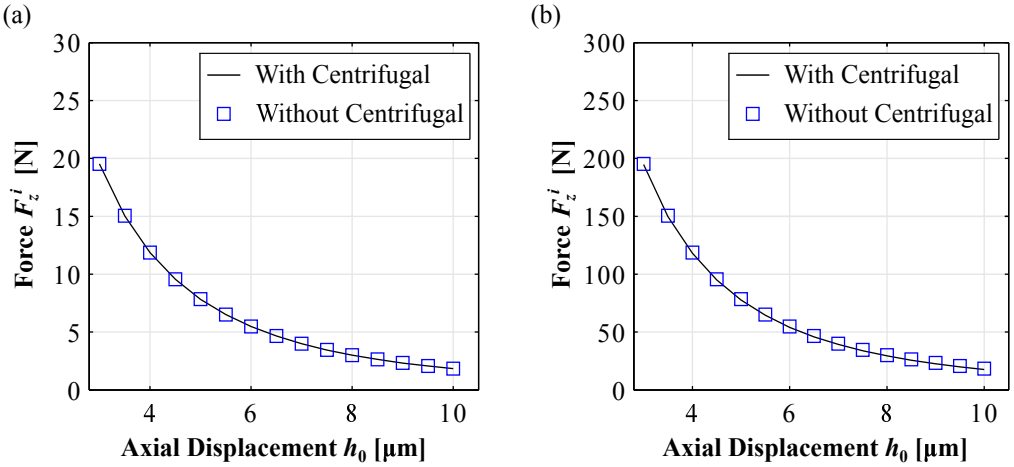

Figure 2.22: Resultant thrust bearing forces F_z^i with and without the centrifugal effects: (a) $\omega = 2000\,\text{rad/s}$, (b) $\omega = 20000\,\text{rad/s}$

be observed that for low axial distances h_0, the centrifugal effects play almost no role for both rotational speeds. Figure 2.23 shows the percentage and absolute errors of the thrust bearing forces when the centrifugal effects are ignored. For high rotational

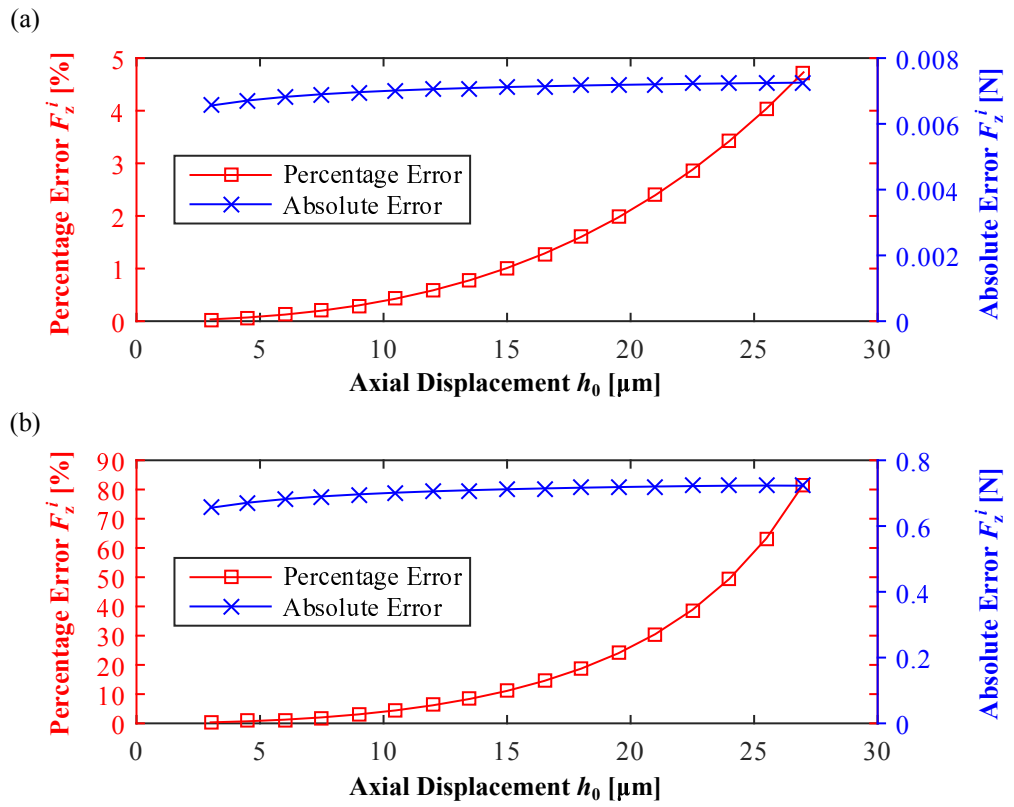

Figure 2.23: Percentage and absolute error of the thrust bearing forces F_z: (a) $\omega = 2000\,\text{rad/s}$, (b) $\omega = 20000\,\text{rad/s}$

speeds the percentage error can be quite large, i.e. it is almost 60% when the axial displacement is $h_0 = 25\,\mu\text{m}$. However, this axial distance is very large so that the

corresponding thrust bearing force becomes very small. As a consequence, the related absolute error is also very small (less than 1 N). For the considered thrust bearing, centrifugal effects have therefore not to be taken into account for investigating the rotor vibrations.

An example, where centrifugal effects may also become apparent, is finally shortly discussed. Concretely, we regard the case where cavitation is generated due to centrifugal effects. Considering an aligned thrust ring, the last term of Eq. (2.2.18) is positive. Therefore, this term produces a reduction in pressures and load capacities. Figure 2.24 shows the pressure distribution without and with centrifugal effects. The

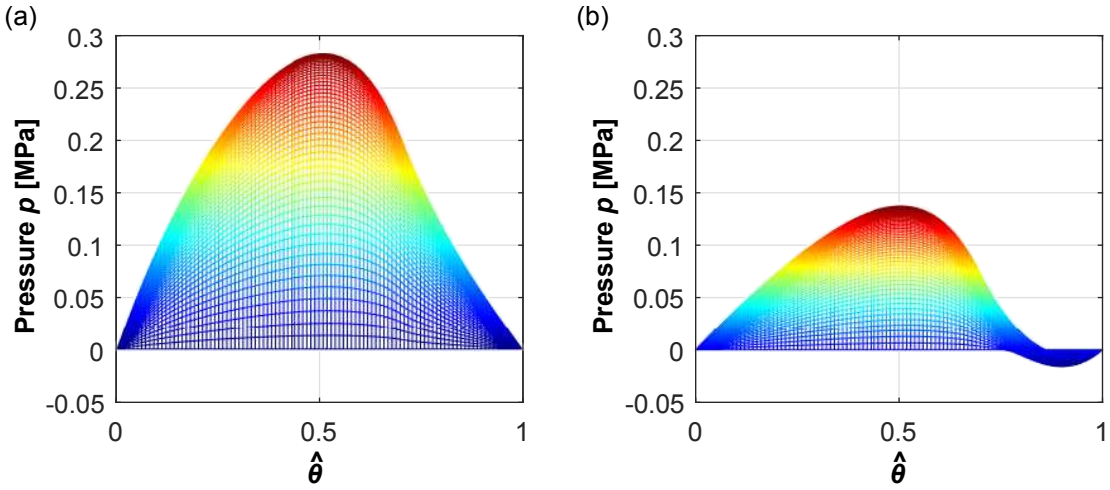

Figure 2.24: Pressure distribution for $h_0 = 30\,\mu m$ and $\omega = 20000\,\mathrm{rad/s}$: (a) without centrifugal effects, (b) with centrifugal effects

difference in the pressure, although it is seemingly large, produces a very small error in the resultant bearing force. It can finally be concluded that centrifugal effects in the fluid film of thrust bearings in small turbocharger applications may usually have only a minor influence on the resultant thrust bearing forces. Despite the fact that the magnitude of the centrifugal effects depend on ω^2, the oil-film thickness occurs with h^3, see Eq. (2.2.18). As a consequence, centrifugal effects may be neglected, if the oil-film thickness is sufficiently small.

2.2.5 Thermohydrodynamic (THD) modeling for thrust bearings

Fluid-film lubrication in thrust and journal bearings is governed by the Navier-Stokes equations. Adopting the common assumptions for thin-film lubrication, the velocities

of the fluid in Cartesian coordinates can be obtained [36]

$$u_x = U_1 + \frac{\partial p}{\partial x}\int_0^z \frac{z}{\mu}\mathrm{d}z + \left(\frac{U_2 - U_1}{F_0} - \frac{F_1}{F_0}\frac{\partial p}{\partial x}\right)\int_0^z \frac{\mathrm{d}z}{\mu}, \tag{2.2.19a}$$

$$u_y = V_1 + \frac{\partial p}{\partial y}\int_0^z \frac{z}{\mu}\mathrm{d}z + \left(\frac{V_2 - V_1}{F_0} - \frac{F_1}{F_0}\frac{\partial p}{\partial y}\right)\int_0^z \frac{\mathrm{d}z}{\mu}. \tag{2.2.19b}$$

$U_{1,2}$ and $V_{1,2}$ are the boundary velocities at the x- and y-direction and the subscripts 1 and 2 denote the bearing and the shaft respectively. The viscosity μ of the oil is assumed to vary across the film thickness. The integral expressions F_0 and F_1 are presented later in this section. Using the velocities of Eq. (2.2.19) and the continuity equation, the generalized Reynolds equation in Cartesian coordinates for a thermohydrodynamic lubrication model is [36, 59, 73, 75]

$$\begin{aligned}
&\frac{\partial}{\partial x}\left((F_2 + G_1)\frac{\partial p}{\partial x}\right) + \frac{\partial}{\partial y}\left((F_2 + G_1)\frac{\partial p}{\partial y}\right) = h\left(\frac{\partial(\rho U)_2}{\partial x} + \frac{\partial(\rho V)_2}{\partial y}\right)\\
&-\frac{\partial}{\partial x}\left(\frac{(U_2 - U_1)(F_3 + G_2)}{F_0} + U_1 G_3\right) - \frac{\partial}{\partial y}\left(\frac{(V_2 - V_1)(F_3 + G_2)}{F_0} + V_1 G_3\right)\\
&+ (\rho w)_2 - (\rho w)_1 + \int_0^h \frac{\partial \rho}{\partial t}\mathrm{d}z,
\end{aligned} \tag{2.2.20}$$

where the integrals F_0, F_1, F_2, F_3 and G_1, G_2, G_3 are calculated as follows

$$\begin{aligned}
&F_0 = \int_0^h \frac{\mathrm{d}z}{\mu}, \quad F_1 = \int_0^h \frac{z\mathrm{d}z}{\mu}, \quad F_2 = \int_0^h \frac{\rho z}{\mu}(z - \frac{F_1}{F_0})\mathrm{d}z, \quad F_3 = \int_0^h \frac{\rho z}{\mu}\mathrm{d}z,\\
&G_1 = \int_0^h \left(z\frac{\partial \rho}{\partial z}\left(\int_0^z \frac{z}{\mu}\mathrm{d}z - \frac{F_1}{F_0}\int_0^z \frac{\mathrm{d}z}{\mu}\right)\right)\mathrm{d}z, \quad G_2 = \int_0^h \left(z\frac{\partial \rho}{\partial z}\int_0^z \frac{\mathrm{d}z}{\mu}\right)\mathrm{d}z,\\
&G_3 = \int_0^h z\frac{\partial \rho}{\partial z}\mathrm{d}z.
\end{aligned} \tag{2.2.21}$$

The variables w_1 and w_2 describe the velocities of the bearing and the shaft across the oil-film. In oil-lubricated bearings, the terms related with compressibility are generally ignored under the assumption that the oil is incompressible. Therefore, the generalized Reynolds equation for oil-film bearing reads

$$\begin{aligned}
\frac{\partial}{\partial x}\left(F_{2_i}\frac{\partial p}{\partial x}\right) + \frac{\partial}{\partial y}\left(F_{2_i}\frac{\partial p}{\partial y}\right) &= h\left(\frac{\partial U_2}{\partial x} + \frac{\partial V_2}{\partial y}\right)\\
&-\frac{\partial}{\partial x}\left(\frac{(U_2 - U_1)F_1}{F_0}\right) - \frac{\partial}{\partial y}\left(\frac{(V_2 - V_1)F_1}{F_0}\right) + w_2 - w_1,
\end{aligned} \tag{2.2.22}$$

where

$$F_{2_i} = \int_0^h \frac{z}{\mu}(z - \frac{F_1}{F_0})\mathrm{d}z. \tag{2.2.23}$$

Adiabatic approach using the generalized Reynolds equation and the 3D energy equation (3D model)

In this subsection, the generalized Reynolds equation and the 3D energy equation are presented. The Reynolds equation is solved on a plane (2D solution) and the energy

equation may be solved in the volume between the thrust ring and a bearing pad (3D solution) or on a plane (2D Solution) as shown in Fig. 2.25.

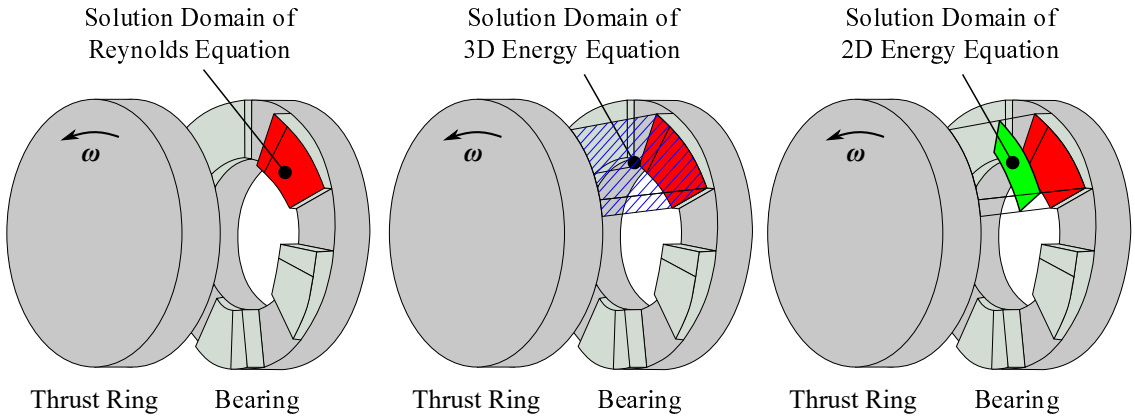

Figure 2.25: Solution domain for the Reynolds and the energy equation

For the 3D model, obviously the 3D solution for the energy equation will be used. The generalized Reynolds equation in cylindrical coordinates describes the pressure distribution p in the oil-film for a hydrodynamic thrust bearing

$$\frac{\partial}{\partial r}\left(rF_{2_i}\frac{\partial p}{\partial r}\right)+\frac{1}{r}\frac{\partial}{\partial\theta}\left(F_{2_i}\frac{\partial p}{\partial\theta}\right)=r\omega\frac{\partial}{\partial\theta}\left(\frac{F_1}{F_0}\right)+r\frac{\partial h}{\partial t}. \tag{2.2.24}$$

The spatial variables θ and r denote the angular and radial coordinates. The rotational speed is given by ω and the oil-film thickness is h. At the boundaries of the pads Dirichlet boundary conditions are assumed, i.e.

$$p(r_1,\theta)=p(r_2,\theta)=0, \qquad p(r,\Theta_i)=p(r,\Theta_i+\theta_0)=0.$$

The temperature T in the oil-film is governed by the 3D energy equation [62]

$$\rho c_p\left(\frac{\partial T}{\partial t}+u_r\frac{\partial T}{\partial r}+\frac{u_\theta}{r}\frac{\partial T}{\partial\theta}+u_z\frac{\partial T}{\partial z}\right)=k\left(\frac{1}{r^2}\frac{\partial^2 T}{\partial\theta^2}+\frac{1}{r}\frac{\partial}{\partial r}\left(r\frac{\partial T}{\partial r}\right)+\frac{\partial^2 T}{\partial z^2}\right)+\mu\left(\left(\frac{\partial u_r}{\partial z}\right)^2+\left(\frac{\partial u_\theta}{\partial z}\right)^2\right). \tag{2.2.25}$$

The terms on the left side describe the time-dependent temperature term as well as the convection of the oil. On the right side the terms related to the conduction of the oil and the viscous dissipation are shown. The velocities in the radial u_r and in the circumferential u_θ direction read

$$u_r=\frac{\partial p}{\partial r}\left(\int_0^z\frac{z}{\mu}\mathrm{d}z-\frac{F_1}{F_0}\int_0^z\frac{\mathrm{d}z}{\mu}\right), \tag{2.2.26a}$$

$$u_\theta=\frac{1}{r}\frac{\partial p}{\partial\theta}\left(\int_0^z\frac{z}{\mu}\mathrm{d}z-\frac{F_1}{F_0}\int_0^z\frac{\mathrm{d}z}{\mu}\right)-\frac{r\omega}{F_0}\int_0^z\frac{\mathrm{d}z}{\mu}+r\omega. \tag{2.2.26b}$$

At this point it is further assumed that the oil velocity in z-direction and the conduction term in the circumferential θ-direction are very small and therefore they can be neglected. The time-dependent temperature term will be omitted from the calculations, however, a physical explanation of its exclusion is presented in section 4.2.6. For the calculations, the following energy equation is used

$$\rho c_p \left(u_r \frac{\partial T}{\partial r} + \frac{u_\theta}{r} \frac{\partial T}{\partial \theta} \right) = k \left(\frac{1}{r} \frac{\partial}{\partial r} \left(r \frac{\partial T}{\partial r} \right) + \frac{\partial^2 T}{\partial z^2} \right) + \mu \left(\left(\frac{\partial u_r}{\partial z} \right)^2 + \left(\frac{\partial u_\theta}{\partial z} \right)^2 \right). \tag{2.2.27}$$

It is assumed that the inlet oil-temperature is constant $T(r, \Theta_i, z) = T_{\text{in}}$ and no mixing exists between fresh oil coming from the engine and circulating oil coming from the previous pad. The mixing process as described in [56] may be important for the determination of the pressure and the temperature distribution, however it will be ignored at this instance. Furthermore, the heat-flux from the oil to the solids (bearing and thrust ring) at their boundaries is considered zero, i.e. $\frac{\partial T}{\partial z} = 0$. At the inner ($r_1$) and at the outer ($r_2$) radius of the bearing pads, we assume no heat exchange, namely $\frac{\partial T}{\partial r} = 0$. The relationship between the oil-temperature and the oil-viscosity is given by

$$\mu = \mu_{\text{in}} e^{-\lambda (T - T_{\text{in}})}, \tag{2.2.28}$$

where μ_{in} is the inlet oil-viscosity, λ is the viscosity-temperature coefficient and T_{in} is the inlet oil-temperature. The 3D model, i.e. the solution of the generalized Reynolds equation and the 3D energy equation, entails the solution of 5 integro-differential equations. Equation (2.2.24) and Eq. (2.2.27) as well as the three integrals F_0, F_1 and F_{2_i} in Eq. (2.2.21) and Eq. (2.2.23) should be solved simultaneously. The solution of this nonlinear system of equations is rather time-consuming, prohibiting run-up simulations.

Plane approach using the standard Reynolds equation and the 2D energy equation (2D-Coupled model)

In this subsection, the 3D energy equation is reduced to a 2D equation by averaging the oil velocities over the film thickness. Additionally, the standard Reynolds equation is used.

Assuming no variation of the oil-viscosity across the oil-film, the generalized Reynolds equation presented in Eq. (2.2.24) is reduced to

$$\frac{\partial}{\partial r} \left(\frac{r h^3}{12 \mu} \frac{\partial p}{\partial r} \right) + \frac{1}{r} \frac{\partial}{\partial \theta} \left(\frac{h^3}{12 \mu} \frac{\partial p}{\partial \theta} \right) = \frac{r \omega}{2} \frac{\partial h}{\partial \theta} + r \frac{\partial h}{\partial t}. \tag{2.2.29}$$

The radial and the circumferential velocities in Eq. (2.2.26), assuming constant oil-viscosity read in the simplified form

$$u_r = \frac{1}{2\mu}\frac{\partial p}{\partial r} z(z-h), \tag{2.2.30a}$$

$$u_\theta = \frac{1}{2\mu r}\frac{\partial p}{\partial \theta} z(z-h) + \frac{h-z}{h}\omega r. \tag{2.2.30b}$$

Since the energy equation is considered here only in two dimensions, the velocities in Eq. (2.2.30) are averaged over the film thickness.

$$\bar{u}_r = -\frac{h^2}{12\mu}\frac{\partial p}{\partial r}, \tag{2.2.31a}$$

$$\bar{u}_\theta = -\frac{h^2}{12\mu r}\frac{\partial p}{\partial \theta} + \frac{r\omega}{2}. \tag{2.2.31b}$$

The 2D energy equation is given by

$$\rho c_p \left(-\frac{h^2}{12\mu}\frac{\partial p}{\partial r}\frac{\partial T}{\partial r} + \frac{-\frac{h^2}{12\mu r}\frac{\partial p}{\partial \theta} + \frac{r\omega}{2}}{r}\frac{\partial T}{\partial \theta} \right) = \mu \left(\left(\frac{1}{12}\left(\frac{h\partial p}{\mu \partial r}\right)^2 \right) + \left(\frac{1}{12}\left(\frac{h\partial p}{\mu r \partial \theta}\right)^2 + \left(\frac{r\omega}{h}\right)^2 \right) \right). \tag{2.2.32}$$

Please note additionally that the conduction terms are neglected. The two equations, Eq. (2.2.29) and Eq. (2.2.32), are coupled and therefore, they should be solved simultaneously at every time-integration step in a run-up simulation.

Decoupling plane approach using the standard Reynolds equation and the 2D energy equation (2D-Decoupled model)

The computational cost of solving the coupled system of Eq. (2.2.29) and Eq. (2.2.32) simultaneously can be overcome by a procedure described in [57,76,95]. The proposed solution ignores the pressure gradients from the oil-velocities in the energy equation. Therefore, the Reynolds and the energy equation are decoupled and they can be solved sequentially. The energy equation now reads

$$\rho c_p \left(\frac{\omega}{2}\frac{\partial T}{\partial \theta} \right) = \mu \left(\frac{r\omega}{h} \right)^2, \tag{2.2.33}$$

while the Reynolds equation remains as in Eq. (2.2.29). Equation (2.2.33) can be directly integrated to obtain an expression for the temperature distribution. Using the temperature-viscosity relationship of Eq. (2.2.28), the viscosity is

$$\mu = \frac{\mu_{\text{in}} c_p \rho}{2\frac{1}{\int_{\Theta_i}^{\Theta_i+\theta} h\,(r,\theta)^2\, d\theta}\omega\lambda\mu_{\text{in}} r^2 + c_p\rho}, \tag{2.2.34}$$

Instead of solving the nonlinear system of equations (Eq. (2.2.29) and Eq. (2.2.32)), the decoupling approach can provide the oil-pressure and the oil-temperature solving only two linear equations. We note here that the Reynolds equation is a nonlinear equation in the pressure when the negative pressures are neglected (Gümbel cavitation approach). The advantage of this decoupling approach is therefore, a highly time-efficient simulation.

Isothermal approach using the simplified Reynolds equation (Isothermal model)

The oil-viscosity in the isothermal case is clearly constant. The Reynolds equation can therefore further be simplified into

$$\frac{\partial}{\partial r}\left(rh^3\frac{\partial p}{\partial r}\right)+\frac{1}{r}\frac{\partial}{\partial \theta}\left(h^3\frac{\partial p}{\partial \theta}\right)=6\mu r\omega\frac{\partial h}{\partial \theta}+12\mu r\frac{\partial h}{\partial t}. \tag{2.2.35}$$

The temperature variations in the oil-film are neglected and therefore no prediction for the increase of the oil-temperature can be made. This model, however, produces the most time-efficient simulations.

2.2.6 Comparisons between THD thrust bearing models

In this section detailed comparisons are performed among the 3D model, the 2D-Coupled model, the 2D-Decoupled model and the isothermal model. The four thrust bearing models are summarized below.

- **3D model:** In this model the generalized Reynolds equation (Eq. 2.2.24) is solved simultaneously with the 3D energy equation (Eq. 2.2.27). These two differential equations together with the integrals F_0, F_1 and F_{2_i} constitute a system of 5 integro-differential equations. In terms of physical accuracy, this is the most complete model used in this work.
- **2D-Coupled model:** In this model the standard Reynolds equation (Eq. 2.2.29) is solved simultaneously with the 2D energy equation (Eq. 2.2.32). Therefore, in this case we have a system of two nonlinear equations.
- **2D-Decoupled model:** In this model the reduced energy equation (Eq. 2.2.33) is initially solved for the determination of the oil-temperature, which is then substituted in the standard Reynolds equation (Eq. 2.2.29). The decoupling of the two equations provides time-efficient simulations.
- **Isothermal model:** In this model only the simplified Reynolds equation (Eq. 2.2.35) is solved for the determination of the oil-pressure distribution. No prediction can be made for the oil-temperature.

For the solution of the Reynolds and the energy equation a Finite Difference approach is used and the resultant sparse linear system is solved using a multi-frontal solver [33, 34]. The comparisons focus on the pressure distributions and the load capacities predicted from the models. Additionally, the temperature distributions predicted from the thermal models are also discussed. Table 2.6 shows the characteristics of the bearing pad and the oil used in the comparisons. Additionally, the thrust ring is considered to be aligned.

Table 2.6: Thrust bearing pad and oil-film characteristics

Parameter	Description	Value	Unit
r_1	Inner radius	3.55	mm
r_2	Outer radius	6.3	mm
θ_0	Angular extent of pad	0.775	rad
L_{wed}/L	Inclined/total length	0.7	-
C_{wed}	Taper height	0.01	mm
h_0	Minimum film thickness	5, 10, 15	μm
ω	Angular velocity	1, 5, 20, 30	krad/s
λ	Viscosity-temperature coefficient	0.0225	1/°C
μ_{in}	Inlet oil-viscosity	7.68	mPa s
k	Thermal conductivity coefficient	0.128	W/(m °C)
c_p	Specific heat capacity	2010	J/(kg °C)
ρ	Oil-density	874.5	kg/m^3

Influence on the pressure distribution

The pressure distributions predicted from the hydrodynamic thrust bearing models are compared here for various rotational speeds and minimum film thicknesses. Figure 2.26 illustrates the oil-pressure distributions in cylindrical coordinates of one bearing pad for all the thrust bearing models at $\omega = 20000\,\text{rad/s}$ and $h_0 = 5\,\mu\text{m}$. This comparison shows that the pressure distribution predicted from the isothermal model is significantly larger than the pressures predicted by the thermal models.
A more detailed comparison for various rotational speeds ω and minimum film thicknesses h_0 is presented in Fig. 2.27. The pressure profile $p(\hat{r} = 0.5, \hat{\theta})$ of all four models is plotted as a function of the nondimensional variables $\hat{r} = r(r_2 - r_1) + r_1$ and $\hat{\theta} = \frac{\theta}{\theta_0}$ at the middle radius of the thrust bearing pad.
For lower rotational speeds, i.e. $\omega = 1000\,\text{rad/s}$, the pressure distributions predicted from all the thrust bearing models are quite similar. A small difference can be ob-

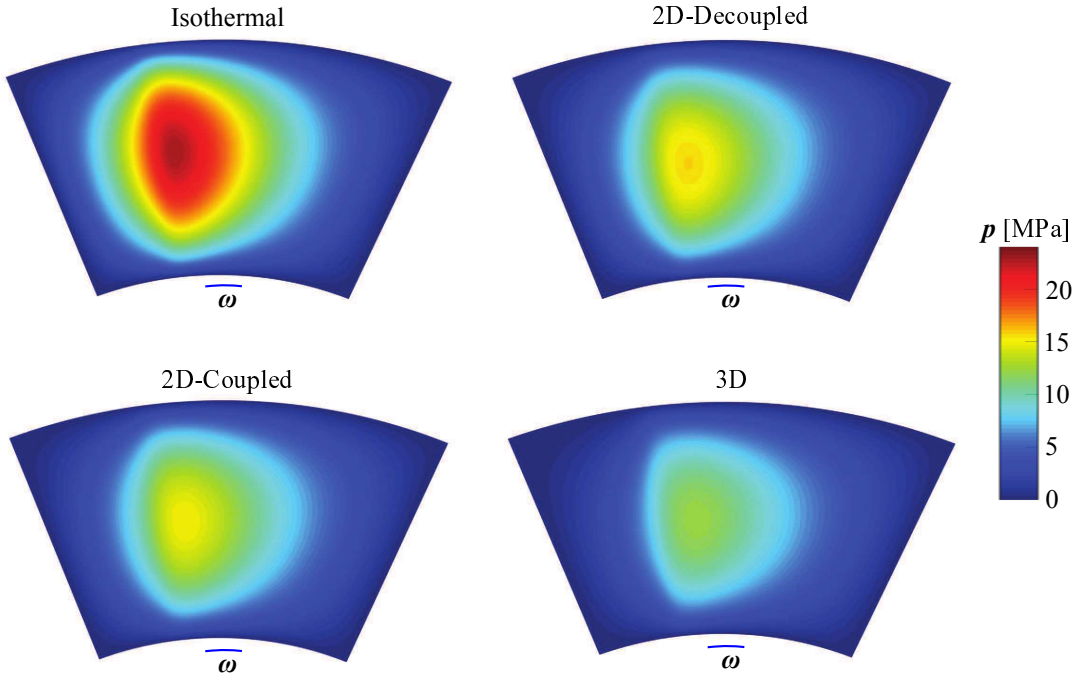

Figure 2.26: Pressure distributions of a bearing pad for $\omega = 20000\,\text{rad/s}$ and film thickness $h_0 = 5\,\mu\text{m}$

served for a low minimum film thickness ($h_0 = 5\,\mu m$). For larger oil-film thicknesses the predictions are almost identical.

As the rotational speed is increased to $\omega = 5000\,\text{rad/s}$, the pressure distributions predicted from the thermal models are clearly lower than the pressure predicted by the isothermal thrust bearing model. The difference is higher for low film thickness ($h_0 = 5\,\mu m$) and is rather small for larger film thicknesses. The thermal models predict very similar pressure distributions, however, the pressure predicted from the 3D model at ($h_0 = 5\,\mu m$) is slightly lower than the pressures from the 2D models.

A further increase in the rotational speed at $\omega = 20000\,\text{rad/s}$ creates a rather large difference between the isothermal and the thermal models. For $h_0 = 5\,\mu m$, the difference of the maximum pressure between the isothermal and the 3D model is almost 80%. At $\omega = 20000\,\text{rad/s}$ and $h_0 = 5\,\mu m$, a difference can be observed between the 3D model and the 2D models. The predictions of the pressure distribution of the two 2D models (2D-Coupled and 2D-Decoupled model) are very similar. A difference can also be observed at a minimum film thickness of $h_0 = 10\,\mu m$.

As the rotational speed is increased at the very high speed of $\omega = 30000\,\text{rad/s}$, the differences between the thermal models are also increased. At this speed, it is clear that the isothermal model is rather inaccurate and at least a 2D model should be used.

It is obvious from the above comparisons that for high rotational speeds ω and high loads (the lower the minimum film thickness h_0, the higher the load that a bearing pad can support) an isothermal thrust bearing model cannot be used for an accurate

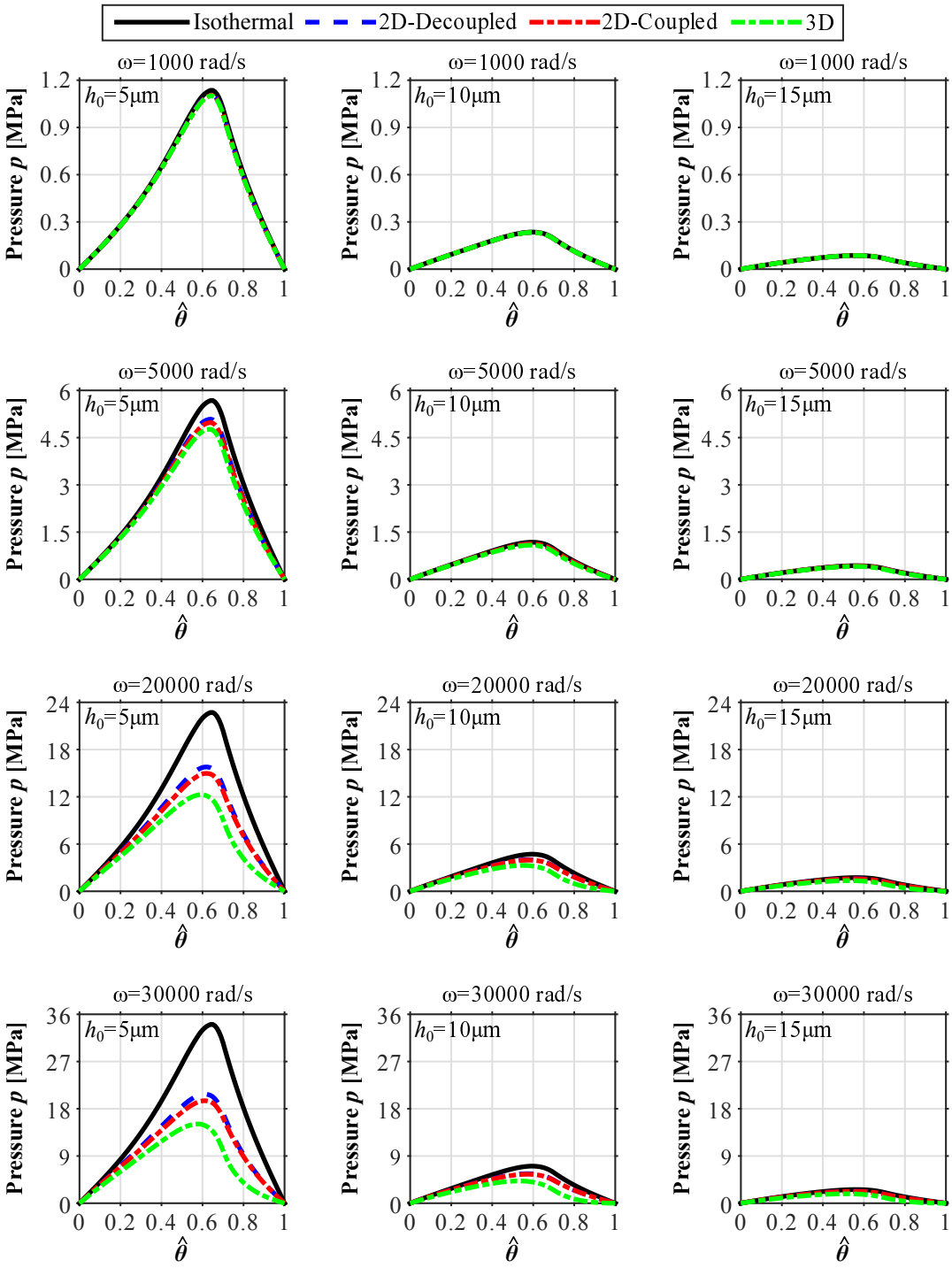

Figure 2.27: Pressure profiles $p(\hat{r} = 0.5, \hat{\theta})$ for various rotational speeds and minimum film thicknesses

prediction of the pressure distribution. On the contrary, despite the differences at the very high rotational speeds, the 2D models can be a very good approximation of the more accurate 3D model. For all rotational speeds and minimum film thicknesses, the 2D-Coupled and the 2D-Decoupled models exhibit very similar predictions for the pressure distribution.

Influence on the thrust bearing force

In rotordynamic simulations, the resultant thrust bearing forces and moments play the most critical role in characterizing the dynamic behavior of a system. Therefore, in this section, comparisons of the thrust bearing forces are provided for various rotational speeds and minimum film thicknesses. In Figure 2.28, the thrust bearing forces F_z for one bearing pad predicted by all four models with rotational speeds $\omega = 1000\,\text{rad/s}$, $\omega = 5000\,\text{rad/s}$, $\omega = 20000\,\text{rad/s}$ and $\omega = 30000\,\text{rad/s}$ are demonstrated. For a low rotational speed $\omega = 1000\,\text{rad/s}$ the thrust bearing forces predicted

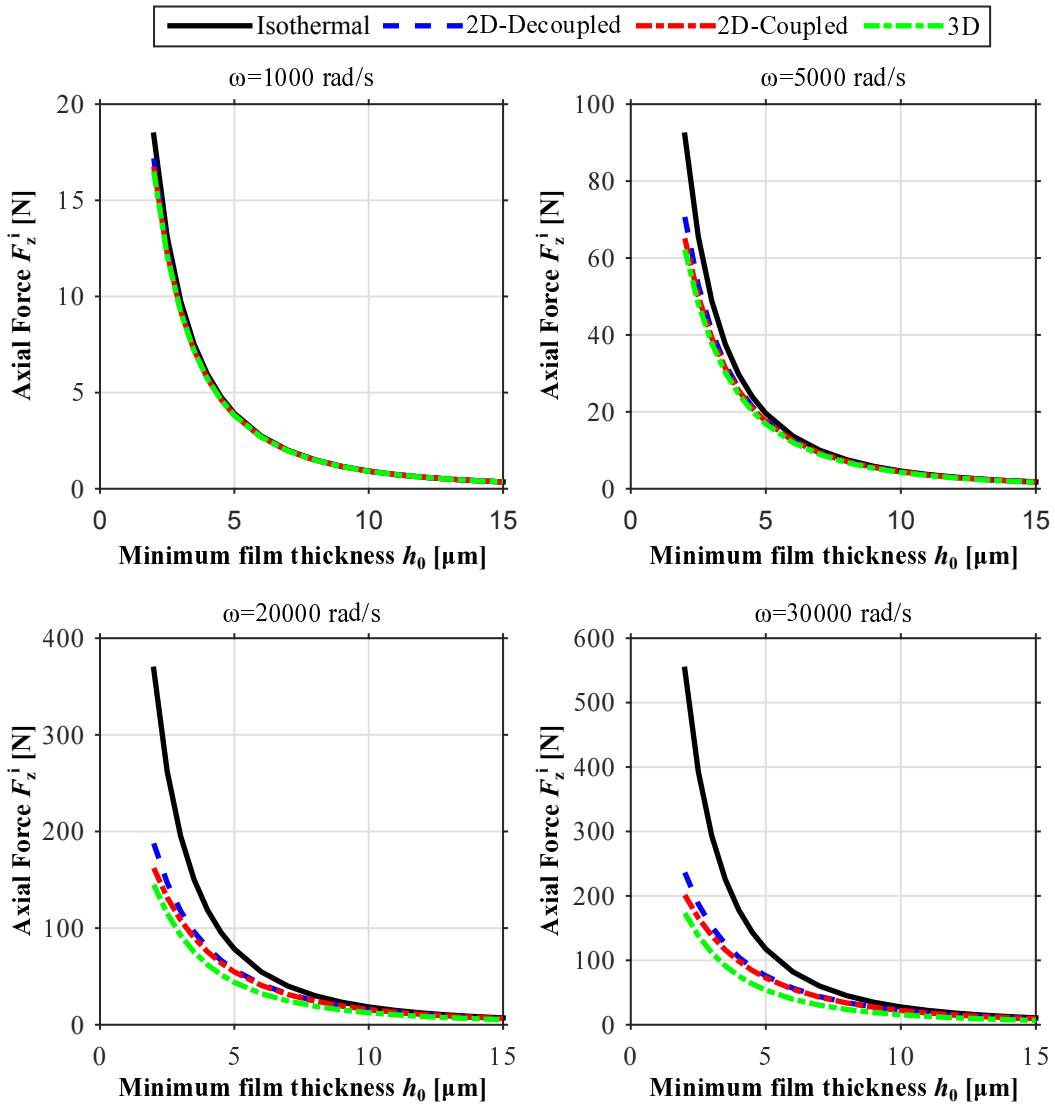

Figure 2.28: Thrust bearing forces F_z produced by all four thrust bearing models for $\omega = 1000\,\text{rad/s}$, $\omega = 5000\,\text{rad/s}$, $\omega = 20000\,\text{rad/s}$ and $\omega = 30000\,\text{rad/s}$

by the thrust bearing models are very similar. As the rotational speed is increased to $\omega = 5000\,\text{rad/s}$, the isothermal model predicts a higher thrust bearing force compared to the thermal models at very low minimum film thicknesses. A further increase of the rotational speed at $\omega = 20000\,\text{rad/s}$ clearly shows that the thrust bearing force

predicted from the isothermal model is much larger than the forces from the thermal models. The same applies for the rotational speed $\omega = 30000\,\mathrm{rad/s}$. As in the pressure distribution, it is also shown here that the isothermal model is not suitable as the rotational speed and the bearing load are increased.

Influence on the temperature distribution

In this section, the temperature variations predicted by the thermal models are presented. Figure 2.29 shows the temperature distributions in cylindrical coordinates of one bearing pad for all the thrust bearing models at $\omega = 20000\,\mathrm{rad/s}$ and $h_0 = 5\,\mu\mathrm{m}$. It is noted here that the increase in the oil-temperature predicted from the isothermal

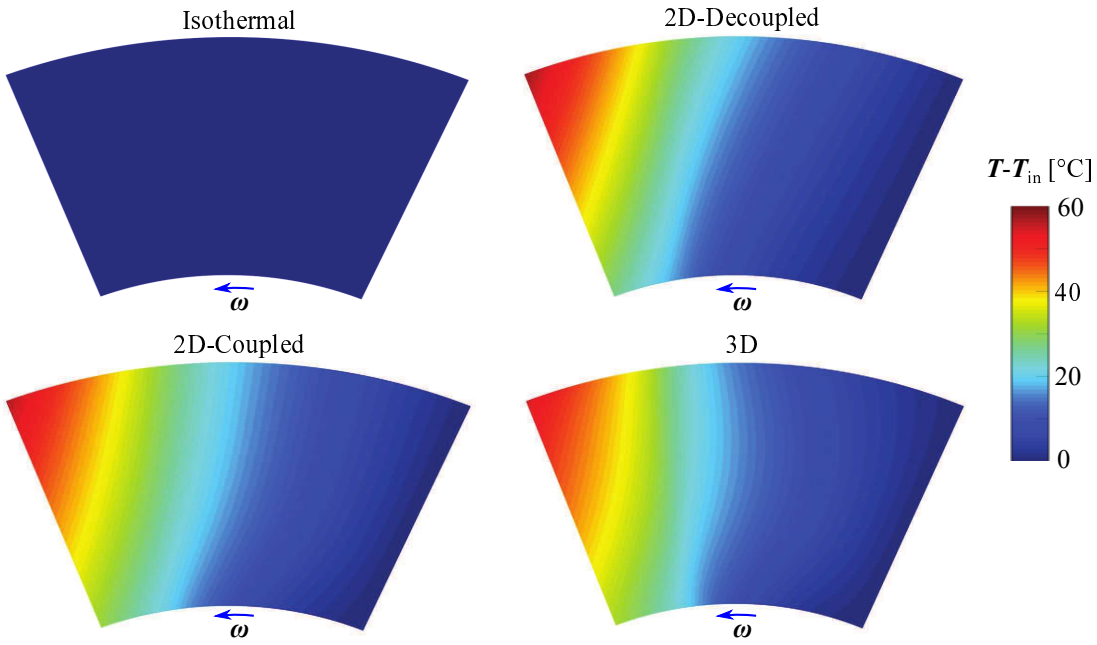

Figure 2.29: Temperature distributions of a bearing pad for $\omega = 20000\,\mathrm{rad/s}$ and film thickness $h_0 = 5\,\mu\mathrm{m}$

model is 0 °C and therefore it will be excluded from further comparisons. Moreover, the temperature distribution predicted from the 3D model is clearly a 3D distribution. For reasons of a concise comparison, this 3D temperature distribution is averaged over the film thickness.
As for the pressure distributions, a more detailed comparison using various rotational speeds ω and minimum film thicknesses h_0 is presented in Fig. 2.30. The temperature profiles at the inner radius $T(r_1, \hat{\theta})$ and at the outer radius $T(r_2, \hat{\theta})$ of a bearing pad for all the thermal models are plotted as a function of the nondimensional variable $\hat{\theta}$.

For a low rotational speed $\omega = 1000\,\mathrm{rad/s}$, all the thrust bearing models show a quite

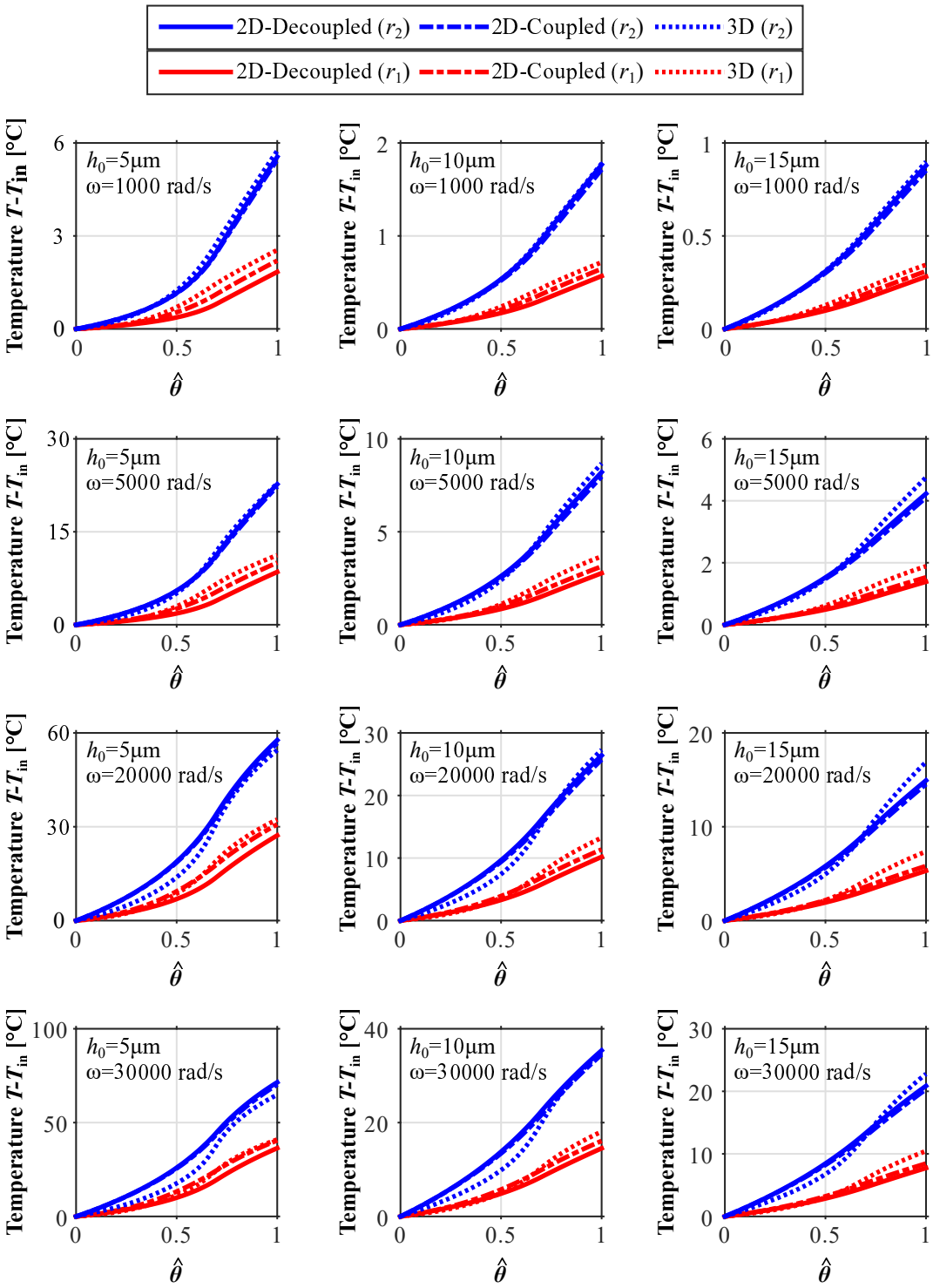

Figure 2.30: Temperature profiles $T(r_1, \hat{\theta})$ and $T(r_2, \hat{\theta})$ using various rotational speeds and minimum film thicknesses

good agreement in their temperature predictions both at the inner and at the outer radius of the pad. The maximum temperature increase is found at the outer radius of the pad when the minimum film thickness is low ($h_0 = 5\,\mu m$). Larger differences between the models are observed at the inner radius, however, in absolute values, these differences are comparatively small. The increase of the rotational speed to $\omega = 5000\,\mathrm{rad/s}$

increases also the maximum temperature from almost 6 °C for $\omega = 1000\,\mathrm{rad/s}$ and $h_0 = 5\,\mu m$ to almost 22 °C for $\omega = 5000\,\mathrm{rad/s}$ and $h_0 = 5\,\mu m$ at the outer radius of the pad. The largest differences between the models are found here also in the inner radius of the bearing pad.

At very high rotational speeds $\omega = 20000\,\mathrm{rad/s}$ and $\omega = 30000\,\mathrm{rad/s}$ a very large increase of the temperature at the trailing edge of the pad is observed. The thermal models show a rather good agreement, although the temperature predicted from the 3D model shows some deviations compared to the other models. As it was mentioned before, however, the temperature predicted from the 3D model is averaged over the film thickness, which makes a direct comparison of the temperature distributions difficult. Figure 2.31 shows the 3D temperature distributions $T(\hat{r}, \hat{\theta}, \hat{z})$ in the oil-film for $\omega = 1000\,\mathrm{rad/s}$, $\omega = 5000\,\mathrm{rad/s}$, $\omega = 20000\,\mathrm{rad/s}$ and $\omega = 30000\,\mathrm{rad/s}$, at a minimum film thickness $h_0 = 5\,\mu m$. The temperature distribution is plotted over the nondi-

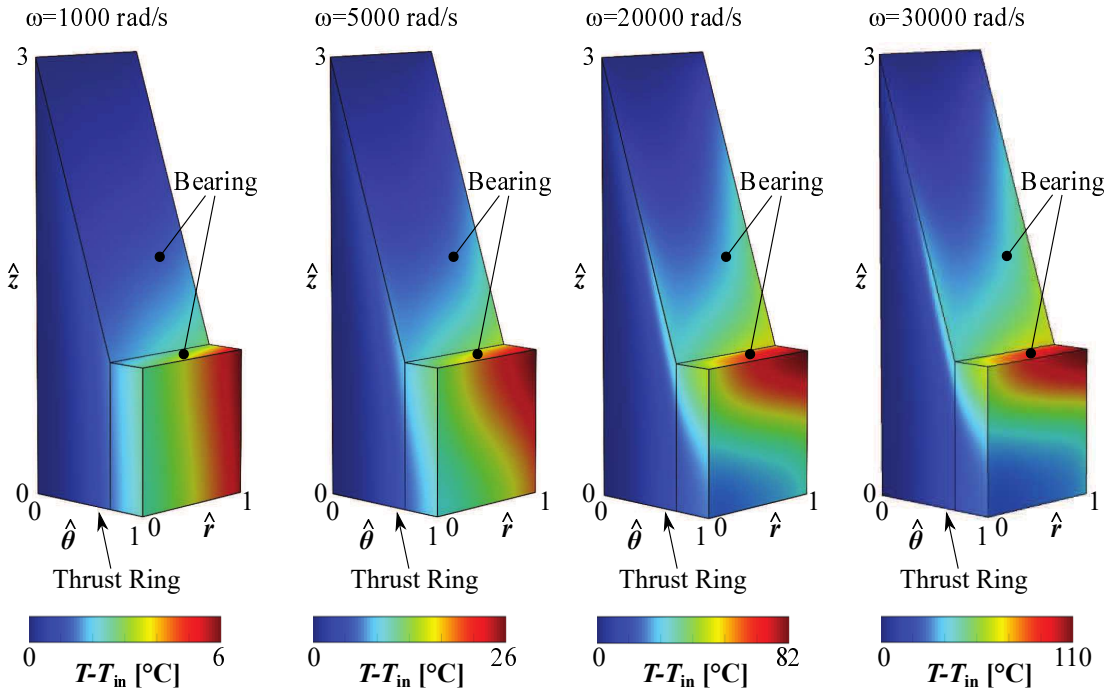

Figure 2.31: Temperature distributions $T(\hat{r}, \hat{\theta}, \hat{z})$ for $h_0 = 5\,\mu m$ at various rotational speeds

mensional coordinates $\hat{r}$, $\hat{\theta}$ and $\hat{z} = \frac{z}{h_0}$. The predicted temperature for low rotational speeds, i.e. $\omega = 1000\,\mathrm{rad/s}$ is almost constant across the oil film (z-direction). As the rotational speed is increased to $\omega = 5000\,\mathrm{rad/s}$ this property is fading and it is totally lost for the very high speeds $\omega = 20000\,\mathrm{rad/s}$ and $\omega = 30000\,\mathrm{rad/s}$. Since in higher rotational speeds, the increase of temperature near the bearing surface is much larger than the temperature near the thrust ring of the rotor, for an accurate prediction of the temperature distribution in the oil-film, the 2D models may be inadequate.

In this section a detailed comparison between four thrust bearing models was performed and it was shown that the isothermal model is quite inaccurate as the rotational speed and the load are increased. The three thermal models show a good agreement and therefore the 2D-Coupled and 2D-Decoupled model can be used as a time-efficient alternative of the more accurate 3D model. Between the 2D-Coupled and the 2D-Decoupled model the difference in the pressure distribution, in the thrust bearing force and in the temperature distribution are rather small and therefore, the 2D-Decoupled model will be used in the transient rotor/bearing simulation due to the advantages discussed in section 2.2.5.

Chapter 3

Multibody Dynamics of Turbocharger Rotor/Bearing Systems

In this section, the principles for multibody simulations of turbocharger rotor/bearing systems are presented. The shaft is considered as a flexible body and the wheels (compressor and turbine) as well as the bearings (radial and thrust) as rigid bodies. The coupling between the flexible and the rigid bodies is discussed in detail. The Finite Element discretization of the flexible shaft leads to large system matrices, imposing a heavy computational cost for transient simulations. A Model Order Reduction (MOR) technique is used leading to a Reduced Order Model (ROM), which is suitable for efficient simulations. The linear vibration modes of a turbocharger rotor are influenced by the thrust and radial bearings. The self-excited oscillations that usually occur in these rotors are related to their linear vibration modes. Therefore, investigations regarding the influence of the bearing stiffness on the vibration modes of a turbocharger rotor are shown.

3.1 Coupling the Rigid and the Elastic Multibody Dynamics

The shaft of the turbocharger rotor is considered as a flexible body and it is discretized using a Finite Element approach (FEA). The large systems matrices resulting from the Finite Element discretization that prevent transient simulations are reduced using a Model Order Reduction (MOR) technique [29, 70, 71]. The shaft is subsequently included in the multibody simulation (MBS) software MSC ADAMS together with the two wheels (the compressor and the turbine) as well as the bearings (radial and thrust).

3.1.1 Craig-Bampton approach

The Component Mode Synthesis (CMS) is a general MOR scheme used in structural mechanics. The three main categories are the fixed-interface, free-interface and

residual-flexible free interface [69]. The Craig-Bampton approach, which will be used in this work, is a fixed interface method and it is based on the idea of the separation between master (or boundary/interface/attachment) and slave (or interior) Degrees of Freedom (DoFs). The user may select the master DoFs, the information of which remains unaltered after the Craig-Bampton approach, since the master DoFs are not subjected to modal superposition. The slave DoFs $\mathbf{x}_s$ are conveyed through a superposition of static modes (constraint modes) as well as dynamic modes (fixed-boundary normal modes or Craig-Bampton modes).

The idea of master and slave nodes applied to an undamped second-order ordinary differential equation is presented in Eq. (3.1.1).

$$\begin{pmatrix} \mathbf{M}_{mm} & \mathbf{M}_{ms} \\ \\ \mathbf{M}_{sm} & \mathbf{M}_{ss} \end{pmatrix} \begin{pmatrix} \ddot{\mathbf{x}}_m \\ \\ \ddot{\mathbf{x}}_s \end{pmatrix} + \begin{pmatrix} \mathbf{K}_{mm} & \mathbf{K}_{ms} \\ \\ \mathbf{K}_{sm} & \mathbf{K}_{ss} \end{pmatrix} \begin{pmatrix} \mathbf{x}_m \\ \\ \mathbf{x}_s \end{pmatrix} = \begin{pmatrix} \mathbf{F}_m \\ \\ \mathbf{F}_s \end{pmatrix}, \quad (3.1.1)$$

where the indexes m and s denote the master and slaved nodes, respectively. The modal coordinates of the constraint ($\mathbf{q}_m$) and the modal coordinates of the Craig-Bampton modes ($\mathbf{q}_s$) are related to the physical coordinates of the master $\mathbf{x}_m$ and the slave $\mathbf{x}_s$ DoFs by

$$\mathbf{x} = \begin{pmatrix} \mathbf{x}_m \\ \\ \mathbf{x}_s \end{pmatrix} = \underbrace{\begin{pmatrix} \mathbf{I}^{m\times m} & \mathbf{0}^{m\times l} \\ \\ \mathbf{\Phi}_s^{s\times m} & \mathbf{\Phi}_{\mathrm{CB}}^{s\times l} \end{pmatrix}}_{\mathbf{T}_{\mathrm{CMS}}} \begin{pmatrix} \mathbf{q}_m \\ \\ \mathbf{q}_s \end{pmatrix}. \quad (3.1.2)$$

The transformation matrix for the Component Mode Synthesis is denoted by $\mathbf{T}_{\mathrm{CMS}}$ and $\mathbf{I}$ is the unit matrix. It can be seen that the modal coordinates of the constraint modes have a one-to-one relationship with the physical displacements of the master DoFs ($\mathbf{x}_m$). The matrix $\mathbf{\Phi}_s$ is given by

$$\mathbf{\Phi}_s = -\mathbf{K}_{ss}^{-1}\mathbf{K}_{sm}. \quad (3.1.3)$$

This matrix is a result of a static (Guyan) reduction. The matrix $\mathbf{\Phi}_{CB}$ consists of l eigenvectors of the internal structure while the master DoFs are fixed. Therefore, considering $\ddot{\mathbf{x}}_m = \mathbf{x}_m = \mathbf{0}$ and $\mathbf{F}_s = \mathbf{0}$, from Eq. 3.1.1 we have

$$\mathbf{M}_{ss}\ddot{\mathbf{x}}_s + \mathbf{K}_{ss}\mathbf{x}_s = \mathbf{0}. \quad (3.1.4)$$

The slave structure has a modal matrix $\mathbf{\Phi}_{ss}$

$$\left(\mathbf{K}_{ss} - \mathbf{M}_{ss}\omega_{ss}^2\right)\mathbf{\Phi}_{ss} = \mathbf{0}. \quad (3.1.5)$$

Calculating the first l eigenvectors, we obtain $\mathbf{\Phi_{CB}}$ and the $\mathbf{\Phi}_{ss}$ can be found by

$$\mathbf{\Phi}_{ss} = \left[\mathbf{\Phi}_{CB}^{s\times l} \;\middle|\; \mathbf{\Phi}_2^{s\times(s-l)}\right], \quad (3.1.6)$$

where $l \ll s = n - m$ and n is the total number of DoFs.

The generalized mass and stiffness matrices using the Craig-Bampton modal basis are

$$\hat{\mathbf{M}} = \mathbf{T}_{\mathrm{CMS}}^{T} \cdot \begin{pmatrix} \mathbf{M}_{mm} & \mathbf{M}_{ms} \\ \\ \mathbf{M}_{sm} & \mathbf{M}_{ss} \end{pmatrix} \cdot \mathbf{T}_{\mathrm{CMS}}, \quad \hat{\mathbf{K}} = \mathbf{T}_{\mathrm{CMS}}^{T} \cdot \begin{pmatrix} \mathbf{K}_{mm} & \mathbf{K}_{ms} \\ \\ \mathbf{K}_{sm} & \mathbf{K}_{ss} \end{pmatrix} \cdot \mathbf{T}_{\mathrm{CMS}}. \tag{3.1.7}$$

The dimensions of the mass and stiffness matrices in the ROM depend on the number m of the master nodes and the number l of the previously mentioned eigenvectors.

$$\mathbf{M}_{\mathrm{CMS}} = \begin{pmatrix} \mathbf{M}^{m\times m} & \mathbf{M}^{m\times l} \\ \\ \mathbf{M}^{l\times m} & \mathbf{I}_{CB}^{l\times l} \end{pmatrix} \quad \text{and} \quad \mathbf{K}_{\mathrm{CMS}} = \begin{pmatrix} \mathbf{K}^{m\times m} & \mathbf{K}^{m\times l} \\ \\ \mathbf{K}^{l\times m} & \mathbf{\Lambda}_{CB}^{l\times l} \end{pmatrix}. \tag{3.1.8}$$

The block matrix $\mathbf{I}_{CB}$ is the unit matrix. $\mathbf{\Lambda}_{CB}$ denotes the eigenvalue matrix and it is defined by

$$\mathbf{\Lambda}_{l\times l} = \mathrm{diag}\left[\omega_i^2\right], \quad i = 1, \ldots, l. \tag{3.1.9}$$

Considering proportional (Rayleigh) damping, the reduced damping matrix can be calculated

$$\mathbf{D}_{\mathrm{CMS}} = \begin{pmatrix} \mathbf{D}^{m\times m} & \mathbf{D}^{m\times l} \\ \\ \mathbf{D}^{l\times m} & \left(d_\alpha \mathbf{I} + d_\beta \mathbf{\Lambda}\right)_{CB}^{l\times l} \end{pmatrix}, \tag{3.1.10}$$

where d_α and d_β are the mass and stiffness proportional damping coefficients.

In Figure 3.1 the modeling of a flexible shaft is illustrated. In this case, six master nodes are selected at the position of

- turbine wheel center of mass
- compressor wheel center of mass
- turbine-side radial bearing
- compressor-side radial bearing
- turbine-side thrust bearing
- compressor-side thrust bearing

If the thrust bearings are not considered in the simulations, the master nodes related with them may be ignored, leading to smaller system matrices.

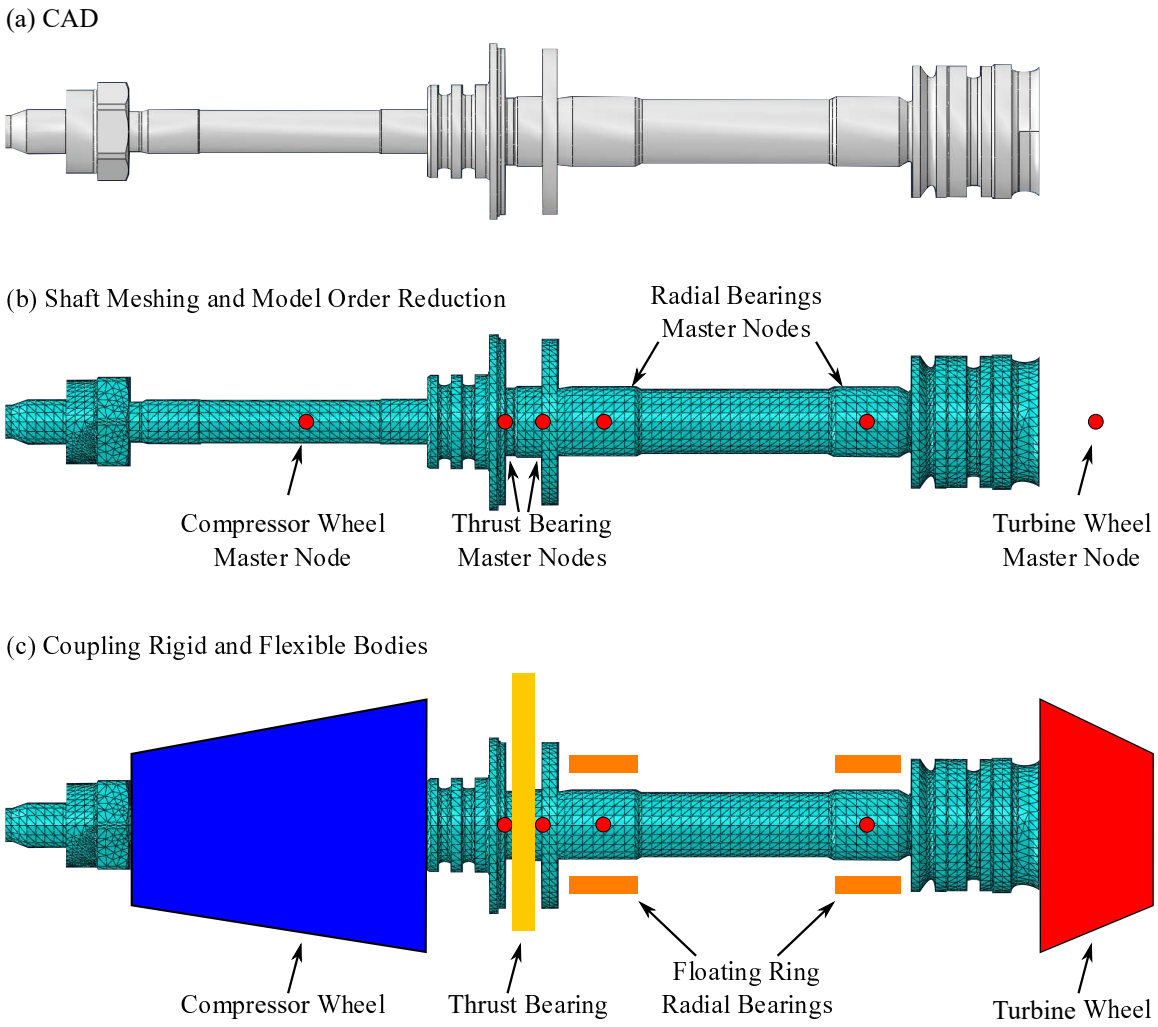

Figure 3.1: Turbocharger rotor modeling: (a) CAD, (b) shaft meshing and Model Order Reduction and (c) coupling rigid and flexible bodies

3.2 Turbocharger Rotor/Bearing Modeling

In Figure 3.2 the modeling approach for a turbocharger rotor/bearing system is depicted. The turbocharger rotor/bearing model is considered as a flexible multibody system [106, 107]. The equations of motion read in the stabilized index-2 formulation [50]

$$\begin{aligned}
\dot{\mathbf{q}} &= \mathbf{K}(\mathbf{q})\mathbf{p} - \mathbf{G}^{\mathrm{T}}(t,\mathbf{q})\boldsymbol{\mu}, \\
\mathbf{M}(t,\mathbf{q})\dot{\mathbf{p}} &= \mathbf{f}_{\mathrm{e}}(t,\mathbf{q},\mathbf{p}) - \mathbf{G}^{\mathrm{T}}(t,\mathbf{q})\boldsymbol{\lambda}, \\
\mathbf{0} &= \mathbf{g}(t,\mathbf{q}), \\
\mathbf{0} &= \dot{\mathbf{g}}(t,\mathbf{q},\mathbf{p}).
\end{aligned} \tag{3.2.1}$$

The system is described by υ generalized coordinates, which are collected in the position vector $\mathbf{q} = (q_1, ..., q_\upsilon)^{\mathrm{T}} \in \mathbb{R}^\upsilon$. The vector $\mathbf{p} = (p_1, ..., p_\upsilon)^{\mathrm{T}} \in \mathbb{R}^\upsilon$ contains the generalized velocities, which are related to the generalized coordinates $\mathbf{q}$ by the kinematical differential equations $\dot{\mathbf{q}} = \mathbf{K}(\mathbf{q})\mathbf{p}$, with $\mathbf{K}(\mathbf{q}) \in \mathbb{R}^{\upsilon\times\upsilon}$. The mass matrix

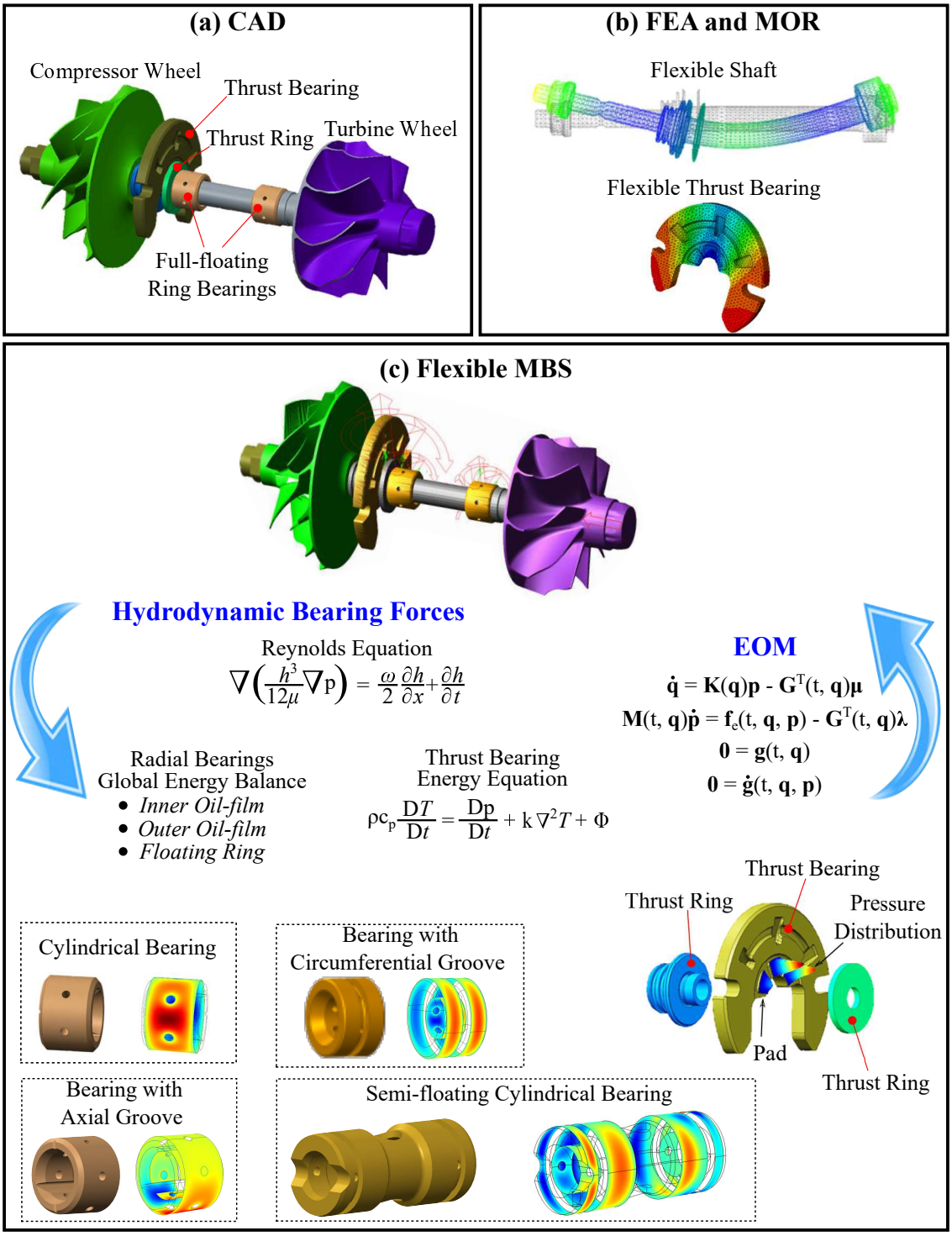

Figure 3.2: Turbocharger rotor/bearing modeling

$\mathbf{M}(t, \mathbf{q}) \in \mathbb{R}^{\upsilon \times \upsilon}$ is assumed to be symmetric and positive definite. The externally applied forces and torques are arranged in the vector $\mathbf{f}_e(t, \mathbf{q}, \mathbf{p})$, which also includes the hydrodynamic bearing forces and torques. The system is constrained by n_c rheonomic algebraic constraint equations $g_i(t, \mathbf{q}) = 0$ $(i = 1, ..., \upsilon_c)$, which are arranged in the constraint vector $\mathbf{g} \in \mathbb{R}^{\upsilon_c}$. The corresponding constraint forces and torques are defined by $\mathbf{G}^T(t, \mathbf{q})\boldsymbol{\lambda}$ with the matrix $\mathbf{G} = \frac{\partial \mathbf{g}}{\partial \mathbf{q}} \in \mathbb{R}^{\upsilon_c \times \upsilon}$ and the vector $\boldsymbol{\lambda} \in \mathbb{R}^{\upsilon_c}$ collecting the

Lagrange multipliers. The additional Lagrange multipliers $\boldsymbol{\mu} \in \mathbb{R}^{\upsilon_c}$ are introduced in order to enforce the hidden constraints $\dot{\mathbf{g}}(t, \mathbf{q}, \mathbf{p}) = \mathbf{0}$.

The equations of motion (EOM) for the multibody system are solved at every time-integration step simultaneously with the equations related with the thermohydrodynamic modeling. The Reynolds equation holds for both the thrust and the radial bearings. A different approach is followed for the thermal modeling of the bearings. For the thrust bearings, the energy equation of the oil is solved simultaneously with the Reynolds equation, following the modeling assumptions presented in the previous chapter. For the radial bearings, a reduced (global) thermal modeling is chosen. It is noted that both the thrust and the radial bearings are assumed as rigid bodies in the following work.

3.3 Vibrational Modes of a Turbocharger Rotor

The vibration modes of a rotor are significantly influenced by the stiffness of the bearings. Figure 3.3 shows the influence of the radial bearing stiffness on the linear modes of a turbocharger rotor.

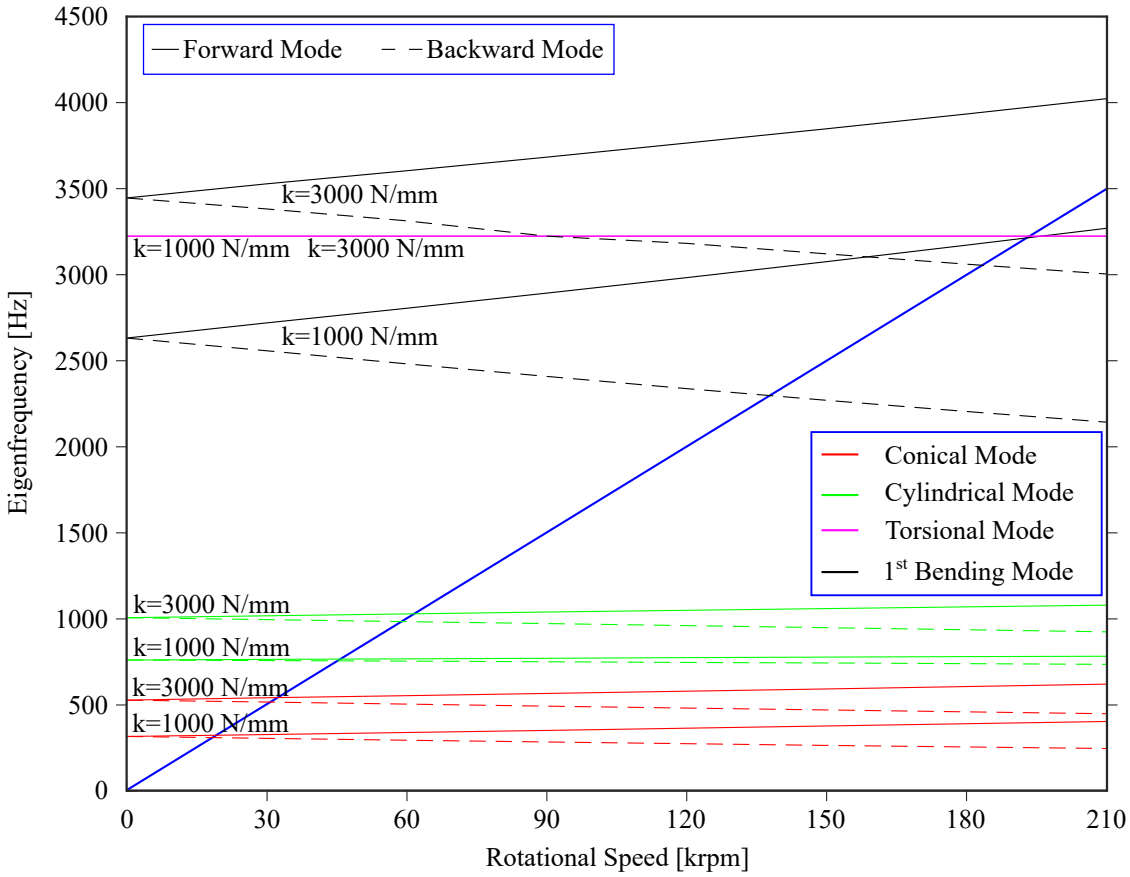

Figure 3.3: Linear vibration modes of a turbocharger rotor for different radial bearing stiffnesses; k =1000 N/mm and k =3000 N/mm

Two radial bearings with different stiffnesses were used, namely k=1000 N/mm and k=3000 N/mm. It can be observed that the eigenfrequencies of the conical mode, the cylindrical mode as well as the 1^{st} bending mode are shifted to higher frequencies as the stiffness of the radial bearings is increased. The torsional mode is unaffected. In this example, the thrust bearing was neglected.

Including the thrust bearing, one axial stiffness k_z and two rotational stiffnesses k_x and k_y are applied to the rotor. The axial stiffness k_z influences mainly the axial mode of the rotor. If the thrust bearing is neglected, the eigenfrequency of the axial mode is zero. The stiffness of the radial bearings is k=1000 N/mm. Figure 3.4 shows the influence of the thrust bearing stiffness on the linear modes of a turbocharger rotor.

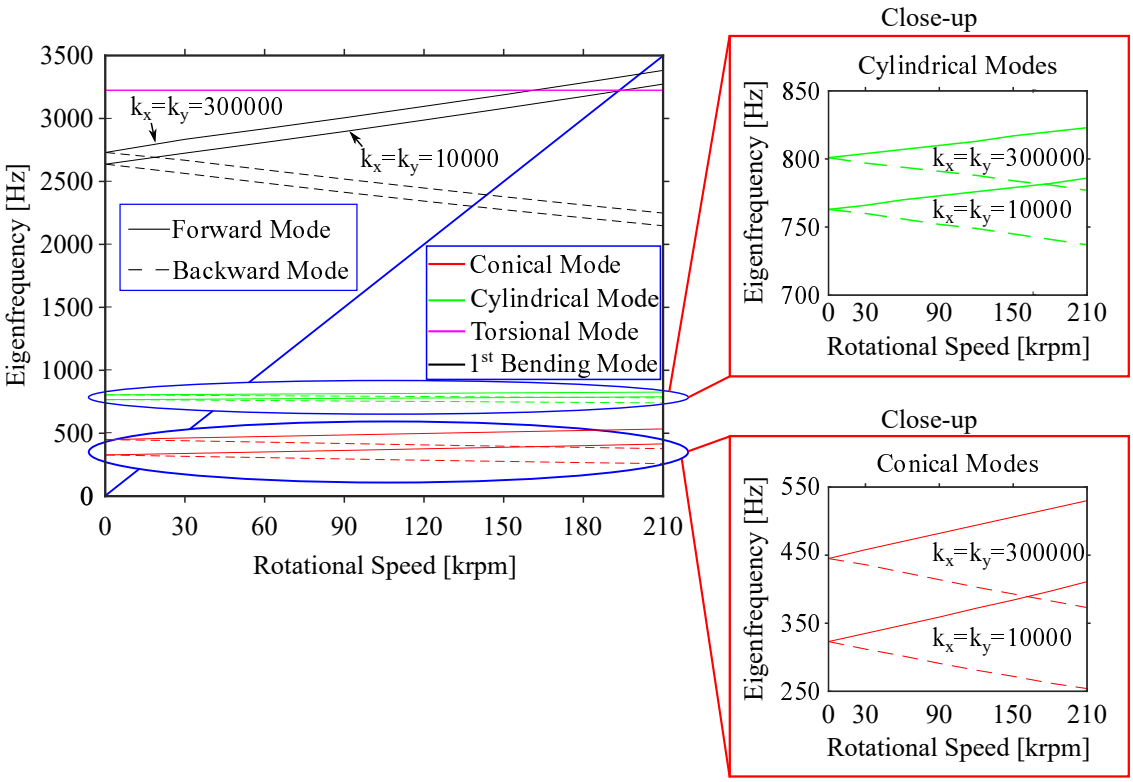

Figure 3.4: Linear vibration modes of a turbocharger rotor for different thrust bearing stiffnesses; $k_x = k_y$ =10000 Nmm/degree and $k_x = k_y$ =300000 Nmm/degree

The axial stiffness k_z has a marginal influence on the rotor modes. The rotational stiffness k_x/k_y exerts, on the contrary to the axial stiffness, a relatively large influence, mainly on the conical mode. However, both the cylindrical as well as the 1^{st} bending mode are also affected.

The rotor of a turbocharger may exhibit self-excited subsynchronous vibrations. The modes of a turbocharger rotor/bearing system are related to these subsynchronous vibrations - namely the gyroscopic conical forward mode which correlates with the first (*sub 1*) and the third (*sub 3*) subsynchronous vibration as well as the gyroscopic cylindrical forward mode which correlates with the second subsynchronous vibration

(*sub 2*) - can be seen in Fig. 3.5 [103,104]. Note that the gyroscopic cylindrical forward mode is not a purely rigid body mode, but exhibits also a slight bending.

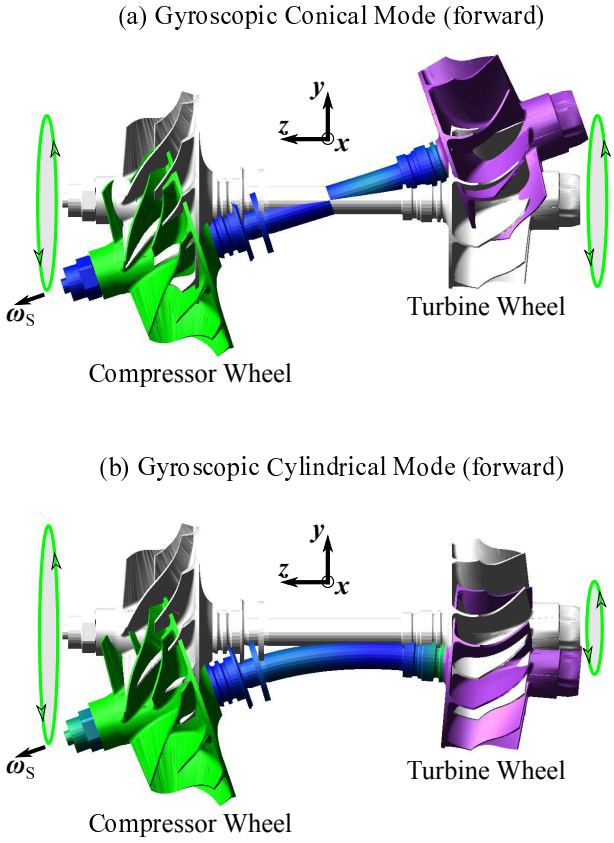

Figure 3.5: Linear vibration modes of a turbocharger rotor

Chapter 4

Radial and Thrust Bearings in Turbocharger Systems

In this chapter, transient simulations of turbocharger rotor/bearing systems using various radial and thrust bearing models are presented. The main focus is the influence of the thrust bearings on the subsynchronous rotor vibrations. Isothermal and thermohydrodynamic thrust bearing models will be tested and the influence of the number of pads, the external axial forces as well as the influence of the oil-viscosity will be discussed in detail. The radial bearing models developed in chapter 2 will be used during the simulations for the thrust bearing models. The importance of the time-dependent temperature term in the energy balance equations for the radial bearings and in the energy equation for the thrust bearing will also be investigated.

4.1 Influence of Radial Bearings on Rotor Vibrations

In this section, the thrust bearing will be neglected as no external axial forces will be exerted on the rotor.

Comparisons between different oil-supply pressures for bearings with circumferential oil-groove are performed. The importance of the time-dependent temperature term in the energy balance equations for the radial bearings is highlighted.

4.1.1 Influence of the oil-supply pressure in bearings with circumferential oil-groove

The pressure at the circumferential oil-groove is assumed to be equal to the oil-supply pressure. Here, four different oil-supply pressures are used, namely p_S=1 bar, p_S=2 bar, p_S=3 bar as well as p_S=4 bar and their influence on the subsynchronous rotor vibration is illustrated in Fig. 4.1. The oil-supply pressure increase, in this case, had a positive influence on the subsynchronous vibrations, reducing their amplitude.

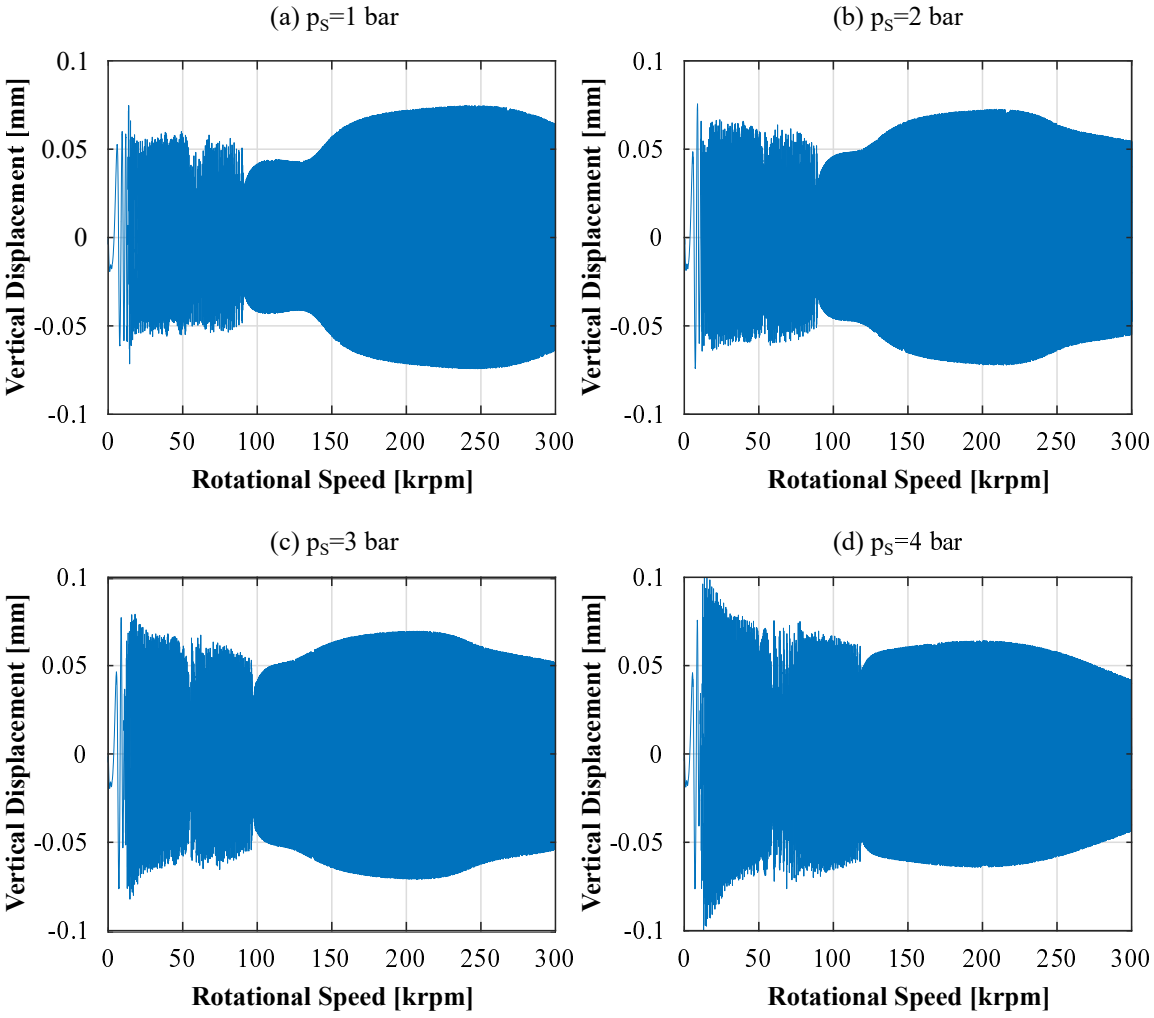

Figure 4.1: Influence of the oil-supply pressure on the compressor wheel vibration in the vertical direction: (a) p_S=1 bar, (b) p_S=2 bar, (c) p_S=3 bar, (d) p_S=4 bar

4.1.2 Thermohydrodynamic bearing model for radial bearings

In this section, a comparison between two thermohydrodynamic models is presented. The first model will neglect the time dependent temperature term $\dot{T}$ from the thermal energy balance equations (Eq. (2.1.22)), while in the second model $\dot{T}$ will be included. Figure 4.2 shows the influence of the time dependent temperature term in the energy balance equations on the compressor wheel vibration in the vertical direction.

The simulation where $\dot{T}$ was neglected became very slow and it broke down after some time. The reason is that the abrupt changes in the bearing clearance impose difficulties on the Newton iteration scheme during the solution of the equations of motion. Until the simulation broke down, the compressor wheel vibrations seem to be very similar in both cases. Therefore, although physically the $\dot{T}$ may not be of high importance, in transient simulations it should always be taken into account.

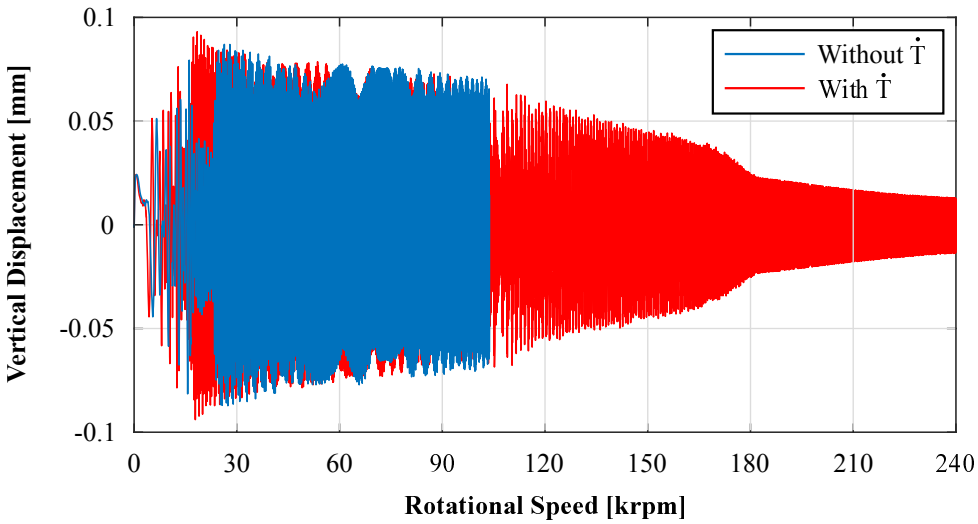

Figure 4.2: Influence of the time dependent temperature term in the energy balance equations on the compressor wheel vibration in the vertical direction

4.2 Influence of Thrust Bearings on Rotor Vibrations

4.2.1 Thrust-load and thrust-free rotor vibrations

Transient simulations are performed neglecting the thrust bearing (thrust-free operation, $F_{axial} = 0$) as well as including the thrust bearing (thrust-load operation, $F_{\text{axial}} \neq 0$). A thrust bearing with 8 equally distributed pads is used ($\Theta_1 = 0\,°$, $\Theta_2 = 45\,°$, $\Theta_3 = 90\,°$, $\Theta_4 = 135\,°$, $\Theta_5 = 180\,°$, $\Theta_6 = 225\,°$, $\Theta_7 = 270\,°$, $\Theta_8 = 315\,°$). The other geometric characteristics of the bearings as well as the relevant simulations parameters are summarized in Table 4.1.

Figure 4.3 shows the prescribed external axial force F_{axial} and the rotational frequency of the turbocharger rotor for the transient simulations. The rotational speed of the turbocharger rotor N is linearly increased from 0 to 210000 rpm. The magnitude of the external axial force is increased during the first second of the simulation until it reaches its maximum value (100 N, except for section 4.2.3) and from $N > 21000$ rpm maintains this magnitude until the end of the run-up. The turbocharger is assumed to be perfectly balanced. In this way, the influence of unbalance is not mixed up with the influence of the thrust bearing on the subsynchronous oscillations.

In Figure 4.4, displacements of the center of mass of the turbine wheel in the vertical direction (y-direction) are shown. The influence of the thrust bearing on the onset point as well as on the amplitude of the subsynchronous (self-excited) oscillations is evident in this example.

The first subsynchronous (*sub 1*) in the thrust-free operation becomes apparent at

Table 4.1: Thrust bearing pad and oil-film characteristics

Parameter	Description	Value	Unit
r_1	Inner radius	3.55	mm
r_2	Outer radius	6.3	mm
θ_0	Angular extent of pad	0.775	rad
L_{wed}/L	Inclined/total length	0.7	-
C_{wed}	Taper height	0.01	mm
λ	Viscosity-temperature coefficient	0.0225	1/°C
F_{axial}	External axial force	100 (see Fig. 4.3)	N
N_{pads}	Number of pads	8	-
m_{rotor}	Rotor mass	≈ 0.1	kg
l_{rotor}	Rotor length	≈ 0.1	m

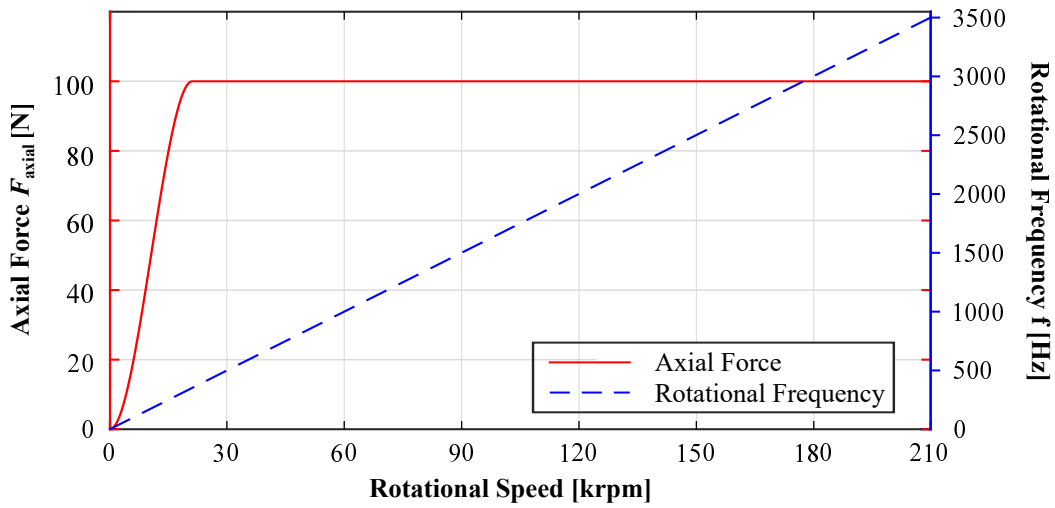

Figure 4.3: External axial force and rotational frequency of the turbocharger rotor

$N \approx 4200\,\text{rpm}$. In the thrust-load operation, *sub 1* is reached at $N \approx 25000\,\text{rpm}$. A similar difference in the onset point of the subsynchronous oscillations is observed for the third subsynchronous *sub 3*. As the thrust bearing is deactivated, *sub 3* appears at $N \approx 92000\,\text{rpm}$. When it is activated, *sub 3* appears at $N \approx 128000\,\text{rpm}$. It should be noted, that *sub 3* is also present at $42000\,\text{rpm} \leq N \leq 63000\,\text{rpm}$ with deactivated thrust bearing, coexisting with the second subsynchronous *sub 2*. On the contrary, *sub 3* exists only for higher rotational speeds when the thrust bearing is activated. Figure 4.4 shows a significant reduction in the amplitudes of the subsynchronous oscillations, especially in the area where *sub 3* dominates.

Figures 4.5 shows the Short Time Fourier Transform (STFT) of the turbine displacements for both cases (deactivated and activated thrust bearing, respectively). As it

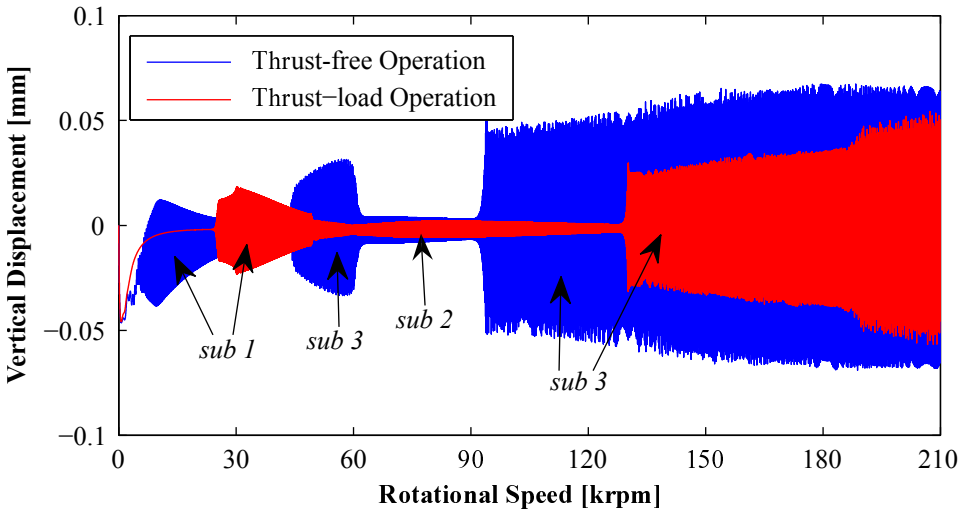

Figure 4.4: Turbine wheel displacements in vertical direction with activated and deactivated thrust bearing

can be observed, the second subsynchronous *sub 2* exhibits low amplitudes for both cases.

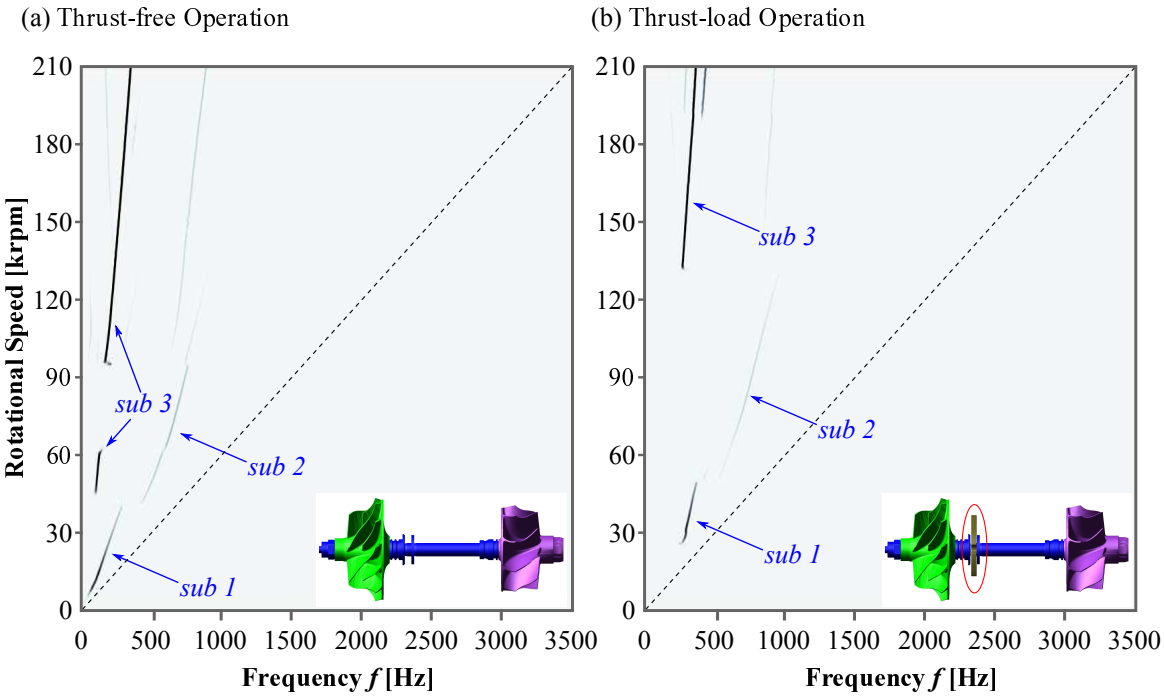

Figure 4.5: Short Time Fourier Transform of the turbine wheel displacements in the vertical direction: (a) thrust-free operation, (b) thrust-load operation

When the thrust bearing is neglected, *sub 2* becomes apparent between 40000 rpm $\leq N \leq$ 92000 rpm, while considering the thrust bearing, *sub 2* appears at 50000 rpm $\leq N \leq$ 126000 rpm. It is evident that the thrust bearing has a quite minor influence on *sub 2*, especially in comparison with *sub 1* and *sub 3*. It should be stressed that the activated thrust bearing does not entail additional subsynchronous oscillations;

only the onset point and the magnitude of the three subsynchronous oscillations are influenced.

The difference in the subsynchronous oscillations in the thrust-free and the thrust-load operations can be explained as follows: The thrust bearing imposes to the rotor/bearing system an additional axial stiffness and damping and also an additional angular stiffness and damping. As explained in [102], the rotor exhibits subsynchronous oscillations related to its conical and to its cylindrical mode. The additional angular stiffness makes the system stiffer and the conical mode is shifted to higher frequencies. On the contrary, additional angular stiffness has only a minor influence on the cylindrical mode. Therefore, the *sub 1* and the *sub 3* oscillations, which are related to the forward gyroscopic conical mode, are mostly influenced. As the stiffness is increasing, the onset point of instability appears at higher rotational speeds.

The influence of the thrust bearing on the first and the second Bryant angle of the thrust ring is presented in Figure 4.6. As it can be seen, removing the thrust bearing,

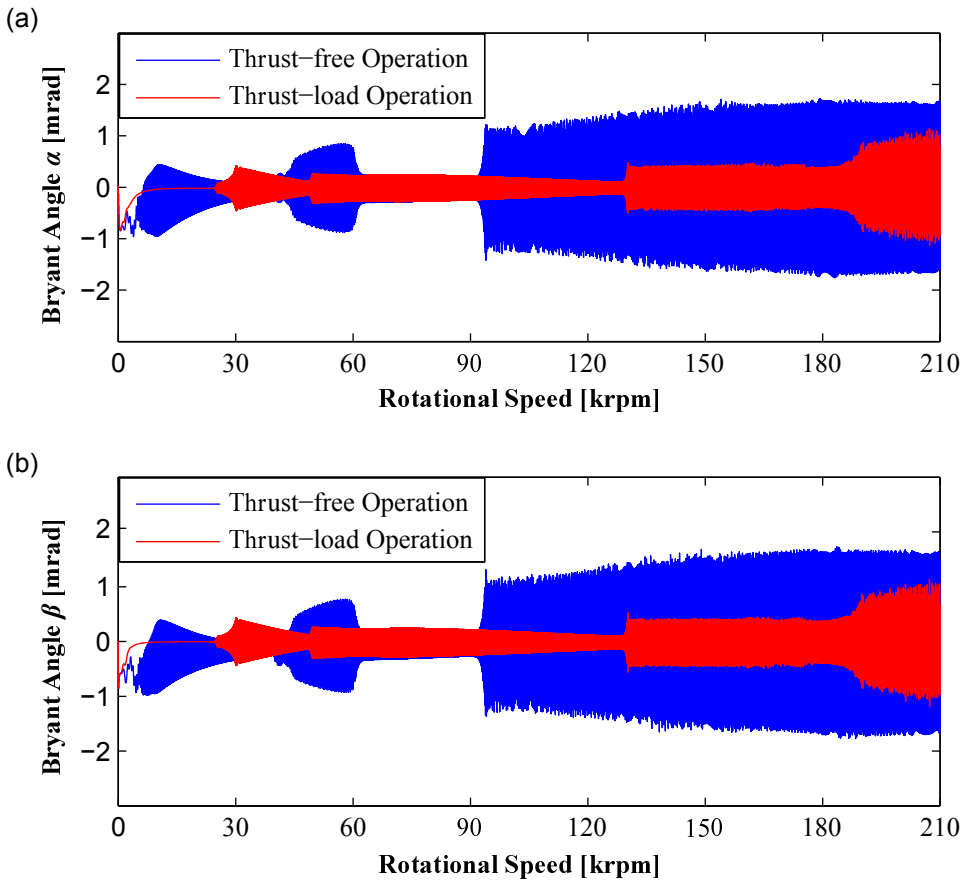

Figure 4.6: Misalignment angles with activated and deactivated thrust bearing: (a) first Bryant angle α, (b) second Bryant angle β

the misalignment angles are much larger as compared with the case that the thrust bearing is considered. Since their magnitude is less than 2 mrad, the linearization of the oil-film thickness function is well justified.

The relative radial bearing eccentricities for the inner and outer bearings are $\varepsilon_{i/o} = e_{i/o}/C_{i/o}$, where $e_{i/o}$ are the radial bearing eccentricities and $C_{i/o}$ are the radial clearances. Figure 4.7 shows the influence of the thrust bearing on the relative bearing eccentricities of the compressor- and turbine-sided full-floating ring bearings.

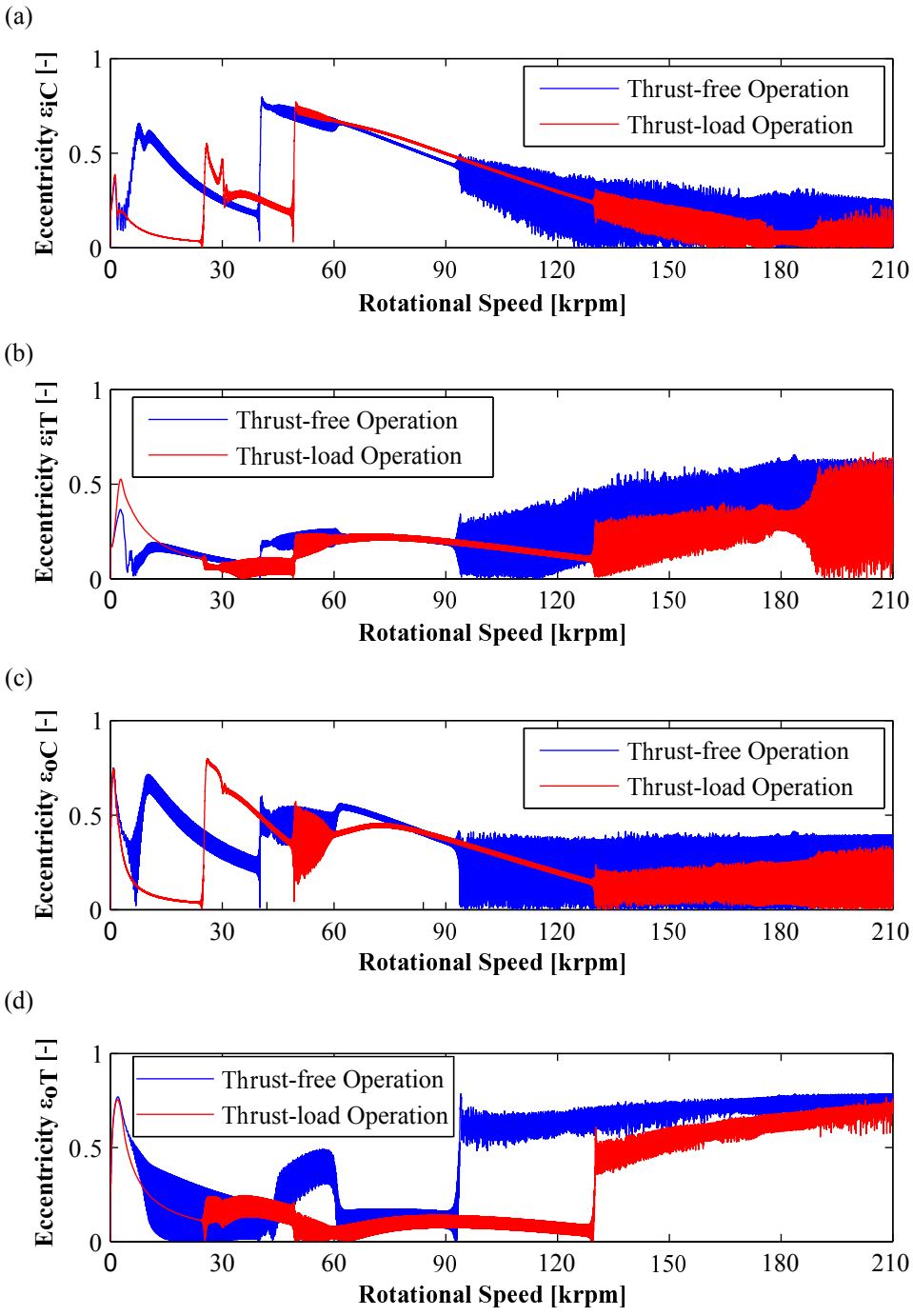

Figure 4.7: Relative bearing eccentricities of: (a) inner oil-film at compressor-side bearing, (b) inner oil-film at turbine-side bearing (c) outer oil-film at compressor-side bearing, (d) outer oil-film at turbine-side bearing

4.2.2 Influence of the number of bearing pads

The number of thrust bearing pads as well as their constellation varies according to the technical application of the rotor. The pads may be symmetrically distributed around the circumference of the bearing or they can appear only in certain areas, i.e. only at the upper part of the bearing. In this section, the influence of the number of pads on the nonlinear oscillations as well as on the axial distance between the bearing and thrust ring is investigated. Thrust bearings with 3 to 8 pads, distributed equidistantly over the circumference, are employed in the transient simulations. It should be mentioned that the angular extent of the pads is always assumed to be $\theta_0 = 0.775\,\text{rad}$. It is noted here that unbalance masses are added at the compressor wheel $u_\text{C} = 0.15\,\text{gmm}$ and the turbine wheel $u_\text{T} = 0.2\,\text{gmm}$ at the same angle. The same unbalance will be used in all the following simulations.

The influence of the number of bearing pads on the axial displacements of the rotor is shown in Fig. 4.8.

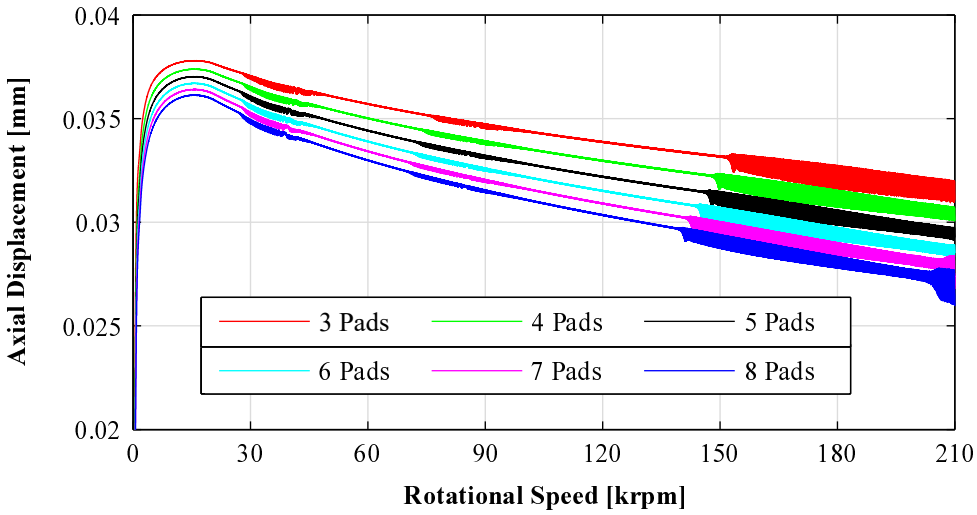

Figure 4.8: Axial displacements of the rotor for different numbers of bearing pads

The axial displacement decreases with the number of pads. This can be explained as follows: As the number of pads becomes larger, the load that each pad must support is lower, since the total external axial load in all cases remains constant ($F_\text{axial} = 100\,\text{N}$). The maximum axial displacement allowed is 0.04 mm, since this is the initial distance between the thrust ring and the thrust bearing. Therefore, the higher the axial displacement of the rotor during the simulation, the lower the distance between the thrust ring and the thrust bearing. Figure 4.9 shows the vertical displacements of the turbine wheel for different number of bearing pads. The increase of the number of pads affects mainly the *sub 3* oscillation, where the onset point of the subsynchronous oscillation is shifted to higher rotational speeds as the number of pads is lower. The *sub 1* remains almost unaffected. The onset point of the *sub 2* is also slightly affected.

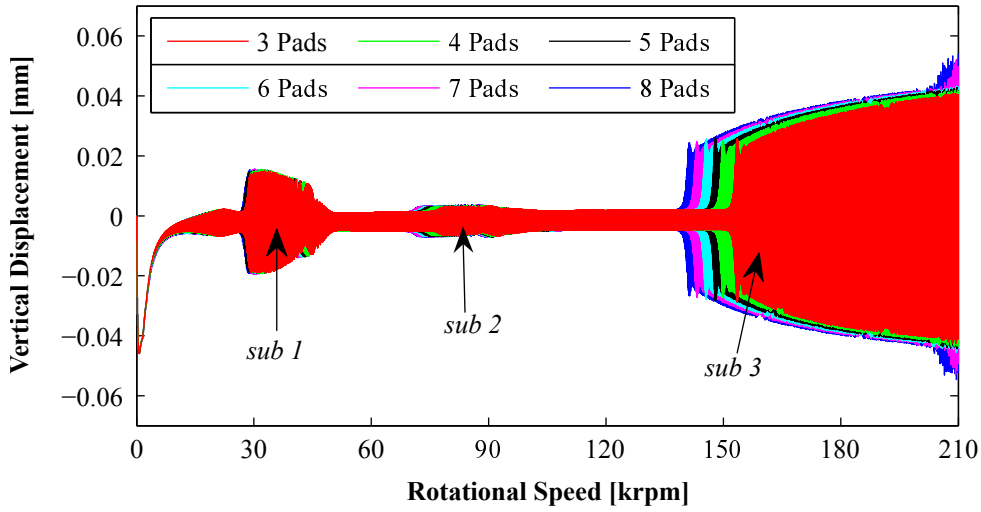

Figure 4.9: Turbine wheel displacements in the vertical direction for different numbers of bearing pads

It is observed that the number of pads has a small influence on the rotor lateral oscillations. All the bearing constellations considered here, show similar frequency content. Figure 4.10 shows the STFT of the turbine wheel displacement in the case of a 6-pad thrust bearing. Low amplitude synchronous oscillation can be observed in Fig. 4.10 due to the added unbalance masses.

4.2.3 Influence of the magnitude of the external axial force

The axial forces acting on the turbine and on the compressor wheel vary in real applications. However, the magnitude of the resultant axial force affects the nonlinear oscillations. Figure 4.11 presents the influence of the magnitude of the external axial force on the axial displacements of the rotor. Forces with magnitudes from 60 N to 140 N are imposed in the transient simulations. As the axial force F_{axial} increases, the distance between the thrust ring and the bearing becomes lower. The onset point of the subsynchronous oscillations is also affected as shown in Fig. 4.12. *Sub 1* is almost unaffected by the increase of the axial force. The largest influence can be seen on *sub 3*. As the axial force increases, the onset point of *sub 3* is shifted to higher rotational speeds. This effect can be explained considering the axial distance between the thrust ring and the bearing pads from Fig. 4.11. As the axial force increases, the axial distance between the bearing and the thrust ring is decreasing. Thereby, the angular stiffness and damping produced by the thrust bearing is changed and the instability point is shifted to higher rotational speeds.

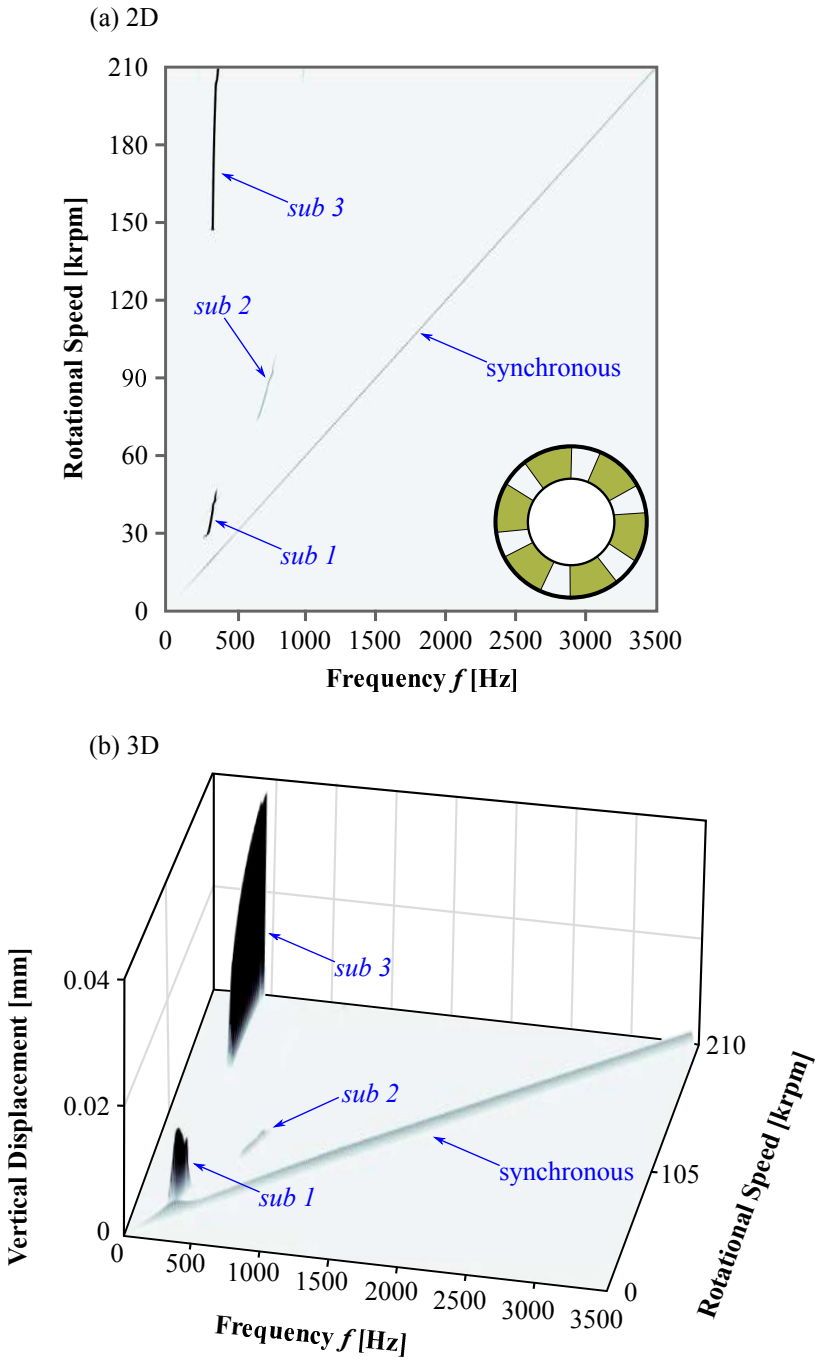

Figure 4.10: Short Time Fourier Transform (2D and 3D) of the turbine wheel displacement in the vertical direction (thrust bearing with 6 Pads)

4.2.4 Influence of the oil-viscosity

In this section, numerical simulations are performed initially using the isothermal thrust bearing model with various constant oil-supply temperatures. The oil-supply temperature is selected to be $T = 30\,°\mathrm{C}$, $T = 60\,°\mathrm{C}$, $T = 90\,°\mathrm{C}$ and $T = 150\,°\mathrm{C}$. During the operation of the turbocharger, the oil-supply temperature for the radial and the thrust bearing can be assumed to be the same. However, for pronouncing

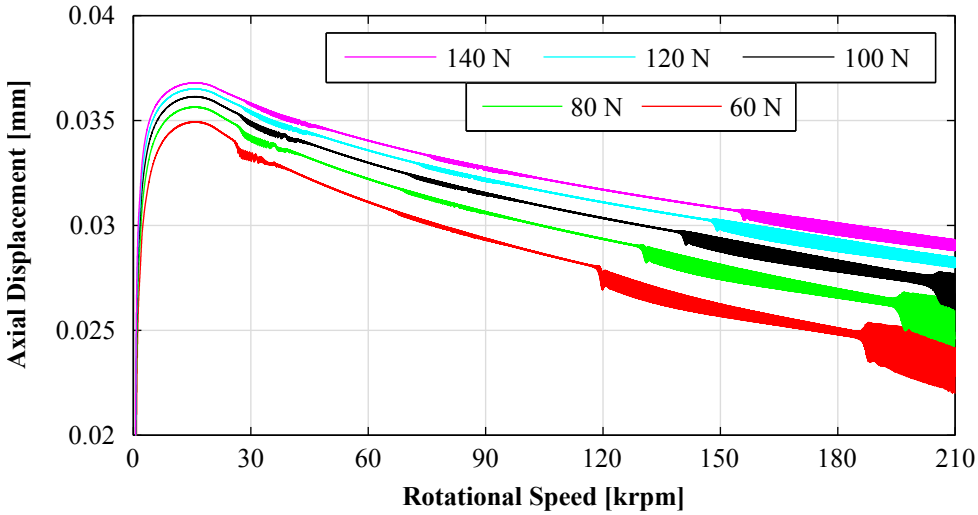

Figure 4.11: Axial displacements of the rotor for external axial forces of different magnitude

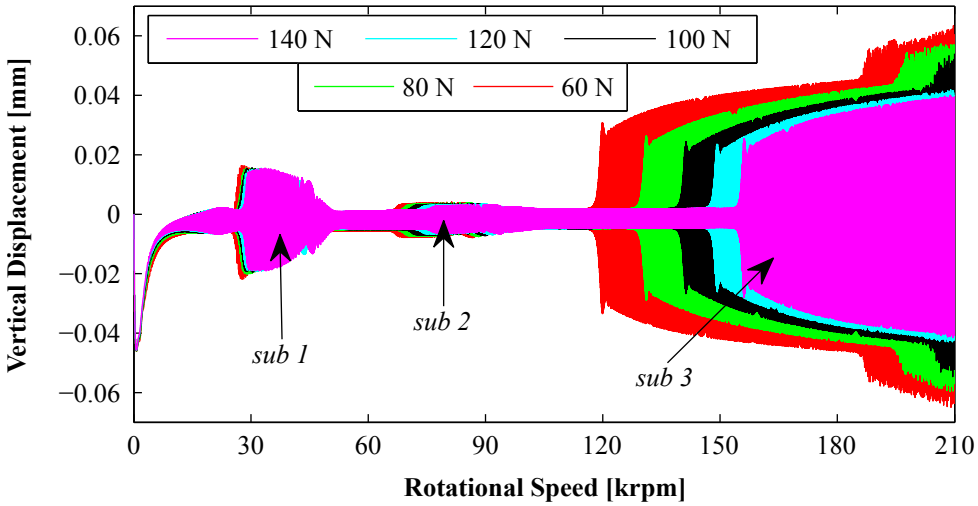

Figure 4.12: Turbine wheel displacements in the vertical direction for external axial forces of different magnitude

the influence of the oil-temperature in the thrust bearing, the oil-supply temperature for the radial bearings should remain constant. Therefore, in the following analysis, simulations will be shown using the same oil-supply temperature for the thrust and the radial bearings ($T_\mathrm{T} = T_\mathrm{R}$) as well as using a constant oil-supply temperature for the radial bearings ($T_\mathrm{R} = 90\,^\circ\mathrm{C}$) and various oil-supply temperatures for the thrust bearing ($T_\mathrm{T} \neq T_\mathrm{R}$) as shown in Fig. 4.13. It is then obvious that the case $T_\mathrm{T} = 90\,^\circ\mathrm{C}$ and $T_\mathrm{R} = 90\,^\circ\mathrm{C}$ will appear twice. It is mentioned here that the unbalance mass on the compressor wheel is $u_\mathrm{C} = 0.06\,\mathrm{gmm}$ and on the turbine wheel is $u_\mathrm{T} = 0.06\,\mathrm{gmm}$ at the same angle.

Figure 4.14 shows the displacement of the compressor wheel in the vertical y-direction for both cases ($T_\mathrm{T} = T_\mathrm{R}$ and $T_\mathrm{T} \neq T_\mathrm{R}$) and for all the aforementioned oil-temperatures.

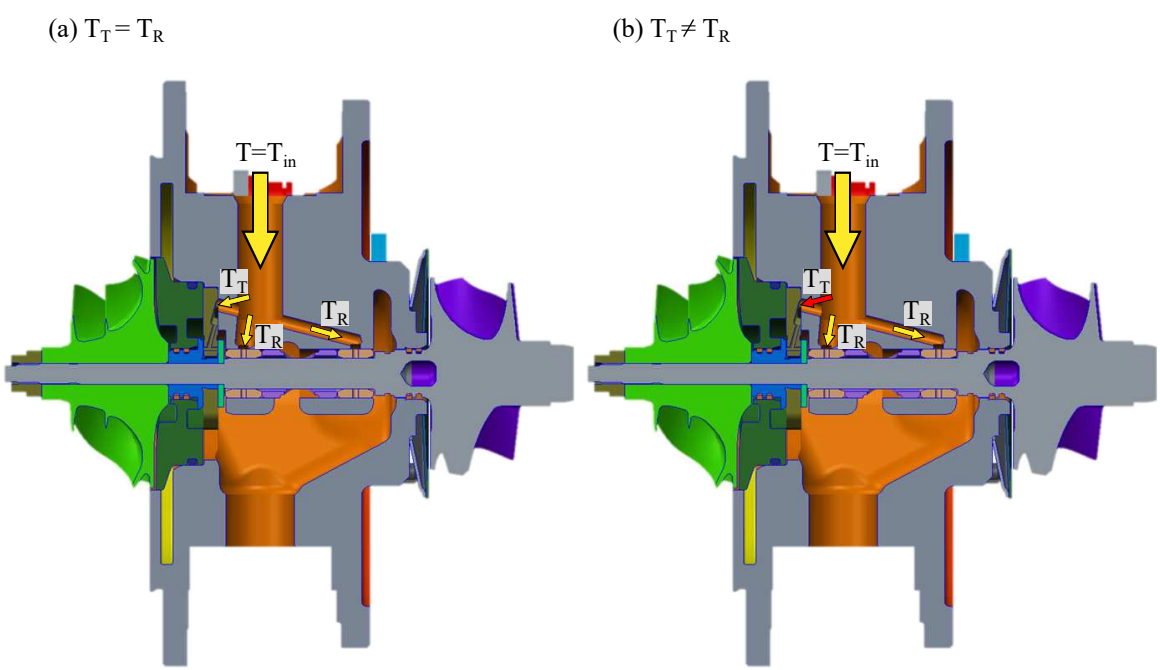

Figure 4.13: Simulation scenarios of the oil-temperature in the thrust and the radial bearings: (a) Common oil-supply temperature for the thrust and radial bearings ($T_\mathrm{T} = T_\mathrm{R}$), (b) constant oil-supply temperature for the radial bearings ($T_\mathrm{T} \neq T_\mathrm{R}$ and $T_\mathrm{R} = 90\,^\circ\mathrm{C}$)

The influence of the oil-temperature in the thrust bearing is pronounced at Fig. 4.14b. Both the first (*sub 1*) and the third (*sub 3*) subsynchronous oscillations appear at higher rotational speeds as the oil-temperature is increased. Considering the Fig. 4.14a, such a conclusion is not always justified since the oil-temperature in the radial bearings also influences the onset point of the self-excited oscillations. However, it can be seen that for higher oil-temperatures, the onset point of the *sub 3* appears in higher rotational speeds. Comparing the amplitudes of the subsynchronous oscillations, we can observe that they decrease as the temperature increases.

Figure 4.15 illustrates the axial displacements of the rotor (z-direction) for both cases ($T_\mathrm{T} = T_\mathrm{R}$ and $T_\mathrm{T} \neq T_\mathrm{R}$) and for all the aforementioned oil-temperatures. Comparing Fig. 4.15a and Fig. 4.15b, it is observed that the axial displacements for both cases are very similar. This outcome is expected since the axial displacements are mainly determined by the thrust bearing and in these cases the thrust bearing and the oil-temperatures therein are identical. It is noted also here that as the oil-temperature increases, the minimum film thickness decreases. This effect can be easily explained as the load capacity of the thrust bearing decreases with the increase of the oil-temperature.

The relative bearing eccentricities ε are shown in Fig. 4.16a using the same oil-supply temperature for the thrust and the radial bearings ($T_\mathrm{T} = T_\mathrm{R}$) and in Fig. 4.16b using a constant oil-supply temperature for the radial bearings ($T_\mathrm{R} = 90\,^\circ\mathrm{C}$). The relative

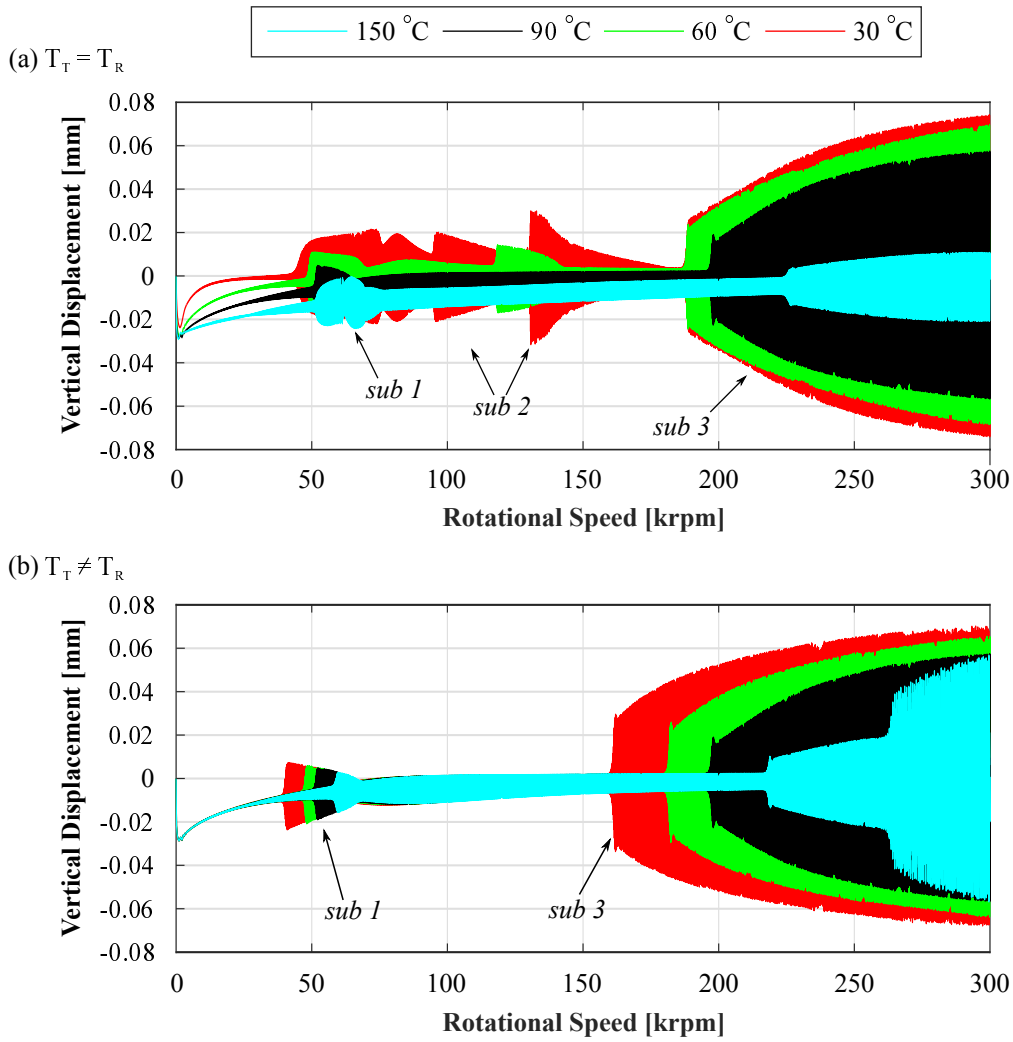

Figure 4.14: Compressor wheel displacements in the vertical direction for different oil-temperatures: (a) common oil-supply temperature ($T_{\mathrm{T}} = T_{\mathrm{R}}$) for the thrust and radial bearings, (b) constant oil-supply temperature for the radial bearing ($T_{\mathrm{T}} \neq T_{\mathrm{R}}$ and $T_{\mathrm{R}} = 90\,^{\circ}\mathrm{C}$)

bearing eccentricity is defined as $\varepsilon_{\mathrm{i,o}} = \frac{e_{\mathrm{i,o}}}{C_{\mathrm{i,o}}}$, where $e_{\mathrm{i,o}}$ is the inner/outer journal eccentricity and $C_{\mathrm{i,o}}$ is the inner/outer clearance of the radial bearings. Relative bearing eccentricities may usually provide a good indication about which oil-film is becoming unstable. In the case of a constant oil-supply temperature for the radial bearings, it can be observed from the inner bearing eccentricities that both inner oil-films (turbine-side and compressor-side) are becoming unstable at $N \approx 50000\,\mathrm{rpm}$. As the oil-temperature is increasing the instability point is shifted towards higher rotational speeds. Similarly, from the outer bearing eccentricities, the instability points from the outer oil-films can be seen. As the oil-temperature in the thrust bearing is increased at $T = 150\,^{\circ}\mathrm{C}$, a qualitatively different behavior is observed. The outer eccentricity of the compressor-side bearing does not increase suddenly as the outer eccentricity of the turbine-side bearing at $N \approx 220000\,\mathrm{rpm}$. On the contrary,

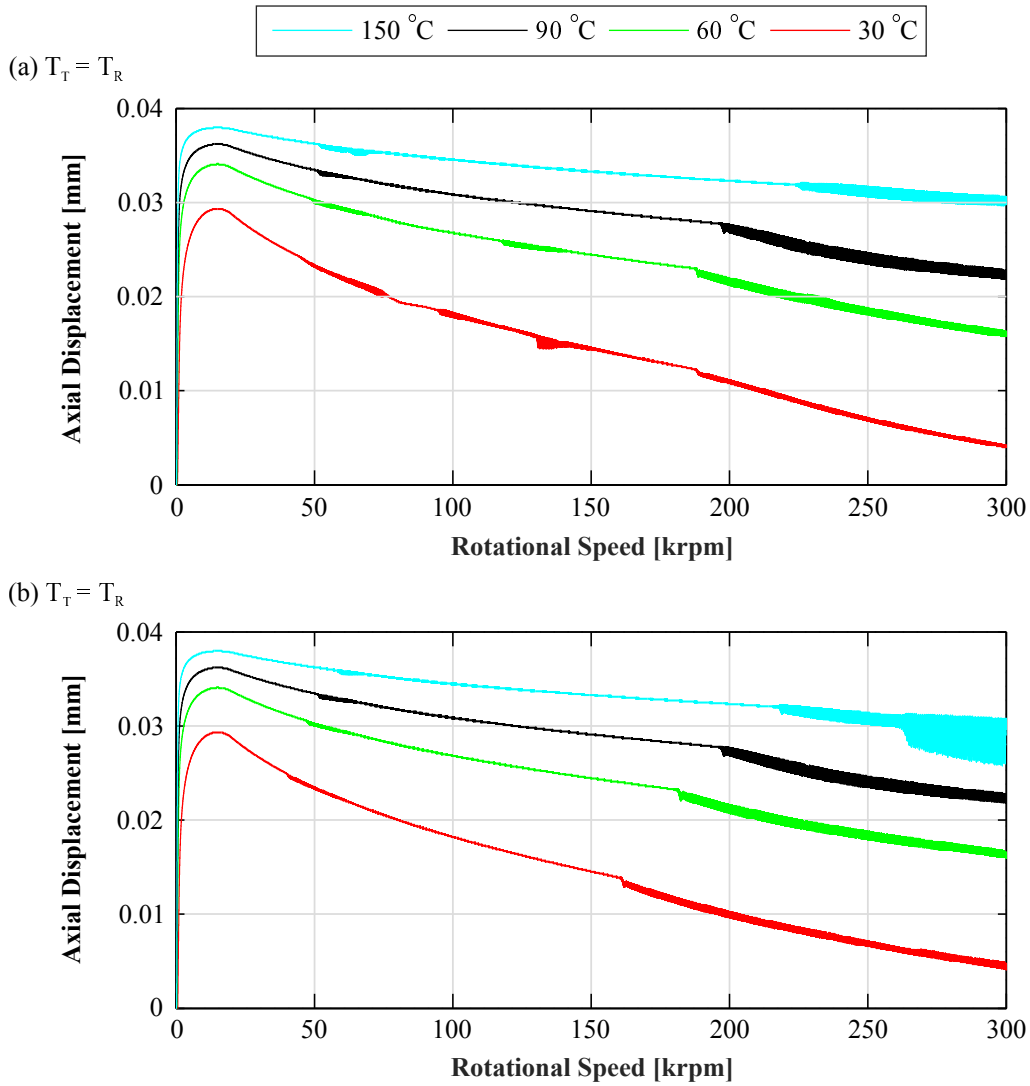

Figure 4.15: Axial displacements of the rotor for different oil-temperatures: (a) common oil-supply temperature ($T_\mathrm{T} = T_\mathrm{R}$) for the thrust and radial bearings, (b) constant oil-supply temperature for the radial bearings ($T_\mathrm{T} \neq T_\mathrm{R}$ and $T_\mathrm{R} = 90\,^\circ\mathrm{C}$)

it maintains its low amplitudes until $N \approx 262000\,\mathrm{rpm}$, where the compressor-side bearing becomes also unstable.

Figure 4.17 shows the spectrogram (Short Time Fourier Transform in logarithmic scale normalized by a reference amplitude $A_{ref} = 10\,\mu m$) of the vertical displacement of the compressor wheel for both cases ($T_\mathrm{T} = T_\mathrm{R}$ and $T_\mathrm{T} \neq T_\mathrm{R}$) and for all the considered oil-temperatures (see Fig. 4.13).

When the oil-supply temperature in the radial bearings is kept constant ($T_\mathrm{T} \neq T_\mathrm{R}$), the *sub 1* oscillation is shifted to higher frequencies f and higher rotational speeds N. The third subsynchronous oscillation *sub 3* exhibits a similar behavior, however, the effect is more pronounced. The influence of the oil-supply temperature on the rotor vibrations is obviously more complicated when a common oil-supply temperature is defined for the thrust and the radial bearings ($T_\mathrm{T} = T_\mathrm{R}$). The frequencies and the

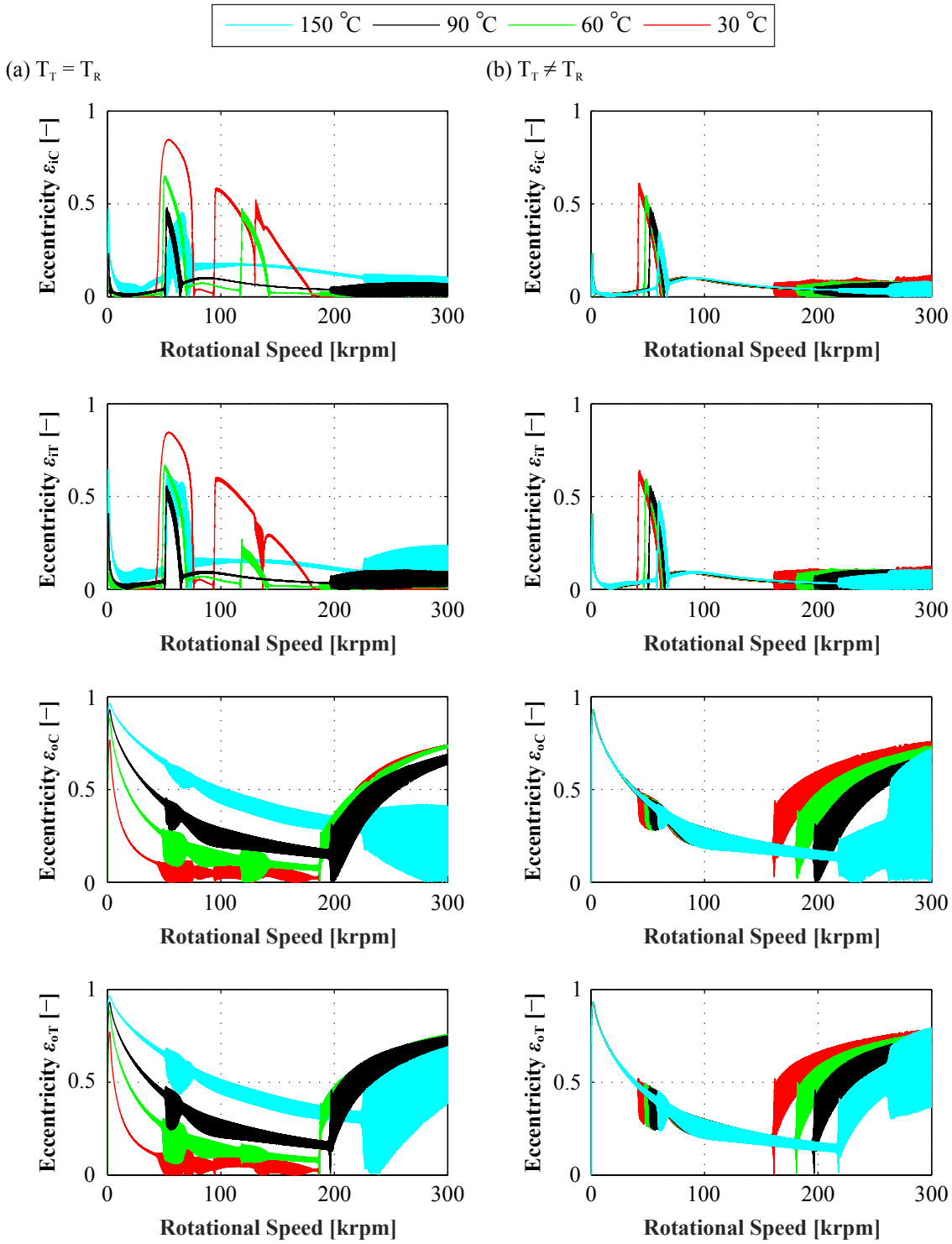

Figure 4.16: Relative bearing eccentricities of the radial bearings: (a) common oil-supply temperature ($T_T = T_R$) for the thrust and radial bearings (left column), (b) constant oil-supply temperature for the radial bearings ($T_T \neq T_R$ and $T_R = 90\,°C$) (right column)

rotational speeds of the onset points of the subsynchronous oscillations are shown in Table 4.2. It can be observed that the second subsynchronous vibration *sub 2* does

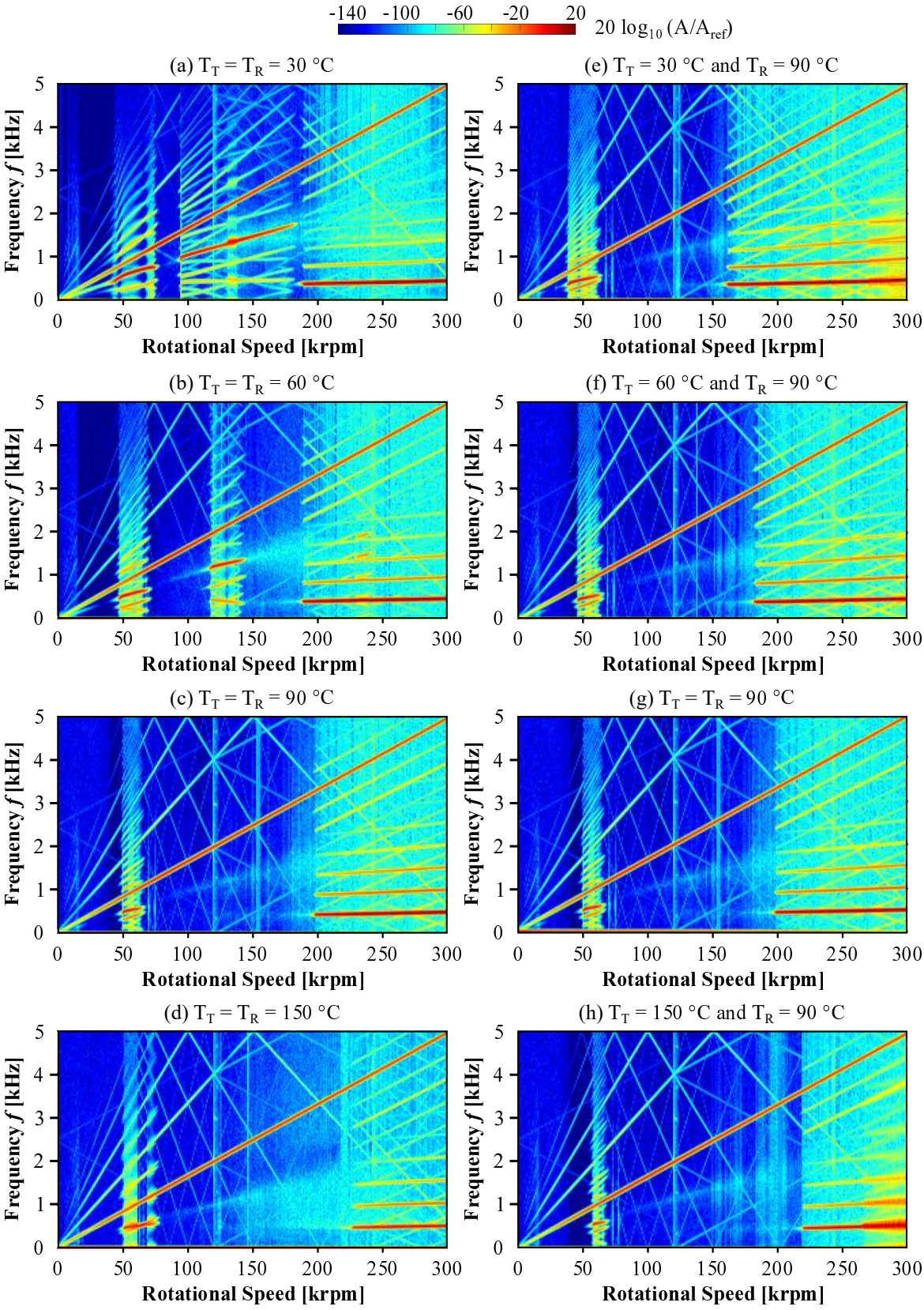

Figure 4.17: Spectrogram of the compressor wheel displacements in the vertical direction: (a)-(d) $T_{\mathrm{T}} = T_{\mathrm{R}}$, (e)-(h) $T_{\mathrm{T}} \neq T_{\mathrm{R}}$ and $T_{\mathrm{R}} = 90\,^{\circ}\mathrm{C}$

Table 4.2: Rotational speed and onset point of the subsynchronous oscillations

Case	Subsynchronous Vibration	Temperature [°C]	Rotational Speed [rpm]	Onset Frequency [Hz]
$T_T = T_R$	*sub 1*	30	43000	449
		60	48100	490
		90	51200	505
		150	51200	466
	sub 2	30	94200	962
		60	116700	1184
		90	n.a.	n.a.
		150	n.a.	n.a.
	sub 3	30	188400	405
		60	188400	430
		90	197600	454
		150	226300	491
$T_T \neq T_R$	*sub 1*	30	41300	420
		60	47000	479
		90	51000	508
		150	58600	586
	sub 2	30	n.a.	n.a.
		60	n.a.	n.a.
		90	n.a.	n.a.
		150	n.a.	n.a.
	sub 3	30	162300	400
		60	181500	440
		90	198800	469
		150	220000	498

not appear always in the simulations. Therefore, the rotational speeds and the onset frequencies are denoted as not applicable (n.a.), when *sub 2* is not present.
In Figure 4.18, the main frequencies (*synchronous*, *sub 1* and *sub 3*) that appear in the spectrogram of Fig. 4.17 for the case of $T_T \neq T_R$ are presented. It is only noted here that the synchronous oscillation does not appear from the beginning of the simulation due to its low amplitude.

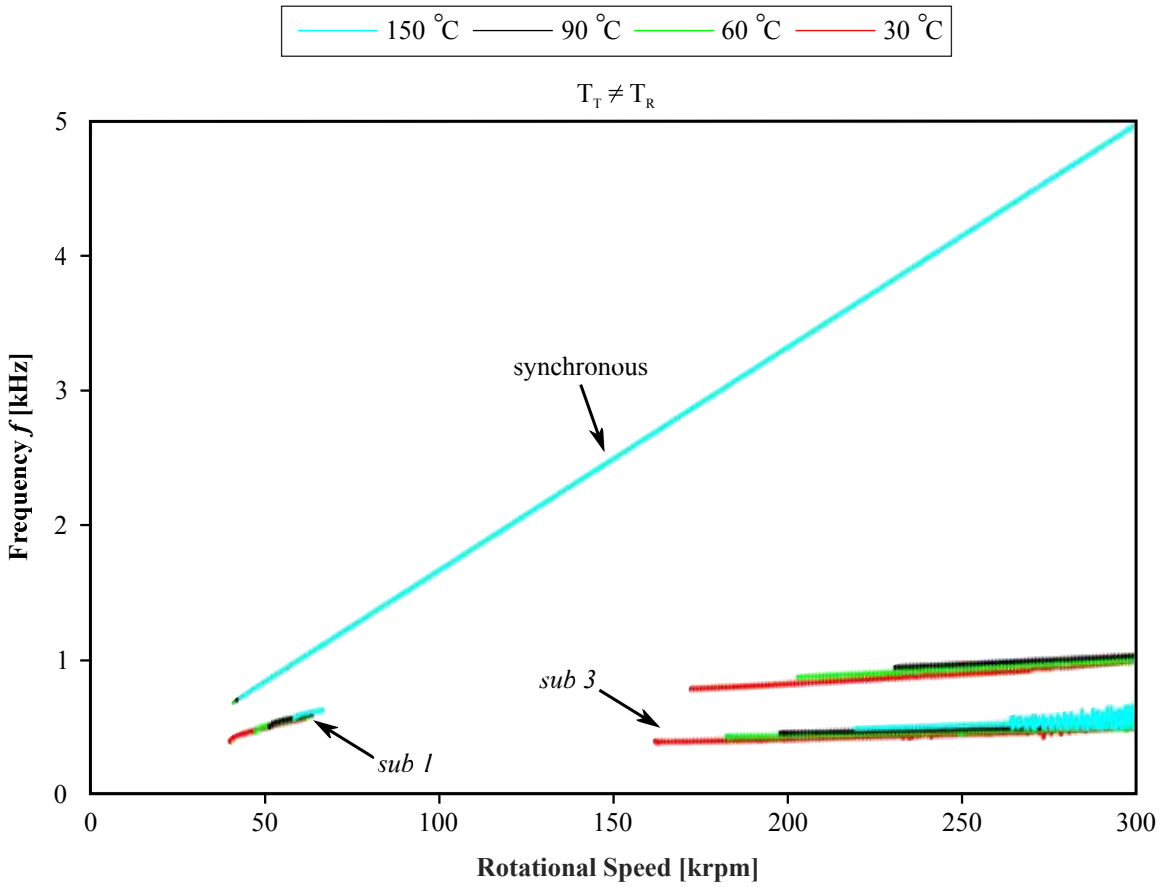

Figure 4.18: Dominating synchronous and subsynchronous oscillations for the case $T_{\mathrm{T}} \neq T_{\mathrm{R}}$ and $T_{\mathrm{R}} = 90\,^{\circ}\mathrm{C}$ of Fig. 4.17

4.2.5 Simulations using a thermohydrodynamic thrust bearing model

Numerical simulations are performed here, comparing the 2D-Decoupled thrust bearing model with the isothermal model using the same oil-supply temperature. Figure 4.19 shows the displacements of the compressor wheel in the vertical y-direction predicted from the 2D-Decoupled model as well as from the isothermal model for the case $T_{\mathrm{T}} \neq T_{\mathrm{R}}$ and for all the aforementioned oil-supply temperatures (see Fig. 4.13b). It can be observed from Fig. 4.19 that both *sub 1* and *sub 3* predicted from the 2D-Decoupled model are only slightly different from those predicted from the isothermal. For $T_T = 30\,^{\circ}\mathrm{C}$, $T_T = 60\,^{\circ}\mathrm{C}$ and $T_T = 90\,^{\circ}\mathrm{C}$ both subsynchronous oscillations are excited earlier in the 2D-Decoupled model. The onset point as well as the amplitude of the *sub 1* vibration exhibit only a marginal difference between the two models. The largest different on the onset point of the *sub 3* vibration between the two models can be seen for $T_T = 60\,^{\circ}\mathrm{C}$. As the temperature is increased at $T_T = 150\,^{\circ}\mathrm{C}$, both the *sub 1* and the *sub 3* are excited in higher rotational speed when the 2D-Decoupled model is used. Moreover, the amplitude of the *sub 3* vibration shows a significant re-

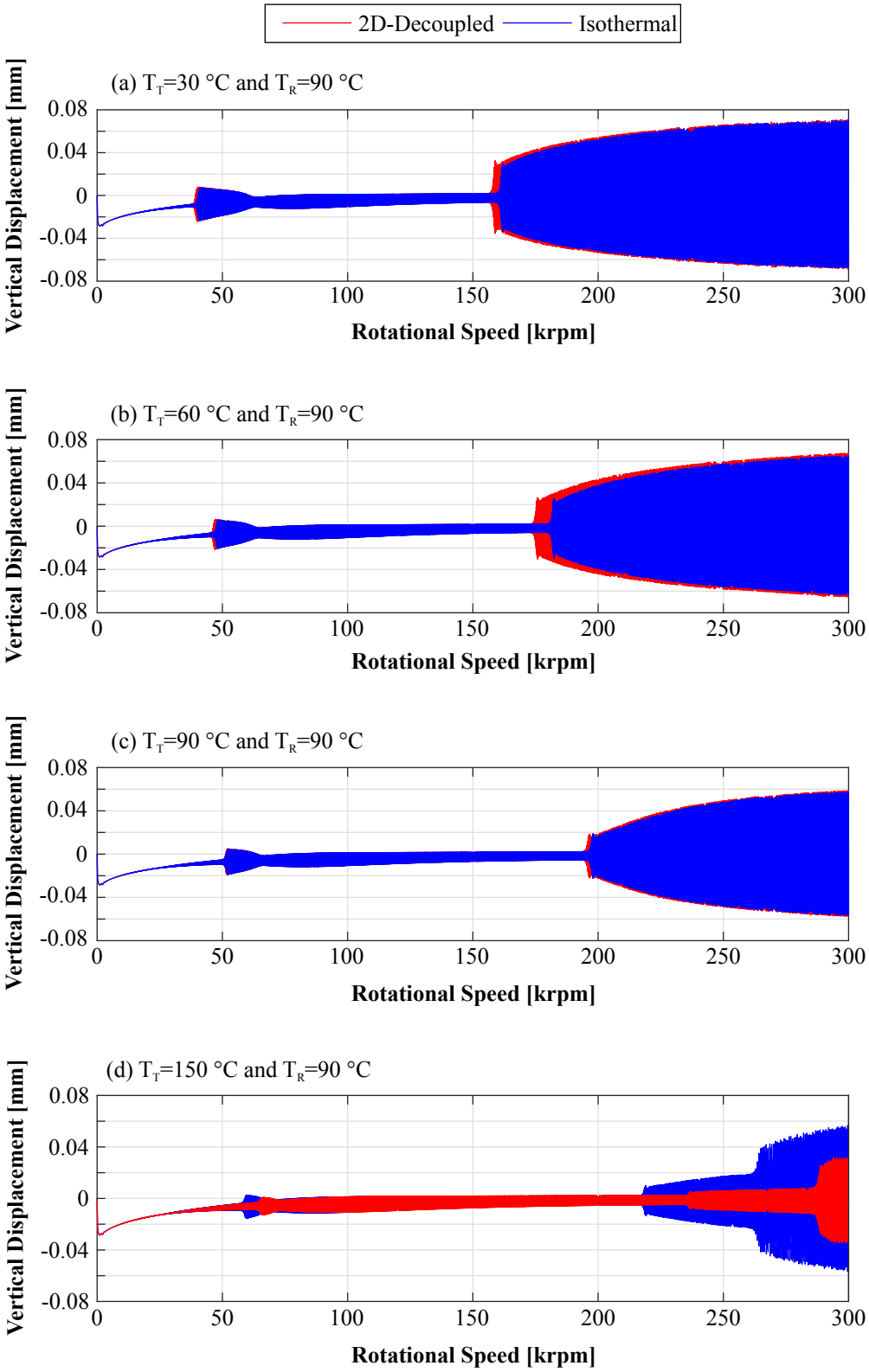

Figure 4.19: Comparison of the compressor wheel displacements in the vertical direction predicted from the 2D-Decoupled model as well as from the isothermal model for different oil-supply temperatures for the case $T_\mathrm{T} \neq T_\mathrm{R}$

duction with the 2D-Decoupled model. Figure 4.20 presents the axial displacements (z-direction) of the rotor for both the isothermal and 2D-Decoupled model for the case $T_{\mathrm{T}} \neq T_{\mathrm{R}}$.

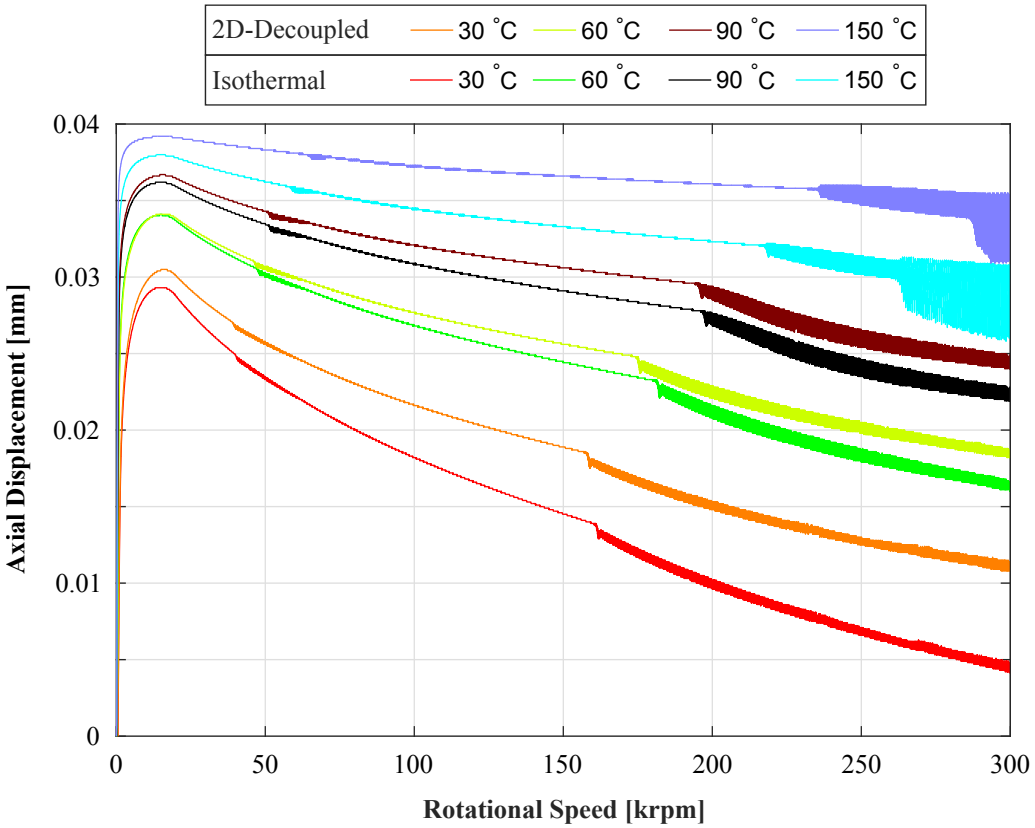

Figure 4.20: Comparison of the rotor axial displacements predicted from the 2D-Decoupled model as well as from the isothermal model for different oil-supply temperatures for the case $T_{\mathrm{T}} \neq T_{\mathrm{R}}$

Using the 2D-Decoupled model, the average oil-temperature of a bearing pad is higher compared to the constant oil-temperature of the isothermal model. Therefore, as it has already been described that the predicted axial force from the thrust bearing is lower for the 2D-Decoupled model in comparison with the isothermal, it is expected that the minimum film thickness in the isothermal case will be larger.

4.2.6 Transient and quasi-static energy equation for thrust bearings

In this section, a physical explanation for the type of the energy equation - transient or quasi-static - that may be used for thrust bearing modeling in transient rotordynamic applications is provided.

The 2D energy equation (see for example [59]) for a transient thermohydrodynamic

analysis of thrust bearings includes the time-dependent temperature term ($\frac{\partial T}{\partial t}$)

$$\rho c_p \left(\frac{\partial T}{\partial t} - \frac{h^2}{12\mu} \frac{\partial p}{\partial r} \frac{\partial T}{\partial r} + \frac{-\frac{h^2}{12\mu r} \frac{\partial p}{\partial \theta} + \frac{r\omega}{2}}{r} \frac{\partial T}{\partial \theta} \right) = \mu \left(\left(\frac{1}{12} \left(\frac{h \partial p}{\mu \partial r} \right)^2 \right) + \left(\frac{1}{12} \left(\frac{h \partial p}{\mu r \partial \theta} \right)^2 + \left(\frac{r\omega}{h} \right)^2 \right) \right). \tag{4.2.1}$$

The solution of this equation, apart from the spatial discretization (r and θ) using for example a Finite Difference method, should be combined with a discretization with respect to time t. For avoiding the time discretization, usually this term is dropped.

In the following, we consider a thrust bearing with 3 pads ($\Theta_1 = 0\,°$, $\Theta_2 = 120\,°$, $\Theta_3 = 240\,°$). We distinguish two cases, as shown in Fig. 4.21.

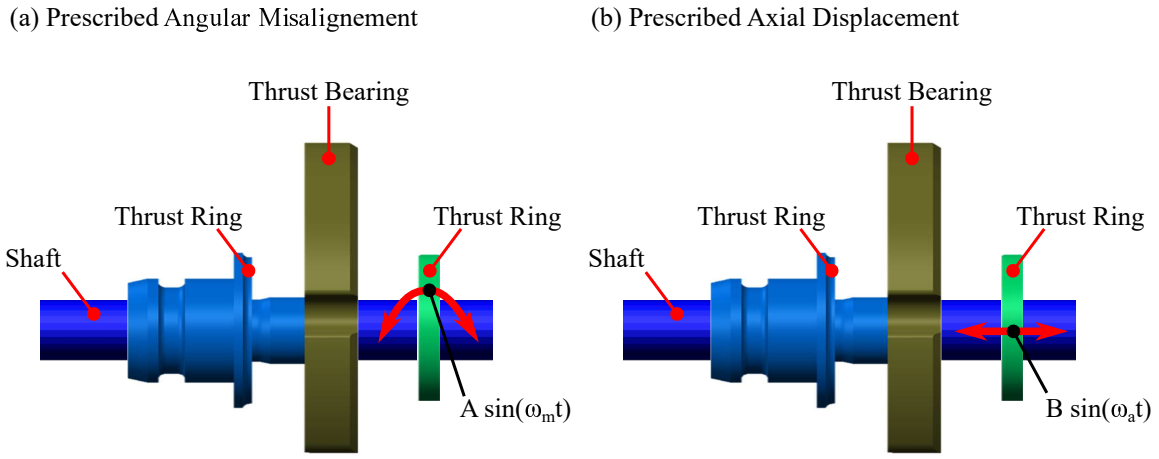

Figure 4.21: Considered cases for determination of the temperature distribution: (a) prescribed angular misalignment of the thrust ring, (b) prescribed axial displacement of the thrust ring

In the first case, a sinusoidal angular motion with amplitude $A = 0.5\,\text{mrad}$ is prescribed for the first α and the second β Bryant angle of the rotor

$$\alpha = A \sin(\omega_m t), \qquad \beta = A \sin(\omega_m t). \tag{4.2.2}$$

In this case the initial minimum film thickness is assumed to be $h_0 = 10\,\mu\text{m}$. It is clear that many other combinations of sines and cosines may be used.

In the second case, a sinusoidal axial motion with amplitude $B = 2\,\mu\text{m}$ is prescribed for the rotor

$$h_0 = B \sin(\omega_a t) + 7\mu m. \tag{4.2.3}$$

As the motions in both cases are prescribed, the following examples cannot fully represent the behavior of a rotor/bearing system, since in a rotordynamic simulation

the displacements and velocities are given through the solution of the equations of motion. However, using this analysis we can gain an insight of the importance of the time-dependent temperature term in the energy equation.

In Figure 4.22, comparisons of the oil-temperature in the first bearing pad (averaged over its surface) predicted from the quasi-static and the transient energy equation are shown. The comparisons are performed for various rotational speeds ω and angular velocities ω_m (see Fig. 4.21a), i.e. $\omega = \omega_m = 1000\,\text{rad/s}$, $\omega = \omega_m = 5000\,\text{rad/s}$, $\omega = \omega_m = 20000\,\text{rad/s}$ and $\omega = \omega_m = 30000\,\text{rad/s}$. It is observed, that in this case

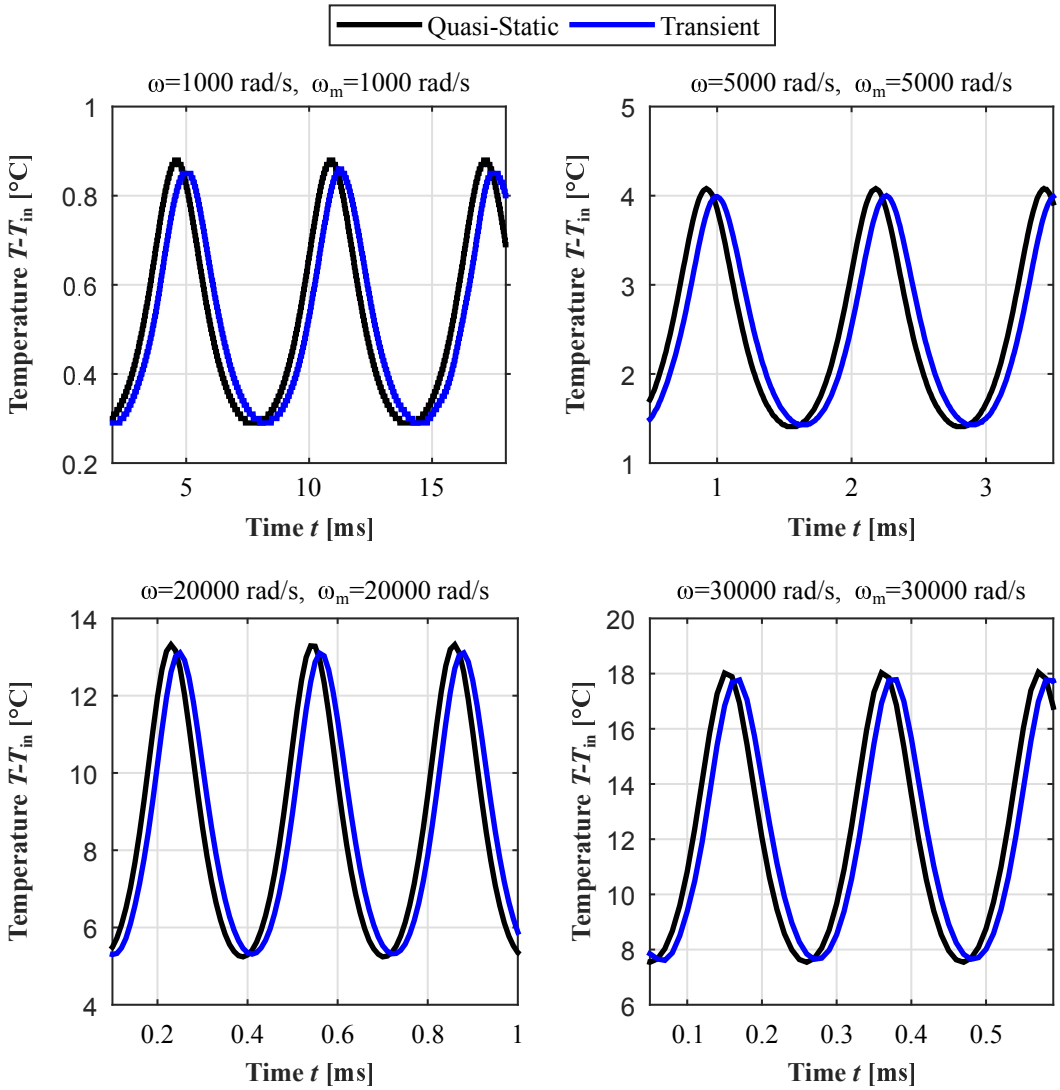

Figure 4.22: Averaged oil-temperatures using the quasi-static and the transient energy equation for various rotational speeds ω and angular velocities ω_m

the two energy equations (quasi-static and transient) predict very similar results. We also note the increase in the average oil-temperature of the pad as the rotational speed is increased. From this example it becomes apparent that the quasi-static energy equation is sufficient for the calculation of the oil-temperature distribution.

In Figure 4.23, similar comparisons are performed as in Fig. 4.22, using a rotational speed $\omega = 5000\,\text{rad/s}$ and two different angular velocities $\omega_m = 1000\,\text{rad/s}$ and $\omega_m = 20000\,\text{rad/s}$. This example mainly refers to the cases where the rotor of the

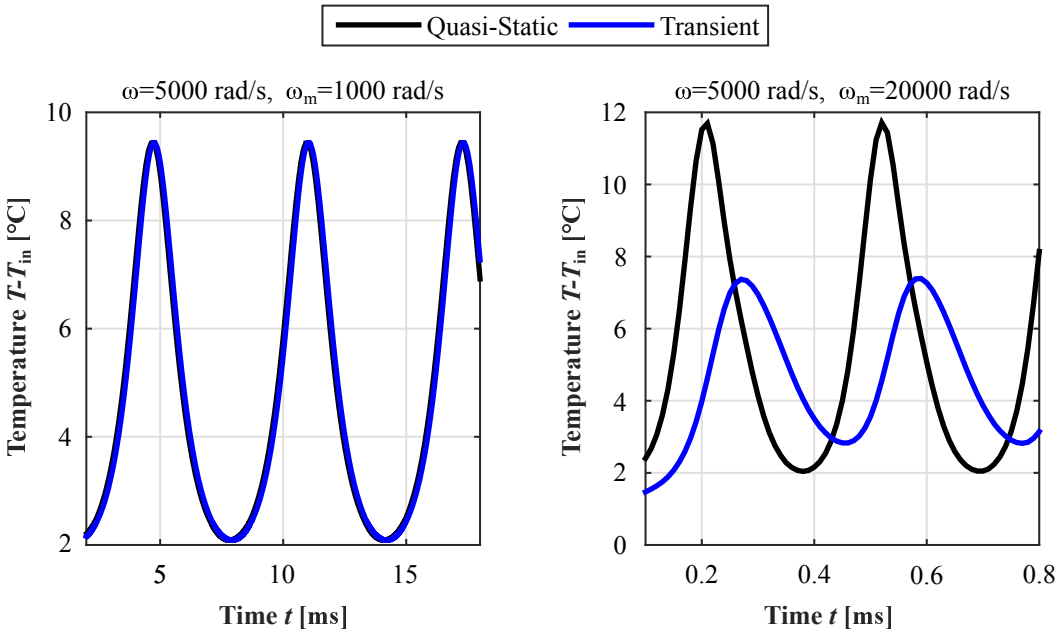

Figure 4.23: Averaged oil-temperatures using the quasi-static and the transient energy equation for rotational speed $\omega = 5000\,\text{rad/s}$ and angular velocities $\omega_m = 1000\,\text{rad/s}$ and $\omega_m = 20000\,\text{rad/s}$

turbocharger system is vibrating in a conical mode (*sub 1*, *sub 3*). Using the angular velocity $\omega_m = 1000\,\text{rad/s}$, the predicted average temperature is identical for the transient and the quasi-static model. However, as the angular velocity was increased to $\omega_m = 20000\,\text{rad/s}$, the average temperatures predicted from the two models show significant differences. Turbochargers supported by hydrodynamic bearings, mainly suffer from large amplitudes subsynchronous oscillations. Therefore, they fall in the category where the rotational speed ω is much larger than the angular velocity ω_m. As a consequence, the temperature distributions predicted by the quasi-static energy equation may be sufficient for the run-up simulations.

Comparisons between the quasi-static and the transient energy equation are performed for a purely axial motion of the rotor (see Fig. 4.21b). The averaged oil-temperatures using a rotational speed $\omega = 5000\,\text{rad/s}$ and two different circular frequencies in the axial direction (axial velocities) $\omega_a = 1000\,\text{rad/s}$ and $\omega_a = 20000\,\text{rad/s}$ are shown in Fig. 4.24.

When the rotational speed is higher than the axial velocity ($\omega = 5000\,\text{rad/s}$ and $\omega_a = 1000\,\text{rad/s}$), the temperature predictions from the quasi-static energy equation are almost identical with the predictions of the transient energy equation. On the contrary, when the axial velocity is much higher than the rotational speed ($\omega = 5000\,\text{rad/s}$

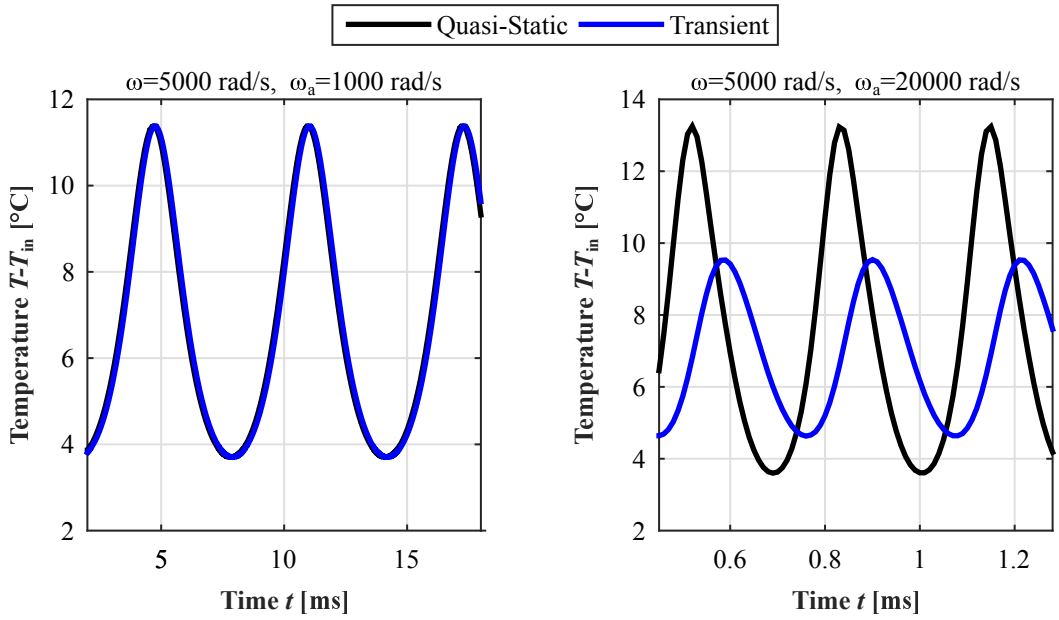

Figure 4.24: Averaged oil-temperatures using the quasi-static and the transient energy equation for rotational speed $\omega = 5000\,\mathrm{rad/s}$ and different axial velocities $\omega_a = 1000\,\mathrm{rad/s}$ and $\omega_a = 20000\,\mathrm{rad/s}$

and $\omega_a = 20000\,\mathrm{rad/s}$), then the quasi-static energy equation should not be used. As explained earlier, in turbocharger applications with hydrodynamic bearings, the rotational speed is always higher than the circular frequency of the self-excited oscillations, which in these cases was represented by ω_a.

It can therefore be concluded that for the prediction of the oil-temperature distribution of thrust bearings in turbocharger applications, the quasi-static energy equation of the oil may be used instead of the transient energy equation.

4.2.7 Comparison between the Global Galerkin and a Finite Difference approach for thrust bearings in transient simulations

In this section, a run-up simulation of the turbocharger rotor/bearing model is performed taking into account a thrust bearing. The thrust bearing is modeled with two different approaches, namely with the Global Galerkin method and with a classical Finite Difference approach. Goal of this section is to compare these two approaches in terms of their numerical efficiency. For a fair comparison, the number of trial functions for the global Galerkin approach and the number of grid points for the Finite Difference approach are chosen in such a way that both methods yield the same approximation error for the resultant bearing forces and moments. A detailed error analysis, which is not shown here for reasons of a concise representation, shows that

a global Galerkin approach with $N = M = 4$ trial functions and a Finite Difference approach with a 21×21-grid yields resultant bearing forces/moments with almost the same error compared to a numerically calculated reference solution.

To further improve the Finite Difference implementation, the symbolic factorization used in the sparse solver was only carried out at the first time-integration step, since the structure of the linear system is constant during a simulation. As a consequence, the simulation time has been reduced by 20%. Figure 4.25 shows the vertical displacements of the turbine wheel for both discretization approaches. It is observed that the

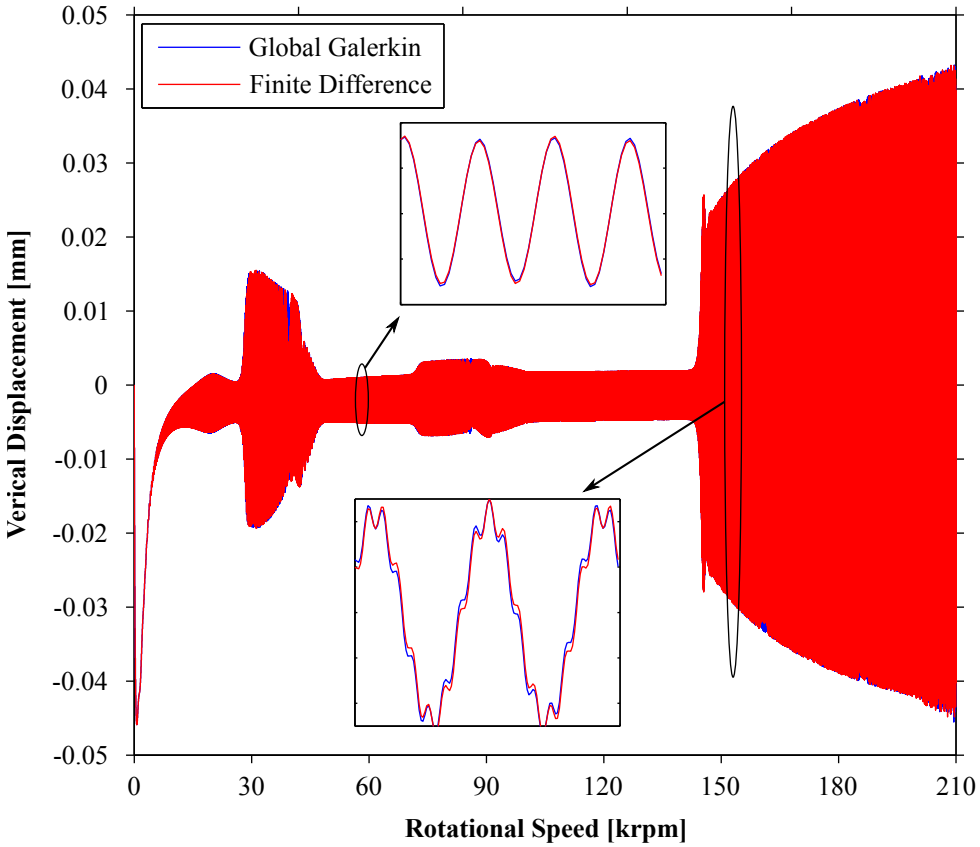

Figure 4.25: Turbine wheel displacements in the vertical direction using the Global Galerkin and a Finite Difference approach

two methods yield almost the same results. The bifurcation points are almost identical as well as the oscillation amplitudes. The simulation time for the rotor run-up using the Finite Difference method is, however, more than 10 times larger than the corresponding simulation time using the Global Galerkin model.

This is the great advantage of the Global Galerkin approach. However, for more complicated pad geometries or for detailed thermohydrodynamic models which take into account the energy equation, the implementation of the Global Galerkin approach might be more cumbersome and a Finite Difference approach might be preferable.

Chapter 5

Thrust Bearing Optimization

The geometric optimization of a thrust bearing is usually performed considering its load capacity and friction losses. Thrust bearings are therefore optimized for supporting a higher load with the minimum friction. This optimum geometric configuration may be found utilizing an optimizer, where the danger of a local minimum is always possible.

In this chapter, a novel approach will be used for calculating optimum bearing geometries. The optimization will be performed using stochastic methods in combination with statistical approaches and Artificial Neural Networks. For stationary rotor operations, the optimization process will be considering the load capacity and the friction losses. In chapter 4, it was shown that the thrust bearings influence the subsynchronous rotor vibrations. Therefore, in transient operations, a more general optimization approach will be used, fulfilling the high load capacity and the low friction losses needs, together with minimizing the rotor subsynchronous vibrations. The robustness of this optimization procedure will be investigated in detail in the following.

5.1 Theoretical Remarks

The optimization procedure steps are summarized below

- Selection of the minimum and maximum geometric characteristics of the thrust bearing pads.
- Selection of the probability density function and the sampling method for the creation of the input configuration space.
- Solution of the Reynolds equation using a Finite Element approach for the complete input space. In this step the output space is created, identifying the load capacity, the friction losses and the angular moments of the thrust bearing.
- Application of statistical methods for the identification of optimum solutions.
- Verification of the optimum solution. In stationary operations this is a trivial issue. For transient operations, run-up simulations are performed comparing the optimized bearing geometry with other configurations.

5.1.1 Parameter space

The geometrical parameters of a thrust bearing, which constitute the input parameter space, are summarized in Table 5.1.

Table 5.1: Geometrical parameters for the optimization

Parameter	Description
r_1	Pad inner radius
r_2	Pad outer radius
θ_0	Angular extent of pad
L_{wed}/L	Inclined/total pad area
C_{wed}	Taper height

The characteristics of the thrust bearing that form the output space are presented in Table 5.2.

Table 5.2: Output space for the optimization

Parameter	Description
F_z	Load capacity
M_x	Moment in x-direction
M_y	Moment in y-direction
Φ	Friction losses
Q_{tot}	Output oil-flow

The output oil-flow is always checked to avoid very high values, however, it will not be considered further in the following optimization. For the solution of the Reynolds equation and the calculation of the output space the following parameters will be assumed constant as shown in Table 5.3. The axial and angular velocities are consider to be zero.

5.1.2 Probability density functions and sampling methods

After the definition of the minimum and maximum geometric parameters, a sampling method is defined followed by a selection of a suitable probability density function. A number of samples is set, usually between 100 and 1000 samples. Therefore, the Reynolds equation should be solved as many times as the number of samples. Four

Table 5.3: Geometrical parameters for optimization

Parameter	Description
h_0	Minimum film thickness
α	First Bryant angle
β	Second Bryant angle
μ	Oil-viscosity
λ	Viscosity-temperature coefficient
T_0	Inlet oil-temperature

different probability density functions are implemented, i.e. uniform, triangular, Gaussian and Weibull. The probability density function of a uniform distribution is

$$f(x) = \begin{cases} \dfrac{1}{b-a} & a \leqslant x \leqslant b, \\ 0 & \text{elsewhere.} \end{cases} \tag{5.1.1}$$

The probability density function of a triangular distribution is

$$f(x) = \begin{cases} \frac{2(x-a)}{(b-a)(c-a)} & a \leq x < c, \\ \frac{2}{b-a} & x = c, \\ \frac{2(b-x)}{(b-a)(b-c)} & c < x \leq b, \\ 0 & \text{elsewhere.} \end{cases} \tag{5.1.2}$$

The probability density function of a Gaussian distribution is

$$f(x) = \frac{1}{\sigma\sqrt{2\pi}} e^{-\frac{(x-\mu)^2}{2\sigma^2}}. \tag{5.1.3}$$

The probability density function of a Weibull distribution is

$$f(x) = \begin{cases} \frac{\kappa}{\lambda}\left(\frac{x}{\lambda}\right)^{\kappa-1} e^{-(x/\lambda)^{\kappa}} & x \geqslant 0, \\ 0 & x < 0. \end{cases} \tag{5.1.4}$$

Figure 5.1 shows the four probability density functions that can be selected.

This kind of optimization is based on the random sampling of the input variables (geometry of the thrust bearing) for creating a parameter space with a large number of samples. It has been shown, see for example [77], that improvements over the random sampling methods can be achieved by alternative sampling methods as the Latin Hypercube Sampling (LHS) and therefore the LHS approach will be used in this work. LHS can be advantageous over a simply random sampling method, but an exhaustive comparison between different sampling methods is out of the scope of this work.

Figure 5.2 shows the comparison between the uniform and the Gaussian distribution using random sampling and Latin Hypercube Sampling (LHS).

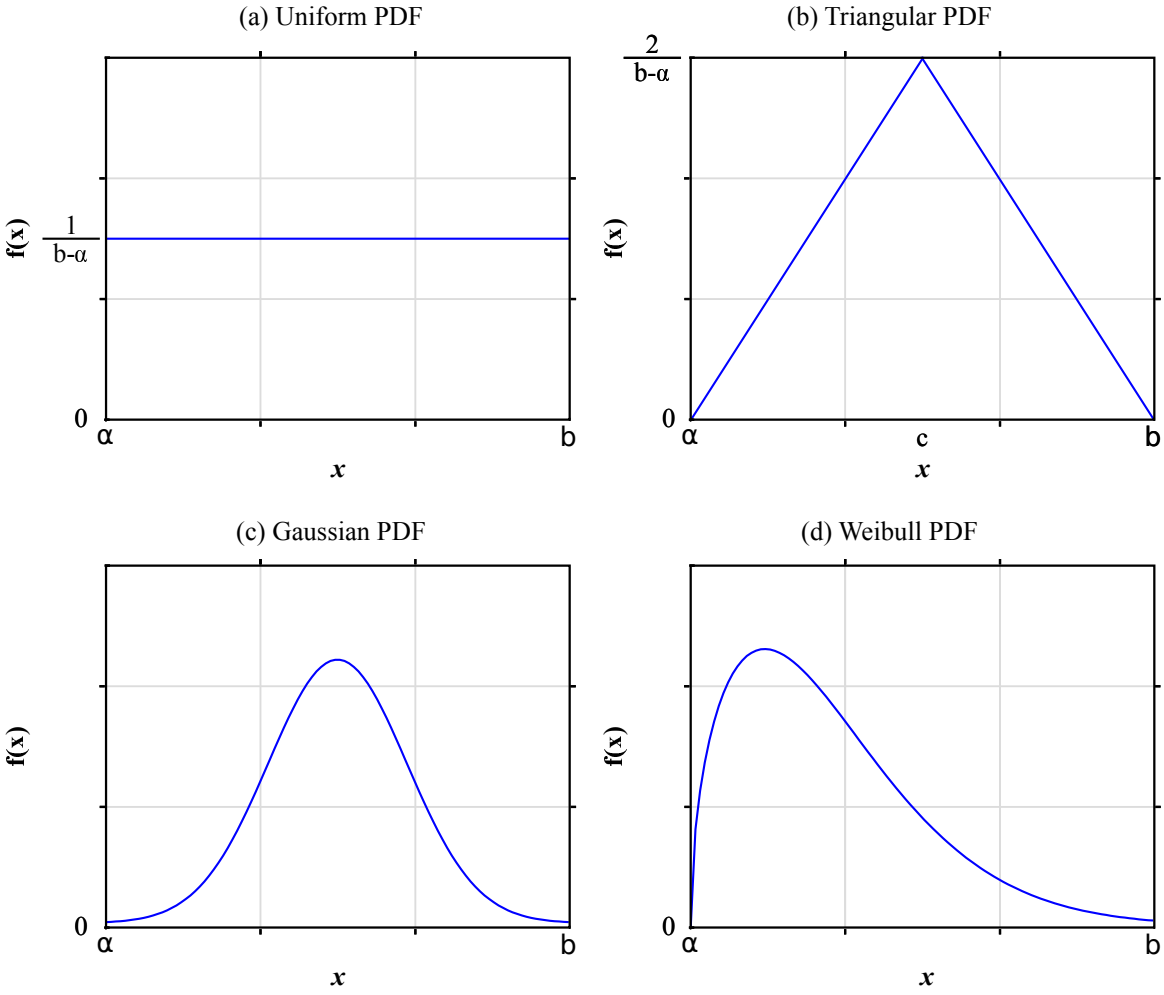

Figure 5.1: Probability density functions: (a) uniform, (b) triangular, (c) Gaussian, (d) Weibull

5.1.3 Statistical methods and Artificial Neural Networks

Due to the large number of samples, statistical methods are needed to identify the correlation between the input and the output space. Several well-known approaches exist, see for example [8, 60], but in this work the Pearson correlation coefficient method will be used. Additionally, the global sensitivity analysis method as well as neural networks approaches, i.e. the Self-organizing maps (SOM) will be utilized.

Linear correlations between the input and the output space can be found using the Pearson correlation coefficient. It is defined between two variables as

$$\rho_{\mathbf{x},\mathbf{y}} = \frac{\mathrm{cov}(\mathbf{X},\mathbf{Y})}{\sigma_{\mathbf{X}}\sigma_{\mathbf{Y}}}, \tag{5.1.5}$$

where $\mathrm{cov}(\mathbf{X},\mathbf{Y})$ is the covariance of the two variables $(\mathbf{X},\mathbf{Y})$ and $\sigma_{\mathbf{X}}$, $\sigma_{\mathbf{Y}}$ are their standard deviations. Therefore, the Pearson coefficient is $-1 \leq \rho \leq 1$. Figure 5.3 shows the Pearson coefficients used for identification of the statistical relationship between the input and the output space of a thrust bearing. Figure 5.3 can be read

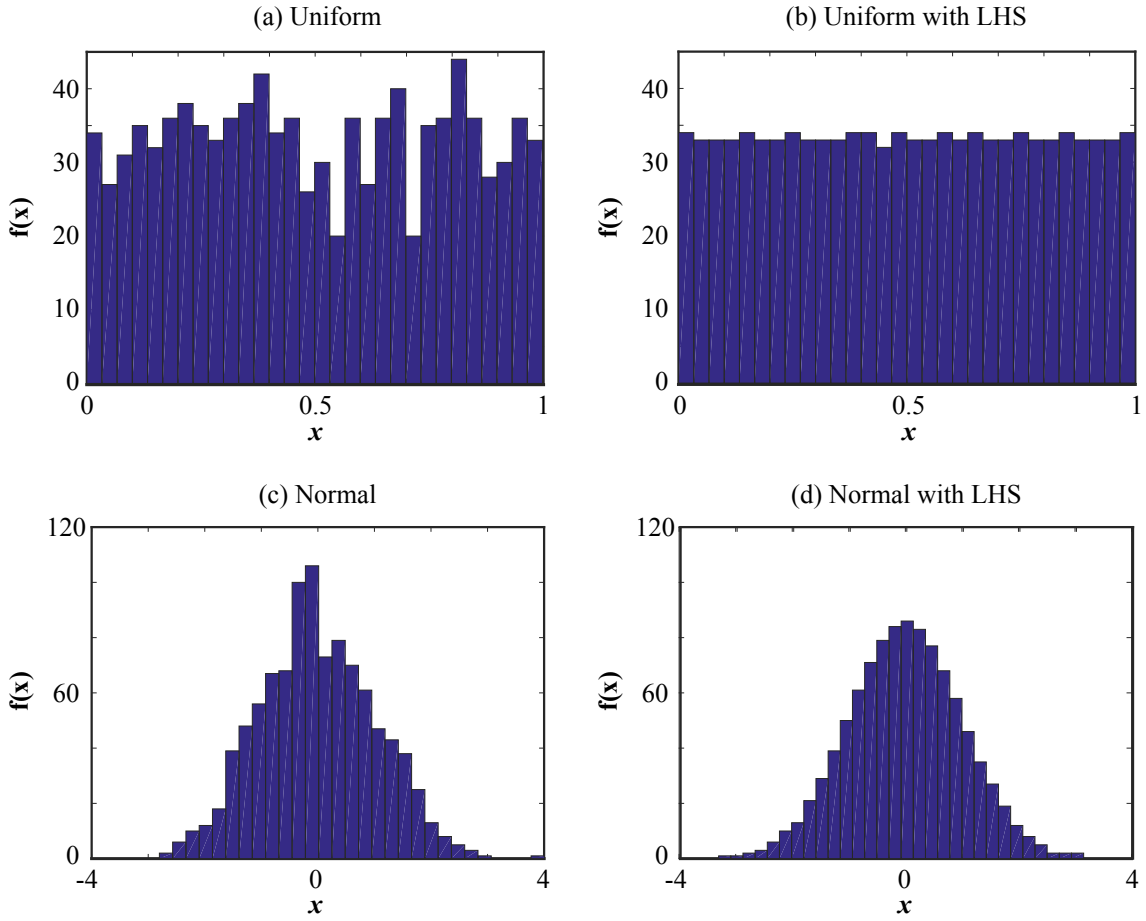

Figure 5.2: Histograms for the probability density functions (a) uniform, (b) uniform with LHS, (c) Gaussian, (d) Gaussian with LHS

as a matrix, where at the lower triangle the values of the Pearson coefficient are shown. At the diagonal the values should be 1. Instead of this, the distribution of the input or output variable is illustrated. At the upper triangle, a scatter plot between the respective variables is depicted. Large positive or negative correlations can be observed for example for the input variable r_2 (outer diameter) and all the output variables. It is therefore suggested that the outer diameter of the bearing has a strong linear relationship with its load capacity as well as its power dissipation. Nonlinear relationships are ignored from the Pearson coefficient as well as the slope of the linear relations between two variables cannot be captured.

The term sensitivity analysis, is used here for the identification of the influence of each input variable to the output space. Among several existing methods for applying a sensitivity analysis study, multiple linear regressions are performed. Each output variable $\mathbf{y}$ is calculated as a linear combination of the input variables $\mathbf{x}$

$$\mathbf{y} = \mathbf{X}\beta + \epsilon, \tag{5.1.6}$$

where ϵ is the regression error and $\mathbf{X}$ is the matrix containing all the input variables.

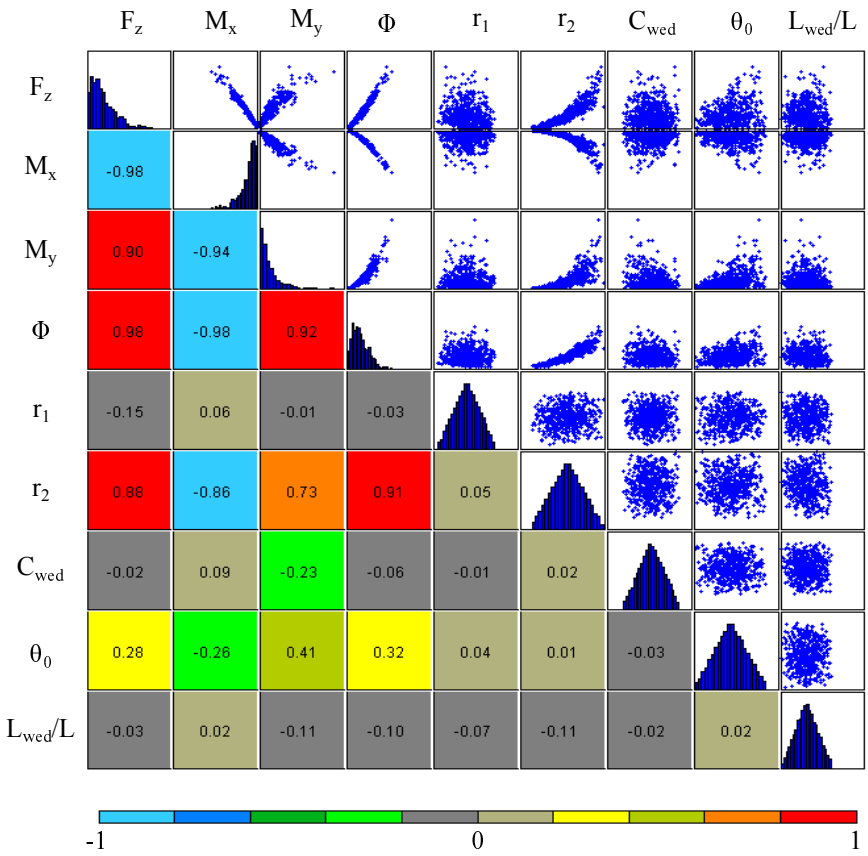

Figure 5.3: Pearson coefficients

The regression coefficients β are obtained through

$$\beta = (\mathbf{X}^T\mathbf{X})^{-1}\mathbf{X}^T\mathbf{y}. \tag{5.1.7}$$

This procedure is performed for every output variable. The Euclidean norm of the regression coefficients of each input variable is calculated and their sensitivity is given as percentage. Figure 5.4 shows the sensitivity analysis applied to the input and output variables of the thrust bearing.

The Self-organizing maps are a category of unsupervised Artificial Neural Networks [67,68]. They are effective in creating spatially organized representations of various input space features, preserving the topological properties of the input space. The nodes or neurons are the components that create the map space of Self-organizing maps and they are associated with a weight vector. Figure 5.5 shows the Self-organizing maps for the input and output variable space. The relationship between the input and the output variables can be seen. For example, the larger the outer radius r_2 and the larger the angular extent of pad θ_0, the larger the load bearing capacity F_z and the larger the friction losses Φ.

Figure 5.6 shows the response surface for the two input variables r_1 and r_2 and the output variable F_z. The response surface approximates the output variables using the

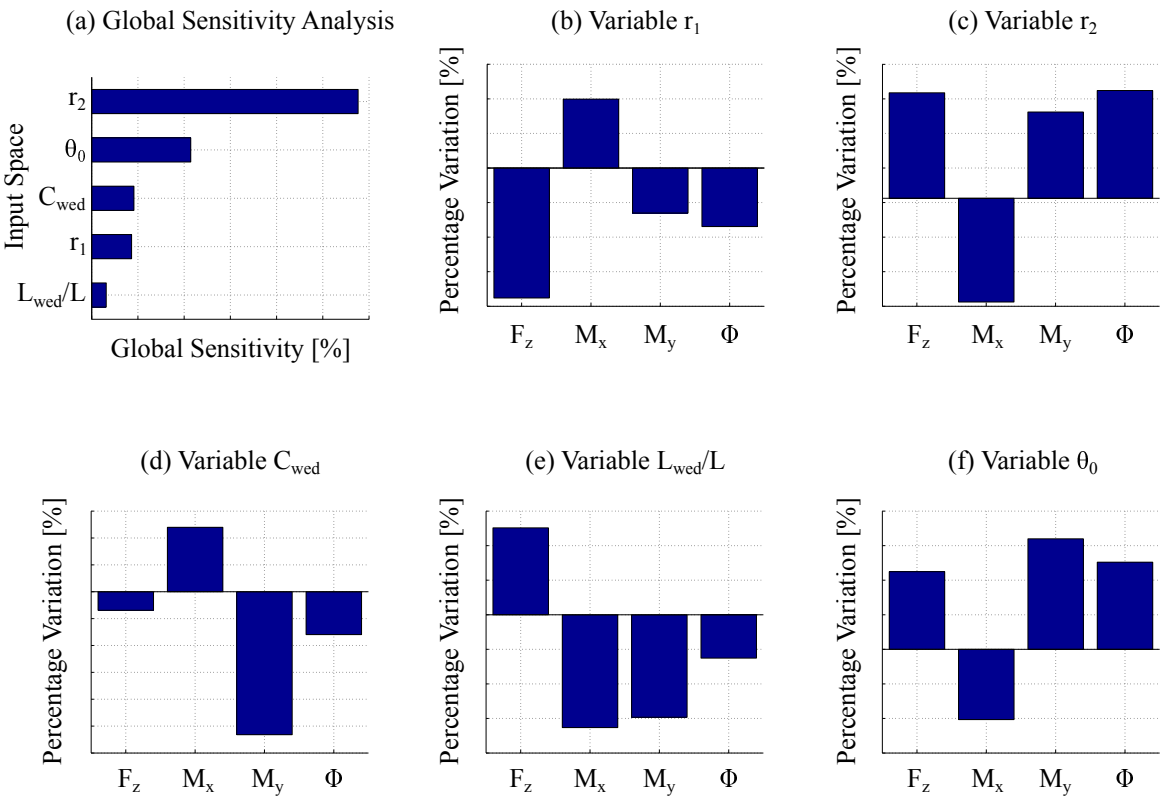

Figure 5.4: Sensitivity analysis of the input variables

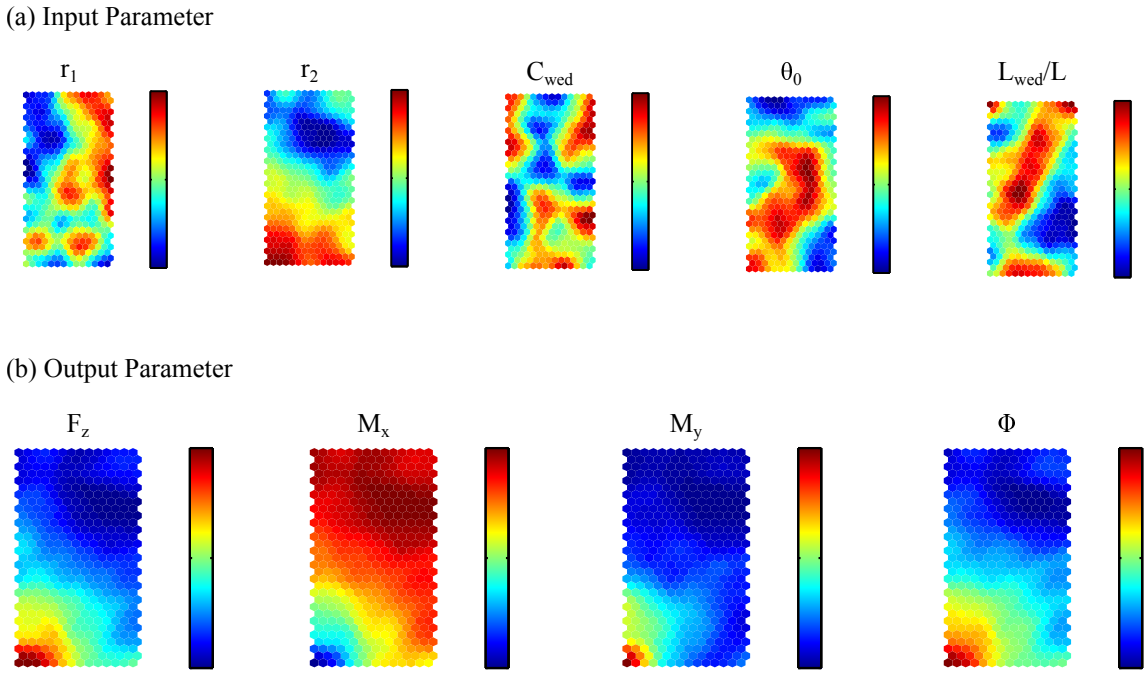

Figure 5.5: Self-organizing maps for the input and output variable space

input variables and some low-order polynomial

$$y = f(\mathbf{x})\beta + \varepsilon, \tag{5.1.8}$$

where y is the response, $f(\mathbf{x})$ is the input vector function, β are the unknown coeffi-

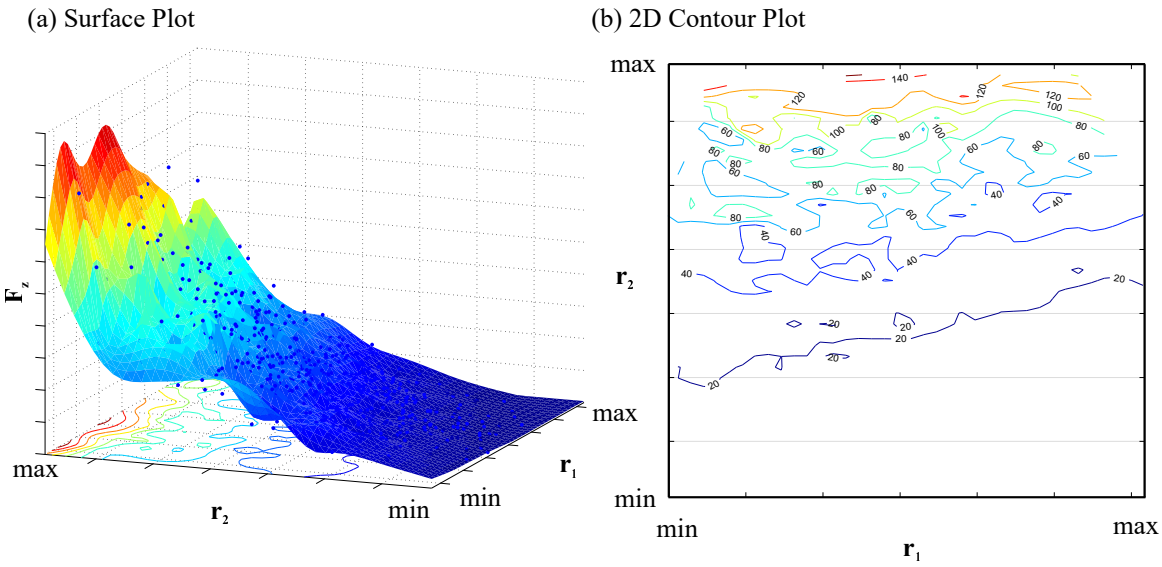

Figure 5.6: Response surface of the load capacity F_z with respect to the inner r_1 and the outer r_2 radius

cients and ε is the error.

5.2 Optimization in Stationary Operations

The optimization of thrust and radial bearings for increased load capacity and minimum friction losses has been thoroughly investigated. In [45], the thrust bearing shape was optimized achieving large load capacity. Using sequential quadratic programming, optimum thrust bearing geometries were identified for step bearings and finite sliders. The optimization has considered isothermal conditions and the centrifugal effects were ignored. For flexible pad thrust bearings, a geometric shape optimization towards a load capacity maximization, was presented in [44]. Hard disk drive (HDD) thrust bearings were optimized in [112]. Partially textured thrust bearings with square-shaped micro-dimples were optimized in [94].

Here, a generic approach is presented for stationary optimizations of thrust bearings. The minimum and the maximum values of the input parameters are given in Table 5.4.

For the solution of the Reynolds equation the following parameters will be used as shown in Table 5.5.

The calculations are performed using 500 samples and the output space (load capacity and friction losses) is created. In Figure 5.7, the Self-organizing maps of a stationary optimization for one thrust bearing pad are illustrated.

The maximum load capacity F_z can be achieved by maximizing the outer radius r_2 and the angular extent of the bearing pad θ_0. It can be observed, however, that the

Table 5.4: Geometrical parameters for the stationary and the transient optimization

Parameter	Value		Unit
	min	max	
r_1	0.0032	0.004	m
r_2	0.0045	0.007	m
θ_0	20	45	°
L_{wed}/L	0.6	0.85	-
C_{wed}	10	35	μm

Table 5.5: Parameters for the Reynolds equation

Parameter	Value	Unit
h_0	5	μm
α	0	rad
β	0	rad
μ	0.00768	Pas
λ	0.0225	1/°C
T_0	90	°C
N_{pad}	5	-
ω	10000	rad/s

maximization of the load capacity comes with the cost of maximizing the friction losses. Therefore, an optimization can be performed by choosing the minimum and the maximum load capacity needed for the specific application. This step can be easily utilized by selecting the appropriate areas in the SOMs. For this thrust bearing with 5 pads, the load capacity for each pad is selected between 25 and 30 N, leading to a maximum resultant thrust bearing force of 150 N.

Using the response surface methodology, areas of the input space that fulfill the requirements for the load capacity can be also identified. In Figure 5.8, the response surface of a stationary optimization for the inner radius, the outer radius and the load capacity of a thrust bearing pad is illustrated.

The minimum and the maximum thrust bearing load capacity of 25 and 30 N can be also observed. The inner and outer radii that satisfy this load capacity are marked at the contour of the 3D plot of Fig. 5.8a as well as at the shaded area of Fig. 5.8b. Various inner radii may deliver the required load capacity but the outer radius should be large as shown in the shaded area of Fig. 5.8b. In Figure 5.9, the response surface for the outer radius, the friction losses and the load capacity of a thrust bearing pad

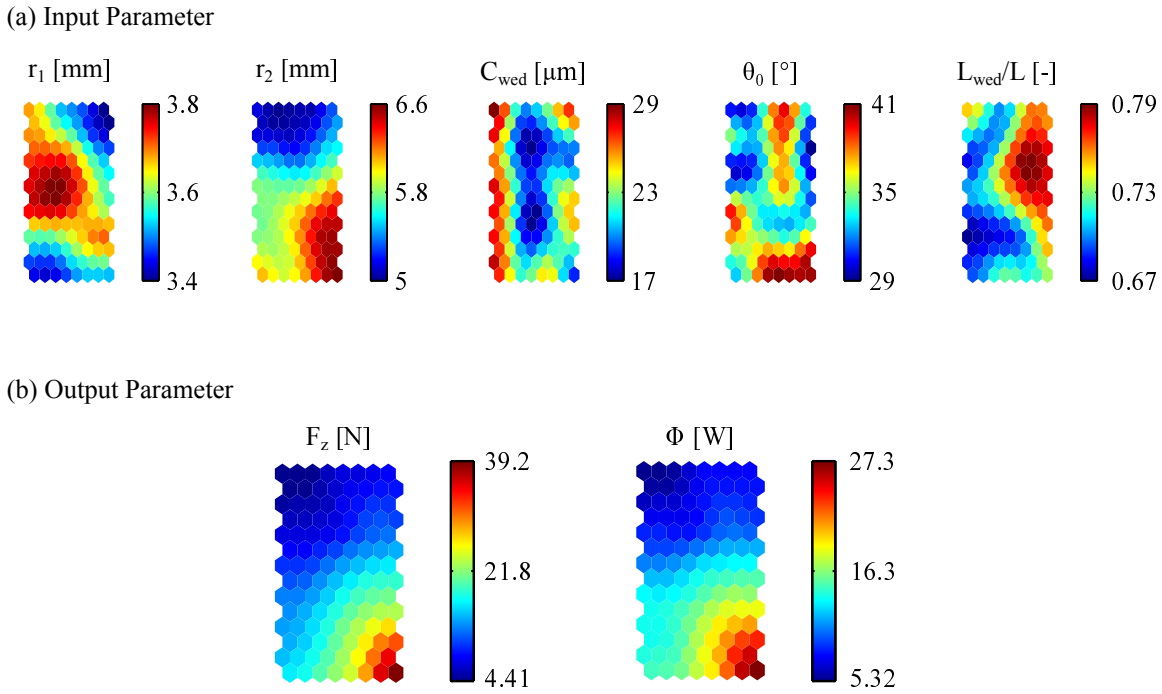

Figure 5.7: Self-organizing maps of a stationary optimization for one thrust bearing pad

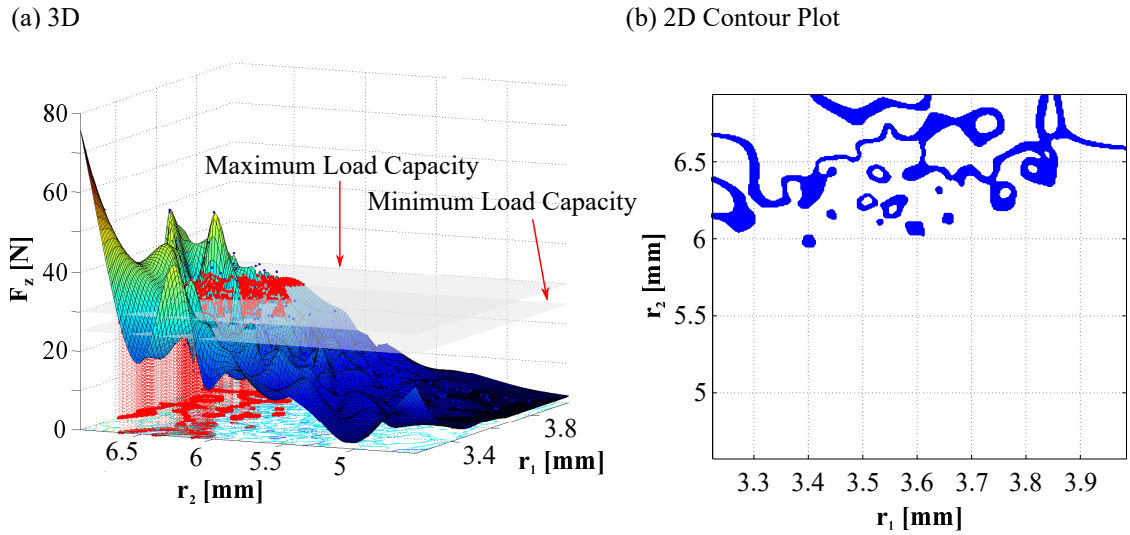

Figure 5.8: Response surface of the thrust bearing load capacity F_z with respect to the inner r_1 and the outer r_2 radius

is illustrated. The shaded area depicts the values with load capacity between 25 and 30 N. Therefore, it becomes also obvious here that for the optimization the largest possible values for the outer radius should be chosen.

An important aspect for the thrust bearing optimization is the taper height. In Figure 5.10 the response surface for the taper height, the friction losses and the load capacity of a thrust bearing pad is shown. The shaded area also here depicts the values with load capacity between 25 and 30 N. It is observed that various values of

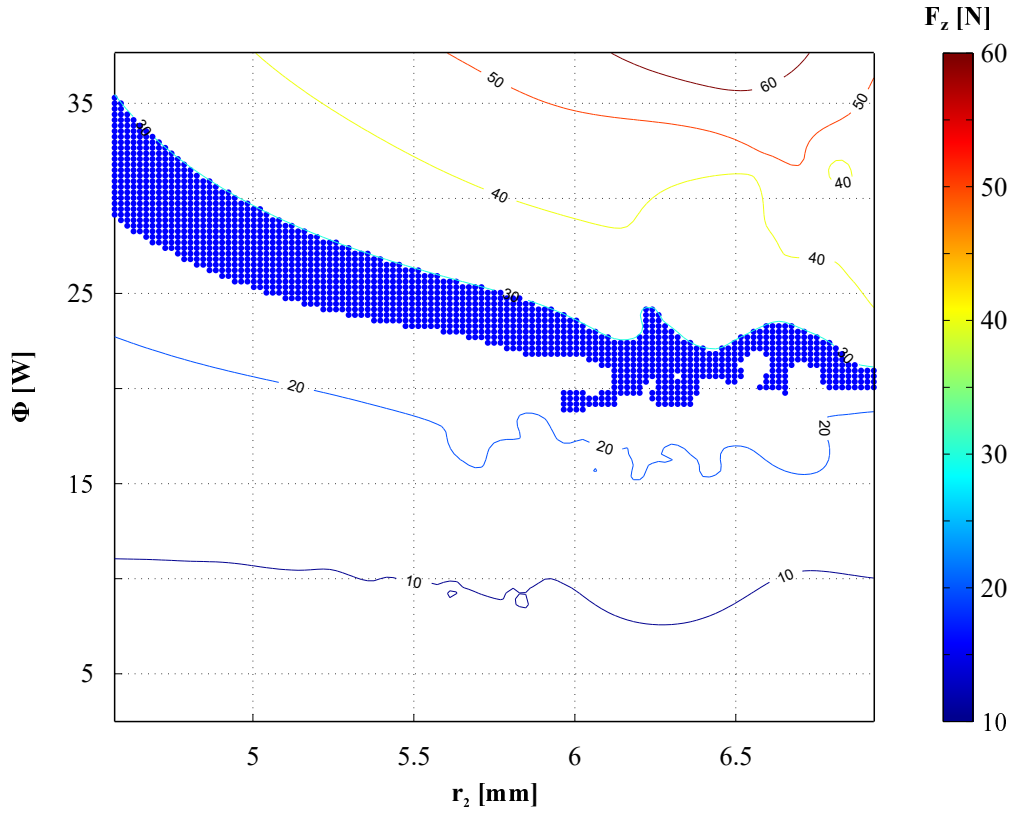

Figure 5.9: Response surface of the thrust bearing load capacity F_z with respect to the outer radius r_2 and the friction losses Φ

the taper height C_{wed} may be used to deliver the desirable load capacity. For larger load capacities, i.e. 50 or 60 N small values of C_{wed} should be used as shown in Fig. 5.10.

5.3 Optimization in Transient Operations

In this section, the stationary optimization procedure is extended to account for the transient operations of the turbocharger rotor. The thrust bearing exerts two moments to the rotor, namely M_x and M_y. These moments influence the subsynchronous vibration as explained in Chapter 4. For the optimization procedure, the same parameters for the Reynolds equation are used as in Table 5.3, except for the first and the second Bryant angle as well as the minimum film thickness. In this case, α=2 mrad, β=0 mrad and h_0=10 μm. The input space for the optimization is the same as in Table 5.4.

Figure 5.11 shows the Pearson coefficients used for a thrust bearing with five pads. It is observed that the outer radius r_2 has also a large influence on the thrust bearing moments M_x and M_y. The sign of the linear correlation, positive or negative, regarding the thrust bearing moments depends on the inclination angles of the rotor (α and β)

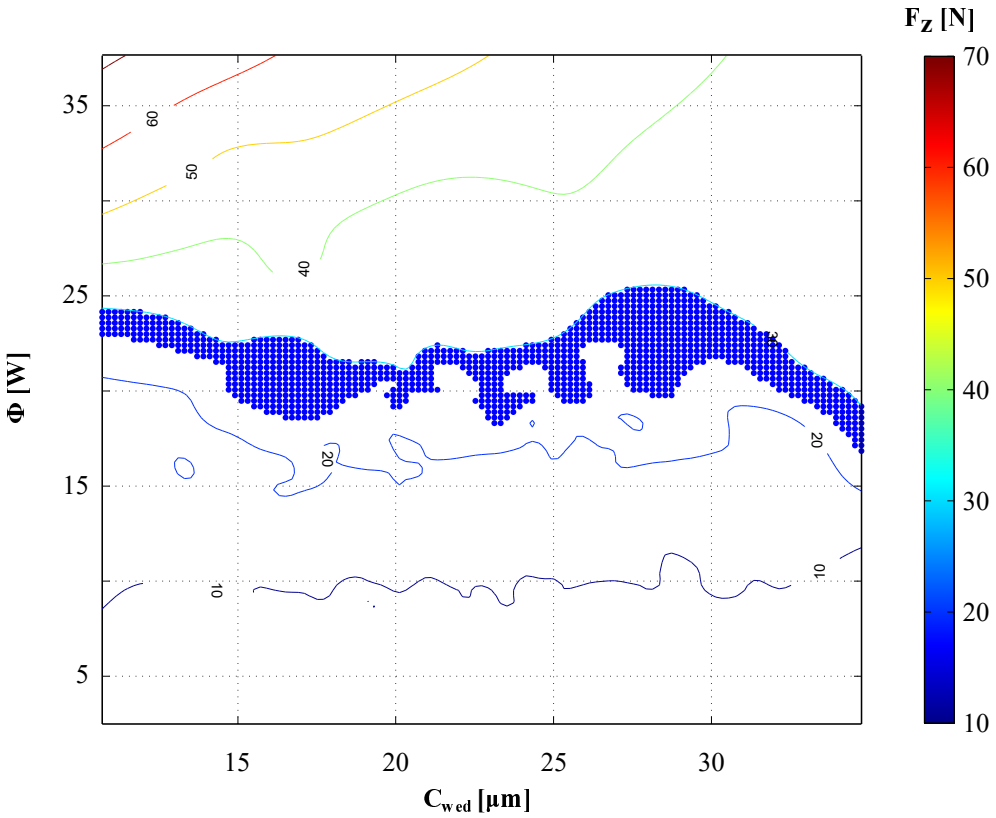

Figure 5.10: Response surface of the thrust bearing load capacity F_z with respect to the taper height C_{wed} and the friction losses Φ

as well as the positioning of the pads on the thrust bearing.

In Figure 5.12 the global sensitivity analysis for the thrust bearing in a bar and in a pie chart is illustrated. The largest influence on the output space is exerted by the outer radius r_2 and angular extent θ_0.

In Figure 5.13, the Self-organizing maps for a transient optimization of a five-pad thrust bearing are shown. The influence of the input space parameter on the thrust bearing moments is similar to the influence on the load capacity and friction losses.

Figure 5.14 shows the response surface of the thrust bearing load capacity F_z as a function of the outer radius r_2 and the thrust bearing moments M_x and M_y. The shaded area depicts the values with load capacity between 50 and 60 N.

In Figure 5.15, the response surface of the friction losses Φ with respect to the load capacity F_z and the thrust bearing moment M_x is illustrated.

Table 5.6 presents three thrust bearing configurations that will be examined in transient simulations. In the configurations shown in Table 5.6, **Case 1** and **Case 2** have almost identical load capacity and very similar friction losses. The second configuration (**Case 2**) has a larger M_x in comparison with the first (**Case 1**) by more than 16%. **Case 3** has larger friction losses than **Case 2** but its M_x is lower. As the higher thrust bearing moments may suppress the subsynchronous vibrations, transient sim-

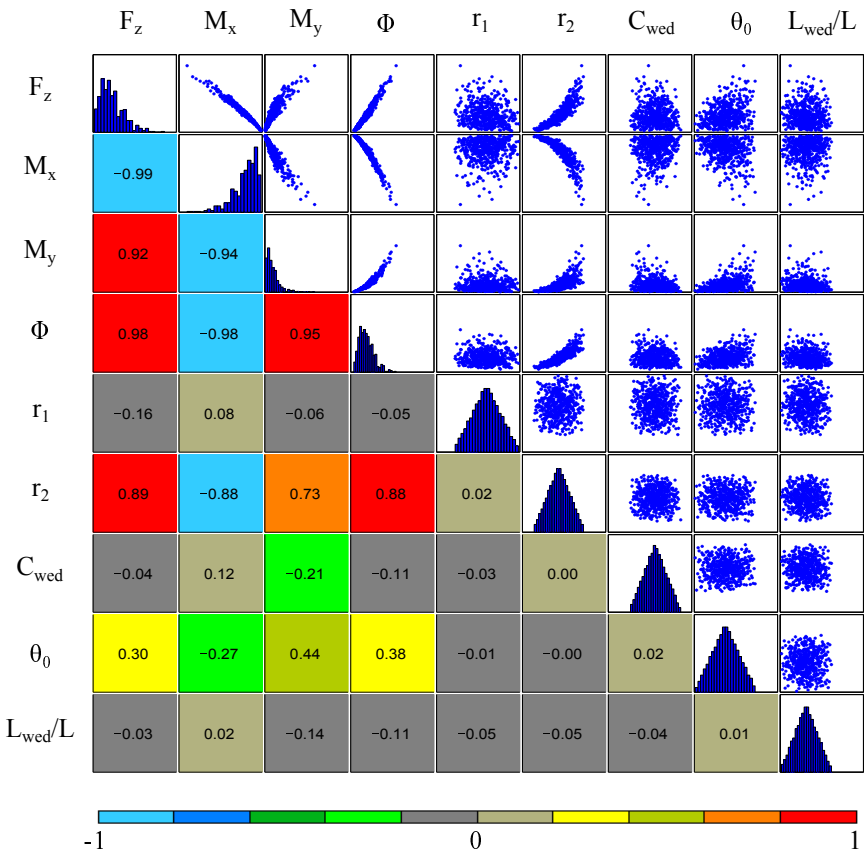

Figure 5.11: Pearson coefficients for a five-pad thrust bearing

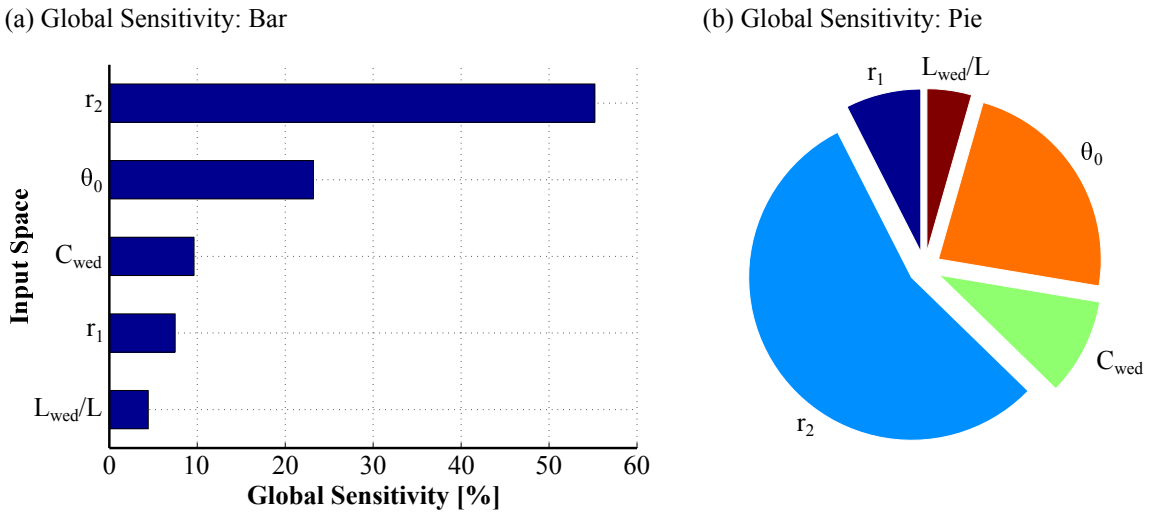

Figure 5.12: Sensitivity analysis for a five-pad thrust bearing: (a) bar chart, (b) pie chart

ulations are performed for illustrating that configurations with similar load capacity and friction losses can exhibit significant differences if their moments are not similar. Therefore, extending the stationary optimization procedure (load capacity and friction losses), a better overall performance can be achieved by selecting configurations

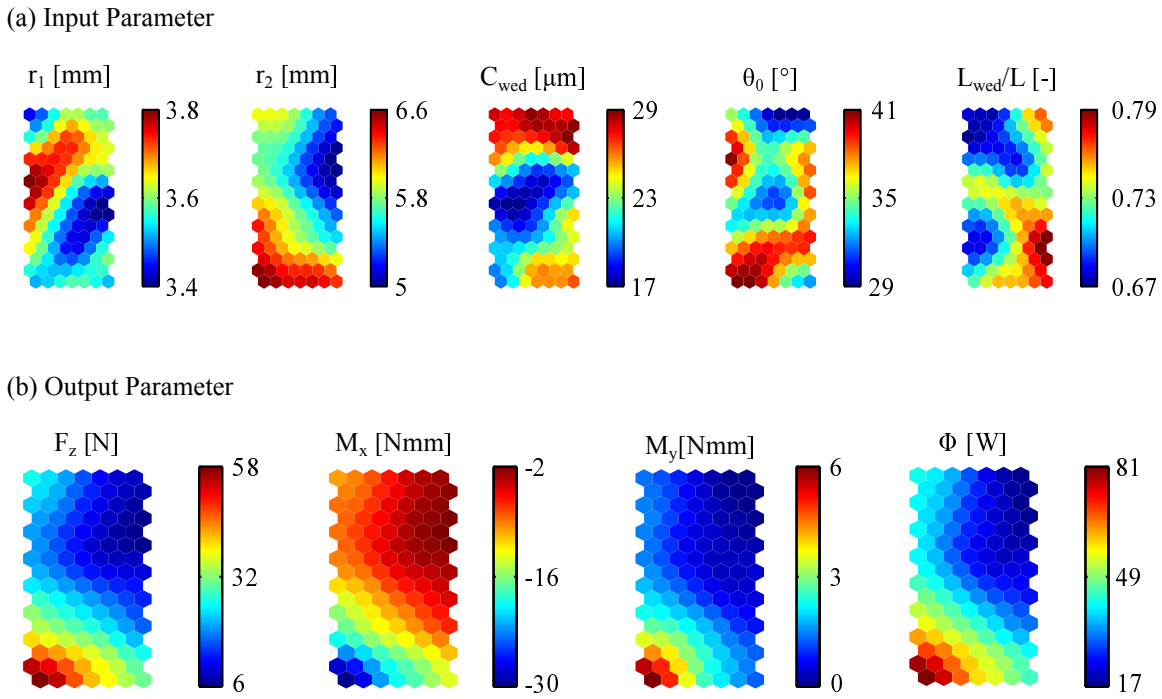

Figure 5.13: Self-Organizing maps of a transient optimization for one thrust bearing pad

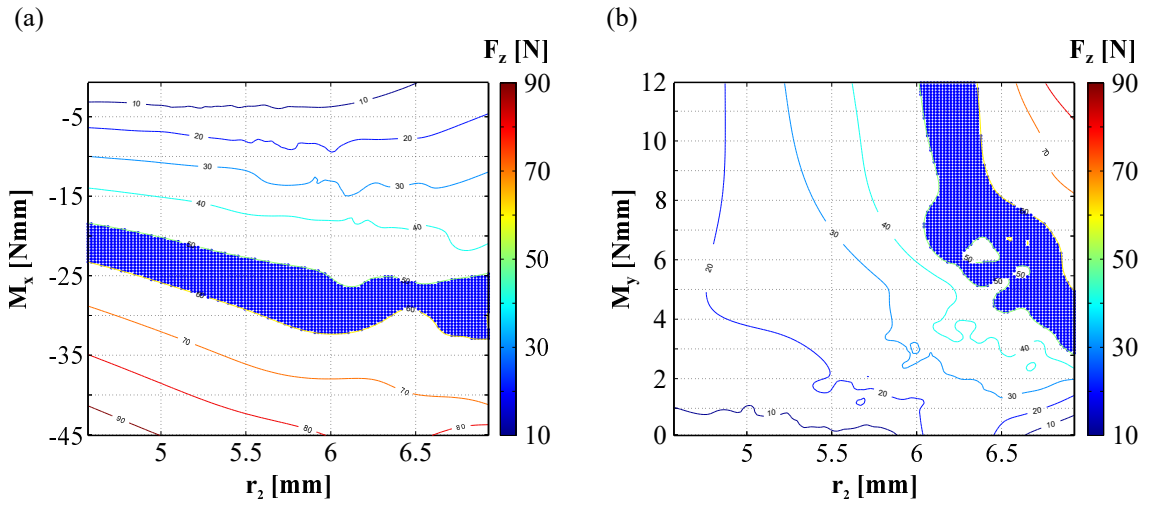

Figure 5.14: Response surface of the thrust bearing load capacity F_z with respect to (a) the outer radius r_2 and the moment M_x, (b) the outer radius r_2 and the moment M_y

with higher thrust bearing moments.

In Figure 5.16, the compressor wheel vibrations in the vertical direction of the three cases described in Table 5.6 are illustrated. The external axial load is F_{axial}=100 N. In these simulations, only the third subsynchronous vibration appears, i.e. the *sub 3*. **Case 2** has the largest thrust bearing moment M_x and the onset point of its *sub 3* is found in a higher rotational speed in comparison with the other cases. Additionally,

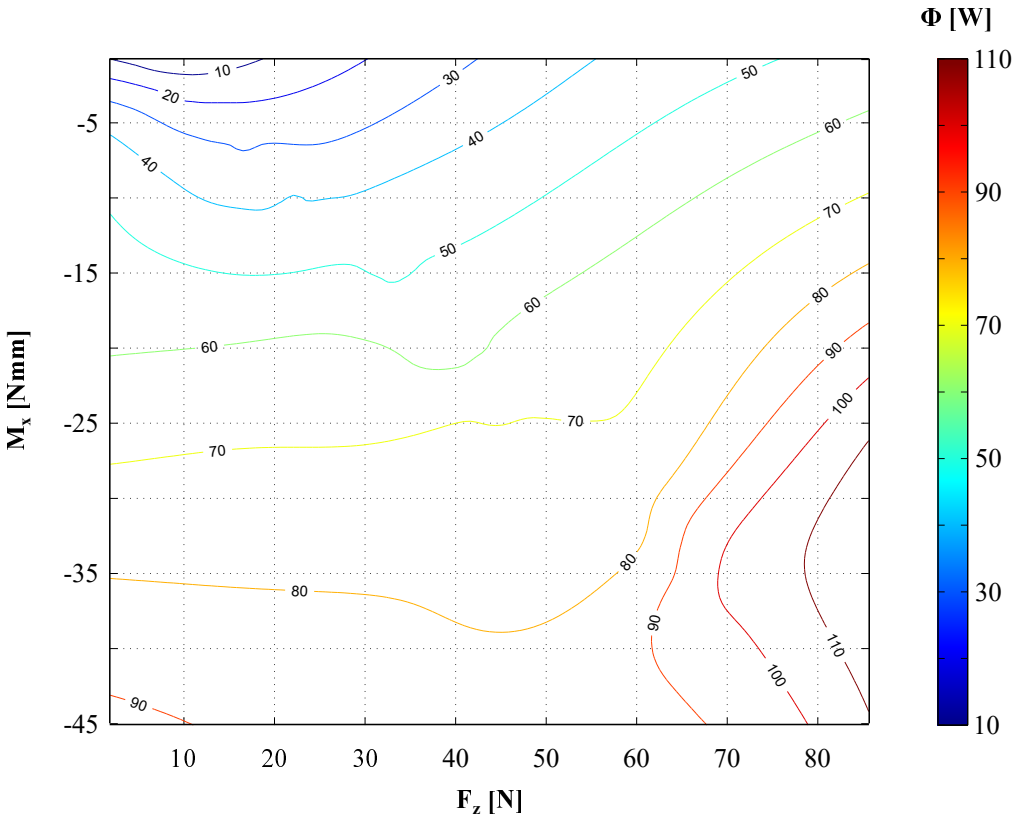

Figure 5.15: Response surface of the thrust bearing friction losses Φ with respect to the load capacity F_z and the moment M_x

Table 5.6: Input and output space of the three bearing configurations for the transient optimization

	r_1 [mm]	r_2 [mm]	θ_0 [°]	C_{wed} [μm]	L_{wed}/L [-]	F_z [N]	M_x [Nmm]	M_y [Nmm]	Φ [W]
Case 1	3.5	6.6	44.9	25	0.71	63.4	-30	7	83.6
Case 2	3.6	6.6	38.1	17	0.71	63.3	-35	7	86.3
Case 3	3.4	6.6	45.8	23	0.64	65.7	-32	9	91.1

lower amplitudes can be observed for this case.

In Figure 5.17, the friction losses in the thrust bearing for the three cases described in Table 5.6 are illustrated. All simulated cases exhibit similar friction losses.

For testing the robustness of the optimization procedure, two different external loads will also be considered, i.e. F_{axial}=150 N and F_{axial}=50 N. It should be noted here that although the optimum bearing solution found cannot be guaranteed for all possible external loads, the optimization procedure seems to hold for all the tested cases.

In Figure 5.18, the compressor wheel vibrations in the vertical direction for the three cases described in Table 5.6 under F_{axial}=150 N are illustrated. As in the case of

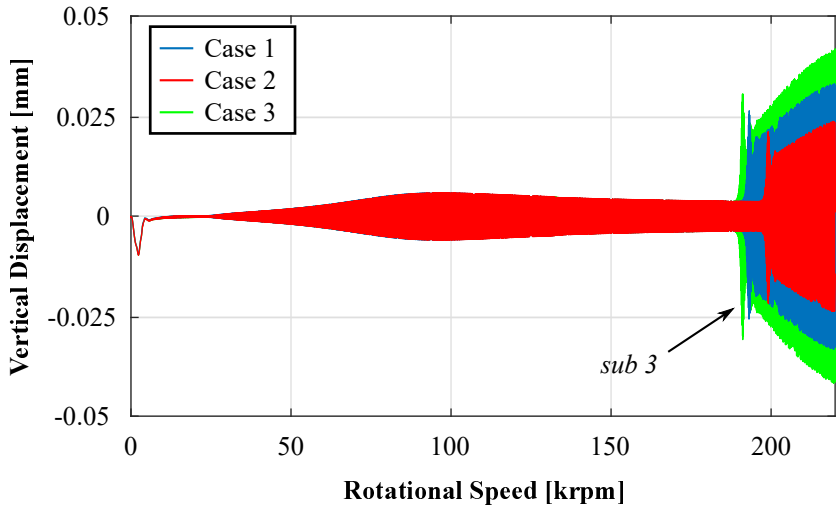

Figure 5.16: Compressor wheel vibrations in the vertical direction for the cases described in Table 5.6 using F_{axial}=100 N

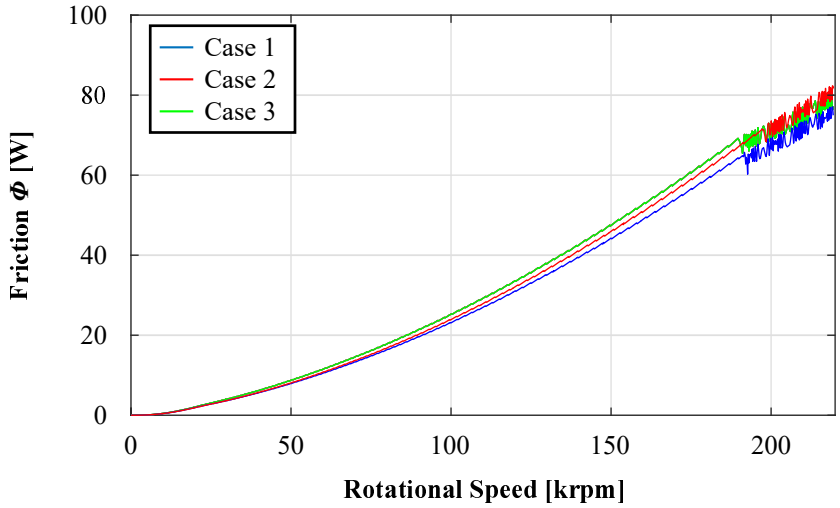

Figure 5.17: Friction losses for one thrust bearing pad for the cases described in Table 5.6

F_{axial}=100 N the best performance is exhibited by the thrust bearing with the highest moment.

With F_{axial}=50 N, the compressor wheel vibrations in the vertical direction for the three cases described in Table 5.6 are illustrated in Figure 5.19. The same pattern for the *sub 3* can be also noted here, however, the effect is not so prominent. The higher external axial loads have suppressed the first subsynchronous vibration *sub 1*. Using a lower axial load F_{axial}=50 N, the *sub 1* appears in the compressor wheel vibration and the same effect as in the *sub 3* is observed. The optimized thrust bearing geometry has affected both subsynchronous vibrations.

Investigating further the transient optimization of thrust bearings, a bearing with a larger inner radius as well as a larger outer radius is selected. The minimum and the

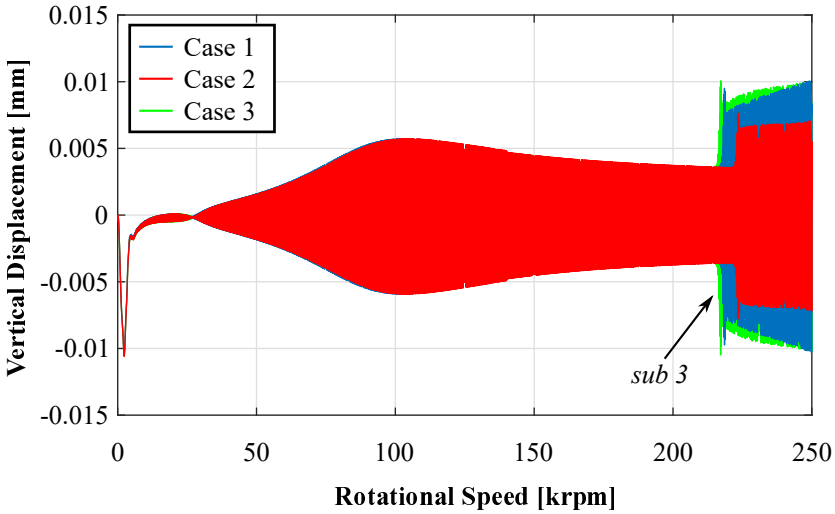

Figure 5.18: Compressor wheel vibrations in the vertical direction for the cases described in Table 5.6 using F_{axial}=150 N

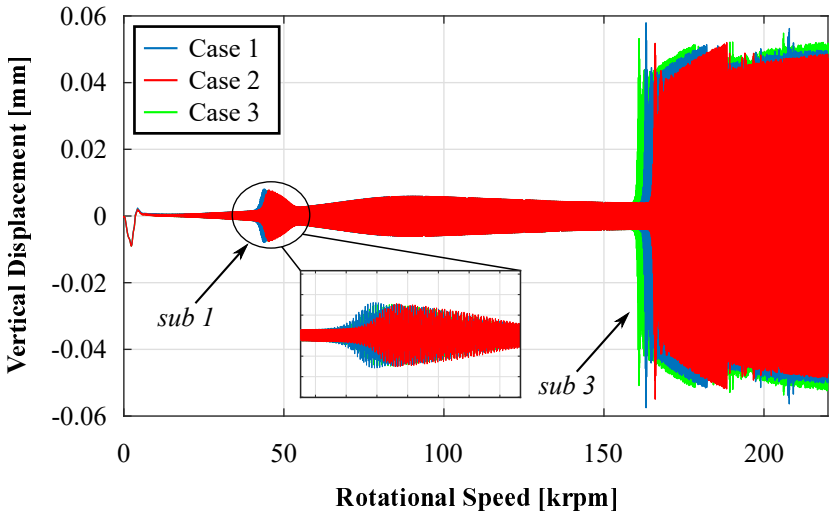

Figure 5.19: Compressor wheel vibrations in the vertical direction for the cases described in Table 5.6 using F_{axial}=50 N

maximum values of the input parameters are given in Table 5.7.

In Figure 5.20, the response surface of the friction losses Φ with respect to the load capacity F_z and the thrust bearing moment M_x is illustrated. For the solution of the Reynolds equation the same parameters as in Table 5.3 will be used, however, in this case the viscosity of the oil is μ=9.788 mPas, the minimum film thickness is h_0=5 μm and the first and second Bryant angles are α=2 mrad and β=1 mrad.

Table 5.8 presents the three larger thrust bearing configurations that will be examined in transient simulations. In the configurations shown in Table 5.8, **Case 4**, **Case 5** and **Case 6** have almost identical load capacity and very similar friction losses. However, **Case 4** presents the higher moment M_x. It is therefore expected that the amplitude of the subsynchronous vibrations in **Case 4** will be lower than those of

Table 5.7: Geometrical parameters for the transient optimization using the thrust bearing with the larger inner and outer radius

Parameter	Value		Unit
	min	max	
r_1	0.0038	0.005	m
r_2	0.006	0.008	m
θ_0	20	45	°
L_{wed}/L	0.6	0.85	-
C_{wed}	10	35	μm

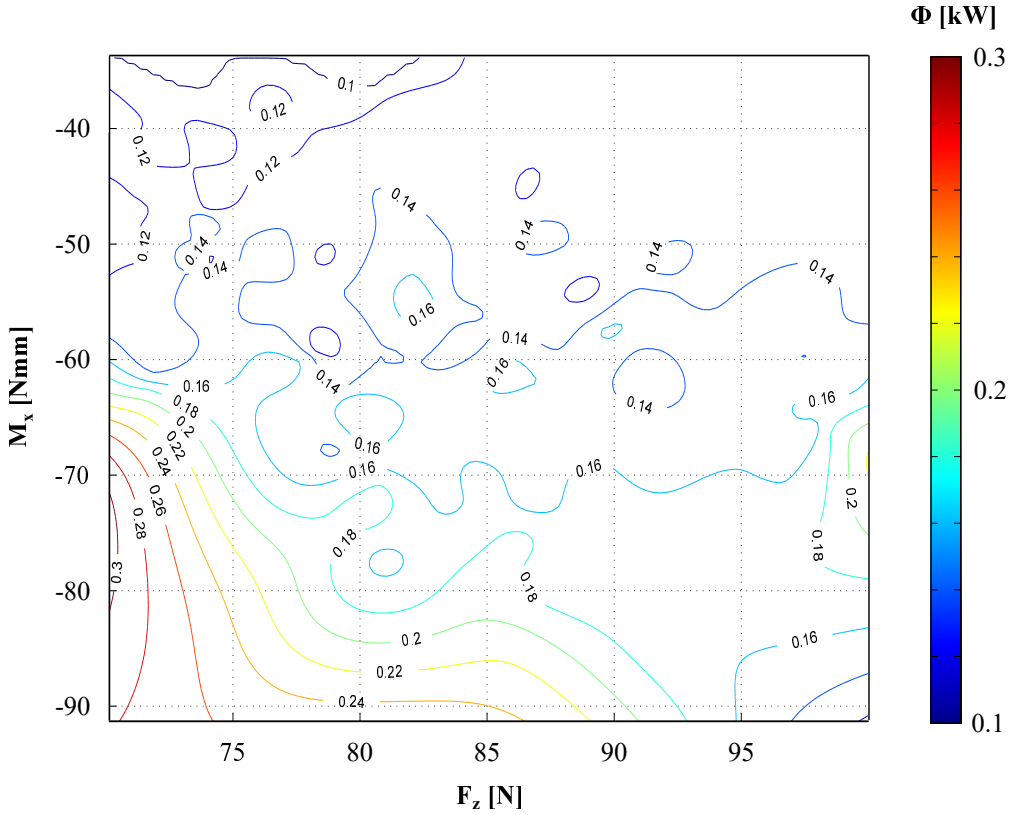

Figure 5.20: Response surface of the thrust bearing friction losses Φ with respect to the load capacity F_z and the moment M_x for the pads with higher inner and outer radius

Case 5 and **Case 6**.

In Figure 5.21, the compressor wheel vibrations in the vertical direction for the three cases described in Table 5.8 are illustrated. The external axial load is F_{axial}=100 N. Here, the same results can also be observed, namely, the higher the thrust bearing moment, the lower the amplitudes of the subsynchronous vibrations. Moreover, the subsynchronous vibrations appear in higher rotational speeds with increasing mo-

Table 5.8: Input and output space of the three bearing configurations with the larger inner and outer radius for the transient optimization

	r_1 [mm]	r_2 [mm]	θ_0 [°]	C_{wed} [μm]	L_{wed}/L [-]	F_z [N]	M_x [Nmm]	M_y [Nmm]	Φ [W]
Case 4	4.34	7.98	23.3	16	0.77	80.27	-68	24	141
Case 5	4.15	7.18	34.41	16	0.65	80.83	-60	15	142
Case 6	3.91	7.01	36.5	24	0.62	80.31	-50	13	138

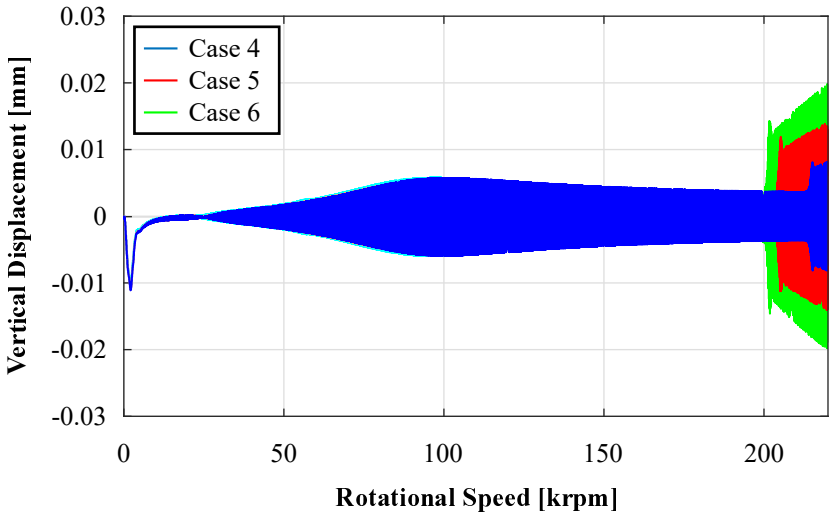

Figure 5.21: Compressor wheel vibrations in the vertical direction for the cases described in Table 5.8 using F_{axial}=100 N

ments.

In this section, it was shown that the stationary optimization of thrust bearings regarding their load capacity and their friction losses can be further extended to improve the overall vibration behavior of turbocharger rotors. This can be succeeded by considering in the optimization procedure also the thrust bearing moments.

Chapter 6

Experimental Validation

In this section, the experimental validation of the radial and the thrust bearing modeling will be performed. A standard shaft-motion test will be presented for the validation of the radial bearing modeling. For the thrust bearing modeling, an appropriate experimental device was utilized and tests were performed using a constant rotor speed.

6.1 Radial Bearings

The basic parameters of the turbocharger rotor/bearing system are summarized in Table 6.1.

Table 6.1: Parameters of the turbocharger rotor/bearing system for the shaft motion tests

Parameter	Value	Unit
Rotor mass	≈ 0.1	kg
Rotor length	≈ 0.1	m
Turbine wheel unbalance	$\approx 2 \times 0.05$ at $0°$	gmm
Compressor wheel unbalance	$\approx 2 \times 0.02$ at $0°$	gmm
L_i/D_i	0.56	-
L_o/D_o	0.45	-
T_s	100	°C
p_s	4	bar

The length and the diameter of the inner/outer bearing are denoted by L_i/L_o and D_i/D_o. The oil-supply pressure is p_s and the oil-supply temperature is T_s.

In Figure 6.1 the spectrogram of the vibrations at the measuring point (shaft nut at compressor-side) in the vertical y-direction is shown both for the experimental as well as the numerical results. Together with low amplitude synchronous vibrations due to imbalance, the first (*sub 1*), the second (*sub 2*) and the third (*sub 3*) subsynchronous vibrations are observed. The *sub 3* dominate the vibration spectrum both in the

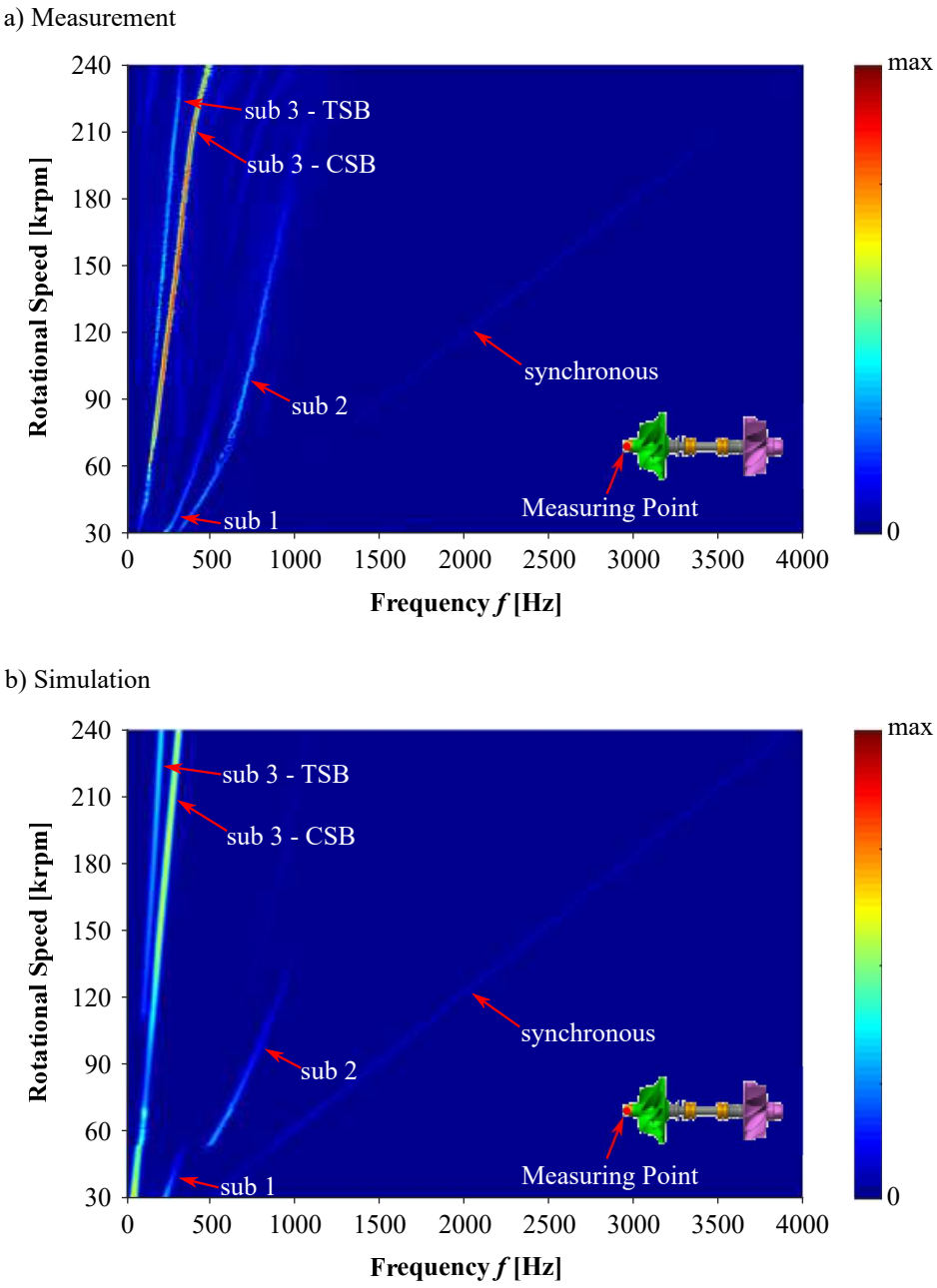

Figure 6.1: Spectrogram of the vibrations at the measuring point: (a) measurement, (b) simulation

measurement and the simulation results. Two *sub 3* frequencies are observed, one from the compressor-side bearing (CSB) and the other from the turbine-side bearing (TSB). The predicted amplitudes and frequencies of the *sub 3* are slightly lower in comparison with the experimental results.

In Figure 6.2, the spectrogram of the vibrations at the turbine wheel in the vertical y-direction is presented. It can be observed that at the turbine wheel the turbine-side *sub 3* has higher amplitudes than the compressor-side *sub 3*. On the contrary, the vibrations at the measuring point (shaft nut at the compressor-side) show that the

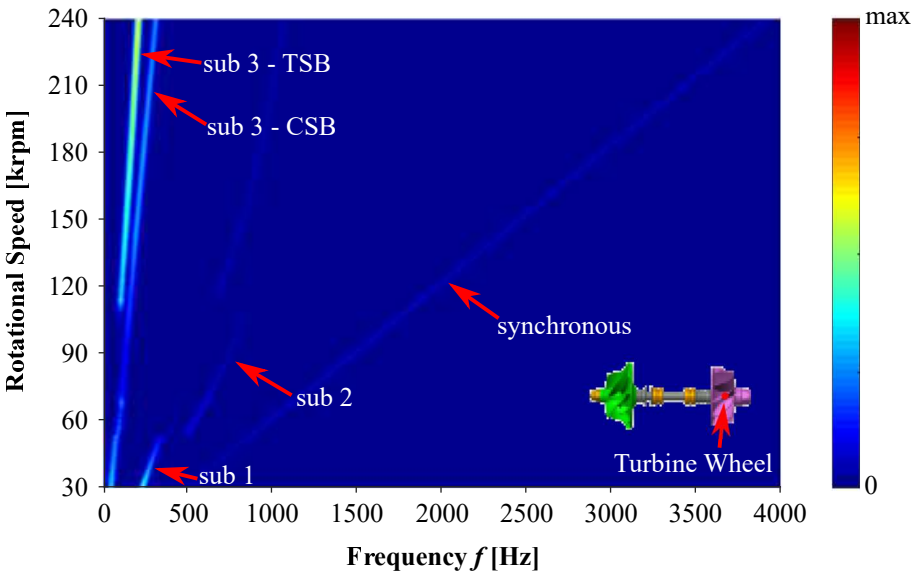

Figure 6.2: Spectrogram of the vibrations at the turbine wheel

turbine-side *sub 3* has lower amplitudes than that of the compressor-side.

In Figure 6.3, the dominant vibration frequencies at the measuring point and the rotational speed of the floating rings are depicted.

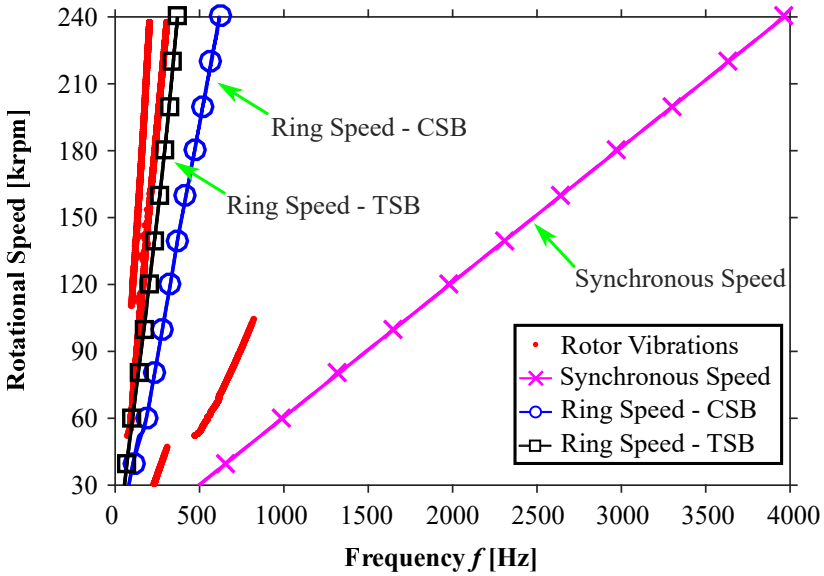

Figure 6.3: Vibration at the measuring point and rotational speed of rings

In Figure 6.4, the oil-temperature increase in the oil-film of the compressor and the turbine-side bearings as well as the percentage of the bearing clearances change are illustrated. The oil-temperature increase in the outer oil-film at the end of the run-up is rather small ($T_o = 107\,°\mathrm{C}$). This is due to the fact that the oil-temperature in the outer oil-film is highly influenced by the inlet oil-temperature ($T_s = 100\,°\mathrm{C}$). On the contrary, the oil-temperature increase in the inner oil-film depends highly on the

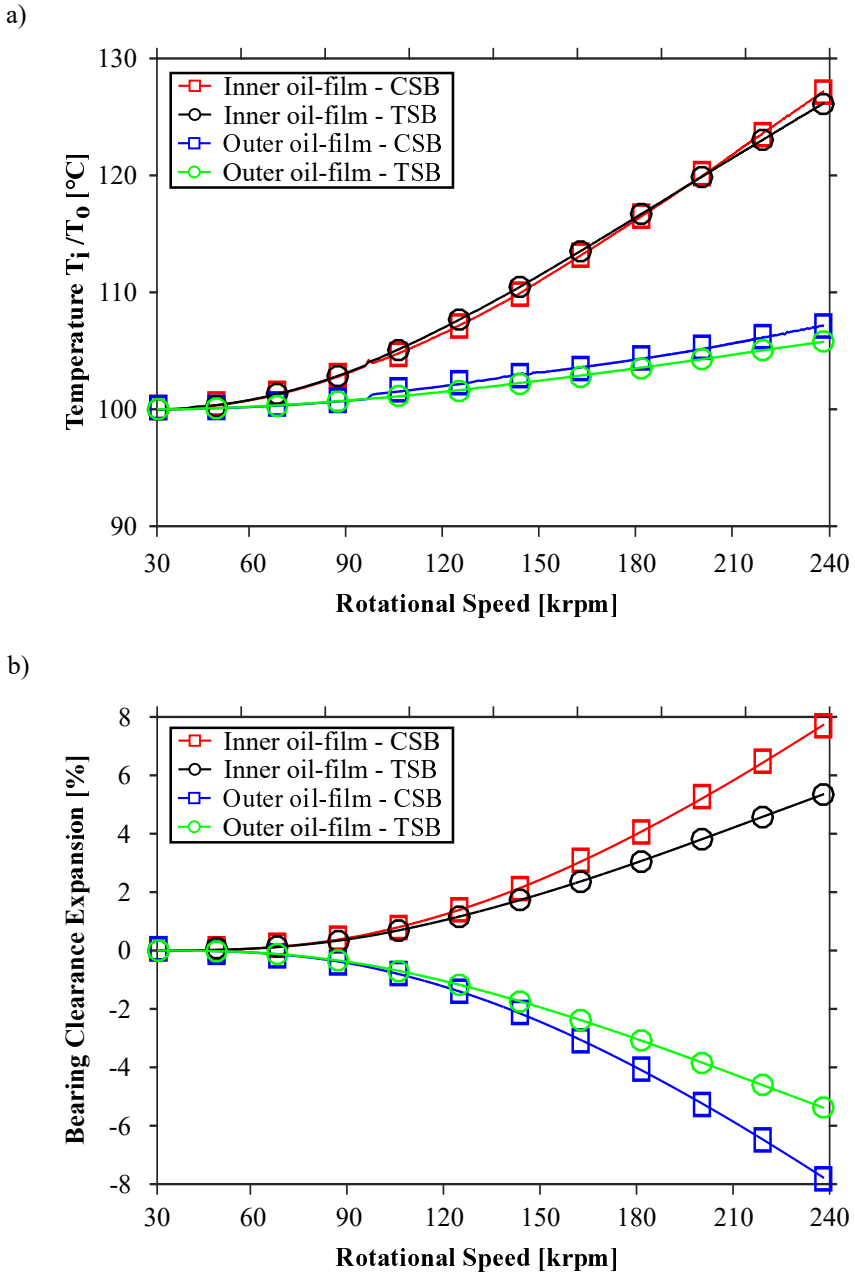

Figure 6.4: (a) Temperature and (b) percentage of radial bearing clearance change for the inner and the outer oil-film

bearing clearance and the relative bearing eccentricity. As the inner bearing clearance is rather small, the temperature in the inner oil-film at the end of the run-up is almost $T_i = 126\,°\mathrm{C}$. Additionally, the relative bearing eccentricity of the inner oil-film is rather low, leading to low axial flow and low convected thermal energy. Therefore, more thermal energy is accumulated in the oil-film. The radial bearing clearance of the inner oil-film at the compressor-side bearing has increased almost 7.7% at the end of the run-up due to the temperature rise of the floating ring. At the outer-gap, the respective decrease is almost 7.8%. Similarly for the turbine-side bearing, the change in the clearances is almost 5.4%.

6.2 Thrust Bearings

The experiment is conducted with a standard series turbocharger core group using the device shown in Fig. 6.5. It consists of the control unit and the experimental set-up.

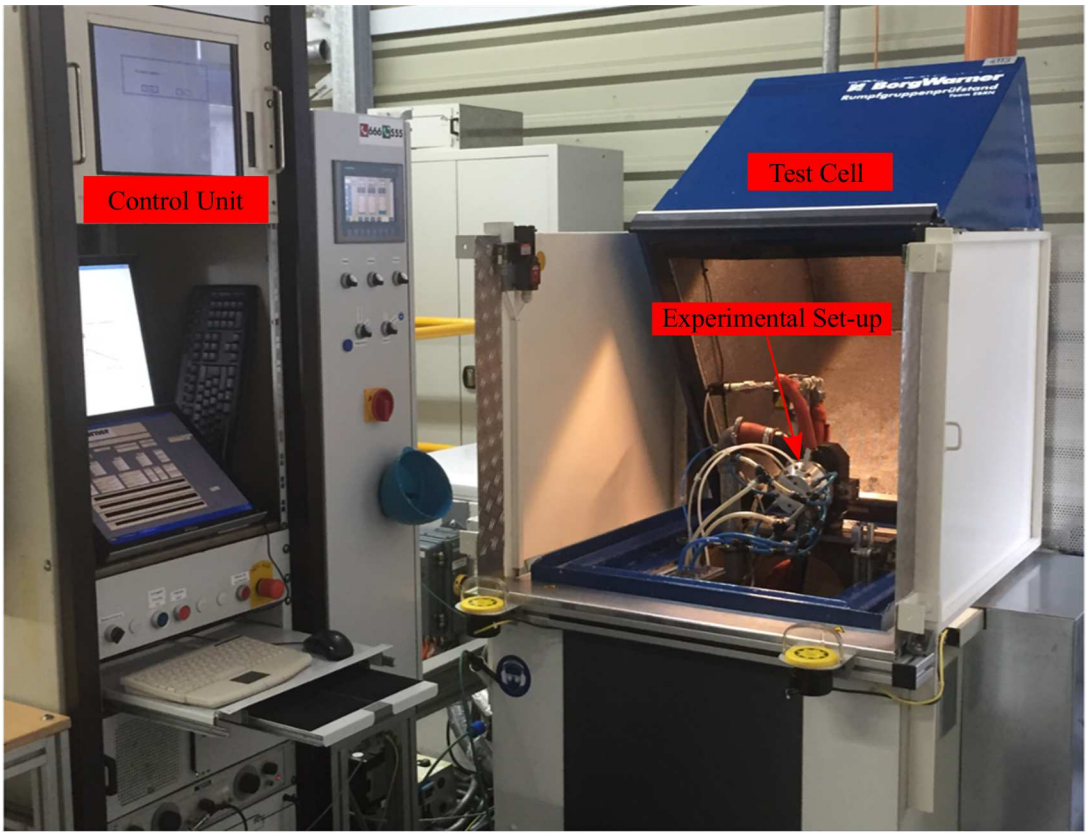

Figure 6.5: Experimental device

The latter is encapsulated in a test cell.

The specifications of the experimental set-up are summarized in Table 6.2. In general, the thrust force depends on the wheel size. In this case, the thrust force is variable, attaining a maximum value of almost 90 N. The oil-temperature can be set down to -20 °C for cold start experiments, whereas in this experiment the oil-temperature was 90 °C.
Single part unbalances and high-speed unbalances have been determined experimentally (see Table 6.3) by a shaft motion test. The experimental set-up and the respective CAD model, which consists of a turbine housing, the core assembly and the compressor chamber, can be seen in Fig. 6.6. The compressor-side is slightly modified from the series design, since the thrust load for displacing the shaft in the axial direction is implemented at this side. The compressor wheel is replaced by a special disc keeping almost identical mass properties compared with the original compressor wheel.

The modified compressor wheel is operating in a closed housing with two pressure chambers on both sides of the wheel (see Fig. 6.6). Various thrust loads can be ap-

Table 6.2: Specifications of the experimental set-up

Test Rig Data		Unit	Minimum	Maximum	Current Test
Turbine	Air Pressure	bar	6	6	6
	Air Temperature	°C	21	21	21
	Air Mass Flow	g/s	0	260	Variable
	Rotor Speed	rpm	0	220000	120000
Oil Supply	Oil Pressure	bar	0	8	2
	Oil Temperature	°C	20 (-20)	130	90
	Oil Flow Rate	l/min	0	17	Variable
	Oil Type	-	Any type	Any type	5W30
Thrust Load	Thrust Direction	-	TS	CS	Both
	Thrust Force	N	200	180	Variable
Controls		-	-	-	Speed

plied in each chamber over the programmable logic controller (PLC) unit. Since the effective thrust load in each operation point is affected by several factors, it is necessary to create a calibration curve, where the pressures in both chambers are regulated for the maximum tested thrust load. Mixed lubrication conditions have to be avoided in this experiment and therefore, the maximum thrust load is regulated to almost 80% of the load capacity of the thrust bearing.
During the test drive, power is applied to the master turbine housing by pressurized cold air, where the mass flow is controlled over the integrated PLC steering unit. It is important to drive the core group with a constant rotor speed ω_S during the whole axial displacement of the shaft from the maximum turbine-side position to the maximum compressor-side position. The inlet oil-temperature (T_{oil}) and the inlet oil-pressure (P_{oil}) are controlled by the PLC steering unit and they remain constant (see Table 6.2). During the experiment, the rotor is displaced in the axial direction from turbine-side to compressor-side with the same maximum thrust load on each side $\pm 90\,\mathrm{N}$. The lateral displacement on a special shaft motion nut and the acceleration of the system with a triaxial sensor on the bearing housing are measured. The displacement sensor at the shaft nut can be seen in Fig. 6.7.

The thrust bearing used in the experimental investigations can be seen in Fig. 6.8. The inner and outer radius of the thrust bearing pads are termed by r_i and r_o, respectively. The angular extent of the pads is θ_0.

The details for the turbocharger rotor/bearing model used in the simulation are col-

(a) Experimental Set-up

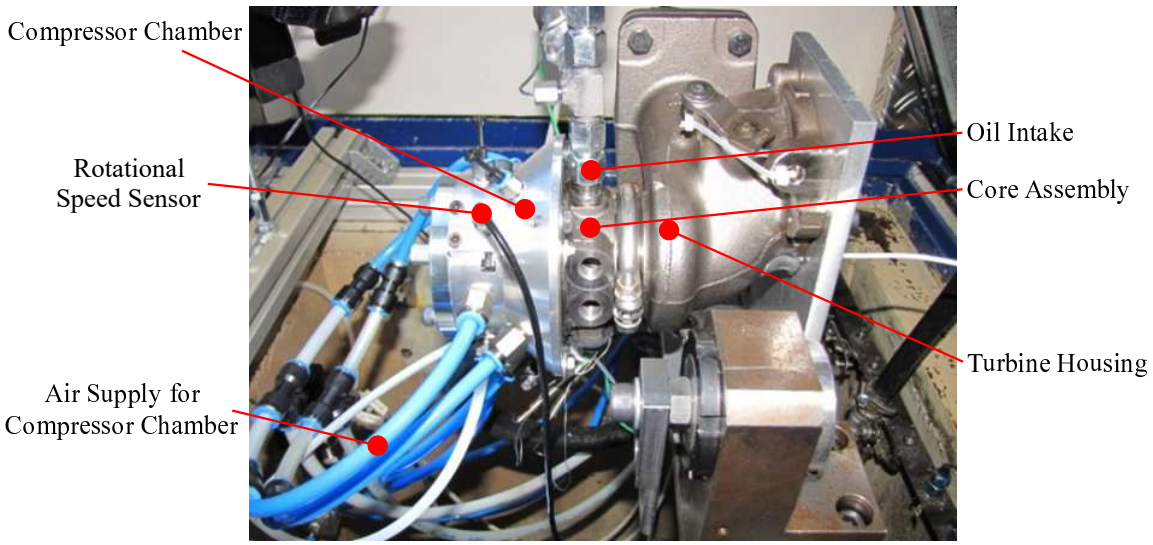

(b) CAD Model

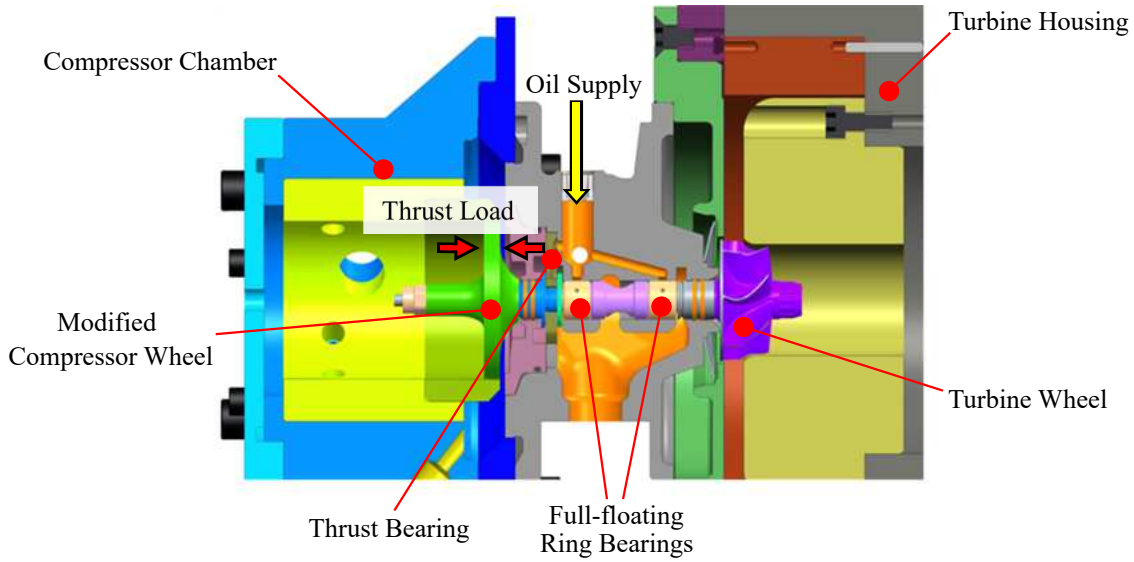

Figure 6.6: (a) Experimental set-up, (b) CAD model

lected in Table 6.3. The lengths of the radial bearings in the inner/outer oil-films are described by L_i/L_o and their diameters by D_i/D_o. Figure 6.9 illustrates the thrust bearing with the compressor-side and the turbine-side thrust ring.

Figures 6.10a and Fig. 6.10b show the time-frequency analysis (Short Time Fourier Transform) for the measured and the simulated rotor vibrations. Instead of time, the axial displacement of the rotor is presented in the x-axis. Additionally, the amplitudes of the measured and the simulated subsynchronous vibrations are depicted in Fig. 6.10c. During the experiment, the rotor is displaced from the turbine side to the compressor side and therefore, three operating points will be considered.

- **Operating Point 1:** The rotor is displaced in the axial z-direction towards

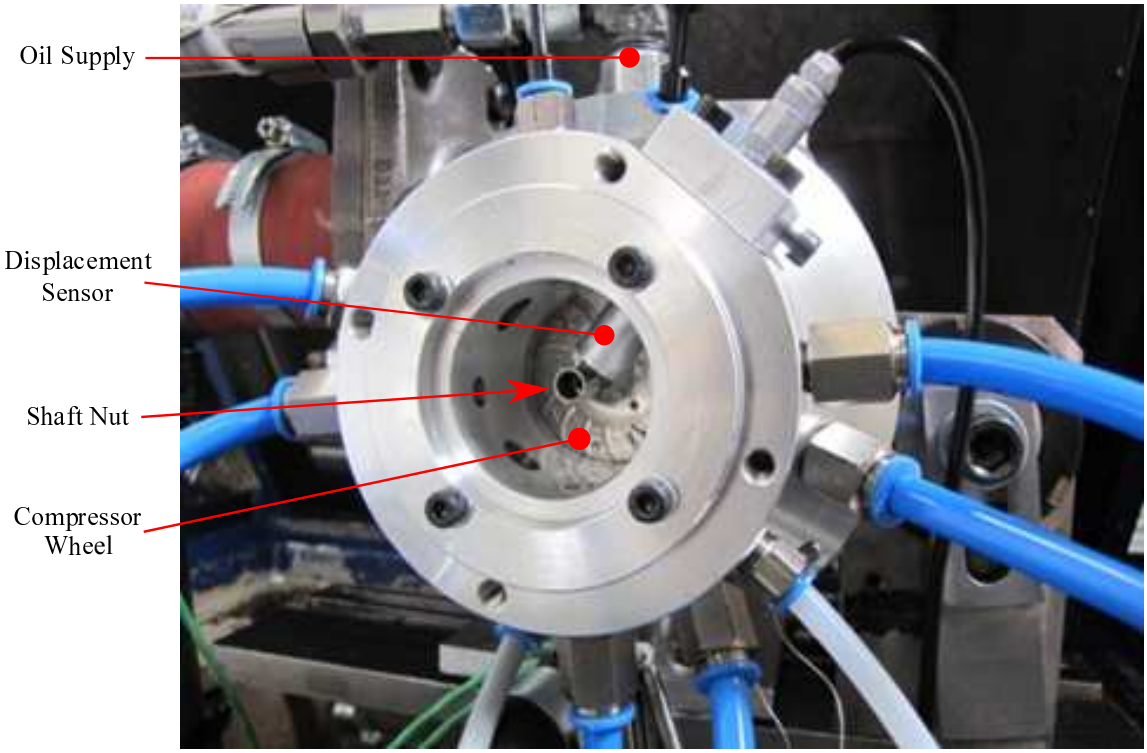

Figure 6.7: Vibration measuring point (shaft nut)

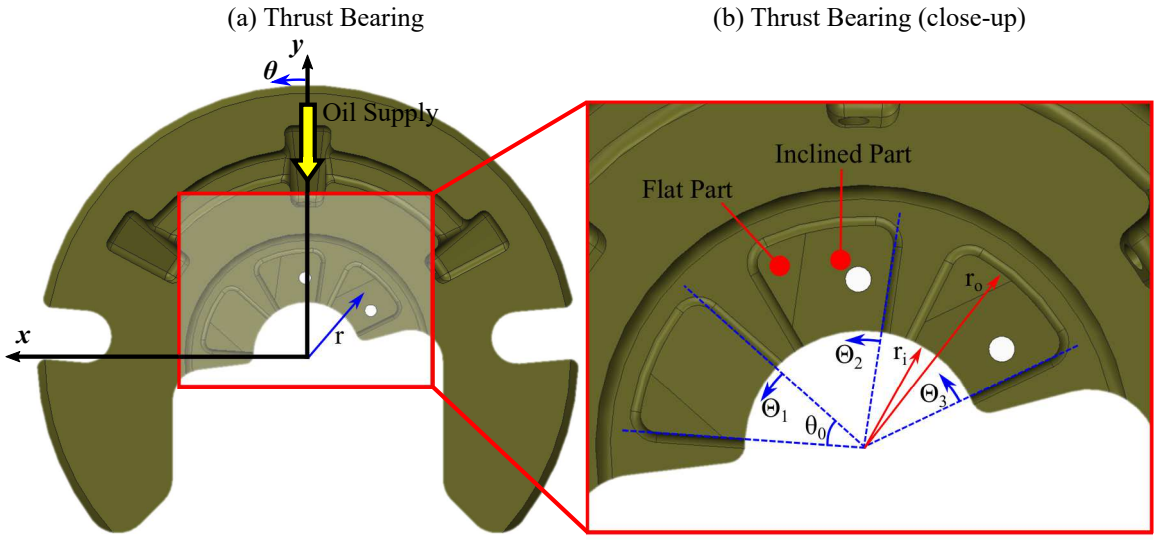

Figure 6.8: Double-sided thrust bearing with 3 pads

the turbine wheel ($z = -40\,\mu m$). The oil-film thickness between the thrust bearing and the compressor-side thrust ring is minimum $h_{\mathrm{CR}} \approx 3\,\mu m$. The respective oil-film thickness between the thrust bearing and the turbine-side thrust ring is $h_{\mathrm{TR}} \approx 85\,\mu m$ making this side of the thrust bearing almost inactive. The subsynchronous vibrations *sub 2* and *sub 3* produced from the full-floating ring bearings are identified with very low amplitudes, 0.016 mm for *sub 2* and 0.032 mm for *sub 3*. Additionally, the synchronous vibration due to unbalance

Table 6.3: Parameters of the turbocharger rotor/bearing system

Parameter	Value	Unit
Rotor mass	≈ 0.1	kg
Rotor length	≈ 0.1	m
Turbine wheel unbalance	$\approx 2 \times 0.03$ at $0°$	gmm
Compressor wheel unbalance	$\approx 2 \times 0.03$ at $0°$	gmm
Shaft nut unbalance	≈ 0.05 at $0°$	gmm
L_i/D_i	0.59	-
L_o/D_o	0.67	-
Number of thrust bearing pads	3	-

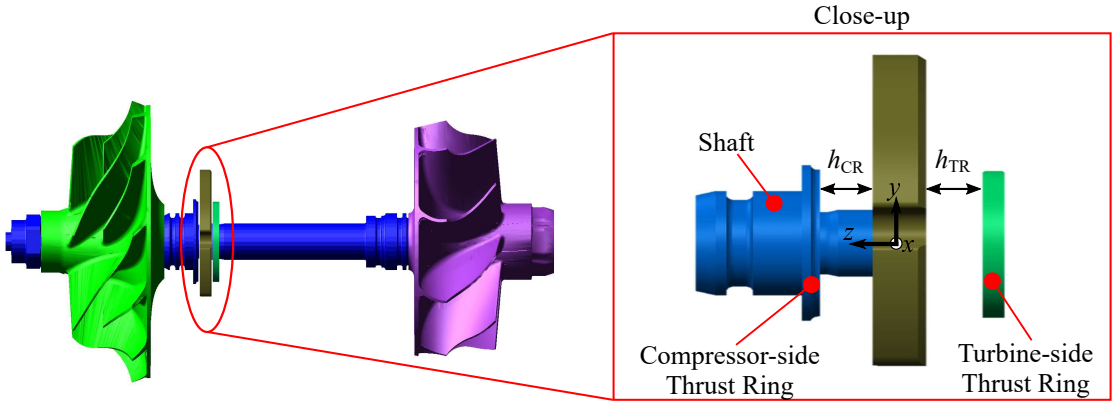

Figure 6.9: Turbocharger rotor and close-up of the thrust bearing and the thrust rings

of the rotor can be seen at a frequency of $f \approx 2100\,\text{Hz}$. Towards the end of this operating point, the oil-film thickness h_{CR} is increasing and the oil-film thickness h_{TR} is decreasing attaining $h_{\text{TR}} = h_{\text{CR}}$ in operating point 2.

- **Operating Point 2:** The rotor is displaced in the axial z-direction at $z = 0\,\mu m$. The thrust bearing has an almost equal distance between the thrust ring from the compressor-side and the thrust ring from the turbine-side ($h_{\text{TR}} = h_{\text{CR}}$) and the resultant thrust bearing forces are almost zero. It is obvious that the gas forces acting in axial direction have a resultant magnitude of almost $0\,\text{N}$ at this stage. Moreover, both oil-film thicknesses at this position are rather high, producing insignificant thrust bearing forces and therefore, the thrust bearing (its stiffness and damping properties) may in general be neglected. At this operating point, the frequencies of the subsynchronous oscillations have slightly decreased (a $50\,\text{Hz}$ decrease in the frequency of *sub 2* and a $70\,\text{Hz}$ decrease in the frequency of *sub 3* is observed) but their amplitudes have significantly increased at $0.018\,\text{mm}$ for *sub 2* and at $0.079\,\text{mm}$ for *sub 3*.

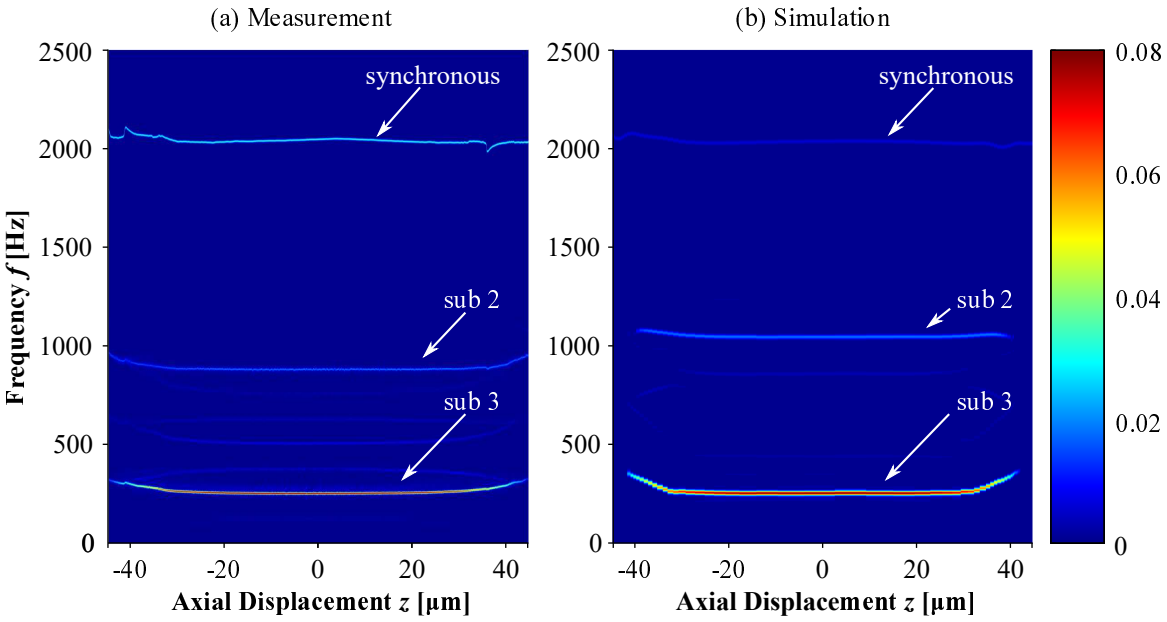

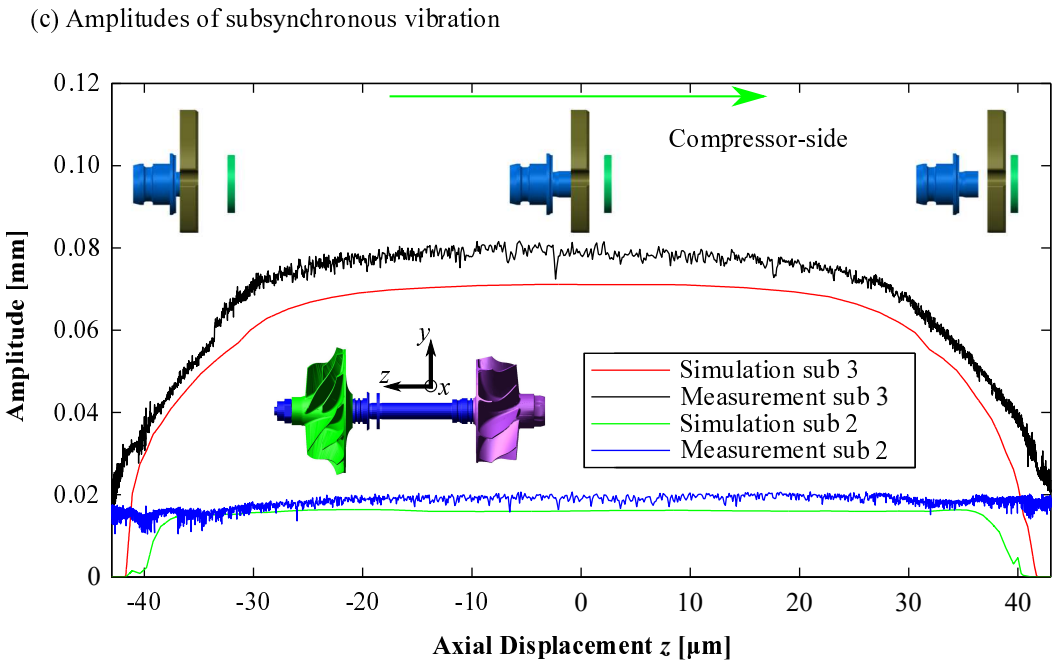

Figure 6.10: (a) Measured and (b) simulated rotor vibrations at the measuring point (shaft nut); (c) Amplitudes of the measured and the simulated subsynchronous vibrations *sub 2* and *sub 3*

- **Operating Point 3:** The rotor is displaced in the axial z-direction towards the compressor wheel ($z = 40\,\mu m$). The oil-film thickness at the compressor-side thrust ring is now $h_{CR} \approx 85\,\mu m$ and at the turbine-side thrust ring $h_{TR} \approx 3\,\mu m$. As it can be seen, the frequencies of the subsynchronous vibrations are slightly increased and their amplitudes are decreased to the same values as in operating point 1.

From the above, it is clear that the thrust bearing influences the amplitude and also the frequency of the subsynchronous vibrations of the rotor. Comparing the measurement results with the numerical simulations, a good agreement may be observed. The amplitudes of the subsynchronous vibrations (*sub 2* and *sub 3*) obtained experimentally have approximately the same amplitudes as those obtained from the simulations. The *sub 3* is encountered at the same frequency both in the experiment and the simulation. The *sub 2* is predicted at a slightly higher frequency in the simulation.

Chapter 7

Conclusions

Exhaust gas turbochargers are extensively used in automotive industry for improving the efficiency of the engine and for lowering the fuel consumption and emissions. The understanding of their rotordynamic and acoustic behavior is mandatory for improving their stability and noise problems. Moreover, the performance of the thrust and the radial bearings can be boosted, namely, their load capacity and their friction losses, allowing for their safe operation without significant wear. Therefore, in this work, thermohydrodynamic bearing modeling approaches were developed both for the radial and the thrust bearings and their influence on the vibration behavior of turbocharger rotors was identified.

The theoretical remarks for both bearing types under hydrodynamic lubrication were discussed in detail. Different modeling accuracy levels − ranging from very accurate to very time-efficient − and modeling approaches − isothermal/thermal, 2D/3D, coupled/decoupled and global/local − were exhaustively investigated. Moreover, the time-efficiency and the accuracy of each model was also shown. A novel semi-analytical solution for the radial bearings using the Global Galerkin approach was proposed. Its novelty is not only highlighted through the reduction in the computation time, but mainly through its ability to couple − in a very efficient way − with a global thermal energy balance model.

The coupling of the hydrodynamics (thrust and radial bearings) with multibody dynamics (rotor and floating rings) in a multibody simulation software was presented. The influence of the thrust and the radial bearing stiffness on the linear vibration modes (conical, cylindrical and first bending mode) of a turbocharger rotor was also discussed.

The time-efficient thermohydrodynamic bearing models were utilized in run-up simulations of a turbocharger rotor. An example of the influence of the oil-supply pressure on the subsynchronous rotor vibrations supported in bearings with circumferential oil-groove was discussed. For the thrust bearing, several studies were presented for identifying the effects of the external axial force, the number of bearing pads as well as the influence of the oil-viscosity on the rotor vibrations. Comparisons between thermohydrodynamic and isothermal models were also shown.

An optimization procedure for thrust bearings in stationary as well as in transient operations was developed. The newly proposed transient optimization approach was

proven to increase the load capacity of the bearing, to lower the friction losses and mainly to act positively towards subsynchronous vibrations by lowering their amplitude and shifting them to higher rotational speeds. The optimization procedure used statistical methods and neural networks instead of an optimizer.

This work was concluded with the experimental validation for both the thrust and the radial bearing models. For the validation of the thrust bearing a special experimental set-up was created. Standard shaft-motion tests were performed for the radial bearing validation. Simulation results were in agreement with the experiments, both for the synchronous and the subsynchronous vibrations. The amplitude, the frequency as well as the onset point of the subsynchronous vibrations were correctly captured in the simulations.

Coupled nonlinear systems with fluid-structure interactions like the turbocharger rotors necessitate further modeling improvements. For radial bearings, mass-conserving cavitation algorithms should be used for a more precise description of the hydrodynamic lubrication. The selection of such an approach will also influence the oil-temperature predictions through the thermohydrodynamic modeling. The influence of the cavitation algorithm on the rotor vibrations, however, will not be very large since the cavitation algorithm used in this work has produced an excellent correlation with the experimental results. Another important issue is the hydraulic pressure coupling between the inner and the outer oil-film. As this coupling will affect both pressure distributions, it is expected to play also a role on the vibration of the rotor. The implementation of mass-conserving algorithms applies also for the thrust bearings. The flexibility of the bearing pads as well as a flexible connection between the thrust bearing and the bearing housing should also be considered. Additionally, wear models could also be developed to identify the influence of the pad wear on the dynamics of the system. Another important aspect in thrust bearings is the modeling of the oil-supply holes, which was neglected in the present work. The mixing between fresh oil coming from the engine and oil coming from a previous pad is always an open issue in thrust bearings. Considering thermal effects, the thermal energy exchange between the thrust bearing and the oil-film as well as the thermal expansion of the thrust bearing and its pads could also be modeled as they may play a role on the turbocharger rotor vibrations during a run-up.

The experimental validation of both the thrust and the radial bearing modeling gives a great confidence at this work, that the main dynamic effects are adequately captured with the existing modeling. However, modeling advancements towards an improved physical and numerical accuracy will always be required.

Bibliography

[1] Alakhramsing, S.; van Ostayen, R.; Eling, R.: Thermo-hydrodynamic analysis of a plain journal bearing on the basis of a new mass conserving cavitation algorithm. In: *Lubricants* 3 (2015).

[2] Almqvist, T.; Glavatskikh, S. B.; Larsson, R.: THD analysis of tilting pad thrust bearings – Comparison between theory and experiments. In: *Journal of Tribology* 122 (1999), pp. 412–417.

[3] Amestoy, P. R.; Duff, I. S.; Koster, J.; L'Excellent, J.-Y.: A fully asynchronous multifrontal solver using distributed dynamic scheduling. In: *SIAM Journal on Matrix Analysis and Applications* 23 (2001), pp. 15–41.

[4] Amestoy, P. R.; Guermouche, A.; L'Excellent, J.-Y.; Pralet, S.: Hybrid scheduling for the parallel solution of linear systems. In: *Parallel Computing* 32 (2006), pp. 136–156.

[5] Argyris, J.; Scharpf, D.: Finite Element formulation of the incompressible lubrication problem. In: *Nuclear Engineering and Design* 11 (1970), pp. 225 – 229.

[6] Barrett, L. E.; Allaire, P. E.; Gunter, E. J.: A finite length bearing correction factor for short bearing theory. In: *Journal of Lubrication Technology* 102 (1980), pp. 283–287.

[7] Bergman, T. L.; Incropera, F. P.; DeWitt, D. P.; Lavine, A. S.: *Fundamentals of heat and mass transfer*. John Wiley & Sons, 2011.

[8] Boddy, R.; Smith, G.: *Statistical methods in practice: For scientists and technologists*. John Wiley & Sons, 2009.

[9] Boncompain, R.; Fillon, M.; Frene, J.: Analysis of thermal effects in hydrodynamic bearings. In: *Journal of Tribology* 108 (1986), pp. 219–224.

[10] Boyaci, A.; Hetzler, H.; Seemann, W.; Proppe, C.; Wauer, J.: Analytical bifurcation analysis of a rotor supported by floating ring bearings. In: *Nonlinear Dynamics* 57 (2009), pp. 497–507.

[11] Boyaci, A.: *Zum Stabilitäts- und Bifurkationsverhalten hochtouriger Rotoren in Gleitlagern*. KIT Scientific Publishing, 2011.

[12] Boyaci, A.; Lu, D.; Schweizer, B.: Stability and bifurcation phenomena of Laval/Jeffcott rotors in semi-floating ring bearings. In: *Nonlinear Dynamics* 79 (2015), pp. 1535–1561.

[13] Boyaci, A.; Seemann, W.; Proppe, C.: Bifurcation analysis of a turbocharger rotor supported by floating ring bearings. In: *IUTAM Symposium on Emerging Trends in Rotor Dynamics* Springer, 2011, pp. 335–347.

[14] Buuren, S. v.: *Modeling and simulation of porous journal bearings in multibody systems*. KIT Scientific Publishing, 2013.

[15] Capone, G.: Analytical description of fluid-dynamic force field in cylindrical journal bearing. In: *L'Energia Elettrica* 3 (1991), pp. 105–110.

[16] Castro, H. F. d.; Cavalca, K. L.; Nordmann, R.: Whirl and whip instabilities in rotor-bearing system considering a nonlinear force model. In: *Journal of Sound and Vibration* 317 (2008), pp. 273 – 293.

[17] Chasalevris, A.: Finite length floating ring bearings: Operational characteristics using analytical methods. In: *Tribology International* 94 (2016), pp. 571 – 590.

[18] Chasalevris, A.; Papadopoulos, C.: A novel semi-analytical method for the dynamics of nonlinear rotor-bearing systems. In: *Mechanism and Machine Theory* 72 (2014), pp. 39 – 59.

[19] Chasalevris, A.; Sfyris, D.: On the analytical evaluation of the lubricant pressure in the finite journal bearing. In: *ASME 2012 International Design Engineering Technical Conferences and Computers and Information in Engineering Conference* American Society of Mechanical Engineers, 2012, pp. 661–671.

[20] Chasalevris, A.; Sfyris, D.: Evaluation of the finite journal bearing characteristics, using the exact analytical solution of the Reynolds equation. In: *Tribology International* 57 (2013), pp. 216 – 234.

[21] Chatzisavvas, I.; Boyaci, A.; Schweizer, B.: Efficient thrust bearing model for high-speed rotordynamic applications. In: *Proceedings of the 9th IFToMM International Conference on Rotor Dynamics*, Springer International Publishing, 2015 (Mechanisms and Machine Science), pp. 969–980.

[22] Chatzisavvas, I.; Boyaci, A.; Koutsovasilis, P.; Schweizer, B.: Influence of the oil temperature of thrust bearings on the vibratory behavior of small

turbochargers. In: *Proceedings of the International Conference on Engineering Vibration*, 2015.

[23] Chatzisavvas, I.; Boyaci, A.; Koutsovasilis, P.; Schweizer, B.: Influence of hydrodynamic thrust bearings on the nonlinear oscillations of high-speed rotors. In: *Journal of Sound and Vibration* 380 (2016), pp. 224 – 241.

[24] Chatzisavvas, I.; Boyaci, A.; Lehn, A.; Mahner, M.; Koutsovasilis, P.; Schweizer, B.: On the influence of thrust bearings on the nonlinear rotor vibrations of turbochargers. In: *Proceedings of ASME Turbo Expo 2016: Turbomachinery Technical Conference and Exposition*, 2016.

[25] Chatzisavvas, I.; Nowald, G.; Schweizer, B.; Koutsovasilis, P.: Experimental and numerical investigations of turbocharger rotors on full-floating ring bearings with circumferential oil-groove. In: *ASME Turbo Expo 2017: Turbomachinery Technical Conference and Exposition*, 2017.

[26] Chen, C. M.; Dareing, D. W.: The contribution of fluid film inertia to the thermohydrodynamic lubrication of sector-pad thrust bearings. In: *Journal of Tribology* 98 (1976), pp. 125–132.

[27] Childs, D. W.: *Turbomachinery rotordynamics: Phenomena, modeling, and analysis*. John Wiley & Sons, 1993.

[28] Clarke, D. M.; Fall, C.; Hayden, G. N.; Wilkinson, T. S.: A steady-state model of a floating ring bearing, including thermal effects. In: *Journal of Tribology* 114 (1992), pp. 141–149.

[29] Craig Jr., R. R.; Bampton, M. C. C.: Coupling of substructures for dynamic analyses. In: *AIAA Journal* 6 (1968), pp. 1313–1319.

[30] Dadouche, A.; Fillon, M.; Bligoud, J.: Experiments on thermal effects in a hydrodynamic thrust bearing. In: *Tribology International* 33 (2000), pp. 167 – 174.

[31] Dadouche, A.; Fillon, M.; Dmochowski, W.: Performance of a hydrodynamic fixed geometry thrust bearing: Comparison between experimental data and numerical results. In: *Tribology Transactions* 49 (2006), pp. 419–426.

[32] Daniel, C.; Göbel, S.; Nitzschke, S.; Woschke, E.; Strackeljan, J.: Numerical simulation of the dynamic behaviour of turbochargers under consideration of full-floating-ring bearings and ball bearings. In: *11th international conference on vibration problems*, 2013.

[33] Davis, T. A.: *Direct methods for sparse linear systems*. Vol. 2. Siam, 2006.

[34] Davis, T. A.; Duff, I. S.: An unsymmetric-pattern multifrontal method for sparse LU factorization. In: *SIAM Journal on Matrix Analysis and Applications* 18 (1997), pp. 140–158.

[35] DIN 31653 Teil 2: *Gleitlager; Hydrodynamische Axial-Gleitlager im stationären Betrieb; Funktionen für die Berechnungen von Axialsegmentlagern.* 1991.

[36] Dowson, D.: A generalized Reynolds equation for fluid-film lubrication. In: *International Journal of Mechanical Sciences* 4 (1962), pp. 159 – 170.

[37] Dowson, D.; March, C. N.: A thermohydrodynamic analysis of journal bearings. In: *Proceedings of the Institution of Mechanical Engineers, Conference Proceedings* 181 (1966), pp. 117–126.

[38] Dowson, D.; Taylor, C. M.: Cavitation in bearings. In: *Annual Review of Fluid Mechanics* 11 (1979), pp. 35–65.

[39] Eling, R.; te Wierik, M.; van Ostayen, R.; Rixen, D.: Towards accurate prediction of unbalance response, oil whirl and oil whip of flexible rotors supported by hydrodynamic bearings. In: *Lubricants* 4 (2016).

[40] Elrod, H. G.: A cavitation algorithm. In: *Journal of Lubrication Technology* 103 (1981), pp. 350–354.

[41] Elrod, H.: Efficient numerical method for computation of the thermohydrodynamics of laminar lubricating films. In: *Journal of Tribology* 113 (1991), pp. 506–511.

[42] Ezzat, H. A.; Rohde, S. M.: A study of the thermohydrodynamic performance of finite slider bearings. In: *Journal of Lubrication Technology* 95 (1973), pp. 298–307.

[43] Ferron, J.; Frene, J.; Boncompain, R.: A study of the thermohydrodynamic performance of a plain journal bearing comparison between theory and experiments. In: *Journal of Tribology* 105 (1983), pp. 422–428.

[44] Fesanghary, M.; Khonsari, M.: On the modeling and shape optimization of hydrodynamic flexible-pad thrust bearings. In: *Proceedings of the IMechE* 227 (2012), pp. 548–558.

[45] Fesanghary, M.; Khonsari, M.: Topological and shape optimization of thrust bearings for enhanced load-carrying capacity. In: *Tribology International* 53 (2012), pp. 12 – 21.

[46] Fillon, M.; Desbordes, H.; Frene, J.; Wai, C. C. H.: A global approach of thermal effects including pad deformations in tilting-pad journal bearings submitted to unbalance load. In: *Journal of Tribology* 118 (1996), pp. 169–174.

[47] Fogg, A.: Fluid film lubrication of parallel thrust surfaces. In: *Proceedings of the Institution of Mechanical Engineers* 155 (1946), pp. 49–67.

[48] Frene, J. (Ed.); Nicolas, D. (Ed.); Degueurce, B. (Ed.); Berthe, D. (Ed.); Godet, M. (Ed.): *Tribology Series*. Vol. 33: *Hydrodynamic lubrication: Bearings and thrust bearings*. Elsevier, 1997.

[49] Gasch, R.; Nordmann, R.; Pfützner, H.: *Rotordynamik*. Springer-Verlag, 2005.

[50] Gear, C.; Leimkuhler, B.; Gupta, G.: Automatic integration of Euler-Lagrange equations with constraints. In: *Journal of Computational and Applied Mathematics* 12 (1985), 77 - 90.

[51] Hamrock, B. J.; Schmid, S. R.; Jacobson, B. O.: *Fundamentals of fluid film lubrication*. Vol. 169. CRC press, 2004.

[52] Hashimoto, H.: The effects of fluid inertia forces on the static characteristics of sector-shaped, high-speed thrust bearings in turbulent flow regime. In: *Journal of Tribology* 111 (1989), pp. 406–412.

[53] Heinrichson, N.; Fuerst, A.; Santos, I. F.: The influence of injection pockets on the performance of tilting-pad thrust bearings – Part II: Comparison between theory and experiment. In: *Journal of Tribology* 129 (2007), pp. 904–912.

[54] Heinrichson, N.; Santos, I. F.; Fuerst, A.: The influence of injection pockets on the performance of tilting-pad thrust bearings – Part I: Theory. In: *Journal of Tribology* 129 (2007), pp. 895–903.

[55] Henry, Y.; Bouyer, J.; Fillon, M.: An experimental hydrodynamic thrust bearing device and its application to the study of a tapered-land thrust bearing. In: *Journal of Tribology* 136 (2014).

[56] Heshmat, H.; Pinkus, O.: Mixing inlet temperatures in hydrodynamic bearings. In: *Journal of Tribology* 108 (1986), pp. 231–244.

[57] Heshmat, H.; Pinkus, O.: Misalignment in thrust bearings including thermal and cavitation effects. In: *Journal of Tribology* 109 (1987), pp. 108–114.

[58] Hoepke, B.; Uhlmann, T.; Pischinger, S.; Lueddecke, B.; Filsinger, D.: Analysis of thrust bearing impact on friction losses in automotive turbochargers. In: *Journal of Engineering for Gas Turbines and Power* 137 (2015).

[59] Hori, Y.: *Hydrodynamic lubrication.* Springer Tokyo, 2006.

[60] Hotelling, H.: New light on the correlation coefficient and its transforms. In: *Journal of the Royal Statistical Society. Series B (Methodological)* 15 (1953), pp. 193–232.

[61] Huebner, K. H.: Solution for the pressure and temperature in thrust bearings operating in the thermohydrodynamic turbulent regime. In: *J. of Lubrication Tech* 96 (1974), pp. 58–68.

[62] Huebner, K. H.: A three-dimensional thermohydrodynamic analysis of sector thrust bearings. In: *A S L E Transactions* 17 (1974), pp. 62–73.

[63] Jiang, P.; Yu, L.: Dynamics of a rotor-bearing system equipped with a hydrodynamic thrust bearing. In: *Journal of Sound and Vibration* 227 (1999), pp. 833 – 872.

[64] Khonsari, M. M.; Booser, E. R.: *Applied tribology: Bearing design and lubrication.* John Wiley & Sons, 2008.

[65] Kim, K. W.; Tanaka, M.; Hori, Y.: A three-dimensional analysis of thermohydrodynamic performance of sector-shaped, tilting-pad thrust bearings. In: *Journal of Tribology* 105 (1983), pp. 406–412.

[66] Kirk, R. G.; Alsaeed, A.; Mondschein, B.: Turbocharger vibration shows nonlinear jump. In: *Journal of Vibration and Control* 18 (2012), pp. 1454–1461.

[67] Kohonen, T.: The self-organizing map. In: *Proceedings of the IEEE* 78 (1990), pp. 1464–1480.

[68] Kohonen, T.: The self-organizing map. In: *Neurocomputing* 21 (1998), 1 - 6.

[69] Koutsovasilis, P.: *Model order reduction in structural mechanics: Coupling the rigid and elastic multi body dynamics.* Vol. 712. VDI Verlag, 2009.

[70] Koutsovasilis, P.; Beitelschmidt, M.: Model order reduction of Finite Element models: Improved component mode synthesis. In: *Mathematical and Computer Modelling of Dynamical Systems* 16 (2010), pp. 57–73.

[71] Koutsovasilis, P.: Improved component mode synthesis and variants. In: *Multibody System Dynamics* 29 (2013), pp. 343–359.

[72] Koutsovasilis, P.; Driot, N.; Lu, D.; Schweizer, B.: Quantification of subsynchronous vibrations for turbocharger rotors with full-floating ring bearings. In: *Archive of Applied Mechanics* 85 (2015), pp. 481–502.

[73] Lehn, A.; Schweizer, B.: Generalized Reynolds equation for fluid film problems with arbitrary boundary conditions: Application to double-sided spiral groove thrust bearings. In: *Archive of Applied Mechanics* (2015), pp. 1 – 18.

[74] Liu, S.; Mou, L.: Hydrodynamic lubrication of thrust bearings with rectangular fixed-incline-pads. In: *Journal of Tribology* 134 (2012).

[75] Mahner, M.; Lehn, A.; Schweizer, B.: Thermogas- and thermohydrodynamic simulation of thrust and slider bearings: Convergence and efficiency of different reduction approaches. In: *Tribology International* (2015), pp. 539 – 554.

[76] McCallion, H.; Yousif, F.; Lloyd, T.: The analysis of thermal effects in a full journal bearing. In: *Journal of Tribology* 92 (1970), pp. 578–587.

[77] McKay, M. D.; Beckman, R. J.; Conover, W. J.: A comparison of three methods for selecting values of input variables in the analysis of output from a computer code. In: *Technometrics* 21 (1979), pp. 239–245.

[78] Mittwollen, N.; Hegel, T.; Glienicke, J.: Effect of hydrodynamic thrust bearing on lateral shaft vibrations. In: *Journal of Tribology* 113(4) (1991), pp. 811–817.

[79] Mori, A.; Tanaka, K.; Mori, H.: Effects of fluid inertia forces on the performance of a plane inclined sector pad for an annular thrust bearing under laminar condition. In: *Journal of Tribology* 107 (1985), pp. 46–52.

[80] Muszynska, A.: Whirl and whip – Rotor/bearing stability problems. In: *Journal of Sound and Vibration* 110 (1986), pp. 443 – 462.

[81] Muszynska, A.: *Rotordynamics*. CRC, 2005.

[82] Newkirk, B.; Taylor, H.: Shaft whipping due to oil action in journal bearings. In: *General Electric Review* 28 (1925), pp. 559–568.

[83] Nicoletti, R.: Comparison between a meshless method and the finite difference method for solving the Reynolds equation in finite bearings. In: *Journal of Tribology* 135 (2013), pp. 044501(9).

[84] Nowald, G.; Boyaci, A.; Schmoll, R.; Koutsovasilis, P.; Schweizer, B.: Influence of circumferential grooves on the non-linear oscillations of turbocharger rotors in floating ring bearings. In: *Proceedings of the 14th IFToMM World Congress*, 2015, pp. 447–453.

[85] Nowald, G.; Boyaci, A.; Schmoll, R.; Koutsovasilis, P.; Driot, N.; Schweizer, B.: Influence of axial grooves in full-floating-ring bearings on the nonlinear oscillations of turbocharger rotors. In: *11th Conference on Vibrations in Rotating Machines*, 2015.

[86] Ocvirk, F. W.: *Short-bearing approximation for full journal bearings.* Technical note 2808, National advisory committee for aeronautics, 1952.

[87] Papadopoulos, C. I.; Efstathiou, E. E.; Nikolakopoulos, P. G.; Kaiktsis, L.: Geometry optimization of textured three-dimensional micro- thrust bearings. In: *Journal of Tribology* 133 (2011).

[88] Papadopoulos, C. I.; Kaiktsis, L.; Fillon, M.: Computational fluid dynamics thermohydrodynamic analysis of three-dimensional sector-pad thrust bearings with rectangular dimples. In: *Journal of Tribology* 136 (2013).

[89] Pinkus, O.: *Thermal aspects of fluid film tribology.* American Society of Mechanical Engineers, 1990.

[90] Pinkus, O.; Sternlicht, B.: *Theory of hydrodynamic lubrication.* McGraw-Hill, 1961.

[91] Pinkus, O.; Bupara, S. S.: Adiabatic solutions for finite journal bearings. In: *Journal of Lubrication Technology* 101 (1979), pp. 492–496.

[92] Pinkus, O.; Lund, J. W.: Centrifugal effects in thrust bearings and seals under laminar conditions. In: *Journal of Tribology* 103 (1981), pp. 126–136.

[93] Porzig, D.: *Systemspezifische Schmierfilmdissipation in den radialen Lagerstellen von Abgasturboladern.* Shaker, 2015.

[94] Rahmani, R.; Shirvani, A.; Shirvani, H.: Optimization of partially textured parallel thrust bearings with square-shaped micro-dimples. In: *Tribology Transactions* 50 (2007), pp. 401–406.

[95] Raimondi, A. A.: An adiabatic solution for the finite slider bearing (L/B = 1). In: *A S L E Transactions* 9 (1966), pp. 283–298.

[96] Reddi, M. M.: Finite-Element solution of the incompressible lubrication problem. In: *Journal of Lubrication Technology* 91 (1969), pp. 524–533.

[97] Riemann, B.; Perini, E. A.; Cavalca, K. L.; Castro, H. F.; Rinderknecht, S.: Oil whip instability control using μ-synthesis technique on a magnetic actuator. In: *Journal of Sound and Vibration* 332 (2013), pp. 654 – 673.

[98] Rohde, S. M.; Li, D. F.: A generalized short bearing theory. In: *Journal of Lubrication Technology* 102 (1980), pp. 278–281.

[99] San Andres, L.; Kerth, J.: Thermal effects on the performance of floating ring bearings for turbochargers. In: *Proceedings of the Institution of Mechanical Engineers, Part J: Journal of Engineering Tribology* 218 (2004), pp. 437–450.

[100] San Andres, L.; Barbarie, V.; Bhattacharya, A.; Gjika, K.: On the effect of thermal energy transport to the performance of (semi) floating ring bearing systems for automotive turbochargers. In: *Journal of Engineering for Gas Turbines and Power* 134 (2012).

[101] Schweizer, B.: Oil whirl, oil whip and whirl/whip synchronization occurring in rotor systems with full-floating ring bearings. In: *Nonlinear Dynamics* 57 (2009), pp. 509–532.

[102] Schweizer, B.: Total instability of turbocharger rotors – Physical explanation of the dynamic failure of rotors with full-floating ring bearings. In: *Journal of Sound and Vibration* 328 (2009), pp. 156 – 190.

[103] Schweizer, B.: Dynamics and stability of turbocharger rotors. In: *Archive of Applied Mechanics* 80 (2010), pp. 1017–1043.

[104] Schweizer, B.; Sievert, M.: Nonlinear oscillations of automotive turbocharger turbines. In: *Journal of Sound and Vibration* 321 (2009), pp. 955 – 975.

[105] Sfyris, D.; Chasalevris, A.: An exact analytical solution of the Reynolds equation for the finite journal bearing lubrication. In: *Tribology International* 55 (2012), pp. 46 – 58.

[106] Shabana, A. A.: *Dynamics of multibody systems*. Cambridge university press, 2013.

[107] Simeon, B.: *Computational flexible multibody dynamics: A differential-algebraic approach*. Springer Science & Business Media, 2013.

[108] Someya, I. T.: Stabilität einer in zylindrischen Gleitlagern laufenden, unwuchtfreien Welle. In: *Ingenieur-Archiv* 33 (1963), pp. 85–108.

[109] Song, Y.; Ren, X.; Gu, C.-W.; Li, X.-S.: Experimental and numerical studies of cavitation effects in a tapered land thrust bearing. In: *Journal of Tribology* 137 (2014).

[110] Storteig, E.; White, M. F.: Dynamic characteristics of hydrodynamically lubricated fixed-pad thrust bearings. In: *Wear* 232 (1999), pp. 250 – 255.

[111] Suh, J.; Palazzolo, A.: Three-dimensional dynamic model of TEHD tilting-pad journal bearing – Part I: Theoretical modeling. In: *Journal of Tribology* 137 (2015).

[112] Sunami, Y.; Ibrahim, M. D.; Hashimoto, H.: Optimum design of oil lubricated thrust bearing for hard disk drive with high speed spindle motor. In: *International Journal of Rotating Machinery* 2013 (2013).

[113] Szeri, A. Z.: *Fluid film lubrication.* Cambridge University Press, 2010.

[114] Tanaka, M.: Thermohydrodynamic performance of a tilting pad journal bearing with spot lubrication. In: *Journal of Tribology* 113 (1991), pp. 615–619.

[115] Tian, L.; Wang, W.; Peng, Z.: Dynamic behaviours of a full floating ring bearing supported turbocharger rotor with engine excitation. In: *Journal of Sound and Vibration* 330 (2011), pp. 4851 – 4874.

[116] Tian, L.; Wang, W.; Peng, Z.: Effects of bearing outer clearance on the dynamic behaviours of the full floating ring bearing supported turbocharger rotor. In: *Mechanical Systems and Signal Processing* 31 (2012), pp. 155 – 175.

[117] Tian, L.; Wang, W.; Peng, Z.: Nonlinear effects of unbalance in the rotor-floating ring bearing system of turbochargers. In: *Mechanical Systems and Signal Processing* 34 (2013), pp. 298 – 320.

[118] Varela, A. C.; Fillon, M.; Santos, I. F.: On the simplifications for the thermal modeling of tilting-pad journal bearings under thermoelastohydrodynamic regime. In: *ASME Turbo Expo 2012: Turbine Technical Conference and Exposition* American Society of Mechanical Engineers, 2012, pp. 823–835.

[119] Vieira, L.; Cavalca, K.; Nomura, P.: Analysis of stiffness and damping coefficients of lubricated thrust bearings. In: *Vibration Problems ICOVP 2011: the 10th International Conferenceon Vibration Problems* ICOVP 2011 Supplement.

[120] Vieira, L. C.; Watanabe, P. N.; Cavalca, K. L.: Analysis of the influence of fluid temperature variation on the behavior of turbocharger lubricated thrust bearings. In: *Proceedings of the 9th IFToMM International Conference on Rotor Dynamics* Springer, 2015, pp. 1091–1101.

[121] Wodtke, M.; Schubert, A.; Fillon, M.; Wasilczuk, M.; Paj?czkowski, P.: Large hydrodynamic thrust bearing: Comparison of the calculations and measurements. In: *Proceedings of the Institution of Mechanical Engineers, Part J: Journal of Engineering Tribology* (2014).

[122] Woschke, E.; Daniel, C.; Nitzschke, S.; Strackeljan, J.: Numerical run-up simulation of a turbocharger with full floating ring bearings. In: *Vibration Problems ICOVP 2011: the 10th International Conferenceon Vibration Problems* ICOVP 2011 Supplement, 2011, pp. 334–339.

[123] Woschke, E.; Göbel, S.; Nitzschke, S.; Daniel, C.; Strackeljan, J.: Influence of bearing geometry of automotive turbochargers on the nonlinear vibrations during run-up. In: *Proceedings of the 9th IFToMM International Conference on Rotor Dynamics* Springer, 2015, pp. 835–844.

[124] Yamamoto, T.; Ishida, Y.: *Linear and nonlinear rotordynamics: A modern treatment with applications*. Vol. 11. John Wiley & Sons, 2001.

[125] Yu, Q.; Jr., T. G. K.: A boundary element cavitation algorithm. In: *Tribology Transactions* 37 (1994), pp. 217–226.